IAHR
AIRH

IAHR
2017

Supported by
Spain Water
and IWHR, China

37th IAHR
WORLD CONGRESS
13-18 August, 2017
Kuala Lumpur, Malaysia

FLOOD DISASTER AND ADAPTATION MEASURES

DEBRIS DYNAMICS AND ASSOCIATED LOADS IN EXTREME HYDRODYNAMIC CONDITIONS

JACOB STOLLE[(1)], NILS GOSEBERG[(2)], CAREN DERSCHUM[(3)], IOAN NISTOR[(4)] & EMIL PETRIU[(5)]

[(1, 4)] Department of Civil Engineering, University of Ottawa, Ottawa, Canada,
jstol065@uottawa.ca (corresponding author), inistor@uottawa.ca
[(2)] Ludwig-Franzius-Institute for Hydraulic, Estuarine and Coastal Engineering,
Leibniz Universität Hannover, Hannover, Germany,
contact@nilsgoseberg.de
[(3)] Department of Architecture, Civil Engineering, and Environmental Science,
Technische Universität Braunschweig, Braunschweig, Germany,
c.derschum@tu-braunschweig.de
[(5)] School of Electrical Engineering and Computer Science,
University of Ottawa, Ottawa, Canada,
petriu@uottawa.ca

ABSTRACT

Large-scale tsunamis are devastating to local coastal communities. Recent events, such as the 2004 Indian Ocean and the 2011 Tohoku Tsunami, have brought to the forefront of research the evaluation of the loads associated with such extreme events. Among the various loads associated with tsunamis, debris entrained within the inundating flows result in loads that are also an important consideration in the design of resilient infrastructure. Current research into debris loads has primarily focused on single debris impacts on structures. This paper presents a study, performed in a dam-break flume at the University of Ottawa (Ottawa, Canada), examining multiple debris motion and impacts on structures. The study compares the debris spreading and loads to currently available design standard. Additionally, the study examines the effect of the hydrodynamic boundary conditions and the number of debris on the debris spreading and the associated loads observed. From the experiments, the authors concludes that the debris spreading and impact velocity was influenced by both the number of debris and by the hydrodynamic boundary conditions. The study also found that the impact of multiple debris results in larger impact forces than those predicted by current design standards.

Keywords: Debris; tsunami; coastal flooding; impact forces; debris motion.

1   INTRODUCTION

Over the past several decades, devastating tsunamis, such as the 2004 Indian Ocean, the 2011 Tohoku Japan, and the 2010 and 2015 Chile, as well as many other extreme hydrodynamic events have led to a push towards the building and design infrastructure resilient to these events (Comfort, 2006). Analysis of the current building codes available for the design of coastal communities have shown that many building codes have failed to explicitly address tsunami load and effects (Esteban et al., 2015). As a result, recent research has made an attempt to understand the various loading conditions within these extreme hydrodynamic events. Yeh et al. (2014) identified, following a field investigation of the 2011 Tohoku Tsunami, that, in addition to the hydraulic loads associated with the inundating tsunami wave, debris loading was a critical load in the failure of many structures.

The focus of debris loads in extreme hydrodynamic conditions was on a single debris impacting a structure. Haehnel and Daly (2004) modelled the impact of a wood log on a structure as a one-degree-of-freedom model, where the structure was rigid and the impact was of short enough duration to neglect damping. The equation of this model is:

$$m_d\ddot{x}+kx=0 \qquad [1]$$

where m_d is the mass of the debris, x is the compression of the debris and of the structure, k is the effective stiffness of the impact. From Eq. [1], the solution for the maximum impact force (F_i) can be computed as:

$$F_i=u_i\sqrt{km_d} \qquad [2]$$

where u_i is the impact velocity of the debris. The effective-stiffness of the impact is a difficult term to quantify. Therefore, there are three methods of estimating the maximum impact force from Eq. [1]: work-energy, contact-stiffness, and impulse momentum. The difference between these models depend on the governing assumptions (Haehnel and Daly, 2002). Each solution requires the impact velocity and mass of the debris, while each method required one additional parameter to solve for the maximum impact force.

The work-energy approach has not been used since it required the stopping distance of the debris, which is a difficult parameter to estimate. Haehnel and Daly (2004) used the contact-stiffness approach, which requires an estimation of the effective stiffness of the impact (combination of the structure and debris stiffness). A full breakdown of the different methods is described in Nistor et al. (2017). The difficulty in assessing models for maximum debris impact in an experimental setting is that the debris does not uniformly impact the structure, due to impact angle or eccentricity of the debris on impact. Additionally, Eq. [1] does not account for fluid drag and inertia, resulting in an adjustment to Eq. [2]:

$$F_i = e\beta u_i\sqrt{k(m_d + Cm_f)} \qquad\qquad [3]$$

where e is the eccentricity of the debris, which can be calculated using the model for ice impact from Matskevitch (1997), β is the impact angle, C is the added mass coefficient, which depends on the debris' geometry, orientation, and degree of submergence, and m_f is the mass of the displaced fluid. Ko et al. (2015) performed in-air and in-water debris impact tests to evaluate the relevancy of the added mass coefficient and determined that the additional impact force was insignificant, with in-water maximum impact forces being less than 5% greater than in-air experiments. However, Shafiei et al. (2016) determined that the additional impact force was a function of the density of the debris (and therefore submergence) and found that the in-water maximum impact forces is up to 50% greater than that recorded for the in-air experiments, indicating proper scaling of the debris needs to be considered when evaluating the in-water impact forces.

The ASCE7 standard has recently released a new chapter (Chapter 6) detailing the loads and effects associated with tsunamis (Chock, 2016). Within this standard, the potential for large debris impact, such as shipping containers and shipping vessels, was evaluated based on a method developed from results from field surveys, performed by Naito et al. (2014), of the 2011 Tohoku Tsunami. The method conservatively estimated the potential impact area from a debris source to be a ±22.5^o angle from the geometric center of the debris source in the inundation direction. Following experimental work, Nistor et al. (2016) confirmed the conservative nature of this proposed spreading angle.

The examinations of multiple debris transport has shown that debris tended to propagate within similar sections of the surge (Yao et al., 2014; Goseberg et al., 2016; Nistor et al., 2016). The current ASCE7 guidelines only consider the design of debris loads for a single debris impact. The likelihood of simultaneous debris impact occurring could result in loads that far exceed the loads predicted from a single debris impact.

To further understand debris loads in tsunami flow conditions, this paper examines the transport of scaled-down shipping containers within tsunami-like flow conditions and the impact forces associated with the shipping containers impacting a structure. The objectives of this paper are to:

- Examine the effect of multiple debris on the transport of the debris, focusing on the effects on the trajectory and impact velocities of the debris.
- Examine the effect of the hydrodynamic boundary condition on the debris transport.
- Examine the effect of multiple debris impact on the maximum impact forces.

The paper is organized as follows: the section on "University of Ottawa Dam-break Facility" details the dam-break flume at the University of Ottawa, the instrumentation used in the experiments, the model debris; the section on "Debris Tracking" explains briefly the camera-based object tracking algorithm used to track the debris motion - a full description of this algorithm can be found in Stolle et al. (2016); the section on "Experimental Protocol" outlines the test matrix analyzed in this paper; while the "Hydrodynamics" examines the repeatability of the hydrodynamic conditions and compares the experimental results to an analytically derived dam-break solution (Ritter, 1892); the section on "Debris Motion" examines the trajectory and velocities of the debris and compares the effects of multiple debris and the hydrodynamic boundary; the section on "Debris Impact Forces" analyzes the maximum impact forces and examine the effects of multiple debris impact; and, finally, the "Discussion" and "Conclusions" sections place the current research in context of previous work and detail the potential next steps in examining debris impact forces.

2   EXPERIMENTAL SETUP

2.1   University of Ottawa dam-break facility

The experiments were performed in the Hydraulics Laboratory of the Department of Civil Engineering University of Ottawa, Canada. For these tests, the experiments were performed in a dam-break flume (DBF), 30 m long, 1.5 m wide, and 0.70 m deep (Figure 1). The reservoir was 21.55 m long and the water was impounded behind a swinging gate, placed on a 0.15 m false floor. The false floor was covered with fixed layer of 0.001 m sand grains, which resulted in an experimentally-determined Darcy-Weisbach friction factor (f) of 0.014. The swinging gate was manually opened to generate the dam-break wave; a counter weight was placed on the top of the gate to aid in the opening of the gate. This wave is compared to the analytical solution for dam-break waves in Section 3.1.

The spatial origin of the experiment (0, 0) was considered to be center of the flume at the upstream edge of gate. The positive y-axis was chosen in the flow direction, using a right-hand coordinate system, the positive x-direction was to the right and the positive z-direction was up.

The debris was placed on the false floor with the centroid of the furthest downstream debris placed center-flume (x = 0 m) at y = 3.20 m. The model of a structure, 0.20 m long, 0.20 m wide, and 0.80 m high, was placed center-flume at y = 7.03 m.
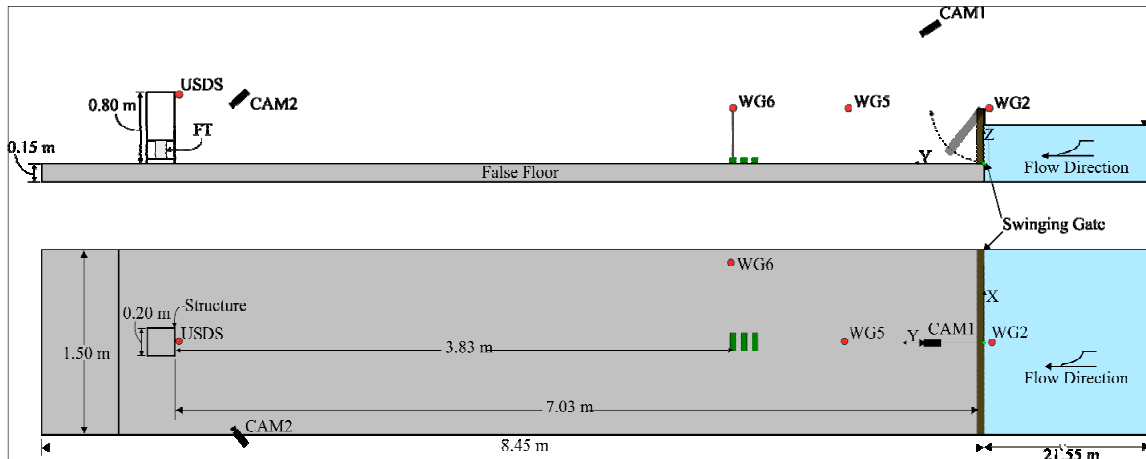
Figure 1. University of Ottawa Dam-break Flume (DBF). 30 m long x 1.5 m wide with a swinging gate. 0.65 m deep at the reservoir, 0.15 m false floor allowing for a maximum impoundment depth in the reservoir at the gate of 0.5 m.

2.1.1 Instrumentation

Figure 1 depicts the various instrumentation used in the DBF, on and around the structural models. One wave gauge (WG2) was placed inside the reservoir (RBR WG-50, capacitance-type) and located 0.01 m upstream of the swinging gate. WG2 was used as the reference gauge to determine the reference time for each experiment. The zero time of each experiment was considered to be at the time the water level began to drop at WG2. Two other wave gauges (WG5 and WG6) were placed at various positions on the false floor to measure the time-history of the water level as the dam-break wave propagated through the flume. Before the wave gauges were placed in the flume, they were calibrated ensuring R^2 values greater than 0.99. To measure the splash-up at the structure, an ultrasonic distance sensor (USDS) was placed right next at the front face of the structure.

Two high-definition cameras (CAM1 and CAM2) were mounted in the flume. CAM1 was mounted center-flume at a height of 2.95 m. The area of interest (AOI) of CAM1 extended the width of the flume from y = 3.00 m to y = 8.45 m. CAM2 was mounted at the edge of the flume at a height of 0.8 m above the flume bed. The AOI of CAM2 was the front of the structure to monitor the number of debris impacts and the water levels at the front and negative-x side of the structure.

The structure was mounted on a Force-Torque Transducer (FT) that could monitor the 3D loads and moments on the structure (x, y, and z-direction). The FT was bolted between two steel plates, which were fixed to the inner face of the structure. The plates were mounted on the false floor using four threaded rods. The mounting left a 0.01 m gap between the structure and the false floor to allow for free motion of the structure without interference from the floor. The FT was placed within the same coordinate system as described in Section 2.1.

2.1.2 Debris

The debris consisted of idealized 20-foot shipping containers (ISO668/688) down-scaled based on Froude scaling at a length scale of 1 in 40. The down-scaled shipping containers were manufactured from positively buoyant polyethylene (PE-HMW, 0.92 g/cm³). Each down-scaled shipping container had overall dimensions of 0.06 x 0.06 x 0.15 m with an approximate draft of 0.025 m.

2.2 Debris tracking

A camera-based image processing algorithm was developed for the tracking of multiple uniform debris in high-velocity flow (Stolle et al., 2016). The objective of the algorithm was to quickly and accurately track the debris through the AOI to provide high-quality data of the motion of the debris. The algorithm used raw images from the camera and using image processing techniques, the authors determined the position and orientation of the debris within each frame. The algorithm was validated using a manual image-by-image selection of the debris for selected experiments from a previous experimental program performed at Waseda University, Tokyo, Japan (Nistor et al., 2016). A full description of the algorithm can be found in Stolle et al. (2016).

2.3 Experimental protocol

The experiments presented in this paper are part of a larger experimental program as a result of a collaboration between the University of Ottawa (Canada), the University of Hannover (Germany), and Waseda University (Japan). The experiments used in this paper are shown in Table 1. Each experimental category was repeated 10 times to allow for a probabilistic evaluation of the debris motion and impact forces. However, due to difficulties in the data collection, an experimental trial in both E03 and E04 could not be used (experiments 305 and 315).

Between each experiment, excess water on the false floor was removed to the point that there was no pools of water. Due to time constraints, the false floor still had a thin layer of water on the surface before the beginning of each experiments. As shown in Figure 2, the water had little effect on the repeatability of the hydraulic boundary condition. However, the presence of the layer of water may be partially responsible for the steeper surge front that was observed during the wave propagation (St-Germain et al., 2013). As the debris' side surfaces were smooth, adhesive forces between the containers are negligible, at least in the presence of water. Experimental conditions were therefore kept identical by drying off all container surfaces before setting containers in place for each experimental trials. Adhesive forces between the containers were therefore kept constant not to affect their dynamics during the propagation of the debris.

Table 1. Experimental Protocol for tests performed at the DBF in the University of Ottawa.

Category	Impoundment Depth [m]	Number of Debris [#]	Repetitions [#]	Experimental Number [#]
E01	0.4	1	10	274 - 283
E02	0.2	1	10	294 - 303
E03	0.4	3	9	304, 306 - 313
E04	0.2	3	9	314, 316-323

3 RESULTS

3.1 Hydrodynamics

Figure 2 shows the comparison of the water depths in the flume to the Ritter solution (Ritter, 1892) for the three wave gauges: WG2 (a), WG5 (b), and WG6 (c). As it can be observed in Figure 2, the experimental results are similar to the analytical solution. In the case of the experimental results, the wave arrived later than predicted by the analytical results. This is a result of the Ritter solution being calculated for a frictionless surface whereas the current experimental surface was rough due to the sand coating. The incoming wave front also has a steeper initial front, which was again a result of the bed roughness in the current experiments (Chanson, 2006). Additionally, as discussed in Section 2.3, the presence of a thin layer of water has slowed down and steepened the incoming wave front (St-Germain et al., 2013). Most importantly, Figure 2 shows that the wave profile was highly repeatable between the experiments. As the purpose of these experiments is to examine the effect of different variables on the maximum impact force, having a highly repeatable hydraulic boundary condition was paramount to deriving meaningful conclusions from the debris experiments.
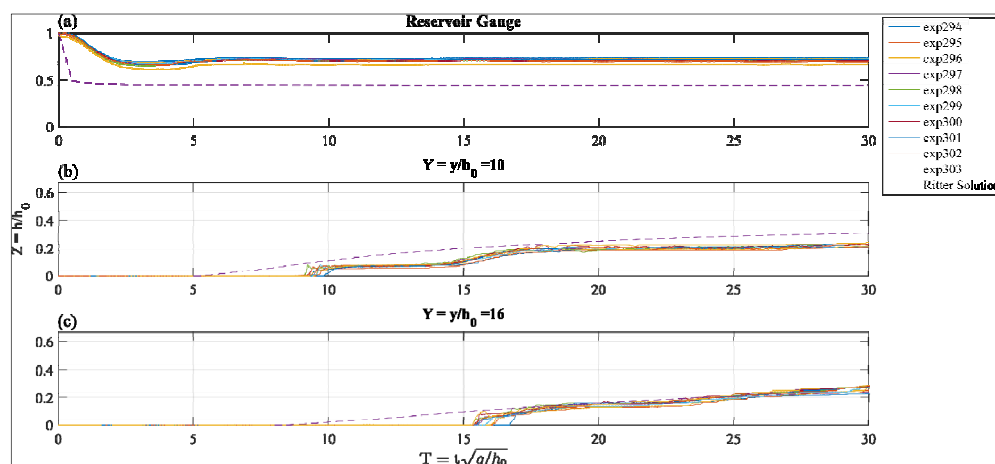

Figure 2. Dimensionless time-history of water levels from an initial impoundment depth of 0.40 m comparing the experimental results (solid line) to the Ritter (1892) solution (dashed line). (a) Reservoir Gauge (WG2); (b) Y = 5 (WG5); and (c) Y = 8 (WG6).

3.2 Debris motion

To evaluate the effects of the number of debris and the hydrodynamic boundary conditions on the debris transport, the positions of the debris from the debris tracking algorithm, outlined in Section 2.2, were

compared between the various experimental categories. The debris position was described using a probability density function (PDF), which describes the likelihood of the debris to have a certain lateral displacement at various y-positions, described by:

$$PDF = f(x,y) = \frac{1}{\sigma\sqrt{2\pi}} e^{-\frac{(x-\mu)^2}{2\sigma^2}}$$

[4]

where σ is the standard deviation of the lateral displacement, and μ is the mean of the lateral displacement. Figure 3 and Figure 4 show the PDF at 0.5 m intervals from the geometric center of the debris source for one debris and three debris, respectively. The blue line represents E01 and E03 (0.4 m impoundment depth) and the orange line represents E02 and E04 (0.2 m impoundment depth). The larger the probability density at lateral position, the more likely the debris moved at the lateral position at each corresponding y-position.

The dashed line in Figure 3 and Figure 4 shows the ±22.5° cone, proposed by the ASCE7 Chapter 6, to evaluate the potential debris impact from a debris source. The line was truncated at x = ±0.75 m as that was the extent of the DBF width. As shown in Figure 3 and Figure 4 the debris propagated well within the conservative boundaries proposed by Naito et al. (2014). Similar to Nistor et al. (2016), as the number of debris increased, the spreading of the debris increased. When the initial entrainment occurred, there was little difference in the spreading as a result of the number of debris. However, as debris propagated further downstream, the spreading angle became much more pronounced, as the probability function began to flatten out.
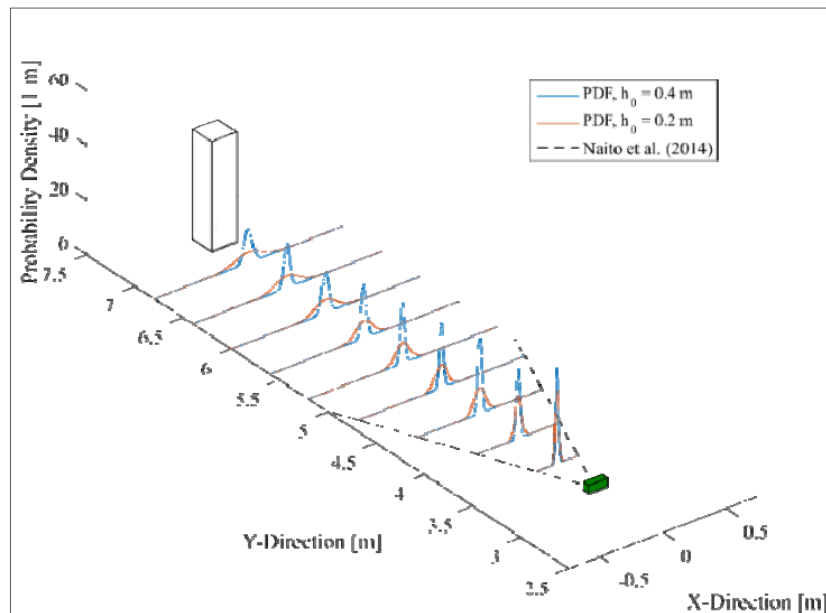

Figure 3. Probability density functions of the lateral displacement of one debris for 0.2 m (E02) and 0.4 m (E01) impoundment depths. The dotted line shows the ±22.5° spreading angle proposed by Naito et al. (2014). The green container indicates the initial position of the debris and the white box represents the structure.

Qualitatively, comparing Figure 3 and Figure 4 shows that the spreading area for the three debris was larger than in the cases with a single debris. However, during the initial 1.0 m of the propagation, there is little difference between the single and three debris cases. As shown in Figure 4, the three debris initially propagated as a single agglomeration, the difference in spreading occurred as the agglomeration rotated and began to separate.

Potentially, as debris propagated as an agglomeration, with the long-axis of the debris perpendicular to the flow direction, the pressure and velocity gradient within the flow acted on the agglomeration as a whole, since there was little space or gaps between the debris. As debris rotated, the difference in the drag force acting on the exposed short-axis of the debris caused the agglomeration to separate. The spatially varying pressure and velocity gradient within the turbulent surge would then cause the separated agglomeration to propagate along different trajectories, resulting in the larger spreading seen in Figure 4.
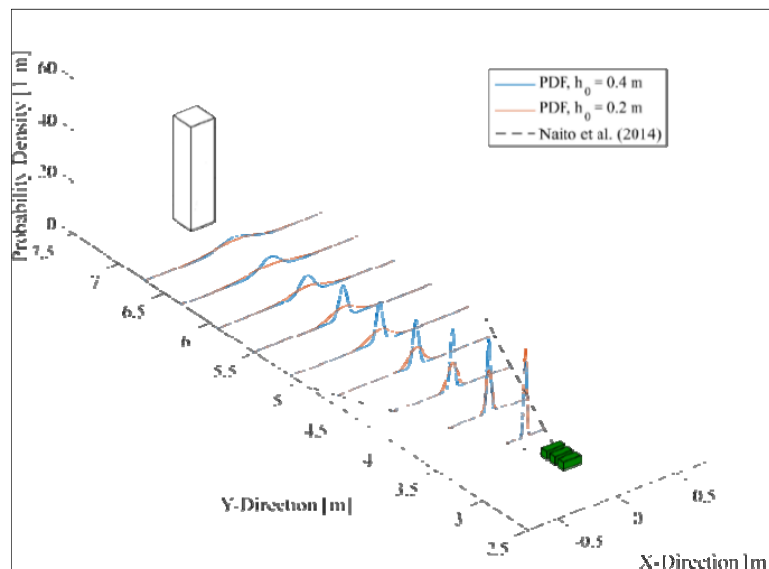
Figure 4. Probability density function of the lateral displacement of three debris for 0.2 m (E04) and 0.4 m (E03) impoundment depth. The dotted line shows the ±22.5° spreading angle proposed by Naito et al. (2014). The green container indicates the initial position of the debris and the white box represents the structure.

Figure 3 and Figure 4 indicate that the hydrodynamic boundary conditions has an effect on the lateral spreading of the debris. In both figures, the smaller impoundment depth (0.2 m) resulted in greater debris spreading, and therefore a flatter probability density function. Examination of video recordings of the experimental runs showed that with the smaller impoundment depth, there was more cases of periodic grounding, where the debris would briefly contact the false floor. As the debris grounded, they would shift around the point where the debris was contacting the false floor resulting in a rapid shift in their orientation. The periodic grounding seemed to be a relatively random process and as a result the effect on the lateral spreading of the debris varied significantly resulting in the almost flat (and therefore random) probability density functions further downstream.

3.3 Debris impact forces

Figure 5 shows the force-time history of Experiment 306 (E03), one of the cases with multiple debris. As can be observed in Figure 5, the surge impacts the structure slightly before the debris impact, as the debris is limited by the surge front velocity (Shafiei et al., 2016). As the surge impacts the structure, a splash-up occurred at the front of the structure as the horizontal momentum of the fluid gets transferred to vertical momentum. The debris impact occurred slightly after the splash-up occurred as the splash can still be observed in Figure 5b. In this case, the agglomeration of debris did not separate as the debris propagated, resulting in the debris impacting the structure as an agglomeration. The impact force profile of the initial impact can be seen in the inset time series, along with the resonance of the structure as it recovered from the initial impact. On impact, the debris agglomeration pivoted, resulting thus in multiple secondary impacts, which can be observed in the secondary peaks occurring ~ 4.0 s.
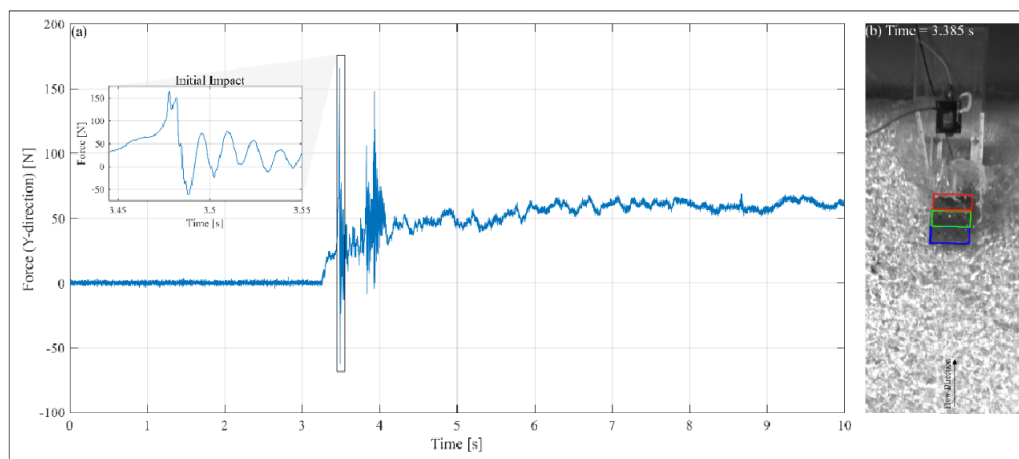

Figure 5. Force-time history for Experiment 306 (E03). The inset shows a magnified view of the impact time series. (b) The image shows the debris slightly before the impact occurs, showing the three debris: D2 (red), D3 (green), and D4 (blue).

Figure 6 shows the debris impact forces compared to the impact velocity. The debris impact force was taken as the maximum y (flow-wise) force acting on the structure (recorded by the FT) once the hydrodynamic

forces had been subtracted from the force-time history. The impact velocity was estimated from the debris tracking algorithm, in the cases where multiple debris impacted simultaneously, the velocities of all the impacting debris were taken and averaged. In the case where multiple non-simultaneous impacts or secondary impacts occurred, only the maximum impact force was considered.

The difference in the hydrodynamic boundary conditions can be observed in Figure 6. In the case of the 0.2 m impoundment depth, the impact velocity was significantly less than the impact velocity observed for the 0.4 m impoundment depth. The number of debris also influenced the impact velocity, with more debris resulting in lower impact velocities. Matsutomi et al. (2008) determined that the increased concentration of debris within a dam-break flow resulted in a slower debris velocity, as the debris acted similar to a roughness element, slowing down the flow velocity and therefore limiting the maximum debris velocity.
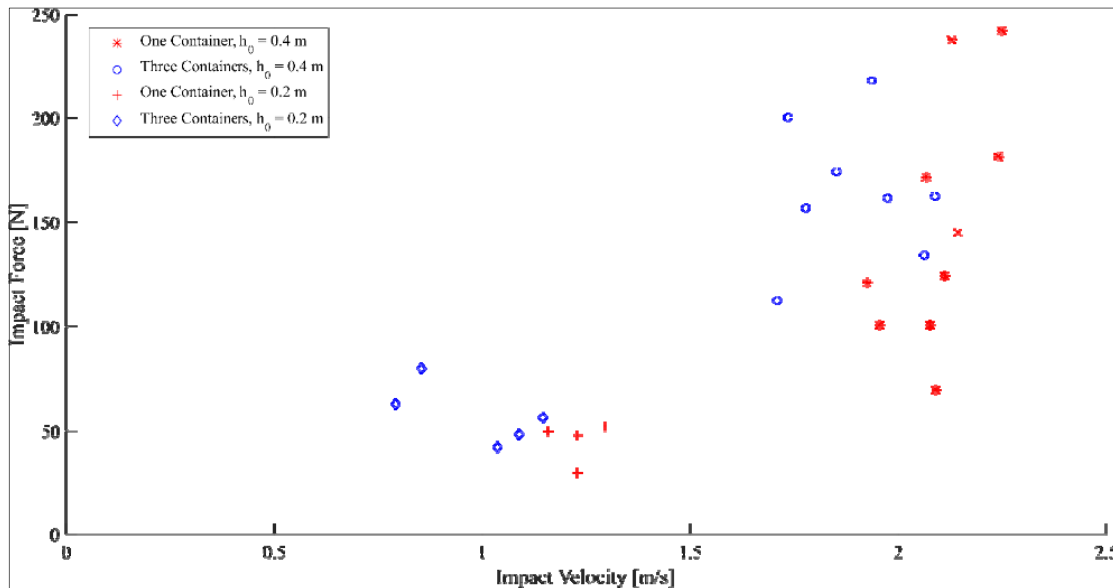

Figure 6. Maximum debris impact force as a function of the impact velocity.

As shown in Figure 6, the impact forces for the three containers for comparable velocities were larger for the cases with three debris. It should be noted that while three debris were present within each experiment, the number of debris impacting the structure varied between 0 and 3, in most cases being less than three. Particularly in the experiments with the 0.2 m impoundment depth, where due to the larger spreading that occurred (Figure 3 and Figure 4), debris often did not impact the structure, resulting in the smaller dataset that can be observed in Figure 6.

4   DISCUSSION

The evaluation of the debris motion within tsunami-like flow conditions indicated that the spreading angle proposed by Naito et al. (2014), from field surveys of the 2011 Tohoku Tsunami, are a conservative estimation of the debris spreading zone. However, as can be observed in Figure 3, the spreading of the debris tended to occur later in the debris propagation. Due to limits of the DBF and current limits of the physical modelling of tsunamis (Madsen et al., 2008), the flume does not allow an adequate model of the time scale length of a tsunami wave. As a result, the conclusions drawn from this study regarding debris spreading only consider the incipient motion of the debris. Further studies will be needed to examine the debris spreading in the later instances of the tsunami wave, as significantly different Froude numbers can be observed (Borrero et al., 2006).

The inundating flow condition significantly affects the debris velocity and momentum, as the debris velocity is limited by the surrounding flow velocity (Matsutomi, 2009). The momentum of the debris is an important factor when considering the lateral spreading of the debris. Bocchiola et al. (2008) examined the transport of large woody debris in river flow conditions and determined that the mass and velocity of the debris significantly influence the effect of macro-roughness features, such as dunes and bars, on the debris transport. Heavier, fast-moving debris tended to propagate through the macro-roughness elements, whereas smaller, slower debris would ground at the elements. The grounding of the debris resulted in the lateral displacement of the debris as the flow would pivot the debris about the grounding point and be pushed laterally. As a result of the slower, shallower flow conditions for the 0.2 m impoundment, grounding occurred often, resulting in increased debris spreading. The roughness of the false floor also affected the grounding

characteristics, and therefore the spreading. A detailed evaluation of roughness and macro-roughness elements needs to be considered in the evaluation of debris spreading.

The slower flow velocities and increased spreading of the debris, as a result of the smaller impoundment depths, contributed to the debris not impacting the structure. Due to the grounding and lateral displacement, debris fell further behind the surge front, resulting in a more developed wake occurring at the structure as debris approached it. The formation of the wake at the structure also generated a flow stagnation zone at the front of the structure along with lateral flow velocities as a result of the water flowing around the structure. The

combination of the reduction of debris velocity as the debris entered the flow stagnation zone, along with lateral velocities, resulted in the debris being pulled around the structure, resulting in significantly reduced or no impact forces. While this phenomena occurred as a result of the slower flow velocities, debris that are entrained after the initial inundating surge, as a result of buildings collapsing (Yao et al., 2014; Yeh et al., 2014), presence of macro-roughness (Bocchiola et al., 2008), debris requiring larger flow depths/flow velocities to be entrained (Braudrick and Grant, 2000), could also experience diversion as a result of the wake formation at a structure.

5   CONCLUSIONS

This paper presents the results of a study examining multiple debris dynamics and impact forces in tsunami-like flow conditions. The experiments were performed at the University of Ottawa (Ottawa, Canada) to evaluate the significance of multiple debris impacting a structure on the maximum impact force. Current design standards only consider the maximum impact force as a result of a single debris impact. An experimental study was performed in the DBF to examine the debris dynamics over a flat, horizontal bottom and impact forces on a structure. The debris was depicted as scaled-down shipping containers (1:40 geometric scaling). This study examined the motion of single debris and three debris sets with two hydrodynamic boundary conditions. The debris was placed on the bottom and the dam-break was released, the debris motion was tracked and analyzed using a debris tracking algorithm presented in Stolle et al. (2016). The hydrodynamic and impact forces on the structure were recorded using a 3D force-torque transducer. Based on the recorded data and their analysis, the authors have drawn the following conclusions:

1) As the number of debris increased, the lateral spreading of the debris increased. The increased number of debris interacted, resulting in pivoting and collisions that increased the lateral motion of the debris.
2) The impact velocity decreased as the number of debris increased. The debris acted as an added roughness element which reduced flow velocities and therefore their velocities.
3) The smaller impoundment depths resulted in slower flow velocities and smaller flow depths causing the debris to periodically ground, which forced the debris to pivot and therefore increasing the lateral spreading of the debris.
4) The increased number of debris resulted in larger debris impact forces on the structure. The larger impact forces could be a result of the increased mass of the impacting debris or a result of more displaced fluid, increasing the hydrodynamic mass associated with the impact.

The presence of large concentrations of debris within the inundating surge of the 2010 Chilean Tsunami and the 2011 Tohoku Tsunami (Takahashi et al., 2010; Yeh et al., 2014) showed the potential for multiple debris impacting a structure simultaneously. Based on this study, multiple debris impact could potentially result in larger debris impacts than predicted by the single debris impact equation. Further research is needed to determine the risk associated with debris impact and the development of conservative estimations of debris impact forces in the cases of large debris concentrations.

REFERENCES

Bocchiola, D., Rulli, M. & Rosso, R. (2008). A Flume Experiment on the Formation of Wood Jams in Rivers. *Water Resources Research*, 44.

Borrero, J.C., Sieh, K., Chlieh, M. & Synolakis, C.E. (2006). Tsunami Inundation Modeling for Western Sumatra. *Proceedings of The National Academy of Sciences,* 103, 19673 - 19677.

Braudrick, C.A. & Grant, G.E. (2000). When do Logs Move in Rivers? *Water Resources Research,* 36, 571 - 583.

Chanson, H. (2006). Tsunami Surges on Dry Coastal Plains: Application of Dam Break Wave Equations. *Coastal Engineering Journal,* 48, 355–370.

Chock, G.Y. (2016). Design for Tsunami Loads and Effects in The ASCE 7-16 Standard. *Journal of Structural Engineering*, 142(11), 1-12.

Comfort, L.K. (2006). Cities at Risk Hurricane Katrina and the Drowning of New Orleans. *Urban Affairs Review* 41, 501–516.

Esteban, M., Takagi, H. & Shibayama, T. (2015). *Handbook of Coastal Disaster Mitigation For Engineers and Planners,* Elsevier.

Goseberg, N., Stolle, J., Nistor, I. & Shibayama, T. (2016). Experimental Analysis of Debris Motion due The Obstruction from Fixed Obstacles in Tsunami-Like Flow Conditions. *Coastal Engineering,* 118, 35–49.

Haehnel, R.B. & Daly, S.F. (2002). *Maximum Impact Force of Woody Debris on Floodplain Structures,* USACE.

Haehnel, R.B. & Daly, S.F. (2004). Maximum Impact Force of Woody Debris on Floodplain Structures. *Journal of Hydraulic Engineering,* 130, 112–120.

Ko, H.T.-S., Cox, D.T., Riggs, H.R. & Naito, C.J. (2015). Hydraulic Experiments on Impact Forces from Tsunami-Driven Debris. *Journal of Waterway, Port, Coastal and Ocean Engineering,* 141(3), 1-11.

Madsen, P.A., Fuhrman, D.R. & Sch Ffer, H.A. (2008). On the Solitary Wave Paradigm for Tsunamis. *Journal 0f Geophysical Research Oceans,* 113(12), 1-22.

Matskevitch, D. (1997). Eccentric Impact of an Ice Feature: Linearized Model. *Cold Regions Science and Technology*, 25(3), 159 -171.

Matsutomi, H. (2009). Method for Estimating Collision Force of Driftwood Accompanying Tsunami Inundation Flow. *Journal of Disaster Research,* 4, 435 - 440.

Matsutomi, H., Fujii, M. & Yamaguchi, T. (2008). Experiments and Development of a Model on the Inundated Flow With Floating Bodies. *Coastal Engineering,* 1458 -1470.

Naito, C., Cercone, C., Riggs, H.R. & Cox, D. (2014). Procedure for Site Assessment of the Potential for Tsunami Debris Impact. *Journal of Waterway, Port, Coastal And Ocean Engineering,* 140, 223–232.

Nistor, I., Goseberg, N., Mikami, T., Shibayama, T., Stolle, J., Nakamura, R. & Matsuba, S. (2016). Hydraulic Experiments on Debris Dynamics over a Horizontal Plane. *Journal of Waterway, Port, Coastal And Ocean Engineering*, 143(3),1 -15.

Nistor, I., Goseberg, N. & Stolle, J. (2017). Tsunami-Driven Debris Motion and Loads. A Critical Review. *Frontiers in Built Environment*, 3, 2.

Ritter, A. (1892). Die Fortpflanzung De Wasserwellen. Zeitschrift Verein Deutscher Ingenieure, 36, 947–954.

Shafiei, S., Melville, B.W., Shamseldin, A.Y., Beskhyroun, S. & Adams, K.N. (2016). Measurements of Tsunami-Borne Debris Impact on Structures Using an Embedded Accelerometer. *Journal of Hydraulic Research,* 54(4),1–15.

St-Germain, P., Nistor, I., Townsend, R. & Shibayama, T. (2013). Smoothed-Particle Hydrodynamics Numerical Modeling Of Structures Impacted by Tsunami Bores. *Journal of Waterway, Port, Coastal, and Ocean Engineering,* 140(1), 66 -81.

Stolle, J., Nistor, I. & Goseberg, N. (2016). Optical Tracking of Floating Shipping Containers in a High-Velocity Flow. *Coastal Engineering Journal,* 58(2),1 -29.

Takahashi, S., Sugano, T., Tomita, T., Arikawa, T., Tatsumi, D., Kashima, H., Murata, S., Matsuoka, Y. & Nakamura, T. (2010). Joint Survey For 2010 Chilean Earthquake and Tsunami Disaster in Ports and Coasts. Port and Airport Res Inst.

Yao, Y., Huang, Z., Lo, E.Y.M. & Shen, H.-T. (2014). A Preliminary Laboratory Study of Motion of Floating Debris Generated by Solitary Waves Running Up a Beach. *Journal of Earthquake and Tsunami,* 8(3), 1-13.

Yeh, H., Barbosa, A.R., Ko, H. & Cawley, J.G. (2014). Tsunami Loadings on Structures: Review and Analysis. *Coastal Engineering Proceedings,* 1.

FLOOD-INDUCED DEBRIS MOTION IN A BUILT-IN ENVIRONMENT

IOAN NISTOR[(1)], NILS GOSEBERG[(2)] & JACOB STOLLE[(3)]

[(1, 3)] Department of Civil Engineering, University of Ottawa, Ottawa, Canada,
inistor@uottawa.ca (corresponding author), jstol065@uottawa.ca
[(2)] Ludwig-Franzuis-Institute for Hydraulic, Estuarine and Coastal Engineering,
Leibniz Universität Hannover, Hannover, Germany,
contact@nilsgoseberg.de

ABSTRACT

Recent tsunami, such as the 2011 Tohoku and the 2015 Chilean, have shown that in addition to hydraulic loading, debris loads are a critical load to consider in the design of tsunami resistant infrastructure. The ASCE7 Chapter 6: Tsunami Loads and Effects represents a new standard that addresses the spatial distribution of debris associated with large-scale debris impact, such as shipping containers and shipping vessels. Many of this standard's prescriptions are based on analysis of a limited data set from a post-tsunami field survey following the 2011 Tohoku Tsunami in Japan. This paper presents result of an experimental study dealing with debris motion in tsunami-like flow conditions that analyzes the motion of debris in a built environment comparing the results to the previous debris motion studies and prescriptions of the ASCE7 standard. From the experiments, the authors concludes that the presence of macro-roughness in a built environment causes the loss of momentum of the inundating surge and the trapping of debris resulting in a reduction of the maximum longitudinal displacement of the debris. The study also found that the debris tended to propagate within the deep, high-velocity jets created by the flow constrictions, creating preferred transport paths for the debris.

Keywords: Debris; tsunami; physical modelling; built environment; coastal engineering.

1   INTRODUCTION

Catastrophic coastal flooding generated by the 2004 Indian Ocean Tsunami, the 2011 Tohoku Tsunami, as well as the 2015 Chilean Tsunami have shown that, hydrodynamic loading aside, debris loading is a major contributor to the extreme damage experienced by coastal infrastructure (Palermo et al., 2013; Takahashi et al., 2011, 2010). While extreme hydrodynamic loading due to coastal flooding events has been the object of intense research during the past decade, few studies dealing with debris impact and loading due to coastal flooding have been conducted. Post-tsunami forensic engineering field investigations conducted by the authors of this paper (Ghobarah et al., 2006; Saatcioglu et al., 2005) and other researchers (Yeh et al., 2014; Chock et al., 2013) revealed that debris loading and debris damming have a significant effect on the structural integrity of buildings and infrastructure in general, especially in high-density urban areas.

The new ASCE-7 Tsunami Loads and Effects Committee (of which the first author is a voting member) has recognized the significant importance of debris loading and proposed several prescriptions pertaining to debris loading as well as debris spatial distribution during a tsunami-induced flood event (Chock, 2016). These prescriptions are based on limited data collected from field investigations conducted in the aftermath of the 2011 Tohoku Tsunami (Naito et al., 2014). Previous prescriptions often resulted in conservative estimations of debris spatial spreading and an inaccurate estimation of associated loading.

The field study performed by Naito et al. (2014) examined the transport of large-scale debris, such as shipping containers and shipping vessels, and proposed a method for estimating the debris spatial spreading. The method considered that debris propagate within a ±22.5° spreading angle from the geometric center of the debris source. The debris inundation limit was based on the concentration of the debris (plan area of the debris/area enclosed by the spreading angle) within the spreading angle. A debris concentration of 2% was selected as a conservative estimation of the spreading area that would contain the field data within the spreading area. The inundation limit could also be truncated by a sufficiently small inundation depth that would limit the propagation of the debris (3 feet or 0.91 m for shipping containers). Due to the relative rare occurrence of extreme tsunami events and difficulties in determining debris sources in field studies, the method proposed by Naito et al. (2014) is difficult to validate with field data.

The few experimental tests examining debris motion have shown that accurate tracking of debris is complicated (Matsutomi, 2009; Imamura et al., 2008). However, recent advancements in debris tracking using

sensor-based (Goseberg et al., 2016; Shafiei et al., 2014) or camera-based (Stolle et al., 2016; Rueben et al., 2014) systems have begun to allow for more detailed evaluation of debris motion. In particular, allowing for the analysis of multiple debris transport within high-velocity flow conditions (Nistor et al., 2016).

Matsutomi et al. (2008) examined the transport of woody debris in dam-break flow conditions, in particularly focusing on the effect of the debris concentration on the surge profile. Matsutomi et al. (2008) determined that the debris entrained within the surge acted as a roughness element, reducing the surge front velocity and increasing the water depth, similar to the effects bed friction on a surge front (Chanson, 2006). Matsutomi et al. (2008) also noted that the debris velocity was limited by the flow velocity, therefore the increase in the debris concentration reduced the debris velocity as well.

Rueben et al. (2014) used a camera-based tracking method to analyze the repeatability of multiple debris motion with a tsunami-like surge. The on-shore trajectory and velocity of the debris was found to be highly repeatable, however the off-shore motion tended to be a random process, likely due to irregularities in the flow field in the off-shore direction. In cases where the rotation of the debris was forced by stationary obstacles, the initial forcing of the rotation resulted in highly variable trajectories and velocities of the debris. A full-breakdown of recent literature in debris transport dynamics can be found in Nistor et al. (2017).

Nistor et al. (2016) examined the effect of the number of debris on the maximum spreading area of the debris, considering two key parameters: the debris spreading angle (θ) and the debris longitudinal displacement (d_{lon}).

$$\theta(t) = \arctan((x(t)-x(t_0)))/((y(t)-y(t_0))) \quad\quad [1]$$

$$d_{lon}(t) = y(t)-y(t_0) \quad\quad [2]$$

where x is the cross-shore direction, y is the flow direction, t_0 indicates the position at the start of the experiment, and t indicates the time. Nistor et al. (2016) determined that increasing the number of debris resulted in an increase in the spreading angle and a decrease in the longitudinal displacement. The decrease in longitudinal displacement contradicts the method presented by Naito et al. (2014). In the case of the Naito et al. (2014) method, as the number of debris increased, a larger spreading area would be required to reach the 2% debris concentration threshold. However, the method by Naito et al. (2014) still provides a conservative estimation of the maximum debris spreading.

To build upon the study presented in Nistor et al. (2016), this study is geared towards investigating and tracking the spatial and temporal displacement of floating debris due to rapid coastal flooding in a built-in port environment. The study introduces fixed obstacles within the path of the debris transport and aims to:

- Examine the effect of fixed obstacles on the inundating surge.
- Determine the effect of the obstacles on the debris dynamics as the debris propagate through the built environment.
- Determine the effect of the obstacles on the maximum spreading area, in particularly focusing on the longitudinal displacement and spreading angle.

The paper is organized as follows: the "Experimental Setup" section presents the laboratory facilities at Waseda University (Tokyo, Japan), the "smart" debris method used to track the debris motion, and the experimental protocol; the "Results" section examines the effect of the obstacles on the hydrodynamic conditions, the debris dynamics, and the maximum spreading area; the "Discussion" section discusses the current research and identify any short coming of the current study; finally, the "Conclusions" section summarizes the findings of this study and places the research in the context of current efforts in the field, identifying future direction in analyzing debris motion.

2   EXPERIMENTAL SETUP

2.1 Waseda University Tsunami Wave Basin (TWB)

The experimental research was a part of a comprehensive series of experimental tests conducted in the recently commissioned Tsunami Wave Basin (TWB) at Waseda University, Tokyo, Japan (Figure 1). On the one side of the TWB, a wave maker, whose operation is based on the release of a constant volume of water with a defined initial head, was installed. After initializing the release of the water, the reservoirs empty under the influence of gravity; a flow characterized by a solitary wave front profile, but extended with an elongated tail flow, was generated. A more detailed description of the wave maker and the wave basin features is provided in Nistor et al. (2016). A horizontal rigid apron area modelling a port environment with container handling facilities was constructed opposite to the wave maker and covering slightly more than half of the length of the TWB (the "Harbor" section). The generated waves propagated across the still-water section of

the TWB (the "Sea" section), as indicated in Figure 1, in blue color. A vertical wall representing the model of a quay wall separated the wave propagation section and the horizontal harbor apron area; a freeboard of 0.015 m existed between those two sections. The origin of the right-handed coordinate system used throughout the tests resided at the midpoint of the uppermost apron edge with the positive y-axis pointing inland. The z-axis pointed positively upwards opposite to the vector of gravity.
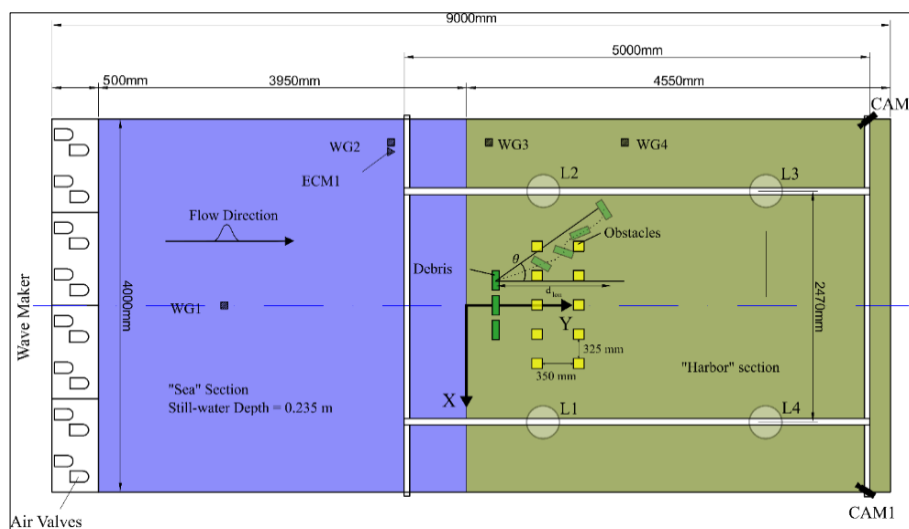

Figure 1. Plan view of the Tsunami Wave Basin (TWB) at Waseda University (Tokyo, Japan). The 4.0 m x 9.0 m basin with a still-water section ("sea" section) and a flat horizontal apron ("Harbor" section). A steel frame overlooked the basin, where the locators and cameras were placed.

2.2 Instrumentation

Figure 1 depicts the location of the instrumentation which were used to record water levels, velocities, image collection and aiding the collection of positional information of the individual container models. Two wave gauges (WG, manufactured by KENEK, Japan) were placed in the "sea" section while the remaining two wave gauges were placed along the initially dry "harbor apron" section. Close to the position of the wave gauge WG2, an electro-magnetic current meter (ECM, also manufactured by KENEK, Japan) was installed with its sensor head submerged 0.07 m below the still water level (z = -0.085 m). The "harbor apron" section was additionally monitored using two high-definition (HD) cameras aiming towards the apron's edge, the debris site and the obstacles; the coverage allowed to analyze the propagation of the tsunami bore front over the apron edge, the debris site and the flow through the obstacles at a sampling frequency of 25 Hz. Four locator antennae were installed below a rigid frame which belonged to a real-time location system capable to track up to 25 individual debris across the physical domain. The real-time location system (RTLS) is part of a six-degree-of-freedom (6DOF) "Smart" debris system, which is further detailed in Section 2.3.

2.3 "Smart" debris

"Smart" debris, described in more detail in Goseberg et al. (2016), were used to track the container models across the physical domain. 20-foot shipping containers (modelled based on the ISO 668/688 standard) were chosen as the debris, based on large-scale debris prescriptions in the ASCE7 Chapter 6 (Chock, 2016). The containers were down-scaled (length scale 1:40) and batch-produced for assuring identical dimensions (0.06 m x 0.06 m x 0.15 m) and weights of a positively buoyant polyethylene (PE-HMW, 0.92 g/cm³). A target weight of W = 14,400 kg as prototype was chosen to model average conditions of shipping containers (Knorr and Kutzner, 2008). Smaller or larger container weights influence the hydrodynamics around the debris, therefore affecting the maximum spreading area after being entrained in a tsunami bore or bore (Shafiei et al., 2016), however due to time constraints only one weight was examined.

The positional information in the two horizontal dimensions (x, y) of the 6DOF "Smart" Debris system was used to track the container models as they moved across the harbor apron area. The three rotational motions and accelerations were also recorded by means of a motion sensor (AHRS) but are not presented within the context of this paper. The positional information was collected as part of the "Smart" debris system by the RTLS (manufacturer: Quuppa Oy, Finland) employing trilateration by means of a Bluetooth Low Energy (BLE)wireless connection between the locators shown in Figure 1 and a single locator tag (Tag). The total weight of a single container model was determined by three repeated weightings which yielded an average total weight of 0.226 kg.

2.4   Experimental protocol

The experiments presented in this paper are part of a larger experimental program as a result of a collaboration between the University of Ottawa (Canada), the University of Hannover (Germany), and Waseda University (Japan). The experiments presented in this paper are listed in Table 1. The experiments examine two different debris configuration (three and six debris) and three obstacle configurations (no obstacles, one row of obstacles, and two rows of obstacles), the various configuration can be observed in Figure 2.
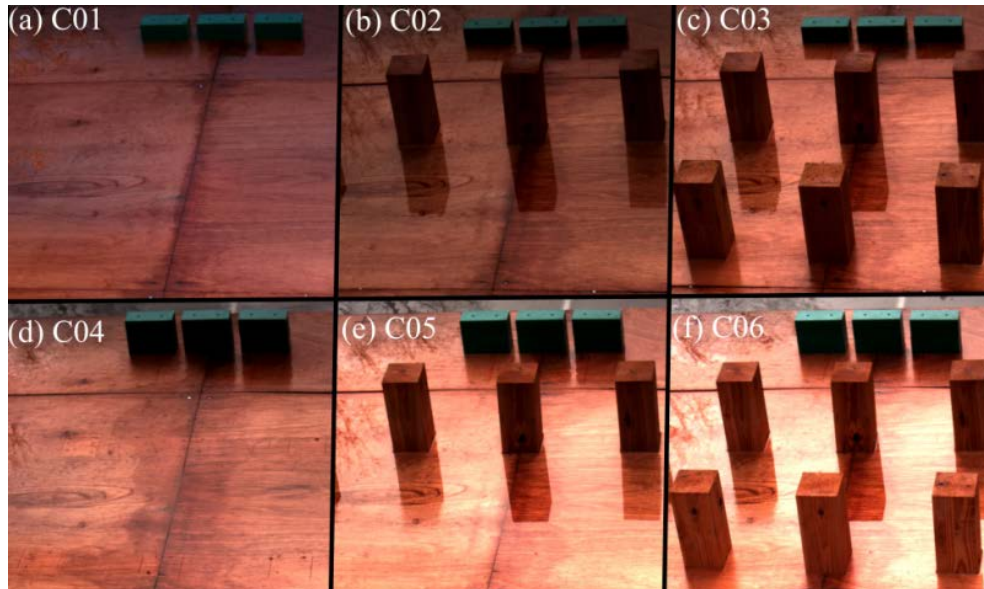
Figure 2. The six experimental categories. (a) Three debris; (b) three debris, one row of obstacles; (c) three debris, two rows of obstacles; (d) six debris; (e) six debris, one row of obstacles; (f) six debris, two row of obstacles.

The centroid of each debris was placed 0.23 m from the apron edge, with 0.03 m spacing between the debris. The obstacles were placed 0.71 m and 1.16 m from the apron edge with 0.35 m spacing in the y-direction and 0.325 m in the x-direction. Before each experiment, excess water was removed from the surface of the apron to have an initially dry horizontal bottom. Each debris was also dried as conceivably the wet surface interaction between the debris, particularly for the stacked formation, could influence the debris-debris interaction.

Table 1. Experimental protocol.

Experimental Test	Number of Debris	Rows of Obstacles	Experiments	Debris ID
C01	3	0	9, 10, 11, 12, 13	D2, D3, D4
C02	3	1	28, 29	D2, D3, D4
C03	3	2	32, 33	D2, D3, D4
C04	6	0	43, 44	D2, D3, D4, D5, D6, D7
C05	6	1	30, 31	D2, D3, D4, D5, D6, D7
C06	6	2	34, 35, 36, 37, 38, 39	D2, D3, D4, D5, D6, D7

3   RESULTS

3.1   Hydrodynamics

For each experiment, the overhead reservoir (wave maker), shown in Figure 1, was filled to 0.665 m above the still-water depth while the "sea" section was kept at 0.225 m still-water depth. The water was then released using the air valves located at the top of the reservoir. The released water was gravity-driven, resulting in a wave profile that propagated through the "sea" section. As can be seen in Figure 3, comparing to the solution for a solitary wave, from Munk (1949), to the WG and ECM placed in the "sea" section show that the wave front has a similar profile to a solitary wave. However, the wave period was around 4.5 s, whereas a typical wave period of a solitary wave is ~ 1.3 s (Madsen et al., 2008). The resulting wave profile was similar to an elongated solitary wave, as described in Goseberg et al. (2013), which has a wave front of a solitary wave with an elongated tail for a prolonged flow condition.
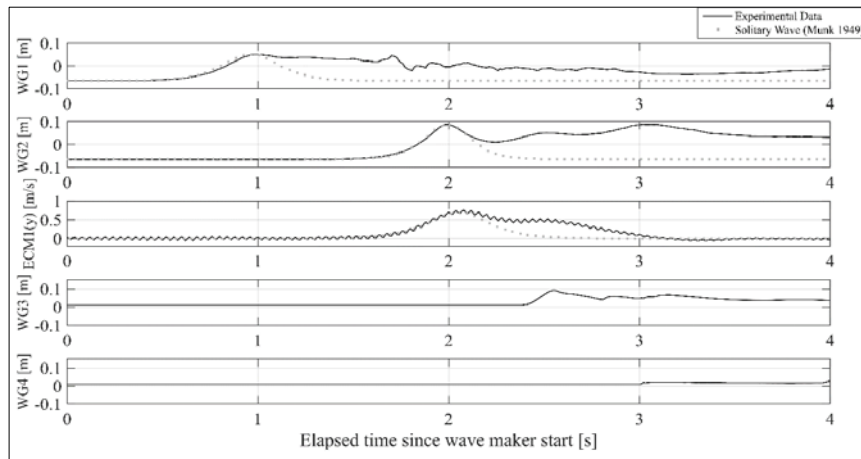
Figure 3. Water surface elevation-time history from the four wave gauges and the velocity time history from the electromagnetic current meter (ECM1) for experiment 33. WG1, WG2, and ECM1 were placed within the "sea" section and each time history was compared to the Munk (1949) solution for a solitary wave. WG3 and WG4 were placed on the "harbor" section.

As the wave reached the vertical quay, wave reflections resulted in strong amplification and breaking as the wave crested the "harbor" section. The broken wave then propagated over the horizontal bottom as a surge (WG3 and WG4). The front of the surge had a water depth around 0.08 m at the debris source, resulting in the rapid entrainment of the debris within its front. Comparing the hydrodynamics between the experimental categories showed that the presence of the obstacles on the horizontal bottom had no effect on the profiles at WG3 and WG4.

3.2 Debris dynamics

The motion of debris is a highly variable process, particularly within a turbulent surge (Nistor et al., 2016; Rueben et al. 2014). However, Rueben et al. (2014) showed that the motion in the on-shore direction tended to be relatively repeatable. Figure 4 shows snapshots from Experiment 37, *qualitatively* examining the debris motion through the obstacles. As discussed in Section 3.1, the surge front (black dashed line) propagated parallel to the vertical quay. As the surge impacted the debris configuration experienced little to no motion, resulting in the formation of a bow-like wave (Figure 4(a)). The water continued to build up behind the debris until the drag force could overcame the static friction, initiating the motion of the bottom row of debris (Debris row 1). Once motion was initiated, the top row of debris (Debris row 2) fell behind the Debris row 1, and was immediately entrained within the surge, forming a debris agglomeration (Figure 4(b)).
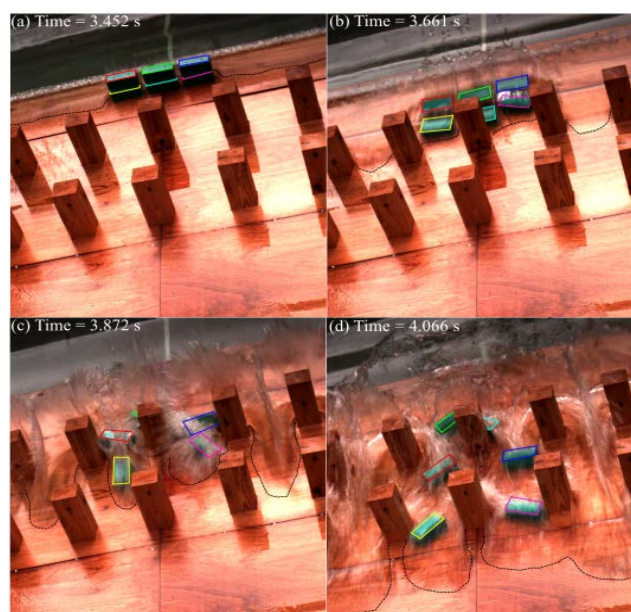

Figure 4. Images captured from Experiment 37, outlining the motion of the six debris: D2 (yellow), D3 (cyan), D4 (magenta), D5 (red), D6 (green), D7 (blue). The black dashed line shows the position of the surge front.

As the debris agglomeration impacted the first row of columns, the debris initially placed directly in front of an obstacle element (D3 and D6) were trapped against the front face of the element. Within the super-critical flow conditions, the debris remained trapped against the first row of obstacles (Figure 4(c)). Since the long-axis of the debris were larger than the width of the obstacles, the debris partially constricted the gaps between the obstacles. The constriction resulted in an exaggeration of the jet feature between the obstacles, resulting in greater accelerations of the flow.

The remainder of the debris (D2, D4, D5, and D7) made contact with the obstacles away from the center of gravity of the debris, resulting in the debris having a forced rotation but not getting trapped at the obstacles. The debris tended to be pushed into the middle of the jet, similar to in studies of debris within river flows where debris tended to propagate within the thalweg of the channel where the deeper, high-velocity flows dominated (Parola 2000). As the obstacles were not staggered, the middle of the jet tended to pass through the second row of obstacles through the center of the second row gap. As a result, the debris often did not contact the second row of obstacles.

3.3   Maximum spreading area

The spreading angles from each of the experimental categories, outlined in Table 1, are displayed in Figure 5. The spreading angles (θ) for each of the categories were compared to the empirical equation developed from Nistor et al. (2016) (dashed line for six debris, dotted line for three debris):

$$\theta=\mp3.69\mp0.80N \qquad\qquad [3]$$

where N is the number of debris in each configuration. The equation from Nistor et al. (2016) was for the same experimental setup without obstacles. The spreading angles are also compared to the $\pm22.5^{\circ}$ spreading angle proposed by Naito et al. (2014).

As can be observed in Figure 5, all debris moved well within the proposed 22.5° spreading angle and are contained within the empirical solution proposed by Nistor et al. (2016). The obstacles appear to have had little to no effect on the general trends of the spreading angle. However, in the case of C03 and C06, there are outliers where the formation of the wake resulted in a larger lateral displacement. As the wake was reforming, the debris would occasionally be pulled into the laterally propagating surge, refracting behind the obstacles. The rapid increase in lateral acceleration resulted in larger lateral displacement than were observed in the cases without obstacles. The phenomena only occurred as the wake was reforming behind the obstacles, after the wake had fully formed the debris remained within the middle of jet. Additionally, the phenomena only occurred in the cases with two rows obstacles. Potentially, the increase in debris velocity due to the local flow constrictions in the gap of the first row of obstacles allowed for the debris to have the momentum to propagate out of the middle of the jet and into reforming wake.
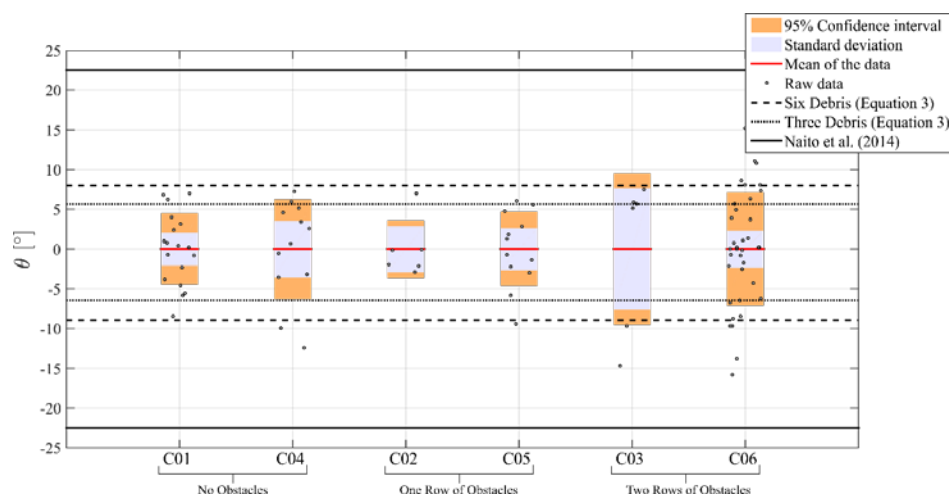

Figure 5. Spreading angle of the debris for each experimental category. The solid black line is the conservatively estimated debris spreading from Naito et al. (2014). The dashed black line shows the predicted spreading angle from Nistor et al. (2016).

$$d_{lon}=3.58-0.09N \qquad\qquad [4]$$

The longitudinal displacement was not compared to the method of Naito et al. (2014) as the difference in the wave period between the experimental tests and the ones in the field data would not derive meaningful conclusions. However, as the wave period used in this experiment has been used to examine debris motion

and near-shore loading forces (Yao et al., 2014; Seiffert et al., 2014; Chinnarasri et al., 2013), the incipient motion and the general characteristics of the debris motion was examined, this is further discussed in Section 4.

As shown in Figure 6, the obstacles have a significant effect on the longitudinal displacement of the debris. The trapping of the debris at the first row of obstacles, as seen in Figure 4, resulted in the multiple cases of debris propagating less than 1 m. The debris remained trapped at the first row of obstacles until the flow velocities had significantly reduced, into the subcritical region. Then, the formation of the flow stagnation zone in front of the obstacles allowed the debris to be released from the face of the first row of obstacles. However, the reduced flow velocity and water depths at that point resulted in smaller displacements before the debris grounded. Additionally, as discussed in Section 3.2, the presence of the obstacles resulted in a loss of momentum of the inundating surge. Therefore, the debris that did not directly impact the obstacles also had smaller longitudinal displacements.

Comparing the experimental categories with one (C02 and C05) and two (C03 and C06) rows of obstacles, there was not a significant difference in the longitudinal displacement of the debris. As was discussed in Section 3.1, due to the wake not completely reforming behind the first row of obstacles, the middle of the jet, where the momentum was greatest, would pass through the gap in the second row of the obstacles. Additionally, the debris tended to propagate within the middle of the jet resulting in the second row of the obstacles rarely being impacted. An adjustment to the arrangement of the obstacles, to allow for the second row to have a large influence on the middle of the jet would likely improved the second rows capability to limit debris displacement.
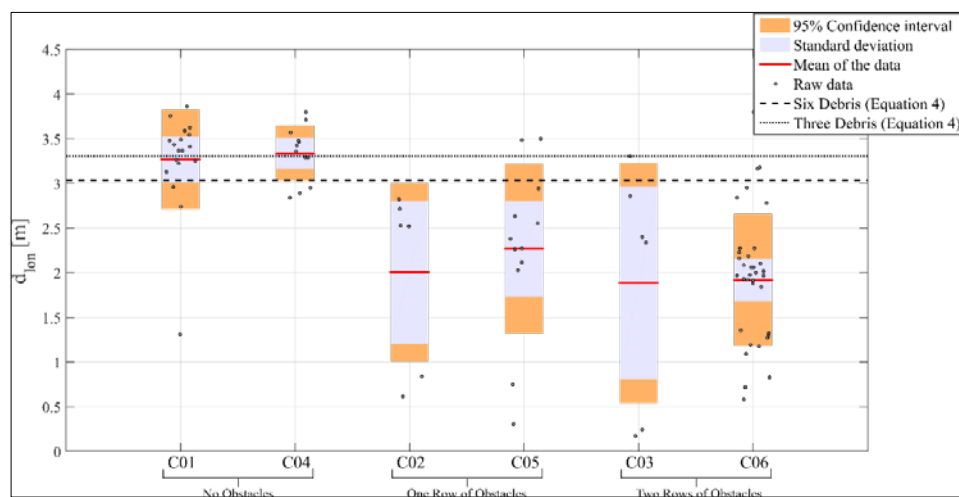

Figure 6. Longitudinal displacement of the debris for each experimental category.
The dashed black line shows the predicted longitudinal displacement from Nistor et al. (2016).

4   DISCUSSION

In this study, an elongated solitary wave was used. However, solitary waves have been shown to have issues accurately modelling physical and time scales, in the context of tsunami research (Madsen et al., 2008). As such, the application of generic, classical solitary waves in the context of tsunami run-up, or propagation was recently challenged. Nevertheless, there is justified grounds to use waves with solitary wave front profiles to investigate near-shore coastal problems such as near-shore impact and debris transport studies (Yao et al., 2014; Seiffert et al., 2014; Chinnarasri et al., 2013). More recently, pump-driven elongated waves with solitary wave profiles have been applied to macro-roughness wave interaction in a laboratory (Goseberg and Schlurmann, 2014). Based on these findings, the application of the elongated solitary wave in this study can be used to investigate the incipient debris motion and general debris characteristics.

The presence of the macro-roughness elements (obstacles) in the experiments resulted in a significantly decreased longitudinal displacement of the debris. The reduction of the displacement was due to the loss of momentum as the inundating wave propagated through the obstacles. However, the particular obstacle setup used in these experiments resulted in the channelization of the flow, reducing thus the effectiveness of the obstacles. As the surge front impacted the obstacles, a jet formed, as a result of the flow constrictions. Within the jet, increased flow depths and velocities, as well as highly turbulent flow passed though the center of the gaps between the obstacles. The channelized flow appeared to not be affected by the second row of obstacles, as the primary flow path did not impact second row. Increasing the spacing between the two rows of obstacles, increasing the gap spacing, or staggering the rows would reduce the channelization of the flow, and potentially could reduce the displacement of the debris.

The gap spacing between the obstacles additionally will determine the debris damming potential. Bocchiola et al. (2006) studied the formation of debris dams in the presence of obstacles within river flow conditions. Bocchiola et al. (2006) identified two types of damming mechanisms: bridging and leaning. Bridging was the more stable mechanism, but can only occur if the debris was trapped on two obstacles, which in the case of this study was not possible due to the gap size between the obstacles. The mechanism by which the debris was trapped in this experiment was leaning, when the debris was caught on one obstacle. Bocchiola et al. (2006) noted that the leaning mechanism was unstable due to the debris needing to be in contact with the column near the central axis of the debris and was highly influenced by the Froude number of the flow. As the debris on the outer edge of the debris configuration impacted the obstacles well away from the central axis of the debris, the debris was never trapped against the obstacles. More detailed analysis of gap spacing in extreme hydrodynamic conditions is needed to better understand the formation of debris damming, and the effects on the hydrodynamic conditions.

5   CONCLUSIONS

This paper examines the transport of multiple debris within a built environment. The experiments were performed in the TWB at Waseda University, Tokyo, Japan. The TWB used a gravity-driven overhead reservoir to create an elongated solitary wave profile. The wave profile propagated over a still-water section, then broke at a vertical quay, propagating over a horizontal bottom as a tsunami-like surge. The inundating surge entrained scaled (1:40 length scale) idealized shipping containers. The motion of the debris was tracked using a novel sensor-based "smart" debris system that allowed the horizontal components of the debris motion to be analyzed. The study examined the effect of obstacles on the hydrodynamic conditions, debris dynamics, and the maximum spreading area of the debris. Based on the results from this study, the authors have drawn the following conclusions:

i.   While the use of a solitary wave in tsunami engineering has been recently challenged, the use of an elongated solitary wave profile can adequately be used to analyze incipient debris motion and the general characteristics of the motion.

ii. The presence of the obstacles on the horizontal bottom resulted in flow constrictions, which formed jets with increased flow depths and velocities. The debris tended to propagate within the middle of the jet.

iii. The obstacles occasionally trapped debris at their front face. However, due to the debris configuration and the highly turbulent flow conditions, the trapping mechanism was highly unstable resulting in the trapping occurring infrequently.

iv. The obstacles acted as a macro-roughness element, resulting in the momentum loss of the inundating surge. The loss of momentum of the wave, along with the occasional trapping of the debris, resulted in smaller longitudinal displacements of the debris.

The presence of macro-roughness elements within tsunami flow conditions has been shown to reduce the longitudinal displacement of the debris, while having negligible effects on the spreading angle. A consideration should be made to how the layout of a built environment will influence debris trajectory and velocity. Further research should investigate debris propagation under deeper, higher velocity flows as this may allow for improved prediction of the preferred paths of debris transport in a built environment.

REFERENCES

Bocchiola, D., Rulli, M. & Rosso, R. (2006). Transport of Large Woody Debris in the Presence of Obstacles. *Geomorphology,* 76, 166–178.

Chanson, H. (2006). Tsunami Surges on Dry Coastal Plains: Application of Dam Break Wave Equations. *Coastal Engineering Journal,* 48, 355–370.

Chinnarasri, C., Thanasisathit, N., Ruangrassamee, A., Weesakul, S. & Lukkunaprasit, P. (2013). The Impact of Tsunami-Induced Bores on Buildings. *Proceedings of the Institution of Civil Engineers: Maritime Engineering,* 166, 14 – 24.

Chock, G., Robertson, I., Kriebel, D., Francis, M. & Nistor, I. (2013). Tohoku, Japan, Earthquake and Tsunami of 2011. Performance of Structures under Tsunami Loads. *ASCE.*

Chock, G.Y. (2016). Design for Tsunami Loads and Effects in The ASCE 7-16 Standard. *Journal of Structural Engineering*, 142(11), 1 - 12.

Ghobarah, A., Saatcioglu, M. & Nistor, I. (2006). The Impact of the 26 December 2004 Earthquake and Tsunami on Structures and Infrastructure. *Engineering Structures,* 28, 312–326.

Goseberg, N., Nistor, I., Mikami, T., Shibayama, T. & Stolle, J. (2016). Non-Invasive 6-DOF Multi-Object Tracking in Violent Flow through "Smart" Debris with Application to Debris-Laden Tsunami Inundation. *Journal of Hydraulic Engineering,* 142(12), 1-17.

Goseberg, N. & Schlurmann, T. (2014). Non-Stationary Flow around Buildings during Run-Up of Tsunami Waves on A Plain Beach. *Coastal Engineering Proceedings,* 1, 21.

Goseberg, N., Wurpts, A. & T. Schlurmann. (2013). Laboratory-Scale Generation of Tsunami and Long Waves. *Coastal Engineering,* 79, 57–74.

Imamura, F., Goto, K. & Ohkubo, S. (2008). A Numerical Model for the Transport of a Boulder by Tsunami. *Journal of Geophysical Research Oceans,* 113, 1978–2012.

Knorr, W., & Kutzner, F. (2008*). Ecotransit Ecological Transport Information, Tool Environmental Method and Data,* IFEU Heidelberg.

Madsen, P.A., Fuhrman, D.R. & Schaffer, H.A. (2008). On The Solitary Wave Paradigm for Tsunamis. *Journal of Geophysical Research Oceans,* 113(C12), 1 - 22.

Matsutomi, H. (2009). Method for Estimating Collision Force of Driftwood Accompanying Tsunami Inundation Flow. *Journal of Disaster Research,* 4, 435 - 440.

Matsutomi, H., Fujii, M. & Yamaguchi, T. (2008). Experiments and Development of a Model on the Inundated Flow with Floating Bodies. *Coastal Engineering*, 1458 - 1470.

Munk, W. H. (1949). The Solitary Wave Theory and its Application to Surf Problems. *Annals of the New York Academy of Sciences,* 51, 376 - 424.

Naito, C., Cercone, C., Riggs, R. & Cox, D. (2014). Procedure for Site Assessment of the Potential for Tsunami Debris Impact. *Journal of Waterway, Port, Coastal and Ocean Engineering,* 140, 223 – 232.

Nistor, I., Goseberg, N., Mikami T., Shibayama, T., Stolle, J., Nakamura, R. & Matsuba, S. (2016). Hydraulic Experiments on Debris Dynamics over a Horizontal Plane. *Journal of Waterway, Port, Coastal and Ocean Engineering*, 143(3), 1 - 15.

Nistor, I., Goseberg, N. & Stolle, J. (2017). Tsunami-Driven Debris Motion and Loads: A Critical Review. *Frontiers in Built Environment* 3, 2.

Palermo, D., Nistor, I., Saatcioglu, M. & Ghobarah, A. (2013). Impact and Damage to Structures during the 27 February 2010 Chile Tsunami. *Canadian Journal of Civil Engineering,* 40, 750–758.

Parola, A. C. (2000). *Debris Forces on Highway Bridges.* Transportation Research Board.

Rueben, M., Cox, D., Holman, R., Shin, S. & Stanley, J. (2014). Optical Measurements of Tsunami Inundation and Debris Movement in a Large-Scale Wave Basin. *Journal of Waterway, Port, Coastal, and Ocean Engineering,* 141(1), 1 - 14.

Saatcioglu, M., Ghobarah, A. & Nistor, I. (2005). Effects of the December 26, 2004 Sumatra Earthquake and Tsunami on Physical Infrastructure. *ISET Journal of Earthquake Technology*, 42, 79–94.

Seiffert, B., Hayatdavoodi, M. & Ertekin, R. C. (2014). Experiments and Computations of Solitary-Wave Forces on a Coastal-Bridge Deck. Part I: Flat Plate. *Coastal Engineering,* 88, 194–209.

Shafiei, S., Melville, B., Beskhyroun, S. & Shamseldin, A. (2014). Preliminary Investigation of the Tsunami-Borne Debris Impact on Structures: A New Method for Impact Force Measurement. *5th IAHR International Symposium on Hydraulic Structures*, University Of Queensland, 1-9.

Shafiei, S., Melville, B.W., Shamseldin, A.Y., Beskhyroun, S. & Adams, K. N. (2016). Measurements of Tsunami-Borne Debris Impact on Structures Using an Embedded Accelerometer. *Journal of Hydraulic Research*, 1, 15.

Stolle, J., Nistor, I. & Goseberg, N. (2016). Optical Tracking of Floating Shipping Containers in a High-Velocity Flow. *Coastal Engineering Journal*, 58(2), 1 - 29.

Takahashi, S., Kuriyama, Y., Tomita, T., Kawai, Y., Arikawa, T. & Tatsumi, D. (2011). Urgent Survey for 2011 Great East Japan Earthquake and Tsunami Disaster in Ports and Coasts. Part I (Tsunami). *Port and Air Port Research Institute.*

Takahashi, S., Sugano, T., Tomita, T., Arikawa, T., Tatsumi, D., Kashima, H., Murata, S., Matsuoka, Y. & Nakamura, T. (2010). *Joint Survey for 2010 Chilean Earthquake and Tsunami Disaster in Ports and Coasts*, Port and Airport Research Institution.

Yao, Y., Huang, Z., Lo, E.Y.M. & Shen, H.-T. (2014). A Preliminary Laboratory Study of Motion of Floating Debris Generated by Solitary Waves Running Up A Beach. *Journal of Earthquake and Tsunami,* 8(3), 1-13.

Yeh, H., Barbosa, R., Ko, H. & Cawley, J. G. (2014). Tsunami Loadings on Structures: Review and Analysis. *Coastal Engineering Proceedings,* 1, 1- 4.

ESTIMATION OF SPATIAL FLOOD DAMAGE COSTS IN JAKARTA, INDONESIA

NURUL F. JANURIYADI[1], SO KAZAMA[2] , IDHAM R. MOE[3] & SHUICHI KURE[4]

[1] Graduate School of Environmental Studies, Tohoku University, Sendai, Miyagi, Japan,
nurul.fajar.januriyadi.p4@dc.tohoku.ac.jp
[2,3] Department of Civil and Environmental Engineering, Tohoku University, Sendai, Miyagi, Japan,
so.kazama.d3@tohoku.ac.jp; idham.moe@gmail.com
[4] Department of Environmental Engineering, Toyama Prefectural University, Imizu, Toyama, Japan,
kure@pu-toyama.ac.jp

ABSTRACT

Flood is one of the natural disasters that gives great impact for human life and its occurrences has been increasing over the years. Floods also caused many damages, both tangible damage and intangible damage. There are many adaptation measures for reducing the flood damage, however for constructing or applying those needs a lot of funds. Therefore, we need to prioritize the flood adaptation measures. In this study, the methodology consists of two parts, flood inundation model and flood damage cost estimation. For asset value data of land use, we obtained some data from Indonesia statistic agency and the other data, we estimated it by comparing the global economic indicators of study site to the other countries. Results showed the expected annual flood damage costs are 595 million USD. Through this study, we can identify the locations with the first priority in applying flood adaptation measures.

Keywords: Asset value; inundation depth; Jakarta flooding; spatial map.

1   INTRODUCTION

Floods are one of the most common and most costly natural disasters in the world. In UNISDR report (2015), since 1995, floods have accounted for 47% of all weather related disasters and affecting 2.3 billion people (56% of all weather related disasters). And also, in the report it was mentioned that high asset values in high-income countries pushed up their recorded losses in the period 1995 – 2015, yet this remained a modest 0.2% of GDP. Much lower absolute losses in low-income countries (US$ 40 billion in total) amounted to a high 5% of GDP. So, it means that the economic growth of low income country will be affected by the occurrences of disasters. For example, in DPR of Korea, 77% of recorded losses were due to floods between 1995 and 2015 (33% of GDP).

Many countries have experienced floods, especially countries with high rainfall intensity. Indonesia is one of country which has high rainfall intensity, and floods occurred almost every year. BNPB recorded that approximately 6000 flood events were occurred between 1994 and 2015 with different magnitude, and 2.2% were occurred in Jakarta city. There are some factors that contributed for flood in Jakarta city, Farid et al. (2011) modelled the flood runoff response to land cover change in Ciliwung River. Abidin et al. (2015) found that the water depths in the flooded areas during 2007 flooding are also spatially coincided with magnitudes of land subsidence in the period of 2000 to 2011. In addition, the main factors that contribute for flooding in Jakarta is rapid urbanization, BPS (Indonesia statistic agency) recorded that number of population in Jakarta increasing approximately 110% between 1971 and 2010. This factor evoked the other factors like land subsidence and land use change.

Moreover, Jakarta is not only a city with high vulnerability of flooding but also has high asset value. In 2014, the gross domestic product (GDP) of Jakarta contributed approximately 16% of total GDP of Indonesia. It means that if a disaster occurs in Jakarta city, it will not only disrupt the Jakarta economy growth but also the Indonesia economic growth. So we need some adaptations for reducing the damage of flood and make the priority level of adaptations. Through this study, we can identify the locations with the first priority in applying flood adaptation measures.

2   STUDY AREA

Study area of this study is Jakarta city that is located in Java Island (see Figure 1). There are thirteen rivers flowing into Jakarta city with the main river is the Ciliwung River. The upstream of Ciliwung River is Gede Pangrango Mountain, which is located in Bogor district with a total area of watershed is approximately 360km^2.
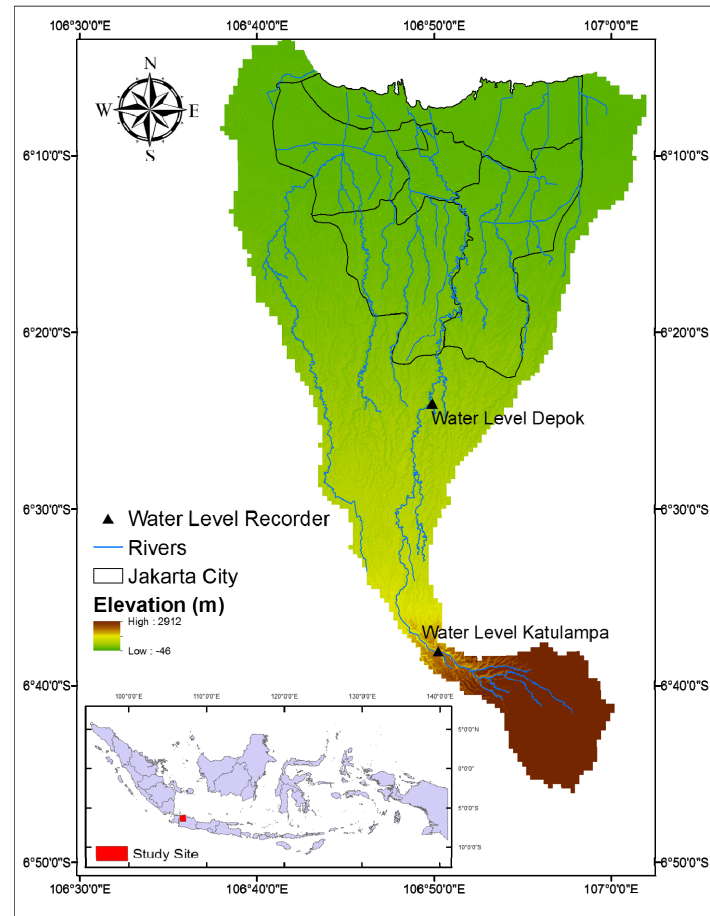
Figure 1. Study area map.

3   METHODOLOGY

In this paper, the methodology consists of two parts, flood inundation model and flood damage cost estimation.

3.1 Flood Inundation Model

Moe et al. (2015; 2016) have developed flood inundation model for Jakarta city, they have succeeded to calibrate the flood inundation model with 2013 Jakarta flood event. The model consists of rainfall runoff model at each sub-basin, flow in river and flood inundation simulation on the land.

3.1.1   Rainfall runoff

For rainfall runoff, we used rainfall runoff model that was proposed by Kure et al. (2008; 2013). The model simulates rainfall runoff process based on the geology and hydrology condition for each sub-basin. For urban areas, it simulates as the Hortonian overland flow and for mountainous areas, simulating as subsurface and saturation overland flow.

3.1.2   Flow in the rivers

For flow in the river, one-dimensional of continuity and momentum equation (Saint-Venant equation) were used for flow in the river. The Saint-Venant equations are written as follows:

$$\frac{\partial A}{\partial t} + \frac{\partial Q}{\partial x} = q_l \qquad\qquad [1]$$

$$\frac{\partial Q}{\partial t} + \frac{\partial \left(\alpha \frac{Q^2}{A} \right)}{\partial x} + gA\frac{\partial h}{\partial x} + \frac{gn^2|Q|Q}{R^{4/3}A} = 0 \qquad\qquad [2]$$

where Q is the discharge (m³/s), A is the area of cross-section (m²), q_l is the lateral inflow or outflow distributed along the x-axis of the watercourse (m³/s), n is the manning's roughness coefficient, α is the momentum distribution coefficient, g is the acceleration of gravity (m/s²), R is the hydraulic radius (m) and h is the water level (m).

3.1.3 Overland flow

For overland flow, the two-dimensional of the continuity and momentum equation were solved numerically for overland flow. The lateral link was used for coupling flow in the river and overland to represent spilling from the river to the flood plain and drainage back into the river.

3.2 Flood damage costs calculation

The procedures for calculating the damage cost for each type of land use were determined based on the flood control economy investigation manual published by the MLIT (2005). For the flood damage costs, there are five main sectors that were calculated for damage costs, *i.e.,* paddy field, crop field, housing, manufacturing and service, for the other land use were categorized as other sectors. The land use map was obtained from BAPPEDA (see Figure 2). In this study area, some economic values were obtained from some Indonesia government office, *i.e.,* Indonesia statistic agency (BPS) and agriculture ministry. And for currency exchange, we used official exchange rate from World Bank website.
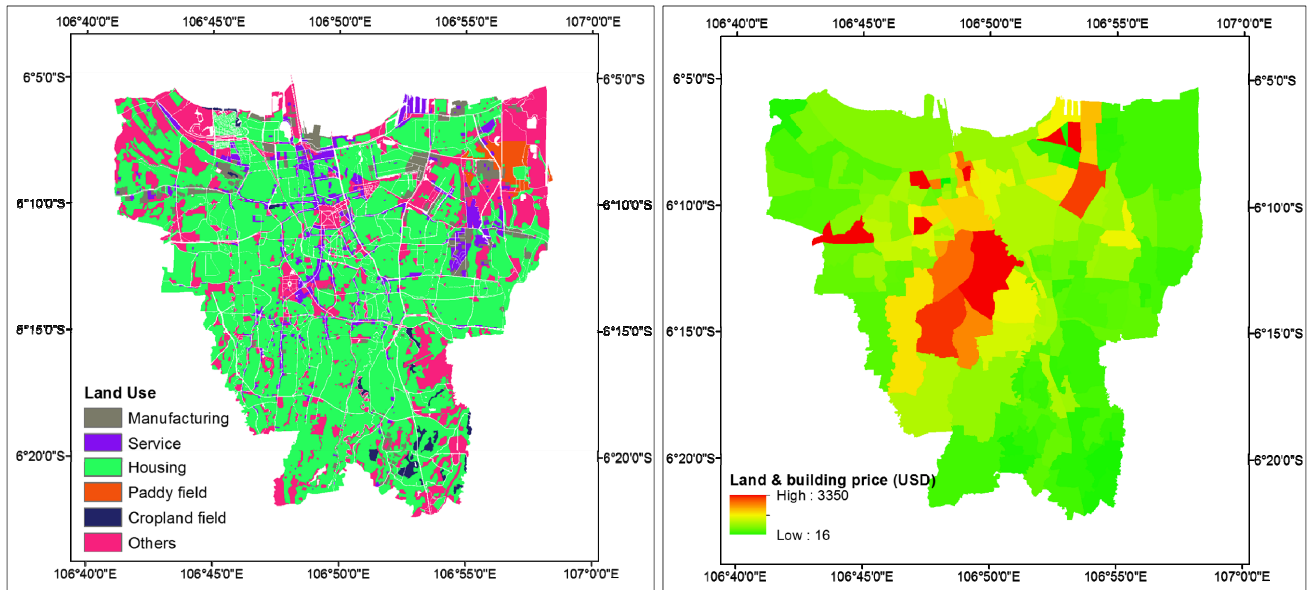

Figure 2. Land use classification map (left), land and building price per m^2 (right).

Paddy field damage was calculated using the following equation:

$$DC_P = 564 \times 266 \times A \times DR_P \qquad [3]$$

where DC_P is flood damage costs for paddy sector (USD), 564 is average rice productivity (ton/km^2), 266 is the average rice price (USD/Ton), A is the inundated area (km^2), and DR_P is the damage rate value for paddy field based on the depth of water.

For crop land damage was calculated using the following equation:

$$DC_C = 1970 \times 435 \times A \times DR_C \qquad [4]$$

where DC_C is flood damage costs for cropland (USD), 1970 is average paddy cabbage productivity (ton/km^2), 435 is the average cabbage price (USD/Ton), A is the inundated area (km^2), and DR_C is the damage rate value for cropland. Cabbage was chosen as crop for damage costs estimation, because it is the most crop that produced in Jakarta. And, we only choose one kind of crop, because if the market demand changes from one kind crop to another crop, the farmer will change their product automatically.

Damage cost for housing area consists of house building damage and house content damage. The housing area damage costs equations are as follows:

$$DC_H = DC_B + DC_{HC} \qquad [5]$$

$$DC_B = Houseprice \times A \times DR_B \qquad [6]$$

$$DC_{HC} = Housecontent \times n \times DR_{HC} \qquad [7]$$

where DC_H is flood damage costs for housing (USD), DC_B is flood damage costs for house building (USD), DC_{HC} is flood damage costs for house content (USD). $Houseprice$ is house prices (USD/m^2). It differs depending on the location. It was obtained by converting the land and building taxes income each district to be land and building sale price (see Figure 2). We also assumed that the building price is half of land price. A is the inundated area (m^2), DR_B is the damage rate value for building. $Housecontent$ is the asset value per house, the average of $Housecontent$ is obtained by equation [8]. n is number of the inundated house and DR_{HC} is the damage rate value for house content.

$$Housecontent = 5.68\,GDP_P - 7.7 \times 10^{-9}\,HFCE - 48644.2 \qquad [8]$$

where GDP_P is gross domestic product per capita (USD) and $HFCE$ is household final consumption expenditure (USD). This equation was obtained by linear regression analysis and the validation result is shown in Figure 3.

The damage costs for manufacturing and service sector were calculated by the following equations:

$$DC_M / DC_S = DC_B + DC_{Fixed} + DC_{Fixed} \qquad [9]$$

$$DC_{Fixed} = FixedAsset \times n_E \times DR_{Fixed} \qquad [10]$$

$$DC_{Stock} = StockAsset \times n_E \times DR_{Stock} \qquad [11]$$

where DC_M and DC_S are flood damage costs for manufacturing and service (USD), respectively. DC_B is flood damage costs for building (USD) was calculated in the same manner as housing building damage. DC_{Fixed} is flood damage costs for fixed asset (USD), DC_{Stock} is flood damage costs for stock asset (USD), and n_E is the number of employees that were influenced by inundation. $FixedAsset$ and $StockAsset$ are the asset value per employee for fixed and stock asset, the asset value for manufacturing and service were calculated by equation [12] and [13].

$$((Fixed/stock)_M)_x = \left(\frac{1}{n} \cdot \sum_{i=1}^{n} \frac{(GDP_M)_x}{(GDP_M)_i} x((Fixed/stock)_M)_i \right) \qquad [12]$$

$$((Fixed/stock)_S)_x = \left(\frac{1}{n} \cdot \sum_{i=1}^{n} \frac{(GDP_S)_x}{(GDP_S)_i} x((Fixed/stock)_S)_i \right) \qquad [13]$$

where GDP_M is gross domestic product from manufacturing sector (USD), GDP_S is gross domestic product from service company sector (USD), and the parameter with subscript M, S, x, i are those parameters related to manufacturing, service, study location and the other country, respectively. For finding the equations, we used the asset value data from three countries statistic agency and analyzed the linear correlation coefficient with each global economic indicator. Subsequently, we selected economic indicators, which have the highest correlation coefficient (see Figure 3).

The flood damage costs for the other sector, we use as the flood damage costs for building. The damage rates were obtained from the flood control economy investigation manual (MLIT 2005). Figure 4 shows the continuous relationship between the damage rate and inundation depth in the case of 1 – 2 days of inundation.
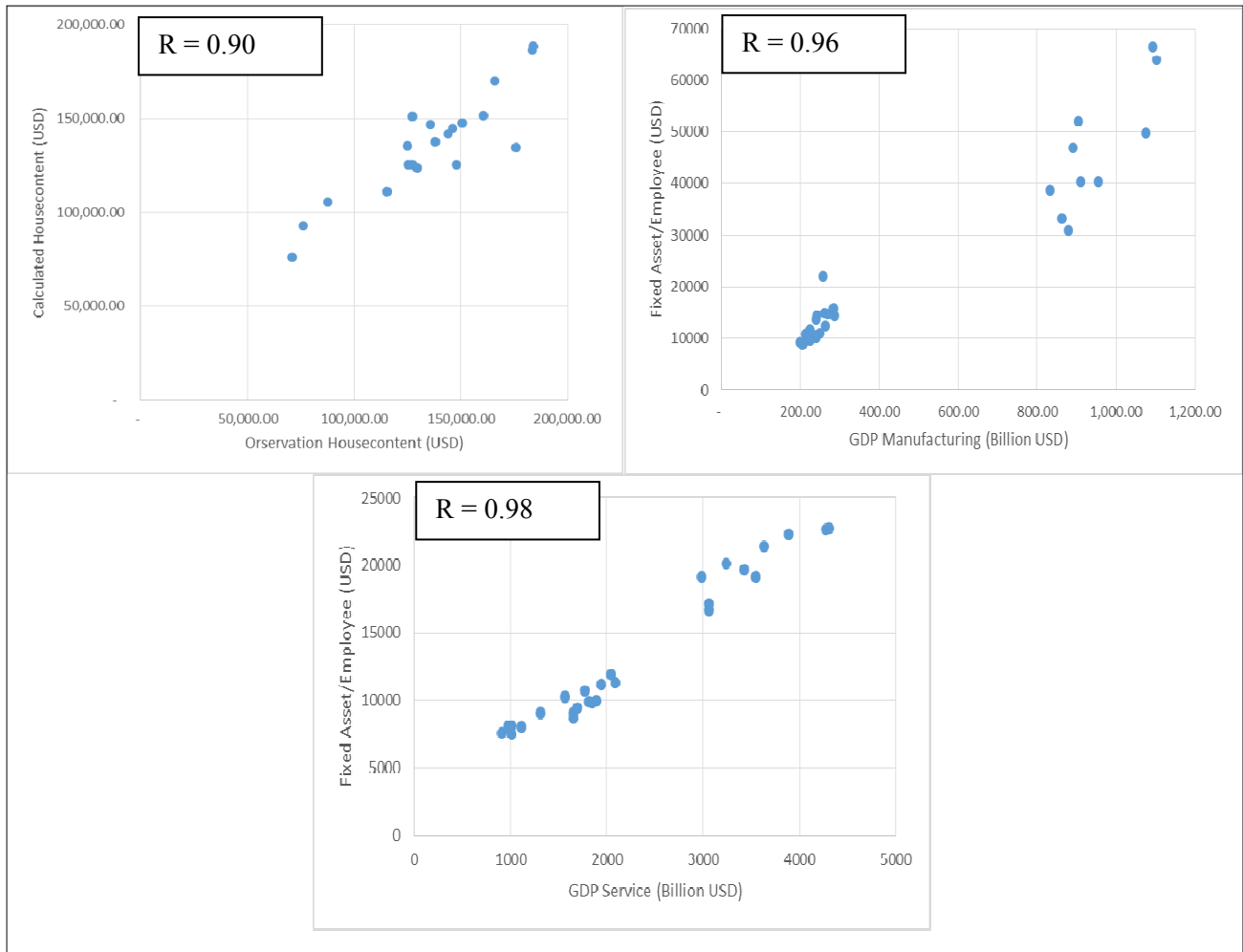
Figure 3. Validation result for house content asset (top left), Correlation between manufacturing asset value and GDP from manufacturing sector (top right) and Correlation between service asset value and GDP from service sector (low middle).
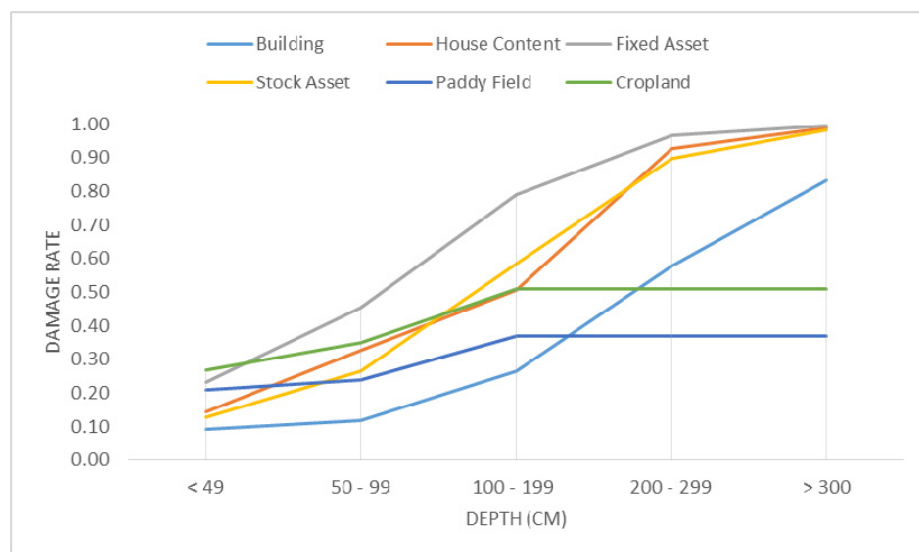

Figure 4. Flood damage rate based on inundation depth.

4   RESULTS AND DISCUSSIONS

We simulated some rainfall return periods into the flood inundation model, we selected 5, 10, 25, 50, and 100 years and calculated the potential flood damage costs. Figure 5 shows the flood damage costs for 5 and 100 years return period. Spatially, the flood damage costs are distributed into three areas, the North West area is the confluence of some rivers (*i.e.,* Angke River, Pasanggrahan River, Mokervart canal, Sekretaris

canal and Cengkareng drain canal), so this area has broad inundation area. And, some manufacturing sectors are located in this area. The second area is the central part, Cilwung River is flowing through this area. This area has high density of house. The third one is the North East area, which is the low elevation area with varied land use.
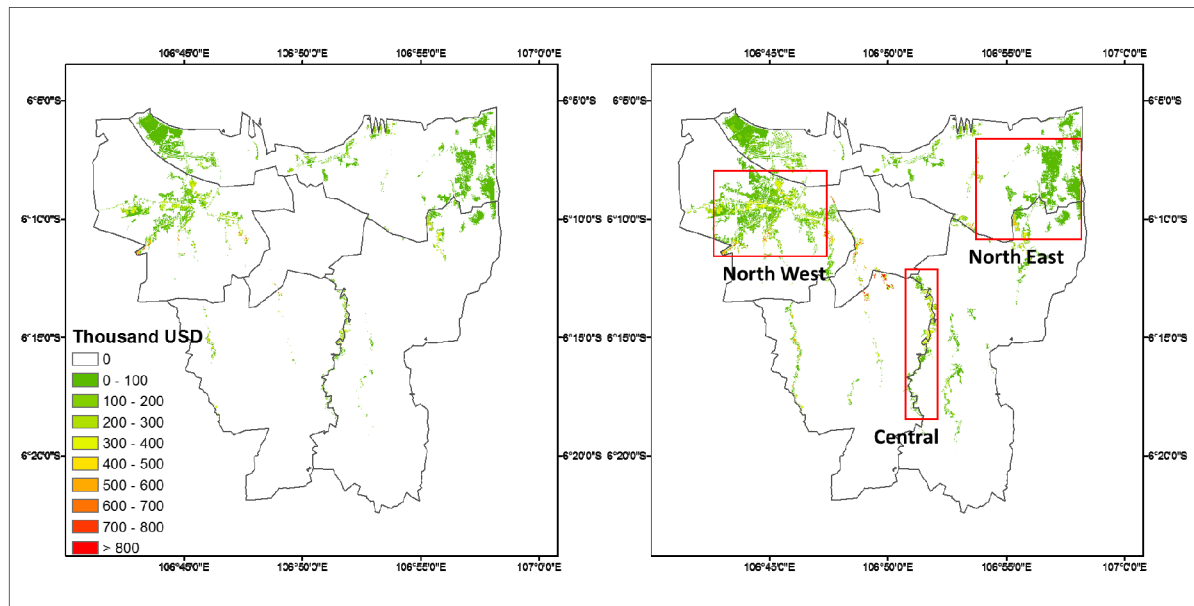

Figure 5. Potential flood damage costs in Jakarta (thousand USD) 5 years (left) and 100 years (right) return period.

The increase of the potential flood damage cost is the same as the benefit to protect. We calculated spatial map of expected annual damage (see Figure 6) for identifying the distribution of annual damage costs same as annual benefit with the total expected annual damage is 595 million USD. This benefit value can be used for benefit cost ratio analysis, so that we can make the priority of adaptation measures for reducing flood damage. In 2014, the expenditure for Jakarta flood control in the Public Ministry regular budget is nearly 145 million USD, which is smaller than the expected damage costs. The adaptation measures should be evaluated according the benefit and cost ratios.

The problems faced by Jakarta are not only flooding but also land subsidence, it needs the adaptation measures that can reduce both flood damage and land subsidence rate. We propose to construct infiltration ponds in the areas with high damage costs. Infiltration ponds can be the retention pond when flood occur, so it can reduce the peak of flood and the remaining water after the flood in the pond can infiltrate into the soil, so it can recharge the ground water. However, we need to combine the infiltration pond with the other adaptation measures either structural or non-structural.
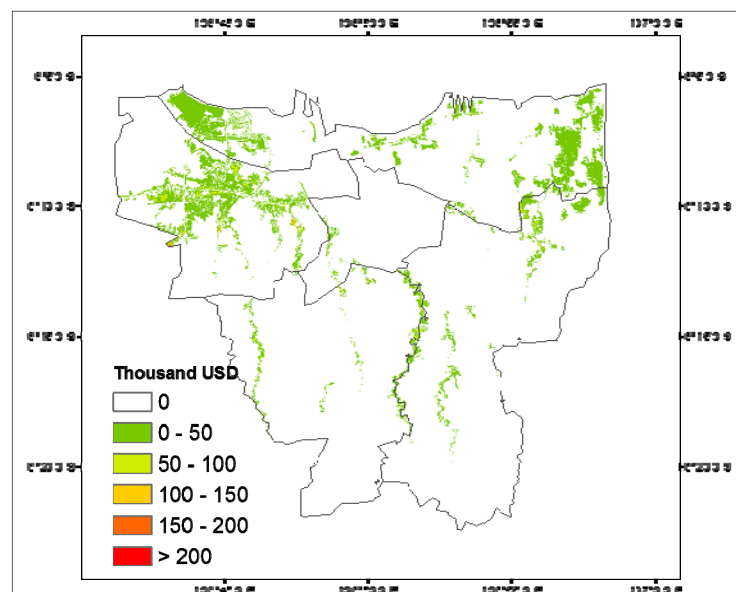

Figure 6. Spatial map of expected annual flood damage costs.

5   CONCLUSIONS

This study developed flood damage costs estimation method based on flood inundation model and valuating the asset values use global economic indicators. The return period rainfalls were used as the input for obtaining the spatial map of flood damage costs each return period. We estimated the expected annual flood damage costs in Jakarta is 595 million USD.

The spatial map assists to identify the most vulnerable areas to flooding in Jakarta. Hence, this study will help the flood control management authority in Jakarta for prioritizing the flood adaptation measures.

ACKNOWLEDGEMENTS

REFERENCES

Abidin, H.Z., Andreas, H., Gumilar, I., Sidiq, T.P. & Brinkman, J.J. (2015). Assessment of Natural Hazards Affecting the Delta City of Jakarta. *3rd AUN/SEED-Net Regional Conference on Natural Disaster (RCND2015),* 25-26 September 2015, Manila, Philippine.

Farid, M., Mano, A., & Udo, K. (2011). Modeling Flood Runoff Response to Land Cover Change with Rainfall Spatial Distribution in Urbanized Catchment. *Journal of Hydraulic Engineering*, 67(4), 19-24.

Kure, S. & Yamada, T. (2004). Nonlinearity of Runoff and Estimation of Effective Rainfall in a Slope. *Proceedings of the 2nd Asia Pacific Association of Hydrology and Water Resources Conference*, 2, 76-85.

Kure, S., Watanabe, A., Akabane, Y., & Yamada, T. (2008). Field Observations of Discharge and Runoff Characteristics in Urban Catchments Area. *Proceedings of 11th International Conference on Urban Drainage*, United Kingdom,.1-10.

Moe, I.R., Kure, S., Farid, M., Udo, K., Kazama, S. & Koshimura, S. (2015). Numerical Simulation of Flooding in Jakarta and Evaluation of a Counter Measure to Mitigate Flood Damage. *Journal of Japan Society of Civil Engineers, Ser. G (Environmental Research)*, 71(5),29-36.

Moe, I.R., Kure, S., Farid, M., Udo, K., Kazama, S., & Koshimura, S. (2016). Evaluation of Flood Inundation in Jakarta using Flood Inundation Model Calibrated by Radar Rainfall. *Journal of Japan Society of Civil Engineers, Ser. B1 (Hydraulic Engineering)*, 72(4), 1243-1248.

Ministry of Land, Infrastructure, Transport and Tourism (MLIT). (2005). *Draft of the Flood Control Economy Investigation Manual (in Japanese)*, Ministry of Land, Infrastructure, Transport and Tourism (MLIT), Tokyo, Japan.

UNISDR. (2015). *The Human Cost of Weather-Related Disasters 1995-2015*, United Nations Office for Disaster Risk Reduction (UNISDR), Paris, France.

TRADITIONAL TECHNIQUE IN JAPAN TO PREVENT BRIDGE BLOCKAGES CAUSED BY DRIFTWOOD USING STAKES

NORIO HARADA[1], KANA NAKATANI[2], YOSHIFUMI SATOFUKA[3] & TAKAHISA MIZUYAMA[4]

[1] Mitsui Consultants Co., Ltd., Osaka, Japan,
harada@mccnet.co.jp
[2] Kyoto University, Kyoto, Japan,
kana2151@kais.kyoto-u.ac.jp
[3] Ritsumeikan University, Shiga, Japan,
satofuka@se.ritsumei.ac.jp
[4] National Graduate Institute for Policy Studies, Tokyo, Japan,
t-mizuyama@grips.ac.jp

ABSTRACT

In Japan, stakes have long been used to control driftwood accumulation and prevent bridges from becoming blocked. However, no formal design code has been established. Thus, stake installations at individual bridges differ. It is important to clarify the function of these stakes. For example, some stakes are used to prevent rubbish from accumulating near piers. In this paper, we describe an experiment to evaluate how effective the traditional stakes are as a countermeasure against the driftwood accumulation. We supplied water and driftwood from a flume and observed the mechanisms by which the stakes prevented driftwood damage. We varied the arrangement of stakes, the distance between them, their angle with respect to the riverbed, and the direction of driftwood flow. Driftwood passed between piers after rotating around stakes. Consequently, we suggest that bridges can be protected by vertical stakes, as these prevent the accumulation of driftwood.

Keywords: Bridge; driftwood; experiment; stake; natural debris.

1   INTRODUCTION

Many areas downstream of downpours and floods have been damaged by debris flow and driftwood. This damage is the result of depletion of mountain forests and landslides due to local downpours caused by global warming (Fujita, 2012). In Japan, recent disaster reports have stated that blockages caused by driftwood have contributed to flooding around and damage to bridges (Ishikawa et al, 2016; Izu-Oshima disaster research committee, 2014). There have been a number of studies concerning bridge damage and countermeasures to prevent the accumulation of driftwood (Nakagawa et al., 1992; Goto et al., 2001; Shimizu et al., 2007; Shibuya et al., 2011). Some researchers (Adachi and Daido, 1957; Ishikawa et al., 1989) have proposed mechanisms to explain the formation of driftwood blockages at bridges and in narrow channels. Adachi and Daido (1957) suggested that the variables determining whether a bridge is blocked by driftwood are as follows: the density of flowing driftwood, the velocity of the surface flow, and the relationship between the bridge-pier interval and the driftwood length. Ishikawa et al. (1989) proposed a model to predict the driftwood-blockage rate experimentally based on the fluid number, width of the narrow channel, and driftwood length and diameter. Nakagawa et al. (1992), Goto et al. (2001), Shimizu et al. (2007) and Shibuya et al. (2011) predicted the behavior of driftwood in flowing rivers numerically. Ishikawa et al. (2007) proposed a countermeasure to prevent bridges from being blocked by installing steel in the bridge beam.

Historically, stakes that control the flow of driftwood have been used to protect Japanese bridges from blockages. These stakes have been installed at, for example, the Togetsu Bridge and the Uji Bridge at the Ise Shrine, as shown in Photo 1. The stakes also prevent other types of natural debris from blocking the bridges. Takebayashi (2014) described how the stakes functioned during the flooding in 2013, as shown in Photo 2. There are many bridges with narrow intervals between their piers. Hence, we need to prevent driftwood and natural debris from accumulating at these bridges. Traditional stakes are an effective countermeasure against blockage by debris. However, design codes have not been established. Thus, the arrangement of stakes differs at individual bridge. At the Togetsu Bridge, which is shown in Photo 1, a stake was installed at every other pier. In other bridges, such as the Uji Bridge, which is also shown in Photo 1, stakes are installed at every pier. Furthermore, no study has been conducted to compare how effective different arrangements of stakes are at preventing blockages, and how their gradient with respect to the riverbed affects the accumulation of debris. We conducted a laboratory-based experiment to observe the effects of stakes on the behavior of driftwood flowing along rivers. Based on our experimental results, we propose an effective plan for using stakes to prevent blockages.

Photo 1. Traditional Japanese technique to prevent damage to historical bridges using stakes
(Right: Togetsu Bridge, Arashi-yama, Kyoto; Left: Uji Bridge, at the Ise shrine, Mie).

Photo 2. Stakes at the Togetsu Bridge during the flooding
event of 2013 [Takebayashi, 2014].

2   DRIFTWOOD CONTROL EXPERIMENT

2.1   Outline

Figure 1 shows the experimental setup; the experimental waterway, which was in the flume, was 20cm high, 20cm wide and 300cm long. We counted the number of small pieces of driftwood blocked by the stakes or piers. These were installed at the downstream edge of the flume, as shown in Figure 2. The stakes and water were supplied to the upper point at a rate of q_{in} cm^3/s. The driftwood was Φ_1 mm in diameter, 10cm in length and had a dry density of 0.75.
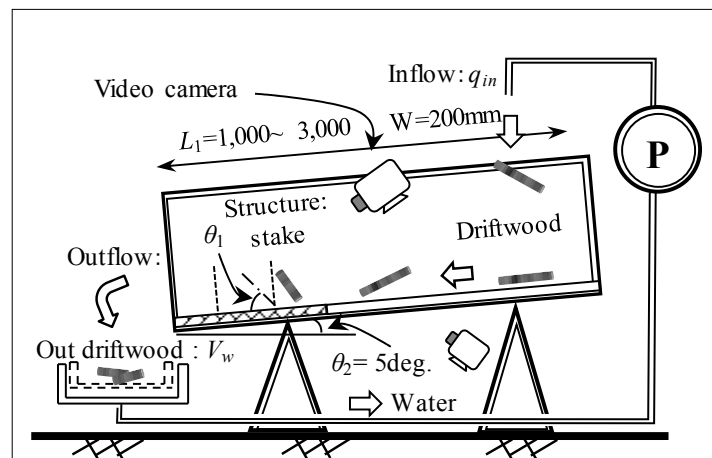

Figure 1. Diagram of the experimental flume.

The flume was inclined at an angle of 5 degrees (Ishikawa et al., 1989). The riverbed was covered in stone grains so that the flow was stable, as in a real river. The stakes and piers were cylindrical, and were 1cm in diameter, as shown in Figure 2. The results of the experiment were easier to control when cylindrical stakes were used rather than prism-shaped stakes, because the flow around prism shaped stakes was disordered. We used a pier interval, L_2, of 5cm, which was half the length of the driftwood, l_1, 10cm. Ishikawa

et al. (1989) reported that driftwood can easily block the space between stakes when the length of the driftwood is longer than the distance between stakes.

Table 1 shows the parameters that we controlled during the experiments. We observed the effect of stakes on driftwood flow as we varied the driftwood diameter, Φ_1, the distance between the stakes, L_3, and the supply point L_1 (the driftwood supply rate, V_w), the direction of the driftwood flow, the arrangement of the stakes, as shown in Figure 3. The inclination of the stakes against the riverbed θ_1, as shown in Figure 4, the distance between the piers and the stakes, L_3, the length of the driftwood, l_1, as shown in Figure 2, and the upstream water supply rate, q_{in}.
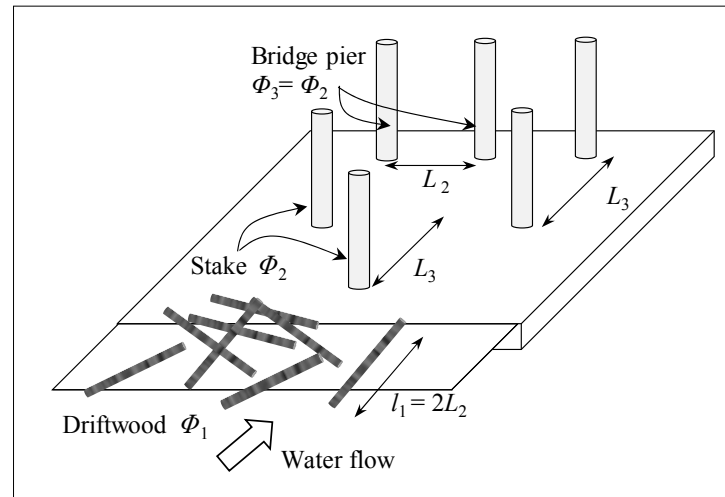

Figure 2. Diagram of the experimental model.

Table 1. Combinations of parameters used in the experiments.

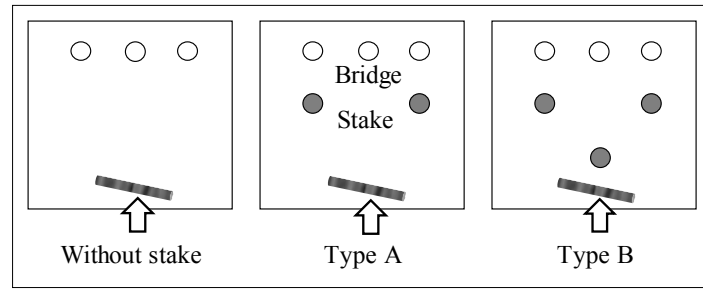| CASE	Φ_1 (mm)	L_1 (mm)	V_w	Direction of flow	Type	θ_1 (deg.)	L_3	q_{in} (l/s)
1-1		1,000		Parallel		Without stake		1.0
1-2								2.3
1-3		2,000		Perpendicular				
1-4								
2-1		1,000					1.0*l_1	1.0
2-2								
2-3			1/s*50s		B	90	1.5*l_1	
2-4								
2-5							1.0*l_1	
2-6	3						0.5*l_1	
2-7		2,000				Without stake		
2-8					A	90	1.0*l_1	
2-9				Parallel			1.5*l_1	
3-1						Non-structure		2.3
3-2			50		B	90	1.5*l_1	
3-3								
3-4		3,000				Without stake		
3-5					B	45	1.5*l_1	
3-6			1/s*50s			135		
4-1	1	2,000				Without stake		

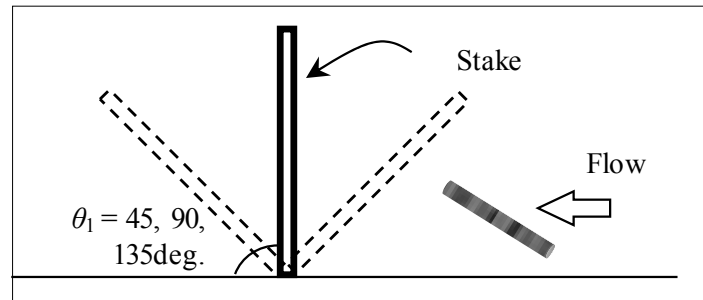**Figure 3**. Different arrangements of stakes.

Figure 4. Angle between the stakes and the riverbed.
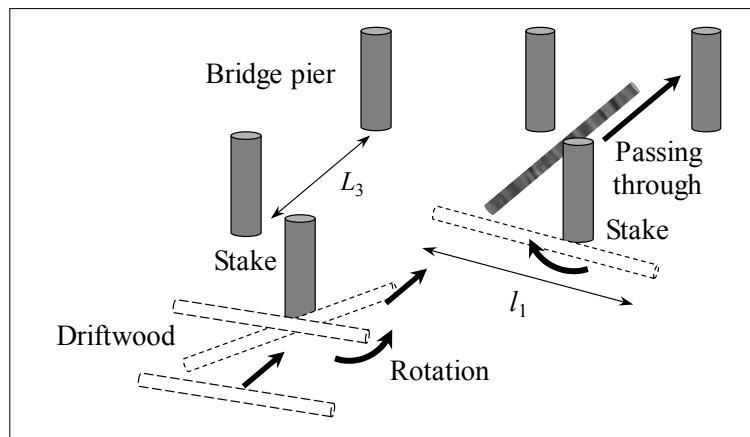

Figure 5. Driftwood control mechanisms observed in this study.

As shown in Figure 3, we proposed a new arrangement of stakes, namely the houndstooth arrangement, which we called Type B. In the Type A arrangement, we used stakes at alternating piers, as these are used at the Togetsu Bridge, as shown in Photo 1. The volume of driftwood supplied was equal to the space between the stakes and the piers. The maximum driftwood volume concentration ratio was approximately 0.3. When the supply water discharge rate was 1.0L/s, the water height was 1.1cm and the Froude number was 1.3. When the supply water discharge rate was 2.3L/s, the water height was 1.9cm and the Froude number was 1.4.

Figure 5 shows the mechanisms we considered for the stakes to control the flow of driftwood under the bridge. As shown in Figure 5, we believe that driftwood rotates around the stakes, enabling it to flow between the piers. The experiment was repeated three times under each condition and was recorded using video cameras, as shown in Figure 1.

2.2 Effect of the arrangement of stakes on driftwood control performance

The non-capture rate, f_{wn}, which is the rate at which driftwood pieces passed through the bridge piers, is given by:

$$f_{wn} = V_{wout} / V_w \qquad [1]$$

where V_{wout} is the number of driftwood pieces that passed under the bridge and V_w is the number of driftwood pieces supplied. Let us start our discussion on the effectiveness of the stakes for controlling driftwood accumulation by describing the results of our experiments.

Figure 6 shows the relationship between the supplied water discharge rate from upstream (q_{in}, as shown in Figure 1) and f_{wn}. f_{wn} increased with q_{in} and the water-flow speed, as shown in Figure 6. In fast-flowing areas, we observed that driftwood passes through bridge piers by rotating smoothly around the stakes, whereas the driftwood pieces did not rotate around the stakes in slow-flowing areas, and so were captured by the stakes or piers. Some of the results in slow-flowing areas agreed with those from fast-flowing areas, which suggests that the capture of driftwood is a probabilistic process.

Figure 7 shows the relationship between the supply direction of the driftwood pieces and f_{wn}. In particular, we studied driftwood flowing perpendicularly and parallel to the direction of flow. The direction of the flow did not have a significant effect on f_{wn}, as shown in Figure 7. We observed that the water flow rotated around the driftwood irregularly, so some driftwood pieces started to flow in the same direction as the water.

Figure 8 shows the relationship between the driftwood supply volume/speed and f_{wn}. We introduced one piece of driftwood per second for 50 seconds, and 50 pieces of driftwood simultaneously. When all the driftwood was released at once, it was captured easily. f_{wn} was affected by differences in the density of the driftwood, as shown in the previous study (Adachi and Daido, 1957). However, the results of experiments where all the driftwood was released at once are very similar to the results of the experiments where driftwood was released slowly, as shown in Figure 8.
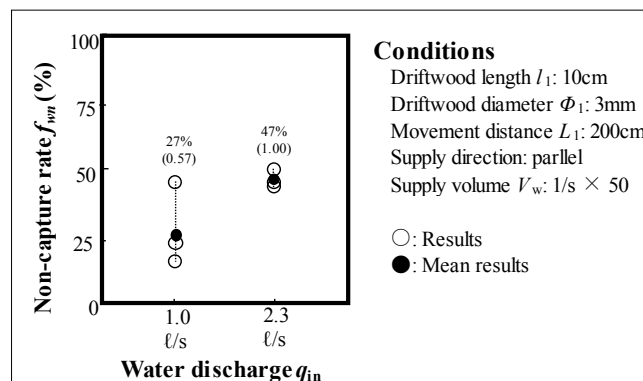

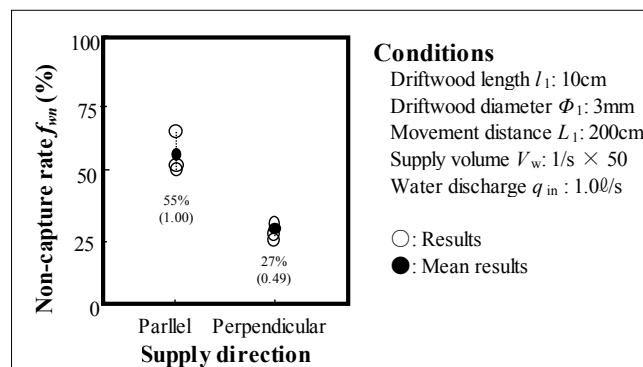**Figure 6**. Effect of water discharge on the non-capture rate, f_{wn}.

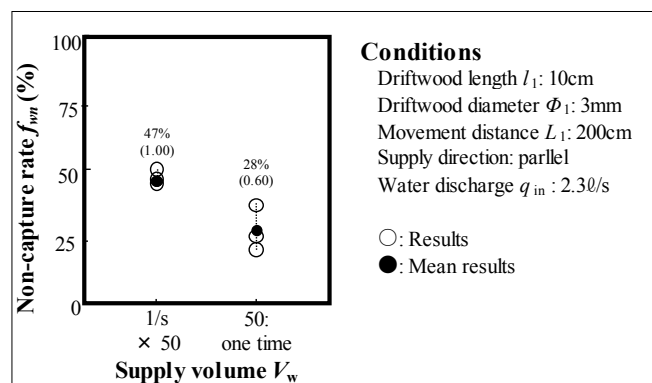**Figure 7**. Effect of the direction at which the driftwood pieces were supplied on f_{wn}.

Figure 8. Effect of the driftwood supply volume/speed on f_{wn}.

Figure 9 shows the relationship between the driftwood diameter (Φ_1) and f_{wn}. f_{wn} increased with Φ_1, as shown in Figure 9. Ishikawa et al. (1989) suggested that there is a relationship between the driftwood capture-rate in narrow flume, the fluid number and the driftwood diameter and length. We observed experimentally that fast-flowing water, as seen when the fluid number was larger, enabled the driftwood captured by stakes or bridge piers to be released by rotating around the stakes. In the future, additional research is required to confirm the release mechanisms.
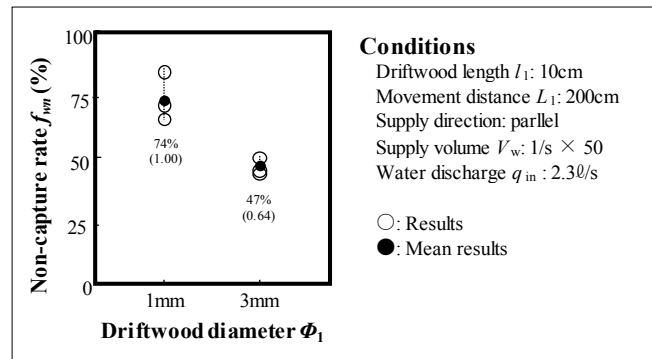

Figure 9. Effect of the driftwood diameter on f_{wn}.

Figure 10 shows the relationship between the arrangement of the stakes and f_{wn}. We tested no-stake, Type A and Type B, as shown in Figure 3. The stakes enable driftwood to pass easily through the bridge piers by rotating around them, as shown in Figure 5. The presence of stakes approximately doubled the driftwood capture rate. Furthermore, the Type B arrangement was more effective than that of Type A, as shown in Figure 10. We observed that some of the driftwood that passed through stakes without contact in the Type A arrangement was captured by bridge piers.
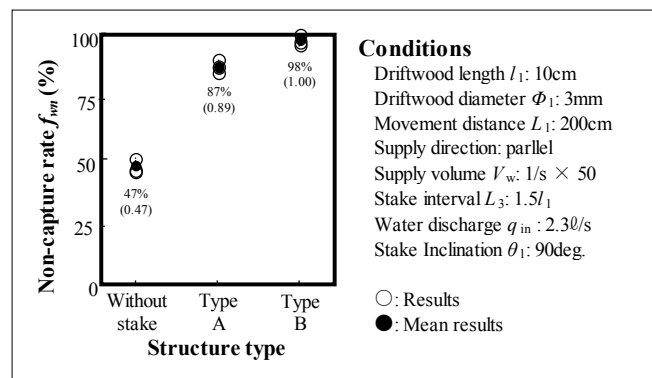

Figure 10. Effect of the arrangement of the stakes, as shown in Figure 3, on f_{wn}.

Figure 11 shows the relationship between L_3, as shown in Figure 2, and f_{wn}. A wide stake interval enabled the driftwood to rotate around the stakes easily, as shown in Figure 11. We concluded that the driftwood cannot rotate around the stakes if the distance between them is not sufficient. Furthermore, when the stakes were separated by more than 1.5 times the length of the driftwood.
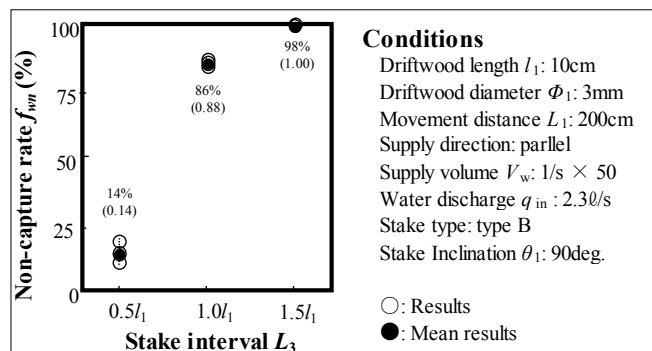

Figure 11. Effect of the distance between the stakes, L_3, as shown in Figure 2, on f_{wn}.

Figure 12 shows the relationship between θ_1, as shown in Figure 4, and f_{wn}. The driftwood rotated most easily around the stakes when they were perpendicular to the riverbed. We observed that the driftwood was not able to rotate easily around the stakes when the stakes pointed upstream or in the direction of the water flow.
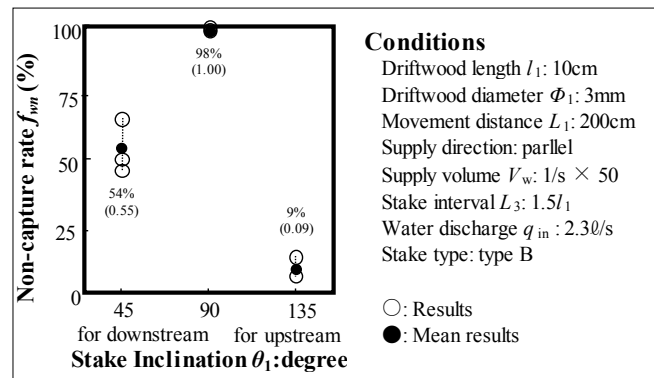

Figure 12. Effect of the inclination of stakes to the riverbed, θ_1 as shown in Figure 4, on f_{wn}.

Consequently, we propose that to control the accumulation of driftwood, stakes should be installed vertically in a houndstooth formation (Type B), with a separation distance (L_3) of 1.5 times the driftwood length, l_1.

3   CONCLUSIONS

To understand the traditional technique of using stakes to prevent driftwood from blocking bridges, we varied the arrangement of the stakes and performed experiments to evaluate their effect on driftwood accumulation. We then proposed an effective stake design based on our experimental results.

The driftwood rotates around the stakes, which enables it to pass through the bridge piers without collision. The effectiveness of the stakes in preventing driftwood accumulation was affected by the water flow speed, the density of the driftwood, the inclination of the stakes to the riverbed and L_3. We proposed a new houndstooth arrangement as an effective counter measure against driftwood blockage.

In the future, field tests and numerical simulations are required to further investigate how stakes can be used to prevent driftwood accumulation.

REFERENCES

Adachi, S. & Daido, A. (1957). Experimental Study on Washed Timbers. *Annuals Disaster Prevention Research Institute*, 1, 41-49.

Fujita, M. (2012). Influence of climate Change on Sediment Disasters. *Journal of the Japan Society of Erosion Control Engineering*, 65(1), 14-20.

Gotoh, H., Sakai, T. & Hayashi, M. (2001). Lagrangian Particle Method for Analysis of Dam-Up Process by Drift Timbers. *Proceedings of Hydraulic Engineering*, 45, 919-924.

Ishikawa, Y., Mizuyama, T. & Fukuzawa, M. (1989). Generation and Flow Mechanisms of Floating Logs Associated with Debris Flow. *Journal of the Japan Society of Erosion Control Engineering*, 42(3), 4-10.

Ishino, K., Hashimaru, D. & Tamai, N. (2006). Research the Fukui Flooding Hazardous in 2004, *JSCE Annual Meeting*, 2, 9-10.

Ishino, K., Watanabe, R. & Anzai, M. (2007). Proposed Counter Measure against the Driftwood on the Bridges. *JSCE Annual Meeting*, 2, 117-118.

Nakagawa, H., Takahashi, T. & Ikeguchi, M. (1992). Numerical Simulation of Drift Wood Behavior. *Disaster Prevention Research Institute Annuals*, 35(B-2), 249-266.

National Research and Development Agency. (2015). *Report on Investigations into Disaster in Izu Oshima Island Caused by Typhoon Wipha in 2013*. Technical note of public works research institute, 4302.

Shibuya, H., Horiguchi, T., Katsuki, S., Ohsumi, H. & Ishikawa, N. (2011). Trap Simulation of Woody Debris by Using Cylindrical Assembled Element with Roots in Distinct Element Method. *Journal of Applied Mechanics, JSCE*, 14, 323-334.

Shimizu, Y. & Osada, K. (2007). Numerical Experiments on Accumulation Process of Driftwoods around Piers by Using a Dem-Flow Coupling Model. *Proceedings of Hydraulic Engineering*, 51, 829-834.

Takebayashi, H. (2014). Research Kyoto and Shiga Flooding Hazardous in 2013. *Journal of Natural Disaster Science*, 33(1), 5-16.

BLOCKING PROBABILITY OF DRIFTWOOD AT OGEE CREST SPILLWAYS WITH PIERS: INFLUENCE OF WOODY DEBRIS CHARACTERISTICS

PALOMA FURLAN[(1)], MICHAEL PFISTER[(2)], JORGE MATOS[(3)] & ANTON J. SCHLEISS[(4)]

[(1,2,4)]Laboratory of Hydraulic Constructions (LCH), École Polytechnique Fédérale de Lausanne, Lausanne, Switzerland
paloma.furlan@epfl.ch; anton.schleiss@epfl.ch
[(1,3)]Instituto Superior Técnico, Universidade de Lisboa, Lisboa, Portugal
jm@civil.ist.utl.pt
[(2)]Haute école d'ingénierie et d'architecture Fribourg (HEIA), HES-SO, Switzerland
michael.pfister@epfl.ch

ABSTRACT

Spillways are designed to evacuate floods in a safe way. They should safely release water in order to avoid dam overtopping with its related damages. Nevertheless, it may be dangerous to assume that a flood is only carrying "clear" water. Large woody debris (LWD) and sediments are often transported by rivers into reservoirs during heavy rainfall events. There is still a lack of knowledge regarding the behaviour of LWD at spillway inlets equipped with piers and gates. The accumulation and blockage of LWD at spillway inlets are a significant problem as they can reduce the discharge capacity of the spillway and consequently, an uncontrolled increase of the water level in the reservoir may occur. Literature provides mainly knowledge on the effect of LWD at bridges in rivers with relatively high flow velocities. However, the latter is hardly applicable for reservoir approach flow conditions. Knowledge of the LWD blockage processes at spillways is important regarding the safety assessment of a dam. The present paper summarizes a series of preliminary laboratory experiments, where the influences of different LWD characteristics are linked to blocking probabilities at an ogee crest spillway equipped with piers. The results highlight the influence of repeatability of events and density of LWD on blocking probabilities under different hydraulic conditions.

Keywords: Large woody debris; blocking probability; ogee crest; spillways; floods.

1 INTRODUCTION

Large floods initiate the transport of sediments and floating material when passing through forested areas. Trees entrained into the stream are called large woody debris (LWD) corresponding typically to stems longer than 1 m and with more than 0.10 m in diameter (Braudrick, Grant, Ishikawa, & Ikeda, 1997). LWD is an important subject for risk evaluation due to its potential to block on bridge pillars, weirs or spillways and avoid them to evacuate properly a flood. When it reduces the discharge capacity, flow velocity also decreases promoting sediment deposition. Thus, an uncontrolled increase of the upstream water level can occur, flooding the upstream area of the structure or overtopping it. In different floods, it has been seen how LWD blocked and affected the functioning of a hydraulic construction such as in Palagnedradam (Switzerland) (Vischer & Trucco, 1985), Sa Teula (Italy) (Galeati, 2009) or Yazagyo dam (Myanmar) (Steijn et al., 2016) causing damages in the structures or increasing the risk connected to those events.

Physical models were used to study interactions between LWD and hydraulic structures. It seems erratic in which position stems reach a construction and so experimental campaigns should have a significant number of test repetitions to infer statistically sound conclusions (Welber, Bertoldi, & Tubino, 2013). Therefore, is of primary importance to conduct enough repetitions of experiments, namely to consider the repeatability as an influential parameter for the consistency of results given the random LWD blocking processes (Schmocker & Hager, 2010). In Braudrick & Grant, (2000, 2001) and Braudrick et al., (1997), it was shown that it is necessary to repeat experiments a certain number of times to have statistical reliable results but no further analysis was presented.

Few articles were found where the effect of the repeatability was considered in the experiments (Table 1). Literature shows a lack of criteria to define reliable numbers of repetitions and it is not considered yet, as a significant variable. Partially, even contradictions were found among the articles.

In the analysis made for LWD in contact with bridges, Bocchiola, Rulli, & Rosso (2008) and De Cicco, Paris, & Solari (2016) mentioned the number of repetitions without further examination of its influence on the results. Schmocker & Hager (2011) presents the analysis and recommendations for reproducibility of experiments in the case of bridge piers, that has been followed by Gschnitzer, Gems, Mazzorana, & Aufleger (2016) in their experimental campaign.

In the case of spillways and check dams, it can be noted in Hartlieb, (2012); Pfister, Capobianco, Tullis, & Schleiss (2013); Shrestha, Nakagawa, Kawaike, Baba, & Zhang (2011) that there is still a lack of unifying

criteria. It was foreseen to have statistical reliable results, improving the accuracy of their experiments but without a clear guideline of how to achieve it.

Table 1. Repeatability of LWD experiments in physical models, literature review.

	Author	Subject of study	Repetitions
1	Bocchiola et al. (2008)	LWD accumulation patterns in dams and bridges	4
2	Schmocker & Hager(2011)	LWD blocking probabilities for bridges	8
3	Shrestha et al.(2011)	LWD blocking probability for slit-check dam	3
4	Hartlieb(2012)	LWD jams at spillways	20
5	Schmocker & Hager (2013)	LWD accumulation at debris rack	3
6	Pfister et al. (2013)	LWD blocking probabilities at PKW	25 to 50
7	De Cicco et al. (2016)	LWD accumulation at bridges piers	10
8	Gschnitzer et al.(2016)	LWD blocking process for bridges	8

LWD can be entrained into a stream for a long period due to decay or a short period due to a flood. Depending on the recruitment and transport process, water content of stems can vary greatly (Gurnell, Piégay, Swanson, & Gregory, 2002). Density of LWD remains as an essential parameter in terms of transport, forces induced to structures and blocking probabilities. For entrainment processes, density of stems is one of the key parameters to define the threshold of movement and transportation, having also a great influence in the drag coefficient and floatability (Braudrick & Grant, 2000; Buxton, 2010; Merten et al., 2010; Crosato, Rajbhandari, Comiti, Cherradi, & Uijttewaal, 2013; Ruiz-Villanueva, Stoffel, Piégay, Gaertner, & Perret, 2014; Lollino et al., 2015; Ruiz-Villanueva, Piégay, Gaertner, Perret, & Stoffel, 2016).

To analyse potential risk due to LWD in hydraulic structures, it is essential to know if the water content (i.e., density) of the stems affects their blocking probabilities or increases its effects as backwater rise and shape of jams against different structures (Schmocker & Hager, 2011; Schmocker et al., 2013; Hartlieb & Obernach, 2014; Piton & Recking, 2016).

Literature gives no explicit numbers of repetitions necessary to have independent results for the case of spillways inlets. The aim of the herein presented study is to consider repeatability as a new parameter and systematically test it to find a compromise between justifiable test effort and accurate probability interpretation.

Further, there is a gap of knowledge in literature regarding density and its effect on blocking probabilities at spillways. It is aimed with this study to quantify the influence of density in blocking probabilities at an ogee crested spillway with piers. This is fundamental to understand how different densities of LWD can represent a different degree of blockage and thus, different blocking probabilities when arriving to an ogee crested spillway.

Both objectives follow a systematic experimental approach with a simplified set-up to understand the influence of replications and density for such tests. It is foreseen to evaluate other parameters related to LWD blockage to have fundamental knowledge of the process before analyzing real cases.

2 PHYSICAL MODEL

2.1 Model set-up

Experiments were conducted at LCH of Ecole Polytechnique Fédérale de Lausanne (EPFL), Switzerland. The flume was 1.50 m wide, 0.70 m high per 10 m long and had a glass side wall to allow visual observation. Water was supplied through a tank upstream of the channel. A tranquillizer wall was placed 2.40 m downstream of the channel inlet to assure a homogenous velocity field (Figure 1).
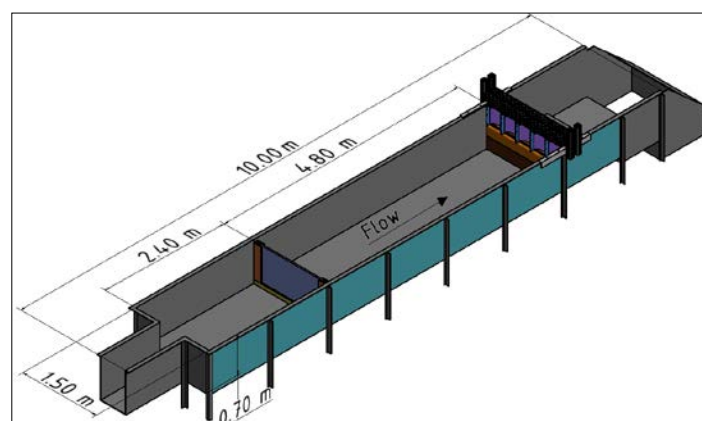

Figure 1. 3D Schematic view of the channel.

The model represented an ogee crested spillway with five bays of width b=0.26 m, created by round-nosed piers, all made with PVC to be considered hydraulically smooth. WES design criteria was followed, considering a design head H_d=0.15 m and a weir height P=0.42 m (Figure 2). The ogee was chosen due to its frequent application and effective discharge capacity. A metallic beam was attached outside the flume to hold the piers above the spillway. The pier nose extruded one time the width of the pier (equal to the diameter of the nose) upstream of the vertical spillway face. In addition, the number of open bays was varied, and partially closed with vertical gates.

The water surface in the channel h [m] was measured using a point gauge (±0.5 mm) in a zone with stagnant water some 2.60 m upstream the ogee. The discharge Q[m^3/s] was measured with a magnetic inductive flow meter (±0.5% at full span). The head H [m] was calculated based on the level measurements and the kinematic head. Photographs were taken systematically with a PeauPro82 3.97mm GoPro H4 Black in order to record each experiment. Visual evaluation of blockage was performed; notes were taken with the results (Block or Pass).

A reservoir approach flow type was analyzed, implying small magnitudes of reservoir flow velocity. Different flow conditions were established by varying the inflow discharge. Ratios of head H[m] to stem diameter d[m] (H/d) ranged from 0.41 to 3.10. These limits were defined based on preliminary experiments.
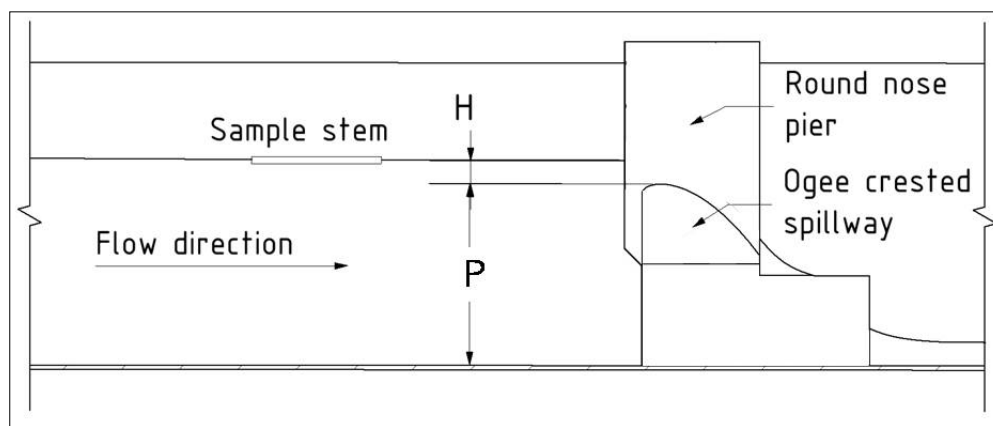

Figure 2. Longitudinal section along the experimental channel with weir.

2.2 Stems

Artificial (PVC) cylindrical stems were chosen to exclude geometrical irregularities of the LWD (Figure 3). Stems were built of plastic pipes with homogeneous weight and volume. Stems were attributed to classes according to their length L [m] and diameter d [m] (Table 2).
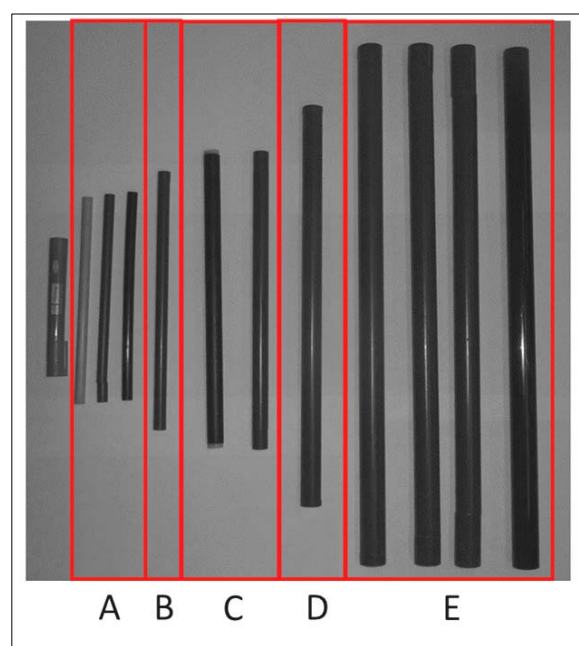

Figure 3. Picture of stems and their classification.

The stem lengths were chosen in relation to the bay width, to cover certain ratios of L/b by keeping $L/d{\approx}20$, as seen in literature. For these particular experiments, classes A, C and E were used.

For each class, different densities were established in relation to databases of average dry wood density along Europe and its standard deviation (Chave et al., 2009). Four typical stem densities ρ_S were tested, being generally $\rho_{S1}{\approx}0.4$ t/m^3; $\rho_{S2}{\approx}0.52$ t/m^3; $\rho_{S3}{\approx}0.63$ t/m^3; $\rho_{S4}{\approx}0.99$ t/m^3. The individual densities relative to water density (ρ) per log type are given in Table 2.

Table 2. Characteristic of stems.

Class	Length L [m]	Diameter d [m]	Length / Bay width L/b [-]	Relative density ρ_S/ρ
A	0.21	0.01	0.80	0.59
				0.79
				0.99
B	0.26	0.012	1.00	0.56
C	0.30	0.016	1.20	0.43
				0.56
				0.97
D	0.40	0.02	1.50	0.63
E	0.52	0.025	2.00	0.40
				0.54
				0.76
				0.99

2.3 Test procedure and parameters

For an experiment, flow depth h and discharge Q were measured without stems as initial condition. A stem was supplied in the centre of the flume parallel to the flow direction, and it was noted if the stem passed or blocked at the spillway inlet. In the latter situation, it was removed and the procedure was repeated. In order to reduce the random component induced by human interaction, stems were supplied with a mechanical device into the stream guaranteeing identical conditions per test. The device was placed at approximately 4.0 m upstream of the ogee to have at least five stem's length between the insertion point and the ogee.

Twenty-eight test combinations were defined. The varied parameters were: Stem class (Table 2); H/d ratio; relative density ρ_S/ρ and amount of open bays (Table 3).

Table 3. Parameters variation.

Class	Ratio H/d	Relative density ρ_S/ρ	Open bays
A	1.00; 1.20; 1.40	0.59; 0.79; 0.99	1; 5
C	0.94; 1.00; 1.06	0.43; 0.56; 0.97	1; 5
E	0.76; 0.96; 1.00	0.40; 0.54; 0.76; 0.99	1; 5

3 EFFECT OF REPEATABILITY

Blocking probabilities $\pi(i)$ were calculated as the number of stems blocked at the inlet of the spillway divided by the number of stems supplied in total. The blocking probability is defined in **Eq. [1]**, where $\pi(i)=$ blocking probability, $R(i)=$ result obtained for each individual stem (pass $R=0$; block $R=1$), $i=$ individual stem and n is the total number of stems supplied.

$$\Pi(i) = \frac{\sum_{i=1}^{n} R(i)}{i} \quad\quad [1]$$

A plot of the results obtained in a particular experiment with class E, density ρ_{s1} and five bays open is shown in Figure 4. It can be noted that the first stem blocked ($R_1=1$ so that $\pi(1)=1$), the second did not ($R_2=0$ so that $\pi(2)=0.5$) and the third one blocked ($R_3=1$ so that $\pi(3)=0.67$). The repetition $i=5$ considers the amount of stems blocked until 5 repetitions (3 stems), divided by the number of stems provided (5 stems) giving $\pi(5)=0.60$. This plot emphasizes the variability of π according to the number of repetitions i. For example, repeating 5 times ($\pi(5)=0.60$) and repeating 30 times ($\pi(30)=0.43$) implies a $\Delta\pi$ of almost 0.20 for this particular case.
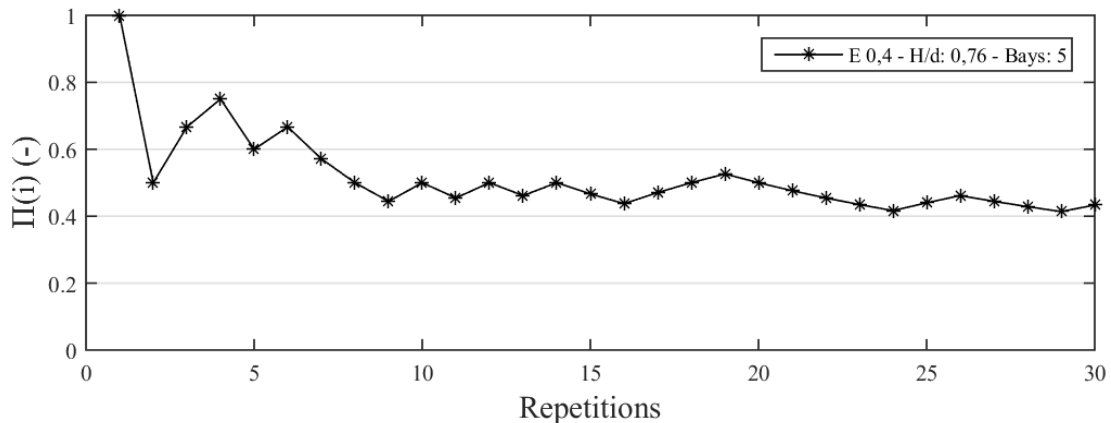
Figure 4. Example of blocking probabilities a function of repetitions. Class E, ρ_1, H/d = 0.76 and five bays.

Figure 5 displays results obtained in an experiment with class E, density ρ_{s1} and one bay open. In this case, the first stem passed, the second did not and the third one either. Repetition i=5 considers 2 stems blocked divided by 5 stems provided, giving $\pi(5)$=0.40 blocking probability. In this situation, repeating 5 times ($\pi(5)$=0.40) and repeating 30 times ($\pi(30)$=0.06) implies a $\Delta\pi$ of more than 0.30.
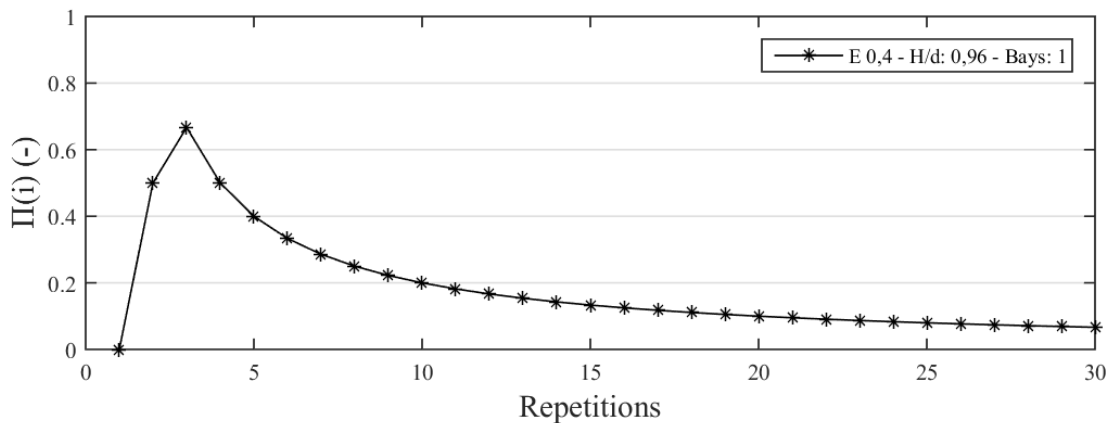

Figure 5. Example of blocking probabilities a function of repetitions. Class E, ρ_1, H/d = 0.96 and one bay.

Analyzing how π developed along the increment of repetitions i, it could be inferred that the repeatability has a strong influence in the variability (or error) of its estimation.

To compare the effect of repeatability on the blocking probabilities along experiments, a relative blocking probability was expressed as indicated in Eq.[2] where $\pi(i)$ is the blocking probability for the current repetition and $\pi(n)$ the blocking probability taking into account the last stem supplied.

$$\frac{\left|\Pi(i) - \Pi(n)\right|}{\Pi(n)} \qquad [2]$$

Plotting the normalized results obtained for the 28 tested parameter combinations (Table 3), it can be seen how much the blocking probability varies for less than i=10 repetitions, regardless of the experiment performed (Figure 6). The standard deviation was calculated per repetition for all the experiments, shown as a black dotted line in the plot. It can be seen how it tends to zero with an increasing number of repetitions.
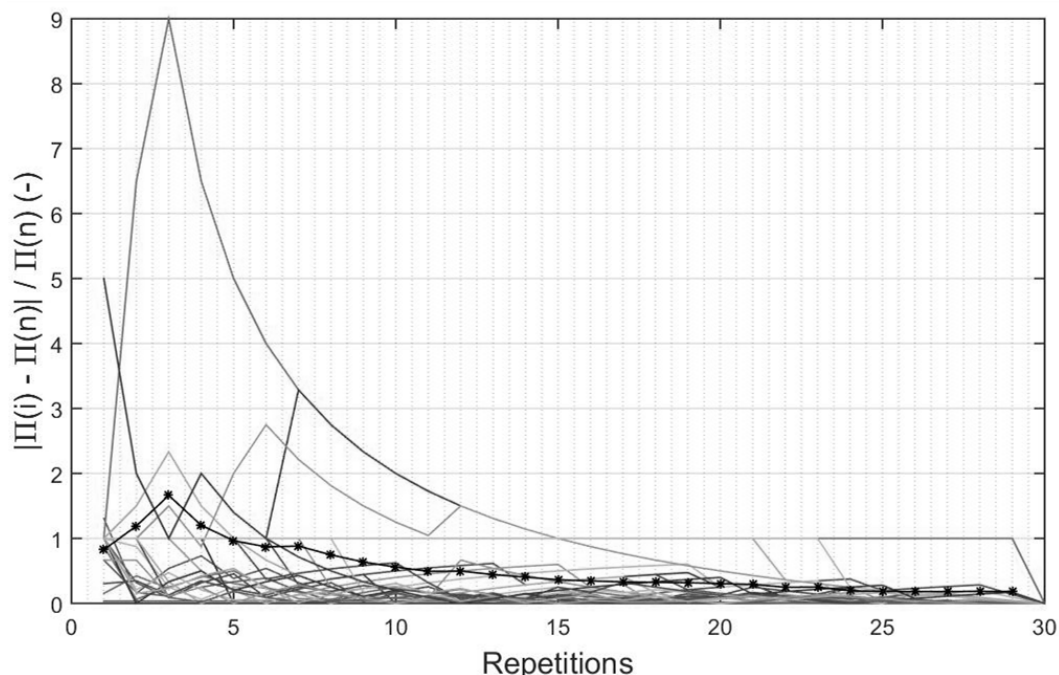
Figure 6. Normalized blocking probabilities as a function of repetitions of all experiments. The black dotted line corresponds to the standard deviation.

4 EFFECT OF DENSITY

Based on the experiments performed, it was also possible to analyze the influence of density on the blocking probabilities of LWD at the ogee crested spillways with piers. Here, the class E is considered as an example. Three different hydraulic combinations were evaluated for that class using four densities (Table 3).

Figure 7 shows the results obtained for class E with a relation of H/d=0.76 and all bays open. Densities were represented with different scales of grey in the plot. It can be seen that higher densities (e.g., ρ_4 in black), for the same hydraulic conditions, imply increments in the final value of π (after 30 repetitions). Between ρ_1 (light) and ρ_4 (heavy), the relative difference in blocking probabilities is $\Delta\pi$=0.57.
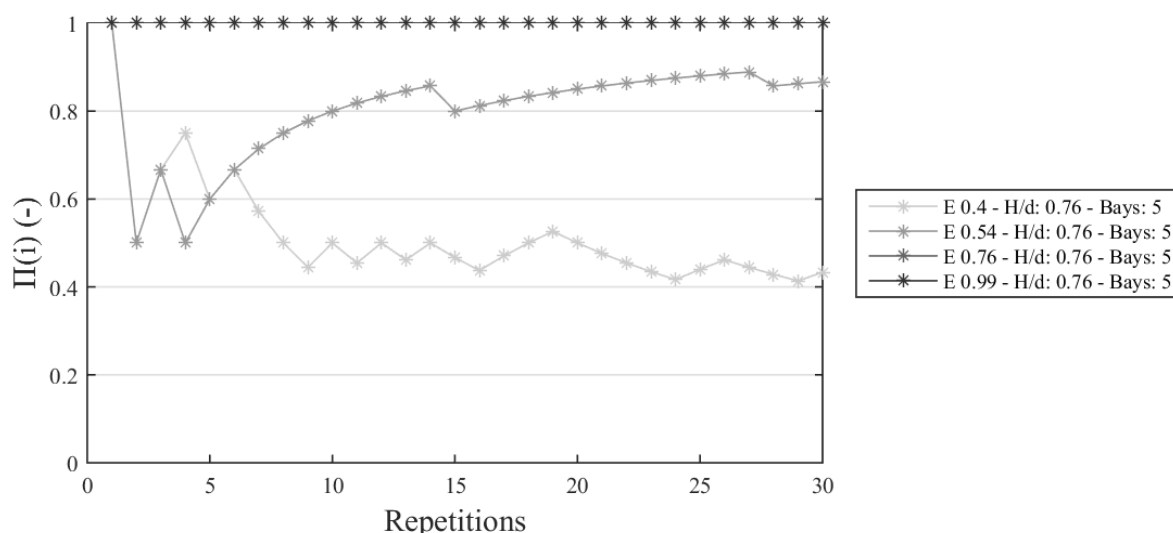

Figure 7. Example of blocking probabilities as a function of repetitions. Class E, H/d=0.76 and five bays open, for changing densities.

If increasing the head ratio to H/d=1.00 (Figure 8), density has the same effect on π as for the lower ratio. The heavier stems with ρ_{s4} blocked ($\pi(30)$=0.96), regardless of the hydraulic condition. A difference was noted for less dense stems where $\pi(30)$ decreased from 0.43 to 0 (for ρ_{s1}) in comparison to Figure 7. In the case of ρ_2 and ρ_3, $\pi(30)$ changed from 0.86 to 0.03 and from 1.0 to 0.20, respectively, showing a strong influence of H/d on π.
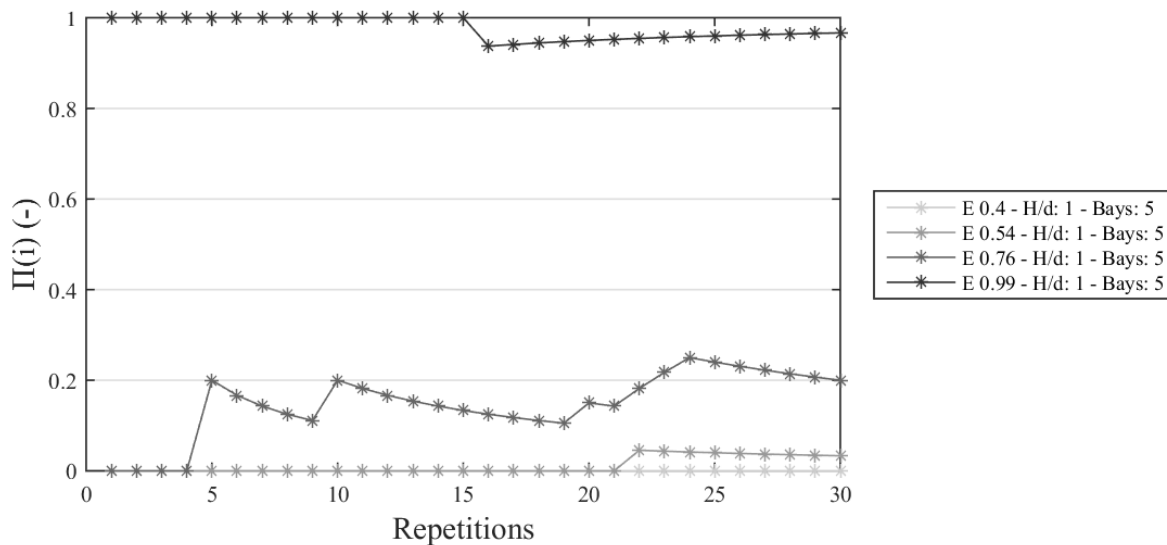
Figure 8. Example of blocking probabilities as a function of repetitions. Class *E, H/d*=1.00 and five bays open, for changing densities.

Finally, the number of open bays was changed for *H/d*=0.96 (Figure 9). It can be seen that $\pi(30)$ for ρ_{s4} was not influenced by the hydraulic conditions or the change of gate configuration, giving always $\pi(30)$ near 1. The number of bays open was tested to analyze if different configurations of open gates would also cause an effect on π. For this class, only density and *H/d* gave clear indications of having an influence on $\pi(30)$.
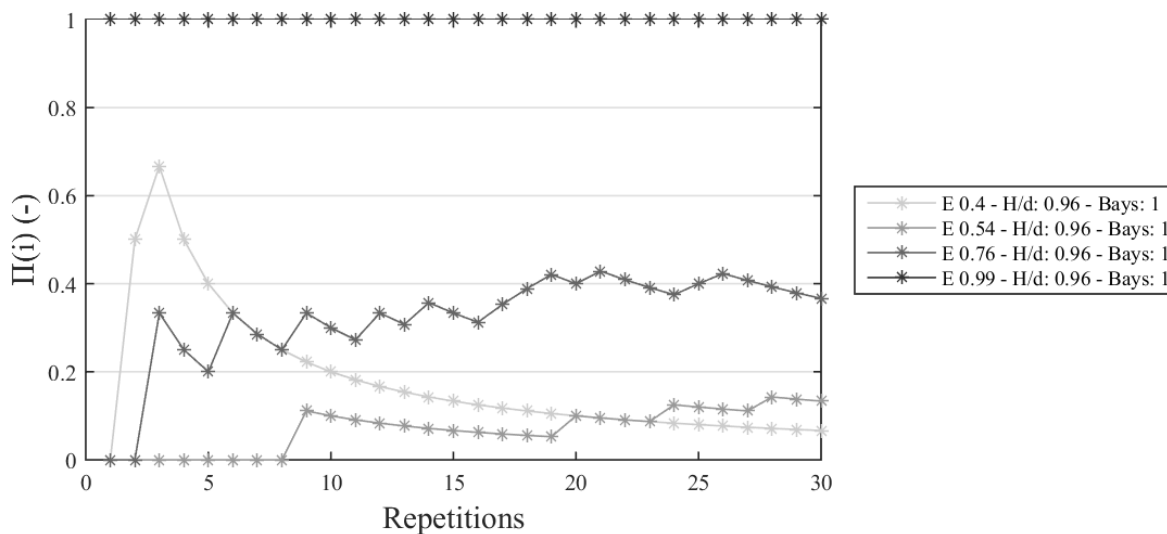

Figure 9. Example of blocking probabilities as a function of repetitions. Class *E, H/d* = 0.96 and one bay open, for changing densities.

5   CONCLUSIONS

The effect of repeatability and density as important parameters to estimate the blocking probabilities of LWD at ogee crested spillways with round nose piers is physically tested. Experiments have shown that the number of repetitions has a strong influence in the final estimation of the blocking probability π. According to the results obtained, some 15 to 25 repetitions should be considered as minimum number for such experiments as it will provide enough data to apply different statistical analysis and will decrease the standard deviation of results. This number of repetitions (for example 24) represents a standard deviation of the relative blocking probability smaller than 0.01 and this is considered acceptable taking into consideration the random nature of LWD processes. Accordingly, the precision aimed with each research will determine the level of incertitude accepted of the results and implicitly the number of repetitions.

For the class evaluated, it is demonstrated that the stem (or trunk) density is an important parameter related to the estimation of the blocking probability π. The blocking probability of individual stems travelling to an ogee crested spillway with round nose piers depends on the density of the stems. Heavier stems tend to block more frequently than lighter stems.

ACKNOWLEDGEMENTS

REFERENCES

Bocchiola, D., Rulli, M.C. & Rosso, R. (2008). A Flume Experiment on the Formation of Wood Jams in Rivers. *Water Resources Research*, 44(2), 1–17.

Braudrick, C.A. & Grant, G.E. (2000). When Do Logs Move in Rivers? *Water Resources Research*, 36(2), 571–583.

Braudrick, C.A. & Grant, G.E. (2001). Transport and Deposition of Large Woody Debris in Streams: A Flume Experiment. *Geomorphology*, 41, 263–283.

Braudrick, C.A., Grant, G.E., Ishikawa, Y. & Ikeda, H. (1997). Dynamics of Wood Transport in Streams: A Flume Experiment. *Earth Surface Processes and Landforms*, 22(7).

Buxton, T.H. (2010). Modeling Entrainment of Waterlogged Large Wood in Stream Channels. *Water Resources Research*, 46(July), 1–15.

Chave, J., Coomes, D.A., Jansen, S., Lewis, S. L., Swenson, N.G. & Zanne, A.E. (2009). Towards A Worldwide Wood Economics Spectrum. *Ecology Letters*, 12(4), 351–366.

Crosato, A., Rajbhandari, N., Comiti, F., Cherradi, X. & Uijttewaal, W. (2013). Flume Experiments on Entrainment of Large Wood in Low-Land Rivers. *Journal of Hydraulic Research*, 51(5), 581–588.

De Cicco, P.N., Paris, E. & Solari, L. (2016). *Wood Accumulation at Bridges : Laboratory Experiments on the Effect of Pier Shape.* In River Flow, Taylor and Francis Group, London, 2341–2345.

Galeati, G.A. (2009). Hydraulic Safety of ENEL Dams. In *Colloque CFBR/SHF Dimensionnement et fonctionnement des évacuateurs de crues, Lyon.*

Gschnitzer, T., Gems, B., Mazzorana, B. & Aufleger, M. (2017). Towards a Robust Assessment of Bridge Clogging Processes in Flood Risk Management. *Geomorphology*, 279, 128–140.

Gurnell, A.M., Piégay, H., Swanson, F.J. & Gregory, S.V. (2002). Large Wood and Fuvial Processes. *Freshwater Biology*, 47(4), 601–619.

Hartlieb, A. (2012). Large Scale Hydraulic Model Tests for Floating Debris Jams at Spillways. In Water Infinitely Deformable but still Limited. *2nd IAHR Europe Congress, 27-29 June, München.* Topic Damage and Risk, (C18),1–6.

Hartlieb, A. & Obernach, A.D.V. (2014). Maßgebende Parameter für den Aufstau durch Schwemmholzverklausungen. In *Tagungsband Internationales Symposium. Wasser- und Flussbau im Alpenraum. Versuchsanstalt für Wasserbau, Hydrologie und Glaziologie, ETH Zürich,* 228, 485–493.

Lollino, G., Grant, G.E., Ruiz-Villanueva, V., Piégay, H., Stoffel, M., Gaertner, V. & Perret, F. (2015). *Engineering Geology for Society and Territory - Volume 3*, Engineering Geology for Society and Territory - Volume 3: River Basins, Reservoir Sedimentation and Water Resources (Vol. 3). Cham: Springer International Publishing, 618.

Merten, E., Finlay, J., Johnson, L., Newman, R., Stefan, H. & Vondracek, B. (2010). Factors Influencing Wood Mobilization in Streams. *Water Resources Research*, 46(10), 1-13.

Pfister, M., Capobianco, D., Tullis, B. & Schleiss, A.J. (2013). Debris-Blocking Sensitivity of Piano Key Weirs under Reservoir-Type Approach Flow. *Journal of Hydraulic Engineering*, 139(11), 1134–1141.

Piton, G. & Recking, A. (2016). Design of Sediment Traps with Open Check Dams. II: Woody Debris. *Journal of Hydraulic Engineering*, 142(2), 1-13.

Ruiz-Villanueva, V., Piégay, H., Gaertner, V., Perret, F. & Stoffel, M. (2016). Wood Density and Moisture Sorption and its Influence on Large Wood Mobility in Rivers. *Catena*, 140(2016), 182–194.

Ruiz-Villanueva, V., Stoffel, M., Piégay, H., Gaertner, V., & Perret, F. (2014). *Wood Density Assessment to Improve Understanding of Large Wood Buoyancy in Rivers.* River Flow 2014, 2503–2508.

Schmocker, L. & Hager, W.H. (2010). *Drift Accumulation at River Bridges.* River flow, 713–720.

Schmocker, L. & Hager, W.H. (2011). Probability of Drift Blockage at Bridge Decks. *Journal of Hydraulic Engineering*, 137(4), 470–479.

Schmocker, L., Hager, W.H. & ASCE, F. (2013). Scale Modeling of Wooden Debris Accumulation at a Debris Rack. *Journal of Hydraulic Engineering*, 139(8), 827–836.

Shrestha, B.B., Nakagawa, H., Kawaike, K., Baba, Y. & Zhang, H. (2011). Driftwood Deposition from Debris flows at Slit-Check Dams and Fans. *Natural Hazards*, 61(2), 577–602.

Steijn, R.C., Barneveld, H., Wijma, E., Beckers, J., Reuzenaar, T., Koopmans, R. & Htet, K.L. (2016). *Dutch Risk Rreduction Team Mission Report - Myanmar.*

Vischer, D.L. & Trucco, G. (1985). The Remodelling of the Spillway of Palagnedra. *Proceedings of the 15th International Congress on Large Dams, ICOLD, Lausanne*, Q59, R8.

Welber, M., Bertoldi, W. & Tubino, M. (2013). Wood Dispersal in Braided Streams: Results from Physical Modeling. *Water Resources Research*, 49(11), 7388–7400.

NUMERICAL SIMULATION FOR VARIATION OF FLOODWATER STAGE DUE TO BUILDINGS ON FLOOD PLAIN

FONG-ZUO LEE[1], JIHN-SUNG LAI[2], TSUNG-HSIEN HUANG[3], CHENG-CHIA HUANG[4], ZHI-XIAN YANG[5] & YONG-JUN LIN[6]

[1,2,3,4,5] Hydrotech Research Institute, National Taiwan University, Taipei, Taiwan,
windleft@gmail.com; jslai525@ntu.edu.tw; htcs33@gmail.com; yen.zhyang@gmail.com
[2] Taiwan Typhoon and Flood Research Institute (TTFRI), National Applied Research Laboratories, Taipei, Taiwan,
[4] Department of Bioenvironmental Systems Engineering, National Taiwan University, Taipei, Taiwan,
chengchiahuang@gmail.com
[6] Center for Weather Climate and Disaster Research, National Taiwan University, Taipei, Taiwan,
vovman@gmail.com

ABSTRACT

It is usual to develop the flood plains along the riverside as a park or housing areas, especially in the highly urbanized areas. Due to limited land in the urban area, flood plains are subjected to be utilized as locations for recreation, exercise or parking space. Lack of flood plain management, flooding may happen frequently. When heavy rainfall occurs, overbank flow used to inundate the flood plains and increases the water stage due to increment of river bed roughness. In this study, the 2D numerical model, SRH-2D, is adapted to investigate the capability of channel conveyance due to the effect of buildings on the flood plains. The buildings and constructions decrease the cross-sectional area of flow on flood plains. The SRH-2D model is a hydraulic, sediment, temperature and vegetation model for river systems under development at the Bureau of Reclamation. It adopts robust and stable numerical schemes with seamless wetting-drying algorithm. The resultant outcome needs that few tuning parameters to arrive at the final solution. Based on various return period flood hydrographs, the SRH-2D is applicable to study the capability for channel conveyance and variation of the floodwater stage due to building effects.

Keywords: Flood plain; numerical simulation; channel conveyance; buildings and constructions; water stage.

1   INTRODUCTION

In recent ten years, climate change already affects the rainfall intensity and frequency in Taiwan significantly, especially in metropolitan Taipei area. Taiwan suffered from the Chi-Chi earthquake with a magnitude reaches 7.3 Richter magnitude scale in 1999. Earthquake-triggered landslides in mountainous areas also could supply a large amount of sediment to river basin. Sediment produced in the upper watershed may not immediately deliver to the lower basin owing to river aggradations. However, there is still a great amount of sediment can be transported and deposited in downstream river, particularly during extreme rainfall events. Therefore, when typhoon or heavy rain fall occurs in Taiwan, the watershed may generate huge amount of sediment yield. And, the land development in the watershed would accelerate soil erosion. Such sediment flow into downstream river reach will induce river bed aggradation and impact water stage rising. In addition, the amount of sediment flow with current will result in water treatment problem during typhoon or heavy rainfall event. In 2012, Typhoon Soala attacked northern Taiwan and flooded high land area in Quchi and Guangxing area of Xindian River basin. In 2015, Typhoon Soudelor also attacked northern Taiwan and induced high-turbid row water that water treatment cannot deal with in Xindian River basin (Taipei Feitsui Reservoir Administration, 2015). Therefore, the Xindian River basin from Quchi area to the Jhihtan Dam is adapted as study area for variation investigation of floodwater stage due to buildings on flood plain.

Based on the literature review, one-dimensional (1D) flow models have been routinely used in practical hydraulic applications, for example, Lee and Hsieh (2003), Brunner (2006), DHI (2002), CCHE1D (Wu and Vieira 2002) and Huang and Greimann (2007). These 1D models will remain useful, particularly for applications with long reaches (e.g., Tamsui River is more than 60 Km) or over a long time period (e.g., over 10 years). Their limitations, however, are well known and there are situations where multi-dimensional modeling is needed. For example, modeling with 3D Navier-Stokes equations is necessary if flow in the neighborhood of hydraulic structures is of interest. For most river flows, however, water depth is shallow relative to width and vertical acceleration is negligible in comparison with gravitational acceleration. So, the two-dimensional (2D) depth-averaged model provides the next level of modeling accuracy for many practical open channel flows. Actually, with increasing computational resources, 2D models may soon be routinely used for river projects. A range of 2D models have been developed and applied to a wide range of problems since the work of Chow and Ben-Zvi (1973). Examples include Harrington et al. (1978), McGuirk and Rodi (1978), Vreugdenhil and Wijbenga (1982), Jin and Steffler (1993), Ye and McCorquodale (1997), Ghamry and

Steffler (2005), Zarrati et al. (2005), Begnudelli and Sanders (2006), Lai (2010) and Guo et al. (2011), among many others. Examples of commercial or public-domain 2D codes include DHI (1996), USACE (1996), CCHE2D (Jia and Wang 2001), TELEMAC (Hervouet and van Haren 1996), etc. In the following, the numerical formulation applicable to arbitrarily shaped cells is presented first for the 2D depth-averaged equations. The method is implemented into a numerical model, SRH-2D and it is applied to a number of open channel flows for the purpose of testing and verification. Further validation and demonstration of the model are achieved by applying the model to a practical natural river flow. An extensive list of applications has been carried out with the proposed numerical model and they are found in Lai (2008) and the associated website. The model is also downloadable from the website. In addition, SRH-2D model is widely used in Taiwan river basin, especially in Tamsui River and Choshui River. Therefore, SRH-2D model is selected to investigate the variation of floodwater stage due to buildings on flood plain.

The purpose of this study is to investigate the flood control of reservoir and analysis the impact of buildings on flood plain when high land is flooded. After basic data collection, collation and analysis, the inundated area between the Quchi area and the Jhihtan dam was surveyed, and two-dimensional (SRH-2D) numerical model is applied for research purpose. Based on various return period flood hydrographs, the SRH-2D is applicable to study the capability for channel conveyance and variation of the floodwater stage due to building effects within Xindian River basin.

2   STUDY AREA

In 2012, Typhoon Soala attacked northern Taiwan and flooded high land area in Quchi and Guangxing area of Xindian River basin. Typhoon Soudelor also attacked northern Taiwan and induced high-turbid row water that water treatment cannot deal with in Xindian River basin in 2015. Therefore, the Xindian River basin from the Quchi area to the Jhihtan dam is adapted as the study area for variation investigation of floodwater stage due to buildings on flood plain, as shown in Figure 1. Quchi and Guangxing areas are located at impounded area of the Jhihtan dam. The study area of river reach is about 2,200m in length and 260m in width. The river topography is aggraded at the dam upstream and is degraded at the downstream of dam in past years. In recent decade, the sediment deposition height is about 1 m within impounded area of the Jhihtan dam. However, the river bed does not change significantly from 2011 to 2014 within study area. Therefore, the fix-bed condition and without sediment transport simulation are both adapted to investigate the variation of floodwater stage due to buildings on flood plain. The average bed slope of study area is about 0.0017. In Figure 1, the function of Quchi weir provides the flow discharge for electric power. There are two flow supplies in the study area, one is from Feitsui reservoir and another is from Nanshi River. Therefore, the inflow discharge of the Jhihtan dam is dominated by the flow control operation of Feitsui reservoir. The flood control operation of Feitsui reservoir should prevent releasing peak discharge accompany with Nanshi River. The study river reach is managed by Taipei Water Management Office, Water Resources Agency, and Ministry of Economic Affairs.
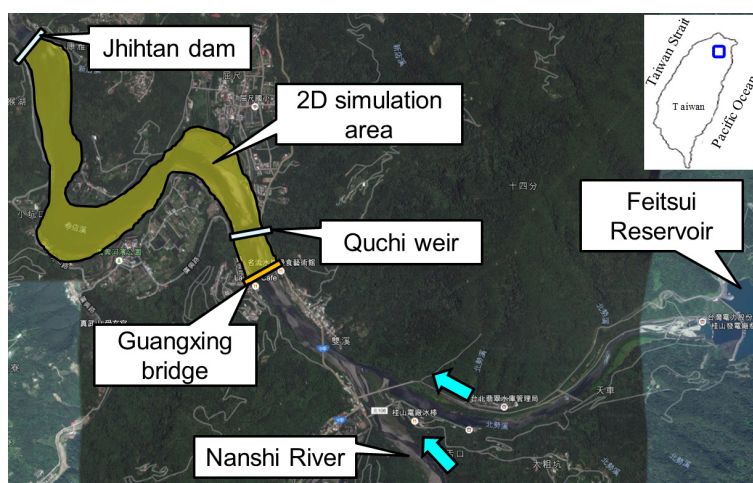

Figure 1. Study area.

3   NUMERICAL MODEL

SRH-2D is a two-dimensional (2D) model and it is particularly useful for problems where 2D effects are important. Examples include flows with in-stream structures, such as weirs, diversion dams, release gates, coffer dams, etc., bends and point bars, perched rivers, and multi-channel systems. 2D models may also be needed if some hydraulic characteristics are important, such as flow recirculation and eddy patterns, lateral variations, flow overtopping banks and levees, differential flow shears on river banks, and interaction between the main channel, vegetated areas and floodplains. Based on the topography survey data in 2011, the

simulation mesh and initial bed elevation is established. The relevant model equations are described as follows (Water Resources Planning Institute, 2009; Lai, Y.G., 2010):

$$\frac{\partial h}{\partial t} + \frac{\partial hU}{\partial x} + \frac{\partial hV}{\partial y} = 0 \tag{1}$$

$$\frac{\partial hU}{\partial t} + \frac{\partial hUU}{\partial x} + \frac{\partial hVU}{\partial y} = \frac{\partial hT_{xx}}{\partial x} + \frac{\partial hT_{xy}}{\partial y} - gh\frac{\partial z}{\partial x} - \frac{\tau_{bx}}{\rho} \tag{2}$$

$$\frac{\partial hV}{\partial t} + \frac{\partial hUV}{\partial x} + \frac{\partial hVV}{\partial y} = \frac{\partial hT_{xy}}{\partial x} + \frac{\partial hT_{yy}}{\partial y} - gh\frac{\partial z}{\partial y} - \frac{\tau_{by}}{\rho} \tag{3}$$

In the above, x and y are horizontal Cartesian coordinates, t is time, h is still water depth, U and V are depth-averaged velocity components in x and y directions, respectively, g is gravitational acceleration, T_{xx}, T_{xy}, and T_{yy} are depth-averaged stresses due to turbulence as well as dispersion, $z = z_b + h$ is water surface elevation, is bed elevation, z_b is water density, and τ_{bx}, τ_{by} are bed shear stresses. The bed stresses are obtained using the Manning's resistance equation as:

$$\left(\tau_{bx}, \tau_{by}\right) = \rho U_*^2 \frac{(U,V)}{\sqrt{U^2+V^2}} = \rho C_f \sqrt{U^2+V^2}\,(U,V) \tag{4}$$

where $C_f = \frac{gn^2}{h^{1/3}}$, n is Manning's roughness coefficient, and U_* is bed frictional velocity. Effective stresses are calculated by the Boussinesq's formulation as:

$$T_{xx} = 2(v+v_t)\frac{\partial U}{\partial x} - \frac{2}{3}k \tag{5}$$

$$T_{xy} = 2(v+v_t)\left(\frac{\partial U}{\partial y} + \frac{\partial V}{\partial x}\right) \tag{6}$$

$$T_{yy} = 2(v+v_t)\frac{\partial V}{\partial y} - \frac{2}{3}k \tag{7}$$

where v is kinematic viscosity of water, v_t is eddy viscosity, and k is turbulent kinetic energy.

The eddy viscosity is calculated with a turbulence model. Two models are used in SRH-2D (Rodi et al., 1993): the depth-averaged parabolic model and the two-equation k-ε model. For the parabolic model, the eddy viscosity is calculated as $v_t = C_t U_* h$ and the frictional velocity, U_* is defined in [4]. The model constant, C_t may range from 0.3 to 1.0 and a default value of C_t =0.7 is used by SRH-2D. For the two-equation k-ε model, the eddy viscosity is calculated as $v_t = C_\mu k^2 / \varepsilon$ with the two additional equations as follows:

$$\frac{\partial hk}{\partial t} + \frac{\partial hUk}{\partial x} + \frac{\partial hVk}{\partial y} = \frac{\partial}{\partial x}\left(\frac{hv_t}{\sigma_k}\frac{\partial k}{\partial x}\right) + \frac{\partial}{\partial y}\left(\frac{hv_t}{\sigma_k}\frac{\partial k}{\partial y}\right) + P_h + P_{kb} - h\varepsilon \tag{8}$$

$$\frac{\partial h\varepsilon}{\partial t} + \frac{\partial hU\varepsilon}{\partial x} + \frac{\partial hV\varepsilon}{\partial y} = \frac{\partial}{\partial x}\left(\frac{h\upsilon_t}{\sigma_\varepsilon}\frac{\partial \varepsilon}{\partial x}\right) + \frac{\partial}{\partial y}\left(\frac{h\upsilon_t}{\sigma_\varepsilon}\frac{\partial \varepsilon}{\partial y}\right) +$$

$$C_{\varepsilon 1}\frac{\varepsilon}{k}P_h + P_{\varepsilon b} - C_{\varepsilon 2}h\frac{\varepsilon^2}{k} \qquad [9]$$

The expressions of some terms, along with the model coefficients, follow the recommendation of Rodi et al. (1993) and they are listed as below:

$$P_h = h\upsilon_t\left[2\left(\frac{\partial U}{\partial x}\right)^2 + 2\left(\frac{\partial V}{\partial y}\right)^2 + \left(\frac{\partial U}{\partial y} + \frac{\partial V}{\partial x}\right)^2\right] \qquad [10]$$

$$P_{kb} = C_f^{-1/2}U_*^3 \quad , P_{\varepsilon b} = C_{\varepsilon\Gamma}C_{\varepsilon 2}C_\mu^{1/2}C_f^{-3/4}U_*^4\big/h \qquad [11]$$

$$C_\mu = 0.09, C_{\varepsilon 1} = 1.44, C_{\varepsilon 2} = 1.92, \sigma_k = 1, \sigma_\varepsilon = 1.3, C_{\varepsilon\Gamma} = 1.8 \sim 3.6 \qquad [12]$$

The terms are added to account for the generation of turbulence energy and dissipation due to bed friction in case of uniform flows.

4   RESULTS AND DISCUSSIONS

Due to buildings on flood plan had been inundated during Typhoon Saola in 2012, the Quchi and Guangxing areas are selected as the study region, as shown in Figure 1. The Figure 1 shows the flood comes from the Nanshi River and Fuitsui reservoir. The main buildings on flood plan are gathering around Quchi area, which located at the right side of the Xindian River. A two-dimensional (2D) model, SRH-2D is adapted to investigate the variation of floodwater stage due to buildings on flood plain. Based on the field survey of cross-sectional surveying, the initial topography of river bed, which includes buildings on flood plan, is established. According to the field survey of inundation area and water depth of Typhoon Saola in 2012, the observed water stage at Quchi hydrological station and inundated depth are compared to the simulation results of model calibration. Figure 2 and Figure 3 show the comparison results between the observed and simulated data. The observed hydrograph of water stage at Quchi hydrological station shows 48-hour variation and water stage has changed about 1.5m during this event. The simulated hydrograph of water stage agrees with the observed data via time. The water stages during flood and after flood are different, as shown in Figure 3. As compared to the water depth around buildings on flood plan area, the simulated water depth is closed to the measured result, where the water depth is about 2.45m. It seems that the adapted two-dimensional (2D) model, SRH-2D is applicable to discuss the variation of floodwater stage due to buildings on flood plain.

Based on the hydrological analysis, the protection plan around Quchi and Guangxing area is 100-year return period. Therefore, 50-year and 100-year return periods flood are considered to investigate the water stage and flow field within study area. 8200m³/s and 9100m³/s represent the flood discharge of 50-year and 100-year return periods, respectively. Figure 4 and Figure 5 show the water depth and flow field of 50-year and 100-year return periods, respectively. The simulated results of flow field show that the main flow was at left side around the Quchi area and at right side around the Guangxing area. It means that the main flow follows the main channel location and flood plan has low flow velocity. However, the water stage rise to the flood plan and buildings on flood plan inundated by water. Based on the 200-year return period flood event, Figure 6 is an example to discuss the impacts of buildings on flood plan. The topography without buildings on flood plan is treated by artificial modification for model simulation. Figure 6a shows the water depth with buildings on flood plan and Figure 6b shows the water depth without buildings on flood plan. The water depth is slightly changed after moving the buildings out of flood plan. The decreasing value of water depth is about 0.7m under 200-year return period flood event. Table 1 shows the simulated floodwater stage on various return period flood event. The impacts of water stage owing to buildings on flood plan are increasing with flood discharge. The difference of water stages range from 0.2m to 0.7m against the return period flood event.

Table 1. Simulated floodwater stage due to buildings on flood plain.

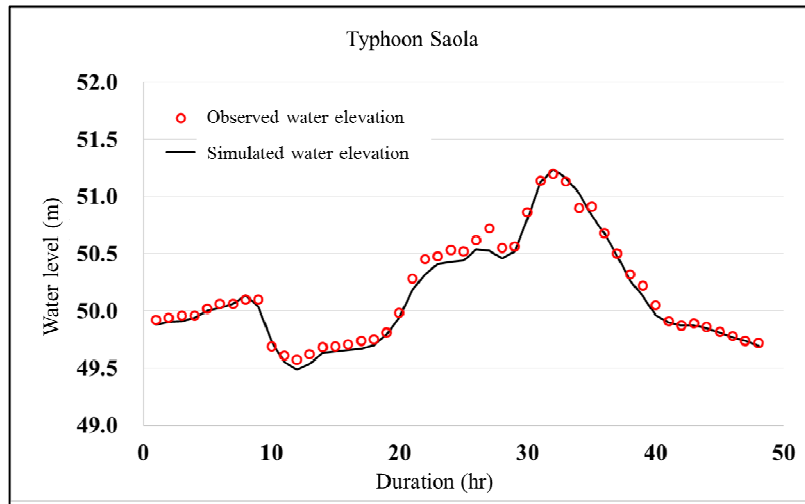| Return period(year)	2	5	10	20	50	100	200
With buildings	2.6	4.8	6.6	8.3	9.6	9.8	10.3
Without buildings	2.4	4.7	6.0	7.8	8.8	9.4	9.6

** Unit : m

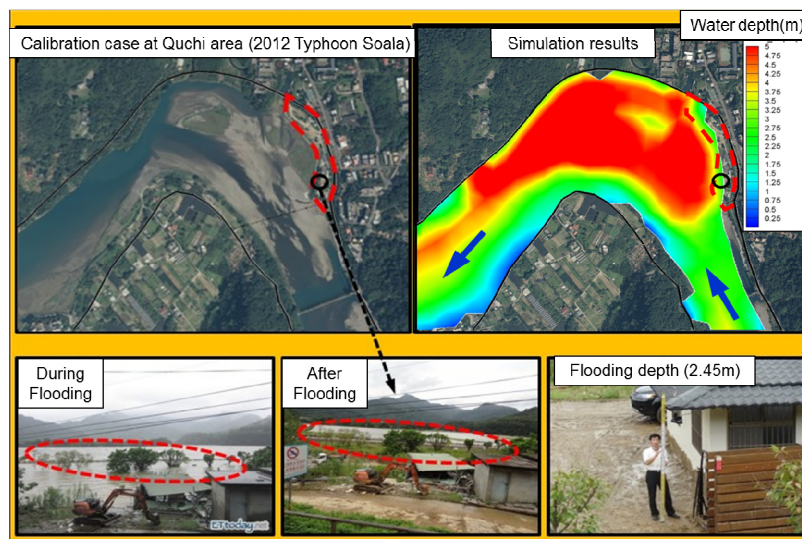**Figure 2**. Model calibration of water stage at Quchi hydrological station.

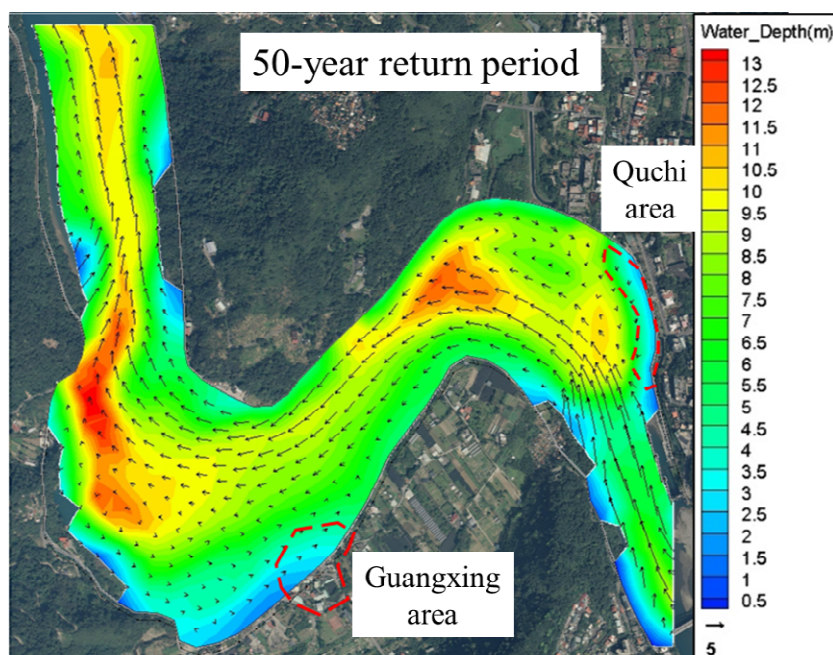**Figure 3**. Model calibration of water stage at flood plain.

Figure 4. Simulated results of flow field and water depth of 50-year return period flood event.
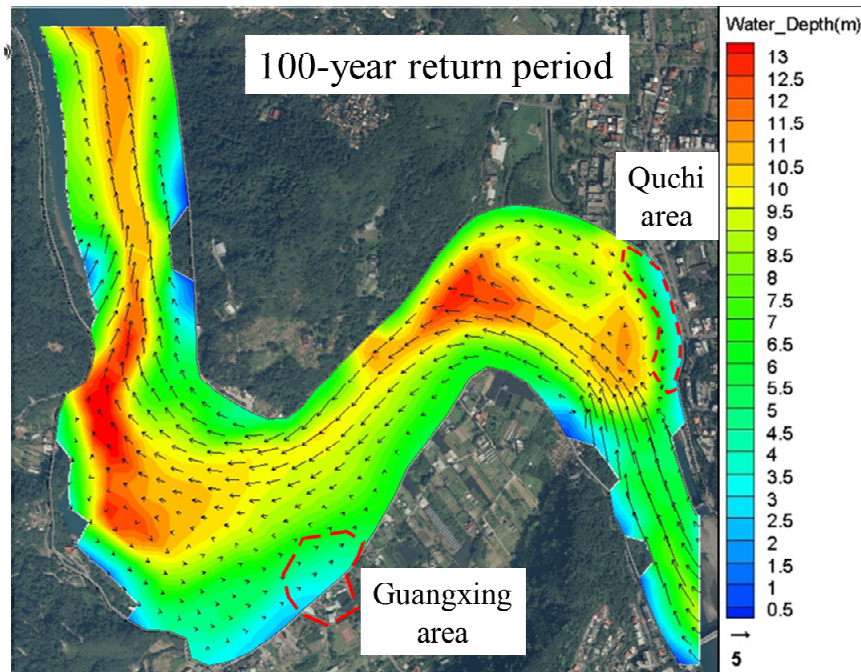
Figure 5. Simulated results of flow field and water depth of 100-year return period flood event.
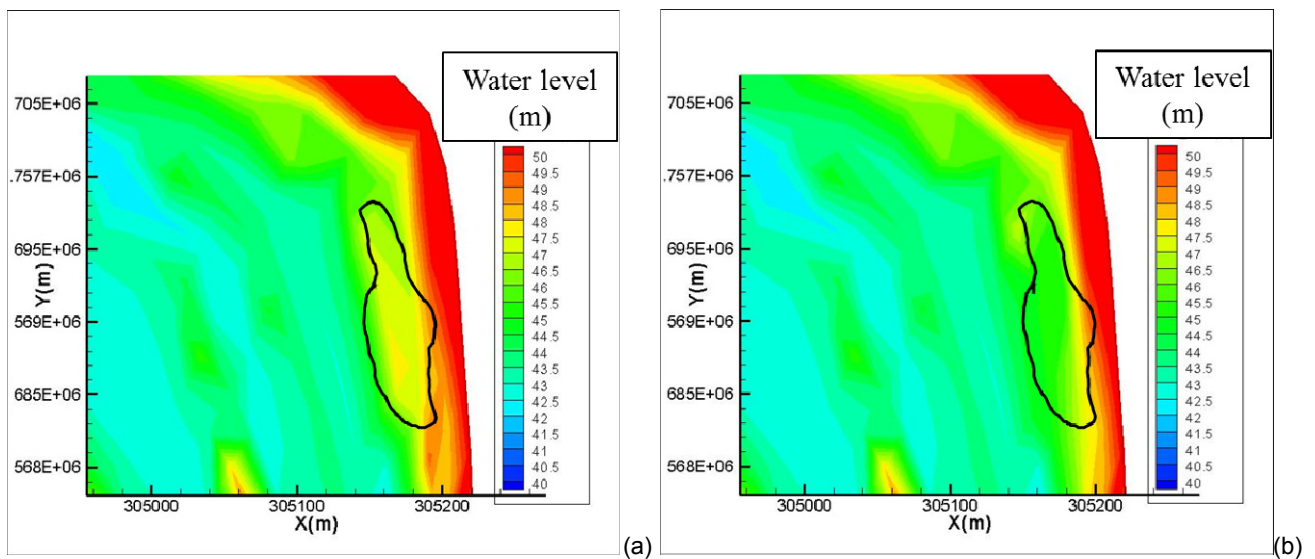

Figure 6. Simulated results of water depth of 200-year return period flood event (a) with buildings on flood plain (b) without buildings on flood plain.

5   CONCLUSIONS

Based on the simulated results of water stage with and without buildings on flood plan, the change of water depth is not significantly. It means that the water depth impact of buildings on flood plan, especially around Quchi area, is not obvious owing to the small number of buildings. As compared to the channel conveyance, the cross section of buildings is relatively small. Therefore, the water stage impact of buildings on flood plan around Quchi area is limited. However, buildings on flood plan affect the water depth is confirmed. So, the management of buildings on flood plan still needs to be taken care to prevent it from affecting the water stage in the future due to the growing number of buildings. In addition, the adapted SRH-2D model is a hydraulic, sediment, temperature and vegetation model for river systems under development at the Bureau of Reclamation. It adopts robust and stable numerical schemes with seamless wetting-drying algorithm. The resultant outcome needs that few tuning parameters to arrive at the final solution. Based on various return period flood hydrographs, the SRH-2D is applicable to study the capability for channel conveyance and variation of the floodwater stage due to building effects in this study. In next step, the mobile-bed effects should be further discussed to understand the impacts of long-team sediment transport.

REFERENCES

Begnudelli, L. & Sanders, B.F. (2006). Unstructured Grid Finite Volume Algorithm for Shallow-Water Flow and Scalar Transport with Wetting and Drying. *J. Hydraul. Eng.*, 132(4), 371–484.

Brunner, G.W. (2006). *HEC-RAS, River Analysis System User's Manual: Version 4.0*. U.S. Army Corps of Engineers, Hydrologic Engineer Center, Davis, Calif.

Chow, V.T. & Ben-Zvi, A. (1973). Hydrodynamic Modeling of Two-Dimensional Watershed Flow. *J. Hydr. Div.*, 99(11), 2023–2040.

Lai, Y.G. (2008). *SRH-2D Version 2: Theory and User's Manual, Sedimentation and River Hydraulics Group*, Technical Service Center, Bureau of Reclamation, Denver, www.usbr.gov/pmts/sediment/.

Lee, H.Y. & Hsieh, H.M. (2003). Numerical Simulations of Scour and Deposition in *a Channel Network. International Journal of Sediment Research*. 18(1), 32-49.

DHI. (2002). *MIKE11, a Modelling System for Rivers and Channels*. Reference manual, DHI Water & Environment, Hørsholm, Denmark.

DHI. (1996). *MIKE21 Hydrodynamic Module Users Guide and Reference Manual*. Danish Hydraulic Institute-USA, Trevose, Pa.

Ghamry, H.K. & Steffler, P.M. (2005). Two-Dimensional Depth Averaged Modeling of Flow in Curved Open Channels. *J. Hydraul. Res.*, 43(1), 44–55.

Guo, W.D., Lai, J.S., Lin, G.F., Lee, F.Z. & Tan, Y.C. (2011). Finite-Volume Multi-Stage Scheme for Advection-Diffusion Modeling in Shallow Water Flow. *Journal of Mechanics*, 27(3), 415-430.

Harrington, R.A., Kouwen, N. & Farquhar, G.J. (1978). Behavior of hydrodynamic finite element model. *Advances in Water Resources,* 1(6), 331-335.

Huang, J.V. & Greimann, B.P. (2007). *User's Manual for SRH-1D V2.0. Sedimentation and River Hydraulics Grou*p, Technical Service Center, Bureau of Reclamation, Denver, (www.usbr.gov/pmts/sediment/).

Hervouet, J.M. & van Haren, L. (1996). *Floodplain processes*, Anderson, M.G., Walling, D.E. & Bates, P.D., eds., Wiley, New York, Chapter C6.

Jia, Y. & Wang, S.S.Y. (2001). CCHE2D: *Two-Dimensional Hydrodynamic and Sediment Transport Model for Unsteady Open Channel Flows Over Loose Bed*. Technical Rep. No. NCCHE-TR-2001-1, School of Engineering, Univ. of Mississippi, Oxford.

Jin, Y.C. & Steffler, P.M. (1993). Predicting Flow in Curved Open Channel by Depth-Averaged Method. *J. Hydraul. Eng.*, 119(1), 109–124.

Lai, Y.G. (2010). Two-Dimensional Depth-Averaged Flow Modeling with an Unstructured Hybrid Mesh. *Journal of Hydraulic Engineering*, 136(1), 12–23.

McGuirk, J.J. & Rodi, W. (1978). A Depth Averaged Mathematical Model for Near Field of Side Discharge into Open Channel Flow. *J. Fluid Mech.*, 86(4), 761–781.

Rodi, W. (1993). Turbulence Models and Their Applications in Hydraulics-a State-of-Arts Review. IAHRM, Balkema, Rotterdam.

Taipei Feitsui Reservoir Administration (2015). *Investigation on Topography Changing and Channel Conveyance of Feitsui Reservoir Downstream River,* National Taiwan University.

U.S. Army Corps of Engineers (USACE) (1996). *Users' Guide to RMA2—Version 4.3. Waterway Experiment Station-Hydraulic Laboratory*, Vicksburg, Miss.

Vreugdenhil, C.B. & Wijbenga, J. (1982). Computation of Flow Pattern in Rivers. *J. Hydr. Div.*, 108(11), 1296–1310.

Water Resources Planning Institute, Water resources agency, Ministry of Economic Affairs (2009). *Rock Erosion Modeling on Selected Alluvial Rivers in Taiwan*, Bureau of Reclamation, U.S.A.

Wu, W. & Vieira, D.A. (2002). *One-Dimensional Channel Network Model CCHE1D version 3.0—Technical Manual*, Technical Rep. No. NCCHE-TR-2002-1, National Center for Computational Hydroscience and Engineering, Univ. of Mississippi, Oxford, Miss.

Ye, J. & McCorquodale, J.A. (1997). Depth Averaged Hydrodynamic Model in Curvilinear Collocated Grid. *J. Hydraul. Eng.*, 123(5), 380–388.

Zarrati, A.R., Tamai, N. & Jin, Y.C. (2005). Mathematical Modeling of Meandering Channels with a Generalized Depth Averaged Model. *J. Hydraul. Eng.*, 131(6), 467–475.

DEVELOPMENT OF AN EMERGENCY FOOD AID PLAN: AN IMMEDIATE ACTION FOR FLOOD DISASTER MANAGEMENT

BALACHANTHAR SATESH [(1)], NOR AZAZI ZAKARIA[(2)] & LEE LAI KUAN[(3)]

[(1,3)] School of Industrial Technology (PPTI),Universiti Sains Malaysia, Gelugor, Penang, Malaysia
[(2)] River Engineering and Urban Drainage Research Centre (REDAC), Universiti Sains Malaysia, Nibong Tebal, Penang, Malaysia.
sateshbala@icloud.com; redac01@usm.my; l.k.lee@usm.my

ABSTRACT

Floods are the most common natural disaster in both developed and developing countries. Categorized as a sudden-onset disaster, flood often creates urgent but temporary food needs. This study aims to develop an emergency food aid plans (EFAPs) for disaster relief via *Nutritionist Pro* software. The selection criteria of foods used in the emergency food aid plan are as follow: readily available in the market, easily distributed and consumed, culturally feasible, cheap and commonly provided by the government and non-governmental organizations (NGOs). Identified foods include bread, instant noodles, biscuits and low-cost canned foods. The 3-day EFAPs are developed based on two scenarios: (A) water and electricity availability; and (B) congregate feeding. The nutritional compositions of the EFAPs lie within 1900 - 2300 kcal. Optimization analysis identifies menu that addresses nutritional requirements for Malaysian adults for as low as RM7.52/d (scenario A) and RM5.81/d (scenario B). This study produces policy-relevant information on the effectiveness and implementation of an emergency food aid approach.

Keywords: Flood disaster; emergency food aid; energy; nutrition; preparedness.

1   INTRODUCTION

Disasters are devastating and deprive affected persons of many rights, including the fundamental right to adequate food recognized universally as early as 1948 under Article 25 of the Universal Declaration of Human Rights (United Nations, 2015). Emergency food aid is an example of a "transfer from donor to recipient countries of food commodities on a totally grant basis" not on "highly concessional terms" (FAO, 1996a). From a global view point, the humanitarian food assistance aims to ensure the consumption of sufficient, safe and nutritious food in anticipation of, during, and in the aftermath of a humanitarian crisis, when food consumption would otherwise be insufficient or inadequate to avert excess mortality, emergency rates of acute malnutrition or detrimental coping mechanisms (Lentz and Barret, 2013).

Several methods have been employed in developing emergency food aid during disasters. Nghiem et al. (2012) have proposed lowest cost foods as a preparation for disaster in New Zealand using diet optimization and linear programming. Meanwhile, Rustiawan (2014) used simple mathematical calculation to estimate the food requirement of victims in the disaster prone areas in Indonesia after the eruption of Mount Sinabung based on the Recommended Daily Intake (RDI) and also estimated the required food cost. Besides nutrient content, cost and cultural preferences, Rossi et al. (2011) have addressed the dietary needs and restrictions of disaster victim with chronic kidney disease (CKD) by developing emergency diet.

An accurate food demand prediction is the basis of creating a rational emergency food supply program after a flood. Moreover, the establishment of a cost effective, nutritionally-balance and socially acceptable EFAP would simulate the understanding of nutritional needs, abate hunger and indirectly prevent acute malnutrition. This study is the first to develop EFAP for national emergence nutrition policy reference and aims to characterize victims' acceptance with regards to preparing for future emergencies. More importantly, information pertaining to the selection and distribution of low cost yet nutritious food items during floods is severely lacking. With the aforementioned issues, this research is conducted to develop an emergency food aid plan for flood disaster relief and preparedness. The diet menu is planned according to the stringent criteria: cost effective, nutritionally- balance, socially acceptable and adhere to the guidelines permitted by the World Food Programme (WFP).

2   METHODOLOGY

2.1 Phase 1

A 3-day emergency food menu was developed based on the principles of dietary planning using Nutritionist Pro (2016) software. A 3-day menu approach was adopted in our study, as recommended by the Federal Emergency Management Agency of United States (FEMA, 2004). The menu was designed into 5 major meals per day as following: breakfast, morning snack, lunch, afternoon snack and dinner. The energy and nutrient composition of food items used in the menu were based on the Malaysian Food Composition

Database (1997) and the USDA Food Composition Database (2016). The primary objective of the current phase was to provide adequate energy, carbohydrate, protein and fat, while simultaneously minimizing the consumption of cholesterol and sodium of the population during floods. The menu was developed based on 2100 kcal of energy with the following macronutrient distribution: 56% of carbohydrate, 16% of protein and 28% of fat. The menu was also developed according to 2 scenarios: (1) (Scenario A: menu to be utilized immediately using ready-to-eat foods particularly in the absence of water and electricity), and (2) (Scenario B: menu to be utilized by the emergency food service personnel to provide congregate feeding at evacuation centers).

2.2 Phase 2

Dietary optimization had been performed using linear programming to create alternative emergency food list. The ultimate aim of the current phase was to identify low cost food items that meet the daily nutritional requirement of the population, including micronutrients. Mathematical modeling (Briend *et al.*, 2003) was performed based on previously designated scenario A and scenario B in Kingsoft Spreadsheets (2013). Main references for the energy and nutrient composition of selected foods were based on the Malaysian Food Composition Database (1997), the Singapore Food Composition Database (2011) and the USDA Food Composition Database (2016). Food prices were derived from Malaysian Consumer Price Guide (2016), online supermarket price data and in-store prices by survey. Food items with 'promotion' or 'reduce to clear' price tag had been ignored, and bulk purchase was avoided to minimize selection bias. Micronutrient requirements were based on the Seal and Thurstans (2013). Diet optimization of food service-oriented emergency diet menu plan was grouped as following: basic nutrients (BN), basic nutrients and vitamins (BN+V) and basic nutrients, vitamins and selected minerals (BN+V+SM).

2.3 Statistical analysis

Descriptive statistics were performed on nutritional contents, and they were calculated as the mean and standard deviation using the independent *t* test or generalized linear model. All tests were 2-tailed at a probability level of 0.05. Statistical analyses were conducted using the SPSS 22.0 statistical software package (IBM SPSS Inc., Chicago, IL).

3 RESULTS

3.1 Development of 3-d emergency food aid plan

Table 1 and Table 2 show the newly developed 3-day emergency food menu for scenario A and scenario B. All foods were derived from six major food groups: (1) Rice, noodle, bread, cereals, cereal products and tubers; (2) Vegetables; (3) Fruits; (4) Fish, poultry, meat and legumes; (5) Milk and milk products, and (6) Fat, oils, sugar and salt. For scenario A, the developed emergency food aid plan ranged between 1400 - 1500 kcal with an average of 60 g protein (16%), 204 g carbohydrate (56%), 47 g fat (28%), 141 mg cholesterol and 1238 mg sodium, respectively. As for congregate feeding at evacuation centers, the average energy and macronutrients contributed by the emergency food aid plan were 1250-1400 kcal, 177 g carbohydrates (51%), 56 g protein (16%), 51 g fat (33%), 137 mg cholesterol and 993 mg sodium, respectively (scenario B).

3.2 Optimization analysis using linear programming

Table 3 illustrates the nutrient constraints and its proportionate nutritional values achieved after the implementation of the optimization process. The diet optimization modeling had been carried out with the addition of basic nutrients (carbohydrate, fat, protein), vitamins (vitamin A, vitamin C, vitamin D, vitamin E, vitamin K, thiamin, riboflavin, niacin, panthothenic acid, pyridoxine, cobalamin, and total folate), selected minerals (sodium, calcium, iron, selenium, zinc, magnesium, and copper), saturated fat, cholesterol and fiber. Combined scenario development and linear programming had identified daily dietary patterns that met key nutrient requirements for as little as a median of RM 5.81/d, up to RM 7.52/d for people whom receiving ready-to-eat emergency food aid, and food service personnel, respectively (Table 4).

Table 1. 3-day emergency menu (Scenario A) (sample).

Day 1	Day 2	Day 3
Breakfast	**Breakfast**	**Breakfast**
Sardine sandwich	Bun with kaya: 2 square pieces (70 g)	Cream crackers: 5 pieces (45 g)
• Wholemeal bread: 3 slices (75 g)	Soy bean milk: 1 pack (250 ml)	Orange juice : 1 pack (250 ml)
• Sardine, canned: (68 g)		
• Margarine: 2 teaspoons (10 g)		
Full cream milk: 1 pack (250 ml)		
Lunch:	**Lunch**	**Lunch**
Bread dipped with chicken curry	Bread dipped with chicken kurma	Bread with anchovies cooked in chili
• Wholemeal bread: 3 slices (75 g)	• White bread: 3 slices (85.5 g)	• Wholemeal bread: 3 slices (75 g)
• Chicken in curry, canned: (100 g)	• Chicken in kurma, canned: (100g)	• Anchovies cooked in chili, canned (60g)
Pineapple in syrup, canned: 1 cup (200 g)	Longan in syrup, canned : 1 cup (200 g)	• Margarine: 2 teaspoons (10 g)
Bottled water	Bottled water	Lychee in syrup, canned: 1 cup (200 g)
		Bottled water
Dinner	**Dinner**	**Dinner**
Tuna mayonnaise sandwich	Bread with prawn cooked in chili	Tuna sandwich
• Wholemeal bread: 2 slices (50 g)	• Wholemeal bread: 3 slices (85.5 g)	• White bread: 3 slices (85.5 g)
• Tuna in mayonnaise, canned: (50 g)	• Prawns cooked in chili, canned:	• Tuna in water, canned: (70 g)
• Margarine: 2 teaspoons (10 g)	• (70 g)	• Margarine: 2 teaspoons (10 g)
Dates: 4 pieces (50 g)	• Margarine: 2 teaspoons (10 g)	Peanut, roasted: (50 g)
Bottled water	Dates: 4 pieces (50 g)	Bottled water
	Bottled water	

Table 2. 3-day emergency menu (Scenario B) (sample).

Day 1	Day 2	Day 3
Breakfast:	**Breakfast:**	**Breakfast:**
Fried Rice Noodles	Sardine Sandwich	Sardine Mayonnaise Sandwich
• Mee-hoon: 2 cups (105 g)	• White bread: 3 slices (85.5 g)	• White bread: 3 slices (85.5 g)
• Fish ball, raw: 5 pieces (44.5 g)	• Sardine, canned: 1 piece (68g)	• Sardine, canned: 1 piece (68 g)
• Chinese mustard leaves, raw: 1 cup (110 g)	• Margarine, soft: 2 teaspoons (10 g)	• Mayonnaise: 1 tablespoon (15 g)
• Vegetable oil: 1 tablespoon (13.4 g)	Chinese yellow pear: 1 fruit (157.2 g)	• Margarine, soft: 2 teaspoons (10 g)
Guava: 1 slice (110.5 g)	Bottled water	Green apple: 1 fruit (102.2 g)
Bottled water		Bottled water
Lunch:	**Lunch:**	**Lunch:**
Rice: 2 scoops (152.6 g)	Rice: 2 scoops (152.6 g)	Rice: 2 scoops (152.6 g)
Fried chicken: 1 medium (90 g)	Chicken Cooked in Soy Sauce	Chicken in curry: 1 medium (96.3 g)
Vegetable Curry	• Chicken breast, raw: 1/2 piece (66g)	Potato: 1 medium (81.7 g)
• Brinjals, raw: 1/2 cup (43 g)	• Potato: 1 medium (81.7 g)	Stir-Fried Cabbage
• Vegetable oil: 1 tablespoon (13.4 g)	• Vegetable oil: 1 teaspoon (6.5 g)	• Cabbage, raw: 1 cup (69 g)
Bottled water	Stir-Fried Bean Sprouts with Turmeric	• Vegetable oil: 1 teaspoon (6.5 g)
	-Bean sprouts, raw: 1 cup (87 g)	Bottled water
	-Vegetable oil: 1 teaspoon (6.5 g)	
	Bottled water	
Dinner:	**Dinner:**	**Dinner:**
Rice: 2 scoops (152.6 g)	Fried Rice	Rice: 2 scoops (152.6 g)
Mackerel in curry: 1 medium (64 g)	Rice: 2 scoops (152.6 g)	Fried mackerel: 1 medium (40.5 g)
Stir-Fried Kangkung	• Cabbage, raw : 1 cup (69 g)	Okra Stir-Fried
• Kangkung, raw: 1 cup (78 g)	• Taukua, raw: 1/2 piece (76 g)	• Okra, raw: 1 cup (97 g)
• Vegetable oil: 1 teaspoon (6.5 g)	• Oil: 1 tablespoon (13.4 g)	• Vegetable oil: 1 teaspoon (6.5 g)
Bottled water	Bottled water	Bottled water

Table 3. Foods per person per day selected by the optimization process.

Food items selected by the optimization process	Total food weights suggested per day (g)	Food items selected by the optimization process	Total food weights suggested per day (g)
White bread	45	Atta flour	75
Whole wheat bread	208	Wheat flour	44
Sardine in tomato sauce canned	70	Rice, raw	204
Prawn cooked in chilli, canned	48	Chicken egg, raw	31
Process peas, canned	49	Sardine, raw	114
Red kidney beans in water, canned	31	Soy bean cake	155
Peanut butter	60	Bitter gourd, raw	188
Dates, dried	14	Carrot, raw	54
Peanuts	50	Chinese mustard leaves, raw	200
Soy bean milk	250	Mung bean sprouts, raw	67
Cereal beverage, powder	100	Guava, raw	200
		Palm oil	18
		Blended oil	27
Number of food items	**11**	**Number of food items**	**13**
Cost to purchase (MYR)	**7.52**	**Cost to purchase (MYR)**	**5.81**

Note:Foods less than 10g were excluded from the table.

Scenario A: Margarine (7g)

Scenario B: Rice noodles (0.5g) and raw spinach (2g)

Table 4. Nutrient targets, constraints and values achieved by the optimization process.

Nutrients (Unit)	Target & Constraint	Achieved Scenario A	Achieved Scenario B
Energy (kcal)	≧2100	2106	2100
CHO (g)	294 g (56%)	294	294
Protein (g)	84 g (16%)	84	84
Total fat (g)	65 g (28%)	65	65
Cholesterol (mg)	≦300	195	300
Saturated fat (g)	≦16.3	2300	16.3
Sodium (mg)	≦2300	20	402
Fiber (g)	≧20	44	20
Vitamin A (IU)	≧1834	2038	12976
Vitamin C (mg)	≧41.6	94.9	597.5
Vitamin D (µg)	≧6.1	12.6	6.1
Vitamin E (mg)	≧8	8	15
Vitamin K (µg)	≧48.2	48.2	48.2
Thiamin (mg)	≧1.1	2.8	1.8
Riboflavin (mg)	≧1.1	2.1	1.8
Niacin (mg)	≧13.8	30.7	19.6
Panthothenic acid (mg)	≧4.6	4.6	4.6
Pyridoxine (mg)	≧1.2	1.9	1.4
Cobalamin (µg)	≧2.2	10.4	10.3
Folate (µg)	≧363	406.4	782
Iron (mg)	≧32	34.9	32
Zinc (mg)	≧12.4	19.3	12.4
Copper (mg)	≧1.1	2.4	2.4
Selenium (µg)	≧27.6	104	39.3
Calcium (mg)	≧989	1048	989
Magnesium (mg)	≧201	506	377

4 DISCUSSION

Emergency food aid is prominent to human being to sustain life. Thus, a proper arrangement and direct consultation on menu planning is necessary to inform both individual and evacuation centers of the appropriate dietary recommendations during flood disaster. The present study is the first in Asia region to design and develop a nutritionally-balanced, cost effective, culturally acceptable, and sustainable emergency food aid plan for disaster preparedness and abatement. Apart from saving lives during emergencies, food aid can help to address underlying vulnerability (Devereux, 2007). Hoddinott et al. (2003) have noted the importance of food aid in smoothing consumption and protecting assets among households facing food stress. According to Edirisinghe (1998), a general point often made in favor of food aid is that it can improve nutrition better than cash because more food is consumed for equivalent values of transfer, which may partly be a consequence of women controlling food in the household (Haddad et al., 1997).

Two 3-day ready-to-eat and food service-oriented emergency food aid plans for the improvement of flood disaster had been designed under acute circumstances. The World Health Organization (WHO, 2002)

proposed provision of food aid consisting of 1900 kcal - 2300 kcal of energy per person per day. However, the newly developed 3-day menu provided only 1250 - 1500 kcal of energy acknowledging severe flood circumstances with provision of 3 meals per day. Nevertheless, the average macronutrient distribution of the two food menu was within the Acceptable Macronutrient Distribution Range (AMDR) proposed by the Institute of Medicine: CHO (45 - 65%), protein (10 - 35%) and fat (20 - 35%) of total energy intake. Cholesterol and sodium intake were also within the recommended intake level of less than 300 mg and 2400 mg, respectively. According to Fisher (2007), type of food aid particularly prepared rather than dry foods is more sensible in the immediate repercussion of sudden-impact disasters than slow-impact disasters. Hence, the developed emergency food menu consisted of foods that can be consumed without cooking such as bread, biscuits, UHT milk, canned proteins, canned vegetables and canned fruits. The canned foods used in the menu were catered towards Malaysian culture and taste preference by using food products made with local recipes such as canned chicken curry, canned sardines, and canned stir-fried anchovies as to avoid rejection and wastage. The recommended canned vegetables and fruits also provide fiber, vitamins, and minerals. Bottled water was provided as it is cheap and mainly required by the victims for hydration, while milk was provided as a source of energy and also calcium source. Further, Violette et al. (2013) also noted that food aid recipients of locally procured foods were generally more satisfied with the local commodities than recipients of donor-sourced foods.

In the United States of America, the Food and Nutrition Service (FNS) of the United States Department of Agriculture (USDA) is responsible for the provision of food assistance to disaster victims. The food assistance is provided via three primary ways: USDA food incorporation into menus for congregate feeding; household food distribution and issuance of temporary financial food assistance known as Disaster Supplemental Assistance Program (S-SNAP). The types of food provided by the FNS include the following: high-quality canned, fresh, frozen and dry products, whole grains, legumes, lean meats, poultry and fish (Abernathy, 2015). Meanwhile, in Japan, the Ministry of Health, Labor and Welfare (MHLW) is responsible for providing nutrition assistance to the disaster victims and the provision of food is supported by the Ministry of Agriculture, Forestry and Fisheries (Sudo, 2015). During the first through the third month of the Great East Japan Earthquake in 2011, MHLW provided the required number of meals and necessary quantity of nutrients for the emergency shelters based on the following nutrients: 2000 kcal, 55 g protein, 1.1 mg thiamine, 1.2 mg riboflavin and 100 mg Vitamin C. Based on the following reference values, the National Institute of Health and Nutrition developed a specific menu to be served in the emergency shelters. The menu consisted of cereals, potatoes and starches, vegetables, fruits, meats, eggs, milk and dairy products and fats and oils (Tsuboyama Kasoka and Purba, 2014). Research focusing on the development of emergency food plan in neighboring countries such as Indonesia indicates the provision of dry and shelf stable foods such as instant noodles, rice, canned sardines and beef and drinking water (Burtha et al., 2008; Rustiawan et al., 2014).

The study was able to identify foods and dietary patterns that addressed nutritional requirements for Malaysian adults for as low as RM 5.81/d. However, increasing the dietary variety and nutrient constraints did increase daily cost when optimized for more expensive alternative foods containing micronutrients such as calcium. Similarly, in New Zealand, the cost of emergency food storage addressing all nutritional recommendations by optimization was higher (US$4.66) rather than addressing dietary energy recommendation alone (US$1.46) (Nghiem et al., 2012). The current study performed dietary optimization using 26 nutrients based on the purpose of immediate consumption, storage and congregate feeding, while the previously mentioned study was based on only 14 nutrients for the purpose of emergency storage. Upcoming research may attempt to investigate on which, how and to what extent the inclusion of essential nutrients may affect the overall costing for the estimation of emergency food aid. Ingredients such as poultry, fish, vegetables and fruits used in designing the congregate feeding menu could be procured from neighboring districts of the disaster affected regions within the country. Advancement in disaster logistics such as cold-chain storage could be utilized to store the wet ingredients.

Future research should clearly specify to what extent the role of emergency food aid resources could be measured for the determination of nutritional status among the flood disaster victims. Further, emergency food products with the following properties: ready-to-eat, long shelf life, easily distributed and nutrient dense should be developed to be used during disasters. Low sodium canned foods should be recommended as current products are high in sodium content, thus restricting its consumption for hypertension and kidney disease patients. Community studies have to be undertaken to evaluate the feasibility of the designated emergency food aid plan among the flood disaster victims.

5   CONCLUSION

Emergency food aid is prominent to human being to sustain life. Thus, a proper arrangement and direct consultation on menu planning is necessary to inform both individual and evacuation centers of the appropriate dietary recommendations during flood disaster. This study establishes the designation of a nutritionally-balanced, cost effective, socially acceptable, and sustainable emergency food aid plan for flood disaster preparedness and abatement. In particular, ready-to-eat and food service-oriented emergency food aid plans have been designed for acute water and electricity shortage and flood victims whom will be

sheltered at evacuation centers. The current study is expected to serve as national emergence nutrition policy reference, and acts as a framework for the government, non-governmental organizations and also by the population at the household level for flood disaster management.

ACKNOWLEDGEMENTS

REFERENCES

Abernathy, T. (2015). Responsibilities of the USDA-Food and Nutrition Service in Nutrition Assistance Response to Natural Disasters. *Journal of Nutritional Science and Vitaminology*, 61, S14.

Briend, A., Darmon, N., Ferguson, E. & Erhardt, J.G. (2003). Linear Programming: A mathematical Tool for Analyzing and Optimizing Children's Diets during the Complementary Feeding Period. *Journal of Pediatric Gastroenterology and Nutrition*, 36(1), 12-22.

Burtha, E.K., Syarief, H. & Sunarti, E. (2008). Pengelolaan Pangan untuk Penaggulangan Bencana di Kabupaten Lampung Barat (Food management for Disaster Mitigation in West Lampung District). *Jurnal Gizi dan Pangan*, 3(3), 250-256.

Devereux, S. (2007). The Impacts of Droughts and Floods on Food Security and Policy Options to Alleviate Negative Effects. *Agricultural Economics*, 37, 47-58.

Edirisinghe, N. (1998). The Food Factor. In Time for Change. *Food Aid and Development Conference,* World Food Programme, Rome.

FAO. (1996a). *Food Aid in Figures, 1994,* Food and Agriculture Organization, Rome, 12.

Federal Emergency Management Agency, (FEMA). (2004). Food and Water in an Emergency. Available at https://www.fema.gov/pdf/library/f&web.pdf on 5/5/2017.

Fisher, D. (2007). Fast food: Regulating Emergency Food Aid in Sudden-Impact Disasters. *Vanderbilt Journal of Transnational Law*, 40(1127), 1127-1153.

Haddad, L., Hoddinott, J. & Alderman. H. (1997). *Intrahousehold Resource Allocation in Developing Countries,* Washington, DC: International Food Policy Research Institute.

Hoddinott, J., Cohen, M. & Bos, M.S. (2003). *Redefining the Role of Food Aid,* International Food Policy Research Institute, Washington, DC.

Lentz, E.C. & Barrett, C.B. (2013). The Economics and Nutritional Impacts of Food Assistance Policies and Programs. *Food Policy*, 42, 151-163.

_ZON_UTARA/index.html on 26/1/2017.

Nghiem, N., Carter, M.A. & Wilson, N. (2012). Emergency Food Storage for Organisations and Citizens in New Zealand: Results of Optimisation Modelling. *The New Zealand Medical Journal,* 125(1367), 49-60.

Rossi, M., Young, V., Martin, J., Douglas, B. & Campbell, K.L. (2011). Nutrition during a Natural Disaster for People with End-Stage Kidney Disease. *Renal Society of Australasia Journal*, 7(3), 69-71.

Rustiawan, A. & Mansur A.R. (2014). Kebutuhan Pangan Pokok untuk Penangulan Bencana di Kabupaten Sleman (Food Needs for Disaster Mitigation in Sleman District). *Jurnal Kesehatan Masyarakat,* 8(1), 19-28.

Seal, A. & Thurstans, S. (2013). Derivation of Nutrient Requirements for Disaster-Affected Populations:

Sphere Project 2011. *Food and Nutrition Bulletin,* 34(1), 45-51.

Sudo, N. (2015). Roles of National and Local Governments and the Dietetic Association in Nutrition Assistance in Response Tonatiral Disasters: Systems and Experiences in Japan and the USA. *Journal of Nutritional Science and Vitaminology*, 61, S13.

Tsuboyama-Kasaoka, N. & Purba, M.B. (2014). Nutrition and Earthquakes: Experience and Recommendations. *Asia Pacific Journal of Clinical Nutrition*, 23(4), 505-513.

United Nation. (2015). The Universal Declaration of Human Rights. Available at http://www.un.org/en/universal- declaration-human-rights/index.html [Assessed on 26/1/2016]

United States Department Agriculture (USDA). (2016). USDA Food Composition Databases. Available at https://ndb.nal.usda.gov/ndb/ on 26/1/2017.

Violette, W.J., Harou, A.P., Upton, J.B., Bell, S.D., Barrett, C.B., Gomez, M.I. & Lentz, E.C. (2013). Recipients' Satisfaction with Locally Procured Food Aid Rations: Comparative Evidence from a Three Country Matched Survey. *World Development,* 49, 30-38.

World Health Organization (WHO). (2000). The Management of Nutrition in Major Emergencies. Available at http://www.who.int/nutrition/publications/emergencies/9241545208/en/ on 26/1/2017.

EVALUATION OF EMPIRICAL EQUATIONS FOR DAM BREACH PARAMETERS AND ITS APPLICATION IN INDIAN DAM FAILURE CASES

SACHIN DHIMAN[(1)] & KANHU CHARAN PATRA[(2)]

[(1,2)] Civil Engineering Department, National Institute of Technology Rourkela, Odisha 769008, India,
sach.dhiman1988@gmail.com; prof_kcpatra@yahoo.com

ABSTRACT

Our society gets huge benefits from the water storage dams, but the consequences are devastating if a dam fails. It causes extensive damage to the life and properties mostly due to short warning time. Important factors governing failure studies are the breaching parameters that help to quantify the risk associated with dam break floods. Many empirical equations have been developed for predicting the breaching parameters associated with peak outflow, and these equations are generally developed by regression analysis from the record of dam failure data. The present paper is focused to develop the empirical formulas for earthen embankments that can predict breach parameters and peak outflow based on past failures. The database of 157 past dam failure cases has been compiled with the inclusion of new 15 dam failure data from India. A multivariable linear and nonlinear regression method for both dimensional and non-dimensional form of breaching parameters and predictors is used to develop the relationship. The results obtained from the regression equations for breach parameters and peak outflow is compared with observed data and the uncertainties in the results are evaluated. The recently developed regression equations for breach parameter predictions along with the older equation for earthen dams are studied for Indian dam failures.

Keywords: Breach parameters; dam safety; Earthen dam; India dam failure cases; regression model.

1 INTRODUCTION

Consequences of natural disasters are devastating causing immense loss to the human life and property. In recent times flood events comes under the top natural disasters. Around the world dam safety has gained maximum awareness as the dam failure produces flash floods at the entire downstream area in a short time. Therefore, in recent years the dam break analysis draws attention from the researchers. Dam break analysis includes data collection, estimation of breach parameters, deriving dam breach outflow to the downstream, preparation of inundation map and then preparation of emergency action plan. Hence, the first step in dam break analysis is to predict accurate breach parameters and for that it is important to understand the dam breaching process. The breach parameters include breach depth, average breach width, breach side slope, breach time and peak outflow.

In general, three types of approaches are used for breach parameter prediction: (1) Comparative approach which is based on comparisons with one or more very similar dams that have failed. (2) Empirical formulas based on case study data, and (3) Physical based dam breach models. Many investigators such as Kirkpatrick (1977), SCS (1981), Singh & Snorrason (1984), MacDonald & Langridge-Monopolis (1984), Bureau of Reclamation (1988), Froehlich (1995a,b and 2008), Zhang (2009) and Pierce (2010) have used analytical approach to predict peak outflow as a function of various dam and reservoir parameters, with the empirical relation developed from case study data. On the other hand, most of the physical-based models depend on hydraulic principles and sediment transport formulas (e.g., Fread, 1977; 1988), Singh & Scarlatos (1985)). Whal et al. (2008) summarized the progress on physical based dam breach model.

All three approaches have their shortcomings. First two models depend largely on case studies and that have high uncertainty. Physical based models lack understanding of the mechanisms of breach development and its inability to model that mechanism. Still, the most acceptable and widely used approach is parametric that make use of breach parameters calculated from regression based formulas. The reliability of breach parameters mostly depends on the number of case study involved in developing the regression equations. Froelich (1995a) used 63 cases for the prediction of average breach width and 21 cases for the prediction of breach formation time. Wahl (1998) compiled 108 case study data and named it super compilation dam failure data. Xu & Zhang (2009) mentioned 75 case study data in his study with inclusion of some data from super compilation. He proposed nonlinear regression model for developing empirical equations. The present study pays great efforts in collecting the dam failures data from the available reports from India.

In India 37 dam failures were recorded out of which 15 dam failure case reports are available. The data of 156 dam failures are used for the study which includes Whal (1998) super compilation, Zhang (2009) and 15 new cases. The data comprises of mostly homogeneous dams of about 61%. The variation of dam height is uniform from 1m to 60m with unknowns of 26.9%. Reservoir capacity largely varies between 1.0 X 10^6 to 1.0

X 10^8 m^3. Most of the embankments failed due to overtopping (51.3%, seepage or piping failure consists of 37.8% and sliding failure consists of 5.8% of all the data, while the rest have failed differently. Table 1 represents dam failure data statistics. Further details of 15 new cases from India are documented in Table 2. Note that the mentioning of dam erodibility as low, medium or high is based on construction era, soil type near the construction place and compaction methods used for making of dam.

Breach shape geometry is either triangular or trapezoidal. Many case histories generally show trapezoidal breach shape. For defining geometric breach parameters as trapezoidal shape one needs to know any three combinations of breach depth (H_b), breach top width (B_t), breach average width (B_{avg}), breach bottom width (B) or breach side slope. Fig 1 shows the breach parameter for trapezoidal shape geometry.
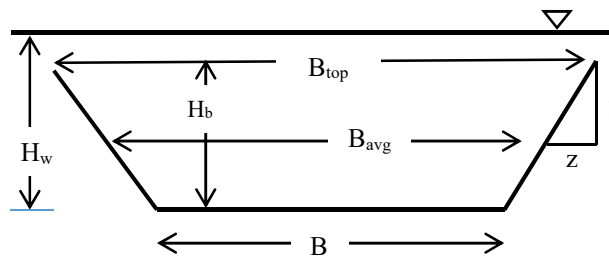
Figure 1 Geometric representation of breach parameters

Two more parameters are set for dam breach analysis. These are the peak discharge or peak outflow rate (Q_p) and failure time (t_f). Following Wahl (1988) failure time is divided into two phenomena that is breach initiation time and breach formation time. The breach initiation time begins with the first flow over or through a dam that will initiate warning, evacuation, or heightened awareness of the potential for dam failure. Breach formation time is the duration of time between the first breaching of the upstream face of the dam until the breach is fully formed. Practically breach initiation time is not possible to evaluate and continuous research is going on physical models of dam for evaluation of parameters. Therefore, the developed failure time equations are breach formation time. In dam break analysis, the peak discharge and time of occurrence of peak discharge are important factors to be evaluated. The time of occurrence of peak discharge is dependent on the exact prediction of breach parameters but more importantly the breach formation time.

Table 1. Dam failure data statistics

Total Numbers of Dam Failure = 156			
Dam Type	**Dam Height (m)**	**Reservoir Capacity (Mm^3)**	**Failure Mode**
Homogeneous dams = 61%	<10 = 18.6%	<1.0 = 21.8%	Overtopping = 51.3%
Dam with corewalls = 10.9%	10-15= 20%	1.0-10 = 17.3%	Seepage erosion/Piping = 37.8%
Zoned filled dams = 5.8%	15-30 = 18.6%	10-100 = 21.8%	Sliding = 5.8 %
Concrete faced dam = 3.2 %	30-60 = 18%	100-1000 = 6.4%	Unknown = 5.1 %
Rockfill & composite dams=3.2%	60-100 = 3.8%	Unknown = 32.7%	
Unknown = 12.2%	Unknown = 6.9%		

Table 2. Indian dam failure list

Sl.No.	Dam name	Year Built	Year Failed	Dam type	Dam height Hd (m)	Dam crest width	U/P slope (H:V)	D/S slope (H:V)	length (m)	Reservoir capacity V_d (10^6)	Design Flood Discharge (m³/s)	Depth of water above breach invert H_w (m)	Failure mode	Dam erodibility	Observed peak Inflow(m³/s)
1	Kodaganar	1974	1977	HD	12.75	6	2:1	2:1	2425	123.00	1274.26	13.2	O	ME	7079
2	Ghurlijor	1956		HD	12.19	3			593.3	2.179	204.46	13.99	O	HE	228
3	Panshet		1961	CD	63.56	6			765	310.61	1162	64.76	S & O	ME	10763
4	Khadakwasla	1879		CD	36.09	4			1539	86.00	2974.82	38	O	HE	16000
5	Palem Vagu		2008	HD	46	6	2.5:1	2.5:1	810	35.60	1416		P	LE	2425
														LE	
6	Palem Vagu	unfinished	2006	HD	36	56	2.5:1	2.5:1	810			36.5	O		
7	Kaddem	1958	1959	HD	30.78	3.28				215.30	4955.44	31.24	O	HE	14158
8	Kaila	1952	1959	HD	23.08	3.5			213.3	13.98			S	HE	
9	Dantiwada	1965	sept, 1973	HD	61	6			4881	464.00	6654	61.6	O	ME	11950
10	Machhu-II	1972	Aug,1979	CD	22.56	6.1	3:1	2:1	5210	100.55	5663	28.66	O	ME	16307
11	Mitti	1982	1988	HD	16.02					17.40		16.1	O	ME	
12	Pratappura	1930	2005	HD	10.67	3			2500	4.12			P	HE	
13	Jamuniya	1915	2002	HD	15.4	3.3			2772	9.209	108		P	HE	1800
14	Nandgavan		2005	CD	18.64				735	2.06	855.16	19.64	O	HE	4100
15	Nanaksagar	1962	aug,1967	HD	16.5				19200	209.80	1600	16.6	O	HE	9711

HD = Homogeneous Dam, CD= Composite Dam, O = Overtopping Failure, P= Piping, S= Seepage, HE= High erodibility, ME=Medium Erodibility, & LE=Low erodibility

2 PAST DEVELOPED REGRESSION EQUATION

In the past many regression equations were developed by various researchers covering several dam failure and safety studies. Some federal agencies have their guidelines published for breach parameters like breach width, breach development time, and side slope in some ranges. Table 3 presents several developed empirical formulas for breach parameter prediction by researchers. Recently Xu & Zhang (2009) have developed a non-dimensional empirical equation based on 75 case studies for breach depth, breach top width, breach average width, peak outflow rate and failure time. They have introduced dam erodibility as one of the control variables in their studies. They characterized erodibility of dam as high, medium and low on the basis of its construction year. Further Wahl (2014) evaluated the developed equation of Xu and Zhang and found acceptable for most of the breach parameters except breach formation time. Table 4 represents the recently developed Xu & Zhang (2009) breach parameters prediction equations.

Table 3 Equations developed by Researchers

Reference	Case	Relation Proposed (S.I. Units, Meters, M³ /S, Hours)
Bureau of Reclamation (1988)		Breach width eq. $B_{avg} = 3h_w$ Failure time eq. $t_f = 0.011(B_{avg})$ Peak flow eq. (1982)$Q_p = 19.1(h_w)^{1.85}$(Envelope eq.)
Froehlich (1995a)	63	Breach width equation $B_{avg} = 0.1803k_o V_w^{0.32} h_b^{0.19}$ Failure time equation $t_f = 0.00254(V_w)^{0.53} h_b^{-0.9}$ Peak flow equation (1995b) $Q_p = 0.607V_w^{0.295} h_w^{1.24}$
Froehlich (2008)		Breach width eq. $B_{avg} = 0.27k_o V_w^{0.333}$ (overtopping, $k_o = 1.3$ & piping , $k_o = 1.0$ &) Failure time eq. $t_f = 0.0176\sqrt{V_w/(gh_b^2)}$

Table 4 Xu and Zhang developed equations

Xu and Zhang (2009)	Dam type (b₁)			Failure mode(b₂)		Erodibility (b₃)		
	DC	FD	HD/ZD	OT	P	HE	ME	LE
Breach Height equations $H_b/H_d = 0.453 - 0.025(H_d/H_r) + B_1$ $B_1 = b_3 + b_4 + b_5$	0.145	0.176	0.132	0.218	0.236	0.254	0.168	0.031
$H_b/H_d = C_1 - 0.025(H_d/H_r)$ $C_1 = b_5$						1.072	0.986	0.858
Breach Average-Width Equation $B/H_b =$ $0.787(H_d/H_r)^{0.133}(V_w^{1/3}/H_w)^{0.652} e^{B_3}$ $B_3 = b_3 + b_4 + b_5$	-0.04	0.026	-0.226	0.149	-0.389	0.291	-0.14	-0.39
$B/H_b = 5.543(V_w^{1/3}/H_w)^{0.739} e^{C_3}$ $C_3 = b_4 + b_5$				-1.207	-1.747	-0.613	1.073	1.268
Breach Top-Width Equations B_t/H_b $= 1.062(H_d/H_r)^{0.092}(V_w^{1/3}/H_w)^{0.508} e^{B_2}$ $B_2 = b_3 + b_4 + b_5$	0.061	0.088	-0.089	0.299	-0.239	0.411	-0.062	-0.289
$B_t/H_b = 0.996(V_w^{1/3}/H_w)^{0.558} e^{c_2}$ $C_2 = b_4 + b_5$				0.258	-0.262	0.377	-0.092	-0.288
Failure Time Equations $T_f/T_r =$ $0.304(H_d/H_r)^{0.707}(V_w^{1/3}/H_w)^{1.228} e^{B_5}$ $B_5 = b_3 + b_4 + b_5$	-0.327	-0.674	-0.189	-0.579	-0.611	-1.205	-0.564	0.579
$T_f/T_r = C_5(H_d/H_r)^{0.707}(V_w^{1/3}/H_w)^{1.228}$ $C_5 = b_5$						0.038	0.066	0.205
Peak flow Equations $Q_p/\sqrt{gV_w^{5/3}} =$ $0.175(H_d/H_r)^{0.199}(V_w^{1/3}/H_w)^{-1.274} e^{B_4}$ $B_4 = b_3 + b_4 + b_5$	-0.503	-0.59	-0.649	-0.705	-1.39	-0.007	-0.375	-1.362

3 METHODOLOGY USED FOR PRESENT BREACH EQUATIONS

This paper evaluates five breaching parameters (breach depth, breach top width, breach average width, peak outflow rate and failure time) individually as outcomes of multivariate regression analysis. We consider three predictors [dam height (H$_d$), reservoir capacity (V), dam average thickness (W)] and three discrete

variables [dam type (X_4), failure mode (X_5), dam erodibility (X_6)] that are expressed as dummy variables in multivariate regression analysis. Xu & Zhang (2009 expressed outcome and predictors non-dimensionally and evaluated it as additive form (linear) and multiplicative form (non-linear). We follow the same approach of additive and multiplicative multivariable regression analysis for dimensionally and non-dimensionally stability. Dimensional and non-dimensional breach parameters are shown in Table 5.

Table 5 Breaching parameters and predictors for multivariate regression

Breaching Parameters	Predictors		
Dimensional (m, m³/s, hr)	**Dimensional (m, hr)**		
$Y_1=H_b$ (Breach Depth)	$X_1=H_d$ (Dam height)		
$Y_2=B_t$ (Breach Top Width)	$X_2 = V^{1/3}$ (Reservoir capacity)		
$Y_3=B_{avg}$ (Average Breach Width)	$X_3=W$ (Average thickness of dam)		
$Y_4=Q_p$ (Peak Discharge)			
$Y_5=T_f$ (Failure time)			
Non-dimensional	**Non-dimensional**		
$Y_1 = H_b/H_d$ (Breach Depth)	$X_1 = H_d/ H_r$ (Dam height)		
$Y_2 = B_t/H_b$ (Breach Top Width)	$X_2 = V_w^{1/3}/H_w$ (Reservoir Shape Coefficient)		
$Y_3 = B_{avg}/H_b$ (Average Breach Width)			
$Y_4 = Q_p/\sqrt{gV_w^{5/3}}$ (Peak Discharge)	Dam Type	X_{41}	X_{42}	X_{43}
$Y_5 = T_f/T_r$ (failure time)	With Corewalls	1^a (e^b)	0(1)	0(1)
	Concrete Faced	0(1)	0(1)	0(1)
	Failure Mode	X_{51}	X_{52}	
	Overtoping	1(e)	0(1)	
	Piping/seepage erosion	0(1)	0(1)	
	Dam Erodibility	X_{61}	X_{62}	X_{63}
	High Erodibility (HE)	1(e)	0(1)	0(1)
	Medium Erodibility (ME)	0(1)	1(e)	0(1)
	Low Erodibility (LE)	0(1)	0(1)	0(1)
	Homogeneous/zoned-fill	0(1)	0(1)	1(e)

Multivariable regression is a linear transformation of the *X* variables such that the sum of squared deviations of the observed and predicted *Y* is minimized. In multivariable linear regression, the value of the dependent variable depends on several independent variables instead of one. This paper is following the multiplicative regression procedure proposed in Xu & Zhang (2009). Here we add one more predictor to the regression equation and carry out the analysis for both dimensional and non-dimensional forms. Additive form (linear) and multiplicative form (nonlinear) as shown below are used to establish empirical relationships.

Additive (linear) multivariate regression equation is written as

$$Y_i = b_0 + b_1X_1 + b_2X_2 + b_3X_3 + (b_{41}X_{41} + b_{42}X_{42}) + (b_{51}X_{51}) + (b_{61}X_{61} + b_{62}X_{62}) \qquad [1]$$

Multiplicative (non-linear) multivariate regression equation is expressed as

$$Y_i = b_0X_1^{b_1}X_2^{b_2}X_3^{b_3}(X_{41}^{b_{41}}X_{42}^{b_{42}})(X_{51}^{b_{51}})(X_{61}^{b_{61}}X_{62}^{b_{62}}) \qquad [2]$$

where, Y_i (i=1, 2…5) are the five breaching parameters (dependent variable) X_{is} = predictors and b_{is} = regression coefficient. Equation (2) can be rearranged to additive form by taking logarithm to both side of equation as

$$lnY_i = lnb_0 + b_1lnX_1 + b_2lnX_2 + b_3lnX_3 + b_{41}lnX_{41} + \ldots \ldots + b_{62}ln \; _{62}) \qquad [3]$$

The process of establishing the empirical formula for dam breach parameters includes the following steps:

1. While selecting predictors (X_1, X_2, X_3, X_4, X_5, and X_6) from the case study for finding breach parameter (Y_i), it may be possible that some predictors are not known. Proper selection of predictors is the first step of finding Y_i.
2. Conduct multivariate regression analysis (additive and multiplicative) for all the six predictors and then carry out the regression by considering different combinations of predictors. The model with higher value of regression coefficient R^2 is preferred.
3. The selected model is used to establish the empirical formula for breach parameters.

4   PROPOSED EMPIRICAL EQUATION

4.1   Breach depth

Two equations are proposed for breach depth. For the formulation of breach depth, the additive and multiplicative regression analysis result for different cases are summarized and a high regression coefficient model is chosen for establishing the empirical formula for beach depth. Eq. [4] and Eq. [5] are developed from the multiplicative nonlinear regression model. Fig. 2 and Fig. 3 show the result for observed versus predicted breach depth from Eq. (4) and Eq. (5) respectively.

$$H_b = 0.618\, H_d^{0.61} V^{0.05} W^{0.18} \tag{4}$$

$$H_b = 0.805 H_d^{0.855} (V)^{0.029} e^{C_1} \tag{5}$$

where, $C_1 = b_1 + b_2$, $b_1 = -0.064$ for overtopping, -0.111 for Piping Failure, $b_2 = 0.246$ for High erodibility, 0.196 for Low erodibility.
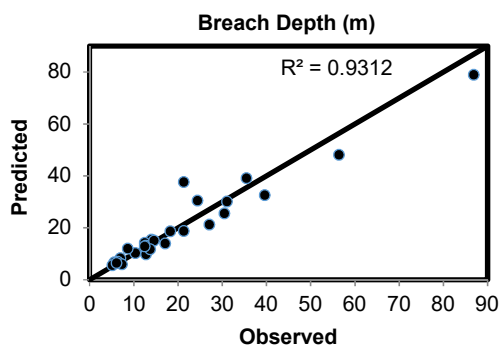
Figure 2. Observed Vs Predicted H_b for Eq. [4]   **Figure 3**. Observed Vs Predicted H_b for Eq. [5]
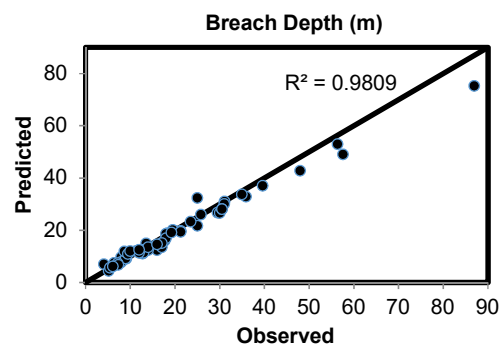
4.2   Breach top width

Using the same analysis procedure, the regression results for all the six breaching parameters and their combination are obtained. The best prediction model has been selected for developing the empirical formula for breach top width. For breach top width the non-dimensional multiplicative model with regression coefficient of 0.628 has been selected. The developed Eq. [6] gives correlation coefficient of 0.83 (Fig.4) for observed versus predicted breach top width.

$$B_t = 0.59(H_b)(H_d)^{0.089}(V_w^{1/3}/H_w)^{0.528} e^{C_2} \tag{6}$$

where, $C_2 = b_1 + b_2 + b_3$, $b_1 = -0.095$ for DC, -0.206 for HD and ZD, $b_2 = 0.447$ for Overtopping, $b_3 = 0.7$ for HE, 0.216 for ME
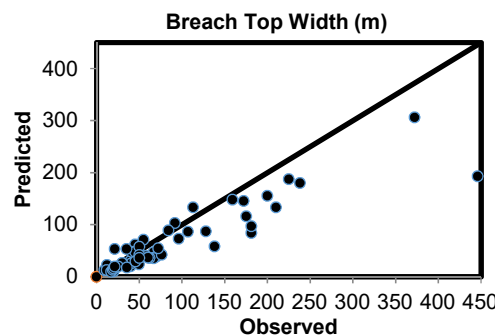
Figure 4. Observed Vs Predicted B_t

4.3   Average breach width

Multiplicative regression model having 0.667 coefficient of determination can be used for the formulation of average breach width (Eq. [7]).

$$B_{avg} = 0.425 H_b H_d^{0.125} (V_w^{0.33}/H_w)^{0.66} e^{C_3} \tag{7}$$

where, $C_3 = b_1 + b_2 + b_3$, b_1 = -0.166 for dam with DC, -0.302 for HD and ZD, b_2 = 0.429 for overtopping, b_3 = 0.628 for HE, 0.238 for ME

4.4 Peak outflow rate

Two new empirical Eq. [8] along with Eq. [9] are proposed for the calculation of peak discharge from the breached dam. Exact prediction of peak discharge is an important task because this can be routed to the downstream. Many factors such as reservoir capacity, height of dam etc. are involved in affecting the peak discharge. With these factors, many researchers have developed empirical formulas for peak discharge. Here, multivariable regression analysis is carried out for peak discharge prediction with new control variables such as breach parameters (breach depth, average breach width etc.) and to bring out the best model by inserting each non-dimensional breach parameter as a predictor with the combination of five predictors (dam height, reservoir shape coefficient, dam type, failure mode, and dam erodibility). It is found that average breach width is the most important factor on peak discharge estimate as compared to the other breach parameters. The linear correlation coefficient for observed peak discharge versus non-dimensional average breach width is 0.46 and it shows an increasing trend i.e. with the increase in breach width, the peak discharge increases. Formulation of peak discharge follows the same procedure as followed in breach depth formulation with the only difference being the inclusion of non-dimensional average breach width as a new predictor.

$$Q_P = (\frac{B_{avg}}{H_b})^{0.641}(V_w)^{0.25}(H_w)^{1.738}e^{C_4} \qquad [8]$$

where, $C_4 = b_1 + b_2 + b_3$, b_1 = 0.416 for DC, 0.113 for HD and ZD, b_2 = 0.218 for Overtoping, b_3 = 0.9 for HE, 0.848 for ME and

$$Q_p = 0.0105(H_d)^{0.272}(H_w)^{1.358}(V_w)^{0.38}e^{C_4} \qquad [9]$$

where, $C_4 = b_1 + b_2 + b_3$, b_1 = 0.176 for DC, 0.033 for HD and ZD, b_2 = 0.75 for Overtopping, b_3 = 1.52 for HE, 1.06 for ME

4.5 Failure time

The reliability of prediction of failure time is too insignificant from the documented data of Xu-Zhang (2009) that does not clearly justify whether it is a breach initiation time or breach formation time. In case study data by Whal (1988) the breach formation time is clearly mentioned but the number of data sets are only a few. Multivariate regression analysis (additive and multiplicative) is carried out. The regression model selected for the formulation of breach failure time is additive form as shown in Eq. [10]

$$T_f = 0.311 + 0.029(H_d) + 0.23(V_w{}^{1/3}/H_w) + C_5 \qquad [10]$$

where, $C_5 = b_1 + b_2 + b_3$, b_1 = 0.164 for DC, 0.725 for HD/ZD, b_2 = 0.145 for Overtopping, b_3 = -2.49 for HE, -2.11 for LE

5 RESULT COMPARISON WITH EXISTING BREACH EQUATION

The observed versus predicted average breach width and peak outflow for present study are compared with that of Xu-Zhang (2009), Froehlich (2008) and Bureau of Reclamation (1988) in Figure 5 and 6. The developed equation in the present study gives a higher degree of accuracy in terms of correlation coefficient as can be seen in the two Figures. The linear equation developed for failure time is better than that proposed by Xu-Zhang (2009) as can be seen in terms of correlation coefficient given in the Figure 7.
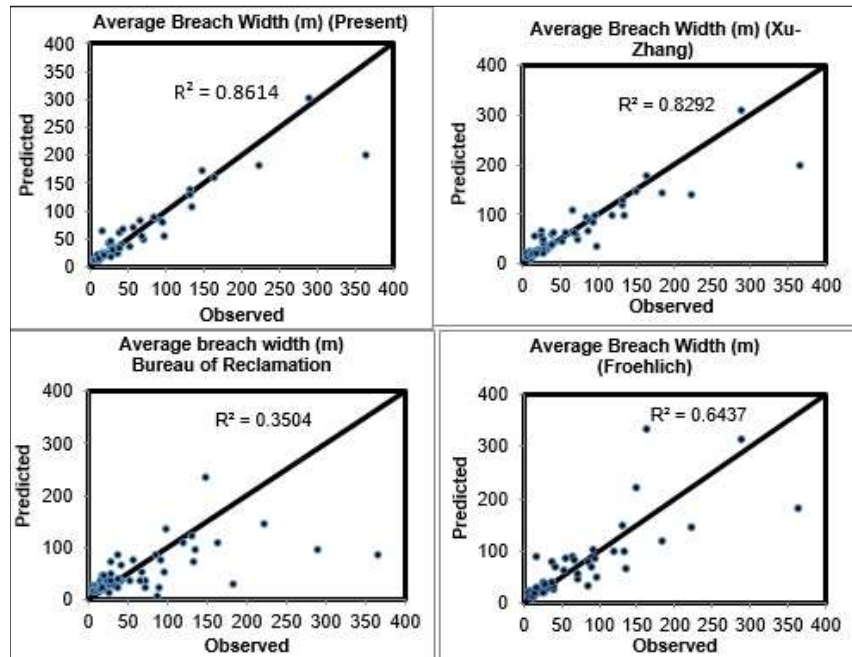
Figure 5 Comparison between average breach width formula developed by different researchers
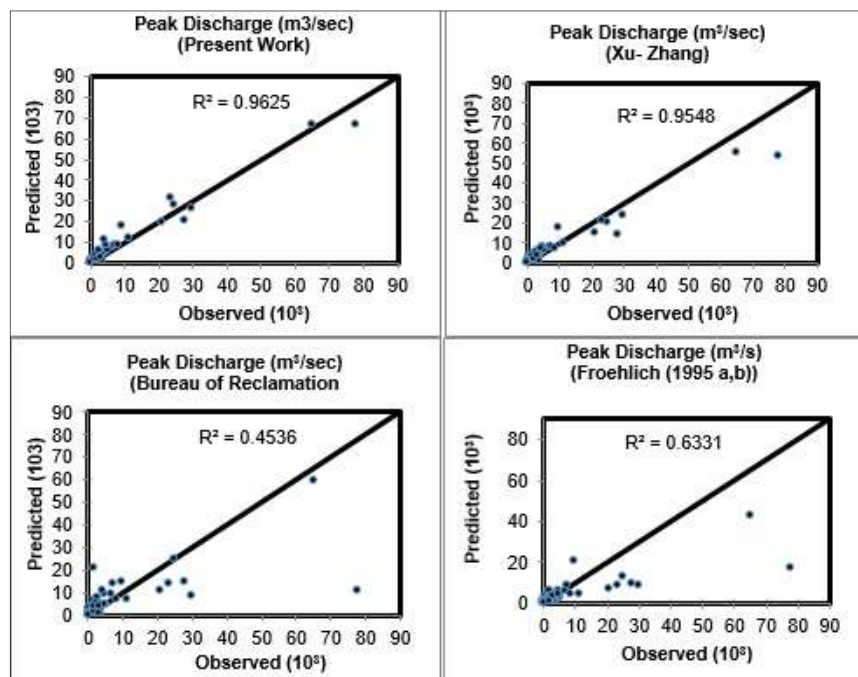

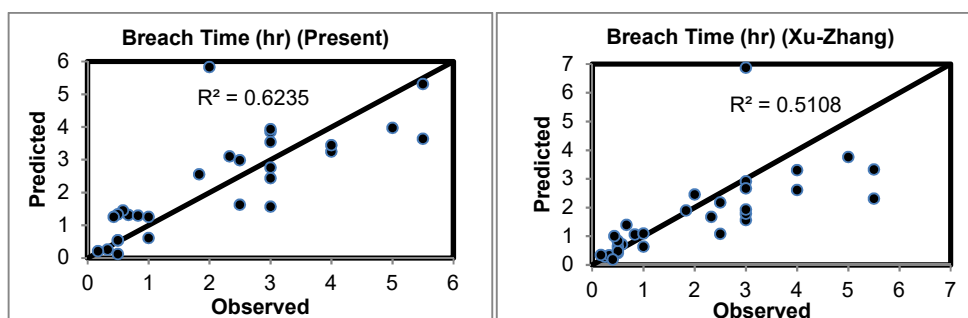**Figure 6** Comparison between peak outflow rate (m³/s) formulas developed by different researcher

Figure 7 Comparison of failure time (hour) with Xu-Zhang (2009) work

6 BREACH PARAMETER PREDICTION FOR INDIAN CASE STUDIES

Case studies carried out using data from Indian dams are presented in Table 6 to demonstrate the application of breach predictor equations and the uncertainties. Whal (1988) study has found large uncertainty in the breach parameters and as such their application for dam break analysis is under question mark. Standard error of estimate has been calculated for breach parameters and it is found that all the breach parameter equations resemble huge difference between observed vs predicted values. If we consider the Standard error of estimate for average breach width calculation the Bureau of Reclamation (1982; 1988), Froehlich (1995) and present work give less uncertainty. In most of the cases the observed data for peak outflow are not available because the discharge measurement stations are not placed at downstream region. It is quite relevant that peak outflow from breached dam is more as compared to the peak inflow to the reservoir. Prediction of breach time using the proposed equation is found quite comparable with that using Froehlich (2008) approach for Indian dams. The equation proposed by Xu-Zhang, overpredicted the breach time. Overprediction of breach time affects the emergency action plan as it under predicts the peak outflow from the dam breach. On the other hand the approach by Bureau of Reclamation underpredicted the breach time. Usually for breach depth calculations, the dam height has been used for the analysis purposes which are quit relevant. The present model for the calculation of breach depth is found to be quite comparable with that proposed by Xu-Zhang which can be adequate for Indian dam failure conditions.

7 CONCLUSIONS

Several techniques are available for estimating the breach parameters resulting from dam overtopping and subsequent failure. These techniques are predominately empirical based on fitting relationships between the key parameters. This paper has presented new equations based on 156 dam failure cases using both linear and nonlinear multivariable regression methods for predicting embankment breach parameters and peak outflow rate. For the first time dam failure data of Indian dams are collected and presented in this paper. Comparisons are made with the other developed empirical equations.

It is found that the present developed equations are better suited to calculate the breach parameters with higher degree of accuracy in terms of correlation coefficient than the other approaches proposed by Bureau of Reclamation (BR), Froehlich and Xu-Zhang. Furthermore, the predictor parameters such as the dam height, reservoir volume and erodibility are more influential factors in order for predicting the breach parameters than the other predictors. Dam average thickness also plays important role for the calculation of breach depth. Developed equations need more analysis and improvement by including more dam failure data. No sensitivity analysis has been carried out in this paper to rank the influence of each parameter affecting the dam failures.

VARIABLES

B, B_{avg} = breach width (average), m
B_t = breach top width, m
g = acceleration due to gravity, 9.8 m/s^2
H_b , h_b = height of breach, m
H_d , h_d = height of dam, m
H_r = dam reference height = 15 m
H_w, h_w = height of water above breach bottom, m

Q_p = peak outflow, m^3/s
t_f, T_f = failure time, hr
T_r = time reference = 1 hr
V_w = volume of water above breach bottom, m^3
V = Storage capacity of reservoir m^3
W = average dam thickness
t_f* = Dimensionless breach formation time, $t_f/\sqrt{gh_b}$

Table 6 Comparisons of breach parameters for dam failure cases in India

DAM	Average Breach Width (m)					Peak Outflow (m³/sec)				Breach time (Hr)					Breach Depth (m)		
	Observed	BR (1982,1988)	Froehlich (2008)	Xu-Zhang	Present	BR (1982,1988)	Froehlich (2008)	Xu-Zhang	Present	Observed	BR (1982,1988)	Froehlich (2008)	Xu-Zhang	Present	Observed	Xu-Zhang	Present
Kodaganar	415	40	158	101	82	2260	3624	6190	4199		1.7	5.2	6.9	8.3	12.2	12.1	13.9
Ghurlijor	60	42	43	56	50	2516	1185	1936	1516		0.5	0.6	0.7	1.3	12	11.6	12.5
Panshet		194	289	321	194	42850	34230	103481	94539		3.2	1.9	1.8	2.7	63	55.8	56.4
Khadakwasla	70	114	173	198	257	15982	12100	31038	19641	4	1.9	1.6	1.5	1.9	36	33.3	35.2
Palem Vagu	90	0	86		32				3992	2	0.9	1.5	5.9	4.0	24	45.9	31.5
Palem Vagu (Unfinished)	215	110				14835								2.1	36	32.8	
Kaddem	137.2	94	224	239	211	11124	12442	35151	39431	4	2.5	3.1	2.7	3.9	30	28.3	31.5
Kaila		0	63		67				4114		0.7	0.9	1.0	1.6	23.08	23.9	21.7
Dantiwada	110	185	322	326	219	39062	36215	114355	89281		3.5	2.7	2.5	3.6	56	53.0	55.1
Machhu-II		86	166	100	145	9484	8931	15333	11374	2	1.8	2.7	4.0	3.8	22.56	21.4	22.5
Mitti dam		48				3263	2604	3591	2894				2.7	3.1		15.1	16.0
Pratappura									735				1.0	2.3		11.3	10.8
Jamuniya	50		51		51				1815	6	0.6	1.1	1.1	2.1	15.4	16.2	15.2
Nandgavan	90	59	46	67	83	4714	1775	2917	3422	0.33	0.5	0.4	0.5	0.1	18.64	17.8	18.0
Nanaksagar	150	50	199	212	164	3453	5637	15523	14131		2.2	5.2	3.9	7.3	16.8	15.6	18.5
Standard Error of Estimate		135.4	121.9	158.9	136.6	13754	11181	46892	35300		2.50	2.29	2.92	2.12	12.2	12.1	13.9

REFERENCES

Bureau of Reclamation. (1982). Guidelines for Defining Inundated Areas Downstream from Bureau of Reclamation Dams. Reclamation Planning Instruction Rep. No. 82-11, U.S. Department of the Interior, Bureau of Reclamation, Denver.

Bureau of Reclamation. (1988). Downstream Hazard Classification Guidelines." ACER Technology Memorandum Rep.No. 11, U.S. Department of The Interior, Bureau of Reclamation, Denver.

Fread, D.L. (1988). BREACH: *An Erosion Model for Earthen Dam Failures*. National Weather Service, Office of Hydrology, Silver Spring, Md, 35.

Froehlich, D.C. (1995a). Embankment Dam Breach Parameters Revisited. *Conference on Water Resources Engineering, ASCE, New York*, 121(1), 887–891.

Froehlich, D.C. (1995a). Peak Outflow from Breached Embankment Dam. *Journal Of Water Resources*. Planning Management, 121(1), 90–97.

Kirkpatrick & Gerald W., (1977). Evaluation Guidelines for Spillway Adequacy. *The Evaluation of Dam Safety, Engineering Foundation Conference,* Pacific Grove, California*, ASCE*, 11, 395-414.

Macdonald, T.C. & Langridge-Monopolis, J. (1984). Breaching Characteristics of Dam Failures. *Journal Of Hydraulic Engineering,* 110(5), 567–586.

Pierce, M.W., Thornton, C.I. & Abt, S.R. (2010). Predicting Peak Outflow From Breached Embankment Dams. *Journal of Hydrologic Engineering*, 15(5), 338–349

SCS (1981). *Simplified Dam-Breach Routing Procedure*. Technical Release No. 66 (Rev. 1). Washington, D.C.: USDA-NRCS.

Singh, V.P. & Scarlatos, C.A. (1985). *Breach Erosion of Earthfill Dams and Flood Routing: BEED Model*. Research Report., Army Research Office, Battelle, Research Triangle Park, North Carolina.

Wahl, T.L. (1998). *Prediction of Embankment Dam Breach Parameters—A Literature Review and Needs Assessment*. Dam Safety Rep. No. DSO-98-004, United State Department of the Interior, Bureau of Reclamation, Denver.

Wahl, T.L. (2004). Uncertainty of Predictions of Embankment Dam Breach Parameters. *Journal of Hydraulic Engineering*, 130(5), 389–397.

Wahl, T.L. (2014). *Evaluation of Erodibility-Based Embankment Dam Breach Equations*. Hydraulic Laboratory Report HL-2014-02, United State Department of the Interior, Bureau of Reclamation, Denver.

Xu, Y. & Zhang, L.M. (2009). Breaching Parameters for Earth and Rockfill Dams. *Journal of Geotechnical and Geoenvironmental Engineering*, 135(12), 1957-1970.

RIVERBED INCISION DAMAGABLE TO HYDRAULIC STRUCTURE AND ITS COUNTERMEASURES

CHANGHAI HAN [(1)], YU YANG [(2)] YANFU LI [(3)] & GAOWEN TAN [(4)]

[(1, 2, 3, 4)] Nanjing Hydraulic Research Institute, State Key Laboratory of Hydrology-Water Resources and Hydraulic Engineering
chhan@nhri.cn

ABSTRACT

Riverbed incision at the downstream of the dam would induce water level fall and water fluctuation. As a result, the original energy dissipater could not be able to dissipate water energy completely and be liable to be destroyed. The main feasible countermeasure is building a lower stilling basin next to the original one. Xiaobudong rubber dam is the world's longest rubber dam project with length of 1135m, which two stage energy dissipation structure is used. Due to excessive sand mining, the riverbed has been sharply incised, and the energy dissipation structure have been destructed. The structure has been reinforced many times, but equally destructed many times. After a heavy flood season, the energy dissipation structure between the first stilling basin and the second still basin have been destroyed along the whole dam, which brought huge economic losses and threat to the rubber dam safety. In this study, based on hydraulic experiment and field investigation, the failure of the energy dissipater of Xiaobudong dam is analyzed. The connection section between the first and second stilling basins has been redesigned, as a result, stable hydraulic jump is formed in the first and also in the second stilling basin. Besides, the limit depth of riverbed incision is also studied. After reinforcement measures are actually implemented, the energy dissipater of the dam is adapt to dissipate the water power, and the energy dissipation structure suffers no damage again. The ideas and measures of the reinforcement in this study can provide a reference for other energy dissipaters facing the similar threat caused by riverbed incision.

Keywords: Riverbed incision; hydraulic structure; two-stage energy dissipater; hydraulic experiment; limited riverbed incision depth.

1   INTRODUCTION

Dam construction, excessive sand mining and other activities cause a significant reduction in river sediment, leading to riverbed incision generally in the middle or lower reaches of river and coastal areas (Mao et al., 2004; Chen et al., 2005). Riverbed incision at the downstream of dam engineering induces the decline of the water level and the increase of water level difference. When the water level difference exceeds the limited value, the energy dissipater cannot meet the energy dissipation requirements (Hu, 2013; Zhu et al., 2010), otherwise the energy dissipation facilities will be destroyed, which will seriously endanger the dam project. Therefore, the engineering measures should be taken in time to avoid the water disaster consequences (Huang et al., 2009). The transformation programs and operation of the appropriate energy dissipation should be taken according to the incision causes and characteristics of the project when the water level of the river dropped(Nai, 2007; Bian, 2007; Zhang et al., 2005; Huang et al., 2009; Chen et al., 2009; Huang et al., 2013; Huang et al., 2012).As an example, after completion of the Xiaobudong project, the phenomenon of man-made over-excavation of river bed sand was serious, which causes the river bed to cut down continuously for many years, and the energy dissipater was repeatedly destroyed and reinforced. The process of reinforcement and destruction not only endangered the dam, but also brought huge losses. It was urgent to fundamentally transform and strengthen the energy dissipation facilities. In this paper, combining with Xiaobudong hydraulic model test and field investigation, the causes of the destruction of energy dissipation and reinforcement measures are studied, which may also provide reference for similar projects.

2   PROJECT OVERVIEW

Xiaobudong rubber dam is the world's longest rubber dam project with 1135m long, including 16 rubber dam sections, 5 regular gates, 1 water diversion sluice, 1 pumping stations and bridge heads in each side of east coast and west coast, controlling drainage area 10287km^2. Other main project characteristics are as below: the river bed slop 0.5‰, the upstream design normal water level 65.5m, the design flood discharge 16000m^3/s, and the check flood discharge 19000m^3/s.

The project was built in 1997. From then on, the dam had experienced floods several times until 2008, which destroyed the energy dissipation facilities five times. Although so much reinforced measures were implemented, the damages could not be prevented. Two-stage energy dissipation structure was used downstream after the fifth energy dissipater reinforcement in February 2009, which consisted of 2 stilling

basins and the slope connection components. The first stilling basin is 9m long with the bottom elevation 60.3m, while the 2nd stilling basin is 15m long with the bottom elevation 56.5m. The two stilling basins were connected by the downstream platform of the first stilling basin, the slope of 1: 4 and the upstream platform of the second stilling basin, as show in Figure 1. The reinforcement structure of the first platform and the slope was severely damaged, and some part were destroyed with whole drift and some with fracture, after it had experienced flood discharge 5640m3/s in July and flood discharge 3120m³/s in August 2009, as shown in Picture 1 and Picture 2.
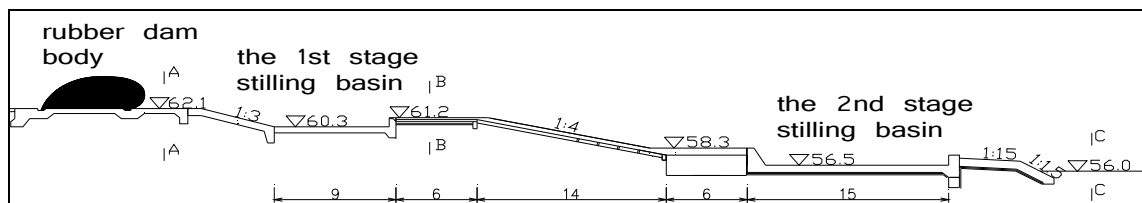
Figure 1. Section of the dissipation structure after the fifth reinforcement in 2009 (unit: m).

Picture 1. The discharge flow in the downstream of rubber dam during flood season.

Picture 2. Destruction of the energy dissipation structure.

3 DESTRUCTION CAUSE ANALYSISOF ENERGY DISSIPATER

According to the engineering data and on-site investigation, there were two main reasons for the energy dissipation destruction on the downstream of the dam.

1) The excessive sand mining in the downstream had incised river bed sharply for many years.

From 1996 to 2005, the average elevation of river bed downstream had dropped from 61.0m to 57.5m, which led to the increase of water level difference. The facilities couldn't meet the energy dissipation requirements any more.

2) The reinforcement which was made in 2009 couldn't avoid the ruining because:

The downstream flow of the dam was varied and complex, while the two stage energy dissipation mechanism was complex. Lack of unified standards or code requirements for the two stage energy dissipater design, it is easy occurred the energy dissipater damage once the layout and size of the dissipater couldn't meet the energy dissipation requirements.

The strength of the reinforcement structure was insufficient. The strength of the second stilling basin, the platform and slope section, should be strong enough to avoid the lifting of the reinforced concrete block, and even the whole drift and destruction.

4 EXPERIMENTALSTUDY ON ENERGY DISSIPATION SCHEME

4.1 Headings model design

A normal model with a scale of 1:40 was adopted, which satisfies the gravitational similarity criterion. The simulation scope of the model test fully reflects the main body part and the energy dissipater layout of the rubber dam, and the adjacent rubber dam on both sides. The downstream river bed possesses enough erosion and protection test sections to ensure the similarity of the downstream flow. Installing measuring weir is used to control hub flow in the inlet of the model. Using the standard stylus to read the water level of upstream and downstream, the accuracy is 0.1mm and the error is ±0.05mm. The velocity is measured by the photoelectric propeller speed meter LS-II developed by Nanjing Hydraulic Research Institute, with initiated flow rate 1cm/s, the precision 0.01cm/s, and the error ± 0.01cm/s.

4.2   Energy dissipation experiment of the fifth strengthening scheme

The model simulates the fifth energy dissipater reinforcement program which was implemented in 2009. The test conditions are determined by combining with the engineering flood standard and the hydrological data of the rubber dam in 2009. There are seven test conditions that flood discharge varies from 2627m^3/s to 19000m^3/s (Table 1).

The observed flow condition is shown in Table 1, and the flow velocity distribution at 8000m^3/s is shown in Figure 2. The experimental results show that both the first and the second stilling basin have a stable hydraulic jump, and the head of hydraulic jump is on the slope and moves up gradually as the flow discharge or the downstream water level rise. Exceptionally, in case of the small flow 2627m^3/s, it is jet flow when the water flows into the second stilling basin, failed to form two stage hydraulic jumps.

The water flow in the connecting platform and slope section between the two stilling basin is supercritical flow. The velocity on the platform is large. When the flow discharge is 4500m^3/s and 8000m^3/s, the velocity is about 4.1m/s and 4.8m/s respectively. The maximum velocity occurs in the slope section. When the flow discharge is 4500m^3/s and 8000m^3/s, the velocity is about 6.4m/s and 7.3m/s respectively.
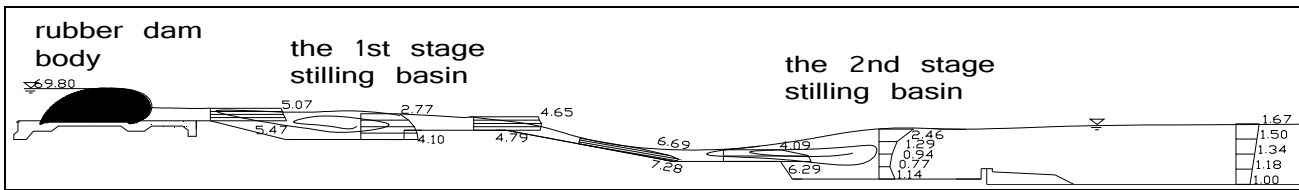
Figure 2. The flow velocity distribution in the downstream of rubber dam with the flow of 8000m^3/s (unit: m/s).

The C-C section with ground elevation of 56.0m is adopted as the calculation datum (Figure 1) and is used to calculate the energy dissipation rate of the two stilling basins. According to the water flow parameters of the A-A and B-B cross-section, the energy dissipation rate of the first stilling basin is calculated by the ratio of the water head difference between A-A and B-B cross-section to the total head of A-A section. According to the water flow parameters of the B-B and C-C cross-section, the energy dissipation rate of the second stilling basin is calculated by the ratio of the water head difference between B-B and C-C cross-section to the total head of B-B section. The water flow energy dissipation rate results are shown in Table 2. The energy dissipation rate of the first stilling basin is about 10% only, resulting in high velocity flow on the connecting platform and slope section between the two stilling basin .

It can be seen that the water level differences between the upstream and downstream are 3.54~5.00m among all level floods, and the bottom velocity of the first and the second stilling basin are small, but the flow velocity on connecting platform and slope section between the two stilling basin is high. Therefore, the connecting platform and slope section between the two stilling basin should be regarded as the focus of reinforcement. If the reinforcement structure is irrational or water sealing for the structure is insufficient, the water would flows into the gap and produce a large uplift pressure which could damage the structure. This can explain why the reinforcement part downstream the first stilling basin is prone to serious damage in the actual operation.

In addition, if the downstream riverbed incision goes on, the water level difference, as well as the flow velocity on the connecting platform and slope section between the two stilling basin, will increase gradually and threaten the energy dissipater safety. Under the condition of small discharge, there could not form a hydraulic jump in the second stilling basin. This would accelerate downstream river bed incision. Therefore, in this study, it is optimized and improved the structure and size of the energy dissipater to avoid the damage itself.

Table 1. The measured bottom velocity at different of positions of different discharges.

Flow(m^3/s)	2627	3410	4500	8000	12000	16000	19000
The 1st stilling basin	1.65	2.13	2.98	4.1	4.73	4.96	5.42
Platform Tanjung	3.33	3.57	4.03	4.79	4.81	5.22	5.48
Slope	5.26	5.45	6.39	7.28	6.73	5.17	6.55
The 2nd stilling basin	0.74	0.88	0.45	1.14	0.78	1	1.34
Downstream river channel	0.85	0.62	0.76	1.00	1.37	1.35	1.51

Table 2. Energy dissipation rate of each stage stilling basin.

Flow (m3/s)	A-A section			B-Bsection			C-C section			1R%	2R%
	Static head （m）	Vhead （m）	Total head (m)	Static head （m）	Vhead （m）	Total head（m）	Static head （m）	V. head（m）	Total head（m）		
2627	6.98	0.67	7.65	6.20	0.57	6.77	4.60	0.04	4.64	11.55	31.48
3410	7.10	0.77	7.87	6.24	0.69	6.93	5.00	0.03	5.03	11.98	27.36
4500	7.30	0.95	8.25	6.48	0.85	7.33	5.81	0.04	5.85	11.18	20.23
8000	7.70	1.41	9.11	7.20	1.16	8.36	6.00	0.09	6.09	8.26	27.14
12000	8.10	1.56	9.66	7.60	1.22	8.82	6.92	0.11	7.03	8.74	20.30
16000	8.66	2.08	10.74	8.32	1.63	9.95	7.68	0.12	7.80	7.34	21.61
19000	8.90	2.64	11.54	8.40	1.98	10.38	8.20	0.16	8.36	10.08	19.42

Note:1R and 2R represent energy dissipation rate of the first and the second stilling basin, respectively.

4.3 Optimization of reinforcement scheme

Because the first stilling basin structure is directly related to the dam safety and the second stilling basin has good energy dissipation effect by the experiment, the structure and size of the first and second stilling basin remain unchanged. The connection platform and slope section are the main parts of damage. Therefore, it is proposed to optimize the connection section between the two stilling basin to improve the energy dissipation effect.

Scheme 1: Abolish the connecting section platform (with the top elevation of 61.2m) and shorten the slope section. By changing the stilling basin layout, three stage energy dissipaters is formed. However, the test results show that there could not form hydraulic jump in the first stilling basin when the discharge capacity is above 8000m3/s because the downstream water level is not enough. Therefore, the energy dissipation layout with three stages is not adaptive.

Scheme 2: Compared with the original scheme, reserve the connecting platform (with the top elevation of 61.2m) unchanged, cancel the platform (with the top elevation of 58.3m) of the second stilling basin and change the slope between the first and second stilling basin from 1: 4 to 1:7. The test results show that it is similar to the original scheme that the water flows into the second stilling basin in the form of jet flow under small discharge. It could not form hydraulic jump in the second stilling basin.

Scheme 3: Compared with the original scheme, lengthening the length of the platform (with the top elevation of 61.2m) by 3.6m, reduce the top elevation from 61.2m to 61.0m and connect the 1: 4 slope directly with the second stilling basin floor (with the top elevation of 56.5m) by cancelling the front platform (with the top elevation of 58.3m) and the notched sill of the second stilling basin. The test results show that under all level floods, the main stream in the second stilling basin is close to the bottom of the basin and form stable hydraulic jump. This phenomenon conforms to the underflow energy dissipation rule. But the main stream in the first stilling basin could not form a stable water jump when the flow discharge is above 16000m3/s.

Scheme 4: On the basis of scheme 3, set up a new ridge at the end of the connecting platform (with the top elevation of 61.0m). After several tests of different sizes, the layout with a new ridge of 0.6m high and 0.5m wide is finally adopted. The test results show that under all level floods, stable energy dissipation hydraulic jumps both in the first and the second stilling basin are formed. The scheme 4 is one of the ideal energy dissipater layout schemes.

Scheme 5: Compared with the original scheme, lengthening the length of the platform (with the top elevation of 61.2m) by 2.0m, increase the top elevation from 61.2m to 61.4m, and connect the 1: 4 slope directly with the second stilling basin floor (with the top elevation of 56.5m) by cancelling the front platform (with the top elevation of 58.3m) and the notched sill of the second stilling basin. The results show that under all level floods stable energy dissipation hydraulic jumps both in the first and the second stilling basin are formed with a good underflow energy dissipation effect, as shown in Figure 3. The scheme is also one of the ideal energy dissipater layout schemes.
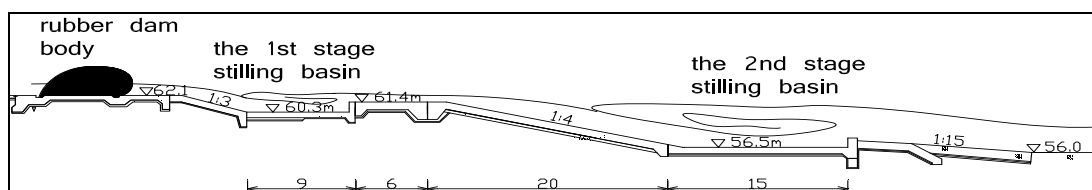

Figure 3. Section of the fifth optimized reinforcement scheme (unit: m).

Above all, the connection platform (with the top elevation of 61.2m) directly affects the flow pattern in the first stilling basin. The hydraulic jump could not form when the platform height is decreased. Scheme 4 and Scheme 5 test results show that when a new ridge is set up or the length of the platform is lengthened the stable hydraulic jump is formed in the first stilling basin.

The front platform (with the top elevation of 58.3m) and the notched sill of the second stilling basin directly influence the flow pattern in the second stilling basin. As to the original scheme, scheme 1 and scheme 2 which the platform and the notched sill is retained, the stable hydraulic jump in the second stilling basin under small flow discharge is not formed. As to the scheme 4 and scheme 5 the platform and the notched sill are removed, the stable energy dissipation hydraulic jump in the second stilling basin is formed. The mainstream flow is close to the bottom of the stilling basin when the water flowing to the second stilling basin. This phenomenon is accord with the bottom flow energy dissipation rule.

Therefore, the scheme 4 and scheme 5 are proposed as optimized reinforcement layout. In addition, it is suggested to strengthen the connection platform and slope section and perfect the sealing and draining facilities. At the same time, aiming to long-term safe operation of the project, it is important to enhance observation the phenomenon of downstream riverbed incision and pay special attention to possible cracks, sealing and draining problems during the actual operation.

The scheme 5 is finally adopted. After the reinforcement in 2010, there is no longer any damage even the discharge is beyond 8000m3/s, indicating that the optimized reinforcement layout is correct. The energy dissipater remains fine and achieves the desired purpose.

5   CONTROL OF DOWNSTREAM RIVERBED INCISION

The downstream riverbed consists of gravel with the median diameter about 1.3mm. It is prone to erosion and incision in actual conditions. With the continuous decline of the downstream water level, there is obvious hydraulic drop downstream the second stilling basin, or the water flows into the downstream river channel in the form of jet flow without forming a hydraulic jump in the second stilling basin, resulting in serious riverbed incision and endanger the safety of energy dissipaters.

As to the recommended energy dissipater structure, the critical downstream water level is observed, as shown in Table 3. For example 8000m3/s, when the downstream water level declines to a certain level, there is no longer hydraulic jump in the second stilling basin, and the water flows into the downstream river in the form of jet flow, as shown in Figure 4. It would cause serious erosion and endanger the safety of downstream energy dissipaters. The allowable value of the downstream riverbed incision increases with the increase of the discharge, as shown in Table 3. As to the recommended energy dissipater, the limited riverbed incision depth of the downstream river cannot exceed 1.0m in order to meet the requirements of downstream water level at all level floods.

In addition, the movable riverbed test shows that laying gravel with the diameter size of 13mm in downstream riverbed could protect the downstream riverbed. There have no obvious scouring under the flow below 4500m^3/s, and the riverbed incision decreases significantly when the discharge is beyond 8000m^3/s. Therefore, it is proposed that the waste concrete stone be used to protect the downstream riverbed for Xiaobudong rubber dam.
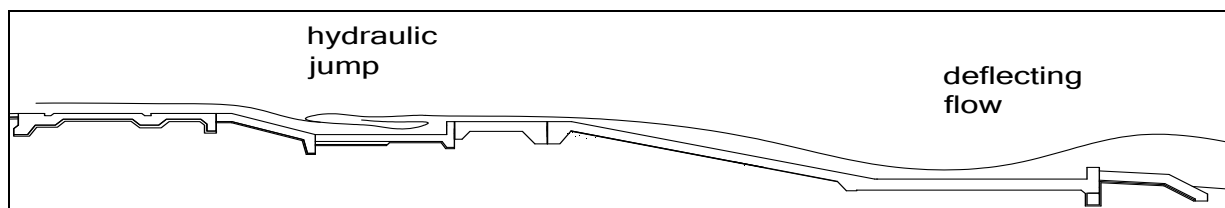
Figure 4. Water flows into the downstream channel in the form of jet flow.

Table 3. Downstream limited water level and limit riverbed incision depth.

Flow(m^3/s)	2627	3410	4500	8000	12000	16000	19000
Normal water level(m)	60.05	60.21	60.94	61.69	62.68	63.51	64.04
Downstream critical water level (m)	58.98	59.17	59.57	60.46	60.82	61.47	62.02
Depth of riverbed incision(m)	1.07	1.02	1.17	1.23	1.86	2.04	2.02

6 CONCLUSIONS

Riverbed incision in the downstream river of dam would induce water level fall and fluctuation. As a result, the original energy dissipater cannot be suitable for energy dissipation and liable to be destroyed. In this study, the two-stage stilling basins of Xiaobudong rubber dam project are analyzed and optimized. It is concluded that (1) The connecting platform and the slope section between the two stilling basins are the supercritical flow areas and the key part need reinforcement. It is proposed that shall be strengthened the intensity of reinforcement and ensure the sealing and drainage facilities. (2) When the elevation of the platform downstream the first stilling basin is reduced dramatically, there cannot form hydraulic jump in the first stilling basin, while a new ridge is set up or the length of the platform is lengthened, a stable hydraulic jump in the first stilling basin is formed. (3) In case of small discharge, under the influence of the front platform and the notched sill of the second stilling basin, the water flow into the second stilling basin in the form of jet flow and cannot produce stable water jump. When the platform and the notched sill are removed, the mainstream flows close to the bottom and forms a stable water jump in the second stilling basin. This phenomenon is accord with the bottom flow energy dissipation rule. (4) As to the recommended energy dissipater of Xiaobudong rubber dam project, the limited riverbed incision depth of the downstream river shall not exceed 1.0m. It is proposed that the waste concrete stone be used to protect the downstream riverbed.

REFERENCES

Bian, J. (2007). Discussion on the Second Class Dispersion and Diffusion Works in Hesheng Rubber Dam Project Reinforced. *Jilin Water Resources*, 9, 20-22.

Chen, J. & Huang, W. (2005). Impact of Multi-Reservoirs on the Yangtze River Water and Sediment Process and Environment. *China Institute of Water Resources academic proceedings* - Theory and practice for the construction of water-saving society.

Chen, Z.Y., Huang, Z.M. & Zhong, Y.M. (2009). Study on the Hydraulic Model Test of Reinforcement Engineering of Guantangchaoan Bridge and Gate Project. *Guangdong Water Resources and Hydropower*, 5, 15-16.

Hu, M. (2013). Research and Test for Energy Dissipation form of Low Head, Large-Unite Discharge Flood Discharging. *Journal of Hydroelectric Engineering*, 5.

Huang, Z.C., Zhuo, Y., Luo, A. & Zhong, Y.M. (2009). Research on Energy Dissipation of Several Barrages with Downstream River Water-Level Degradating and their Rebuilding. *China Rural Water and Hydropower*, 8, 83-86, 90.

Huang, Z.M., Chen, Z.Y., Zhong, Y.M. & He, X.H. (2009). Study on the Energy Dissipation Problems and Transformation of Liuxi River Lixi's Sluice. *Guangdong Water Resources and Hydropower*, 3, 3-6.

Huang, Z.M., Chen, Z.Y., Zhu, H.H. & Zhong, Y.M. (2013). Layout of Primary and Secondary Stilling Basin Downstream Low Head Barrage. *Advances in Science and Technology of Water Resources*, 6, 33-36.

Huang, Z.M., Zhong, Y.M. & He, X.H. (2012). Research on Flood Discharging Operation of Huizhou Dongjiang Water-Control Project Dam. *Design of Water Resources & Hydroelectric Engineering*, 31(1), 47-50.

Mao, Y. & Huang, C.A. (2004). Experimental Study on Effect of Sand Mining on Riverbed Deformation. *Journal of Hydraulic Engineering*, 5, 1-7.

Nai, R.S. (2007). The Sluice Energy Dissipation Structure Reconstruction Design in Chaozhou Water Supply Complex. *Jilin Water Resources*, 11, 3-7.

Zhu, S.H., Han, J., Yue, Y.C. & Lin, H.X. (2010). Dongjiang River Incision Impact on the Water Level of Huangdaxian River Reach. *Pearl River*, 31(1), 17-19. (In Chinese)

Zhang, C.L., Huang, Z.M. & Jiang, W. (2005). Dam Downstream River Bed Scour Analysis and Research of Qingxi Hydropower Station. *Guangdong Water Resources and Hydropower*, 3, 1-4.

EFFECT OF DOWNSTREAM REVET TO THE EMBANKMENT ON TIME OF FAILURE DUE TO OVERTOPPING

NURUDEEN TOMIWA AMO[1], JUNJI YAGISAWA[2] & NORIO TANAKA[3]

[1,2,3] Graduate School of Science and Engineering, Saitama University
[2,3] International Institute for Resilient Society, Saitama University
tanaka01@mail.saitama-u.ac.jp

ABSTRACT

Embankment, levee or dyke is one of the oldest and widely used defense structures against river flooding across the globe. Meanwhile this research work looks into the collapse phenomenon in river embankment because of the overtopping events, it has been well known that severe erosion occurs at top of embankment slope. To prevent that severe erosion, it is important to cover the top of embankment slope by some materials. However, it has not been revealed what is a suitable revet length for delaying the time of embankment failure. Therefore, objective of this study is to elucidate the effect of revet length on time of embankment failure by conducting flume experiments. A trapezoidal shaped embankment model (silica sand: d_{50}=0.3mm) is constructed (by compaction) perpendicular to the river flow in a glass-sided flume with a constant flow discharge upon overtopping of embankment. An acrylic plate (as pavement model) is set at embankment top and revet models with different length are connected to this acrylic plate in each experimental case. Some parameters considered to describe time of failure are overtopping permeability, length of revet on the downstream slope. Phreatic surface (zero pore pressure head) is observed in Case 2(embankment with 4cm revet) but it rises in Case 3(6cm revet). Also strong matric suction is observed in Case 2 with the cluster of pore pressure head at the top of downstream slope and embankment layer interface meanwhile Case 3 shows increasingly positive pore pressure (sharp drop in shear strength) at the downstream top of the slope. Therefore, Case 2 highlights the zone of peak shear strength attainable before reduction. In this embankment model, Case 0 (no revet) and Case 3(6cm revet) saw rapid erosion 60 seconds after overtopping. These two phenomenon should be avoided to prolong embankment lifespan.

Keyword: Downstream revet; time of failure, river embankment, over topping permeability, gradient permeability.

1   INTRODUCTION

Embankment, levee or dyke is one of the oldest and widely used defense structures against river flooding across the globe. In the context of this research work, we refer to embankment as a river embankment (compacted silica sand) built perpendicularly to a river. Embankment failure is considered to be a situation where flood water passes over or through an embankment in an increasingly uncontrolled manner due to failure of the embankment structure (Morris et. al., 2009) leading to a hole in the dyke. Embankment failure causes inundation of coastal houses and infrastructures and in record time been a major concern over generations. Yearly, devastating flood events are being recorded causing high financial deficit and human losses. To reduce this unpleasant aftermath, many European countries embanked their rivers. However, events of river embankment failure still occurs in France such as Arno river embankment. The same applies to Japan where many of their rivers are also embanked. This flood defense system helps make available extensive portion of alluvial landscape for human settlement and other activities thus reducing the size of flood prone areas. The occurrence of embankment breach is not limited to Japan alone as the road embankment in the southeastern Delta, California, USA collapsed (See Photo 1) below.

Photo 1. Shows the embankment breach due to overtopping and seepage along Jones Tract in California (June, 2004).

The lack of communication on the part of the group maintaining the embankment structure and increased flood events are some of the reason for its collapse (Robert Bea, 2010).

It has been well known during overtopping of embankments that severe erosion occurs at top of embankment slope. As such, it is important to cover the top of embankment slope by some material like acrylic plate. However, it has not been revealed suitable revet length for delaying time of embankment failure.

Several researchers and authors like Tsujimoto et al. (2006), Powledge et.al. (1989), Tingsanchali et. al. (2003) Pickert et.al. (2011), Fujita et. al. (1987) and Islam et. al. (1994) have one thing in common. Their research field centers around scour mechanisms and foundation levee, breach processes, combination of levee breach process and side overflow, sedimentation and overflow area in the flume (Bhattarai et. al. (2015)). In all their research, the time of failure was often reported with great uncertainty.

Since many events of embankment breach was as a result of overtopping flow therefore we focused on studying the seepage process along the downstream slope when protected using a revet model solely to establish the suitable revet length to delaying embankment time of failure.

2   EXPERIMENTAL SET-UP AND METHOD

2.1   River embankment model

(a) A trapezoidal shaped embankment model

(b) A schematic diagram of embankment and revet models
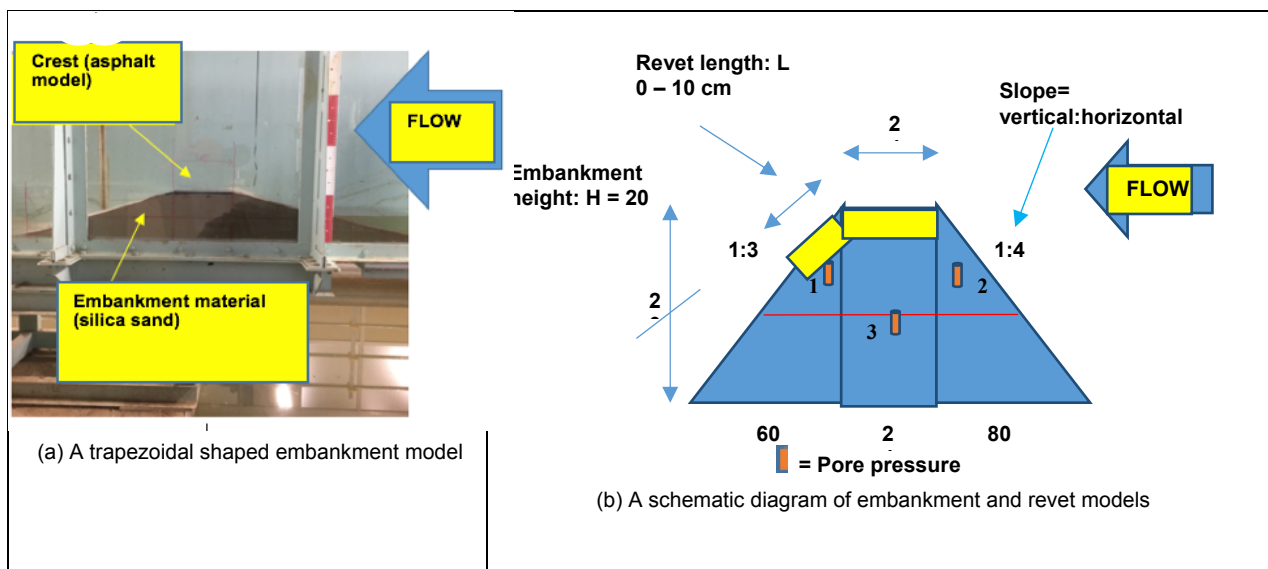
Figure 1. Experimental condition.

The breach test was performed in glass sided flume (see Figure 1) as a river and the embankment was placed perpendicular to the river flow and having transparent Poly Vinyl Chloride (PVC) wall at both side of the embankment.

The schematic diagram of the embankment model is shown in Figure 1. The maximum discharge provided was 0.17 liters/s. The horizontal channel is 0.5 m wide, 1.15m high and 6.5 m long while the embankment opening at the side of the channel is 0.5 m at a distance of 1.6 m from the upstream.

The intake is equipped with a flow straightener and a pump to generate undisturbed flow from the water tank (and a plate with holes used to prevent a turbulent flow) situated few meters away. The tank supplies water continuously from the upstream end. The eroded sediment and the resulting water flow were collected by an underground reservoir at the tail end of the flume. Three pore pressure transducers were fixed at the set positions to monitor the pore pressure over the whole process of the experiment. Table 2 shows the coordinates of all the pore pressure transducers.

The side and aerial view of experimental set-up is as shown in Figure 2 below. The parameters investigated include embankment height H =0.2m, downstream revet length, L_0 =0m, L_1 =0.02m, L_2 =0.04m, L_3 =0.06, L_4 =0.08m and length/height ratio: 0, 0.1, 0.2,0.3 ,0.4 respectively as shown in Table 1. In addition, embankment crest width, b=0.5m, embankment length L=1.64m and flume discharge, Q= 0.17 liters/s. The upstream slope of embankment is S_u =1:4 (V:H) and downstream slope is S_d=1:3 (V:H). The (1.64 x 0.5) m^2 river embankment model was constructed near the center of the flume.

| (a) Side view of experimental model | (b) Aerial view of experimental model |
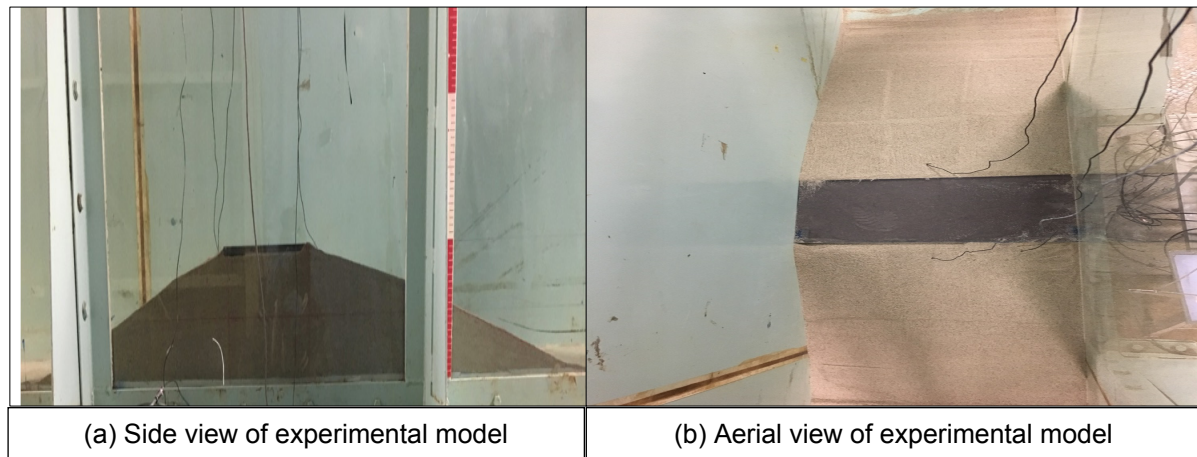
Figure 2. A view of experimental model with installed pore pressure transducers.

Table 1. Experimental condition and overbed time of failure.

Case	L(cm)	H(cm)	L/H
0	0	20	0
1	2	20	0.1
2	4	20	0.2
3	6	20	0.3
4	8	20	0.4

3   EXPERIMENTAL PROCEDURE

All experiments were conducted at the Hydraulic and Environmental laboratory, Saitama University, Saitama, Japan using a constant flow discharge (1.5cm/1min) in a flume Q_{in} referred to as the inflow to obtain the simple boundary condition. The procedures include:

I.   Preparation of materials

The embankment material (silica sand) was provided at 0% moisture content by weight, three pore pressure transducers installed and a Sony HD Camera provided.

II.   Fixing of pore pressure transducers and compaction as shown in Figure 2

The first layer of the embankment (10cm) was first thoroughly mixed and then compacted with the aid of a wooden-hand compactor and transducer 3 was embedded in it. Then, the other two transducers were fixed in designated holes and a certain amount of soil was added into the holes and compacted again to ensure close contact with the surrounding soil. The influence of the transducers was ignored as its scale to the overall embankment is very small.

III.   Installation of acrylic plate and revet model.

Acrylic plate with revet lengths of 0, 2, 4, 6, 8 cm were set up at the downstream slope of the embankment for every case 0-4.

IV.   Discharge of air from the catheters of pore pressure transducers

Despite the pore pressure transducers being calibrated and air trapped in the catheters will influence the sensitivity of pore pressure transducers, discharge of air from the catheters of these transducers are difficult in this situation. As such, the air in the unsaturated zone dissipate during overtopping and results at this time is reviewed.

V.   Calibration of the pore pressure transducers and monitoring of the preset line of seepage field in the embankment.

Each pore pressure transducer was calibrated by comparing the data from the pore pressure transducers with those stated in the manufacturer's manual.

VI.   Steady rise in the upstream water level

Before water was fed into the flume from the tank, there was neither water at the upstream nor the downstream end of the embankment model. The water rose steadily to 20 cm in 13 min 20s in every case. Water was added and regulated to a steady and uniform state before overtopping the embankment. In the process, the water flow overtopped the embankment crest and the pattern of the gradient permeability was studied while the downstream gate was left open.

VII.   Allowing the upstream water level to flow over the embankment and the water level rise kept steady until a clear failure is observed.

The pore pressures at the preset positions were recorded with the aid of pore pressure transducers and a data acquisition system. Each test reading (time of failure) was taken once a visible

breach was observed both at the upstream, downstream points and underlying soil (silica sand). Observation of the experiment continued until the entire embankment material (silica sand) was washed out and the flow of water reached its equilibrium state.

This experiment is therefore limited to the dynamic change in lateral widening processes, the velocity of overtopping water and the overtop permeability. To represent an actual embankment layout, the hydraulic model consisted of a main channel symbolizing an actual river perpendicular to the upstream slope of the embankment.

Furthermore, the basic upstream boundary condition was obtained by selecting the constant steady inflow scenario. In the prototype, an embankment was overtopped once the river water level exceeded its crest elevation. The Sony HD Camera was placed such that it could record the process of overtop seepage of water in the river embankment. It was also used to record the video on the downstream infiltration of overtop water while the breach discharge, sediment discharge, seepage movement (both gradient and overtop) permeability were analyzed using the recorded images of the optical instrument (Sony camera). The movement of seepage (upstream and overtop infiltration) was recorded to analyze the role of the seepage gradient in the breach characteristics and in addition to help in performing numerical simulation in the future.
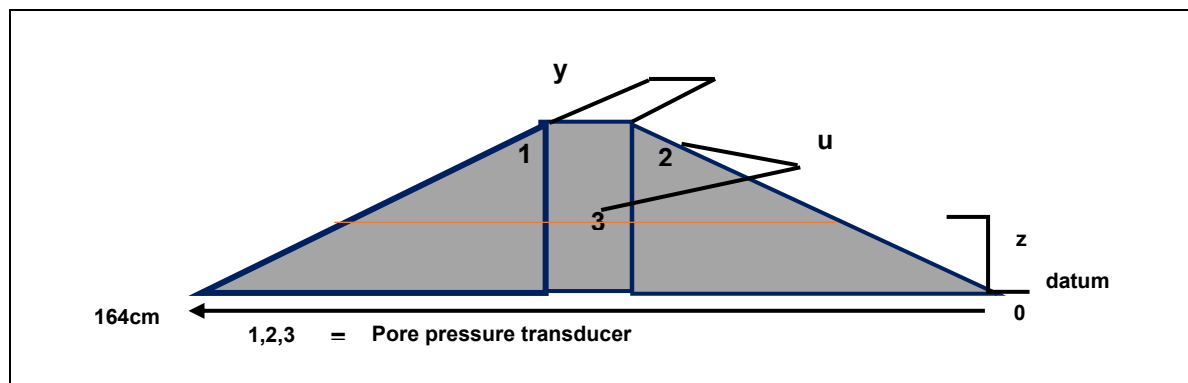
Figure 3. Shows the experimental model with installed pore pressure transducers.

Table 2. Shows the coordinates of pore pressure transducers in embankment.

Points	x (m)	y (m)	z (m)
1	1.06	0.25	0.18
2	0.92	0.25	0.18
3	0.78	0.25	0.10

4 RESULTS AND DISCUSSIONS

4.1 Variation in pore pressure head and development of phreatic surface

Table 3 shows the distribution of pore pressure head in the embankment with varying revet length. The development of phreatic surface (zero pore pressure head) in Table 3 is outlined in case 2 for both transducers 1 and 3. It can be seen that the distribution of the pore pressure head in the embankment in case 2 is very different from the way it was before and proceeding cases 3 and 4.

In Table 3 and 4 - case 2, the phreatic surface and gradient permeability for both transducers 1 and 3 can be observed and seen to be near saturation (60 seconds after overtopping) at the upper part of downstream slope and the shear strength gradually reducing but in the proceeding case 3, an increasing positive pore pressure head was observed at the top downstream slope throughout the experimental process while a waterfall and a saturated zone was also observed (after 60s of overtopping embankment) in Table 4, case 3 depicting rapid erosion. In Table 3 case 4, the phreatic zone below which is a saturated soil can be seen to be fully saturated, risen but steady throughout the experimental process but was quite visible in case 2.

Table 3. Variation in the distribution of pore pressure head.

A CHART SHOWING THE DISTRIBUTION OF PORE PRESSURE HEAD FOR VARYING REVET LENGTH.			
CASE	**LENGTH OF REVET**	**L/H**	
0	0	0	
1	2	0.1	
2	4	0.2	
3	6	0.3	
4	8	0.4	

H-CH1= pore pressure head at channel 1 (transducer 1),

H-CH2= pore pressure head at channel 2 (transducer 2)

H-CH2= pore pressure head at channel 3 (transducer 3)
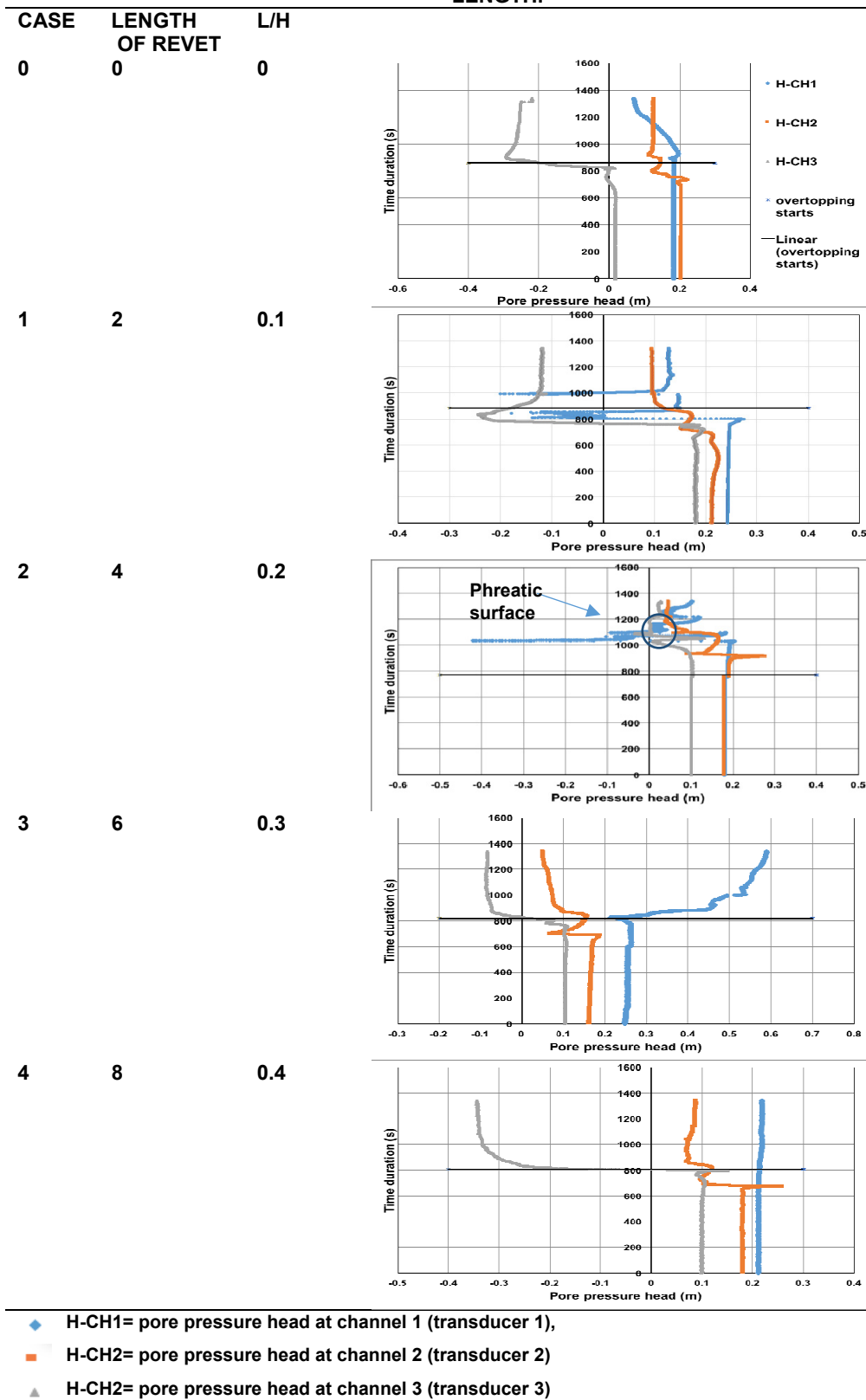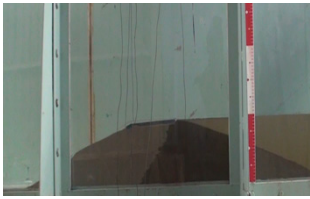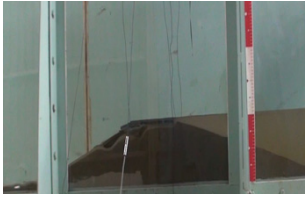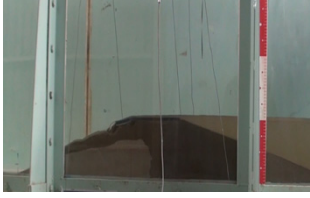
Table 4. The gradient permeability for 60s, 90s after overtopping of embankment.

	Before Overtopping	After 60 seconds	After 90 seconds
Case 0 (no revet)			
Case 1 (2cm revet)			
Case 2 (4cm revet)			
Case 3 (6cm revet)			
Case 4 (8cm revet)			

The initial time of failure is defined as the period when a visible breach is established between the revet and embankment from the time overtopping starts while the final time of failure is defined as the period when a visible breach is established between the pavement (asphalt model) and the embankment on the upstream from the time overtopping starts. The time of failure of the embankment can be attributed to the following factors:

I. Reduction in shear strength.

It is well known that dry sand in the test has a relatively minimal tensile strength. Therefore, as overtopping begins, the degree of saturation of the embankment progressively increases. At first, the tensile strength increases to a maximum depending on the particle size and porosity followed by a reduction to zero near full saturation (Lu et al., 2009).

In this embankment model, the maximum shear strength was attained for a 4cm revet length. This illustrates that as water rises up an embankment, water percolates into soil pores and the cohesion forces holding soil particles weakens and becomes loose, matric suction dissipates gradually while it gets more saturated. In reference to Table 3, case 2, phreatic surface appears; the point where pore pressure equals zero below which is expected a saturated zone of soil mass and Table 4, next case 3

after 60s of overtopping further highlights the emergence of a small waterfall creating a strong erosion power, thus reducing the ability of the embankment to resist seepage failure thus reducing its time of failure.
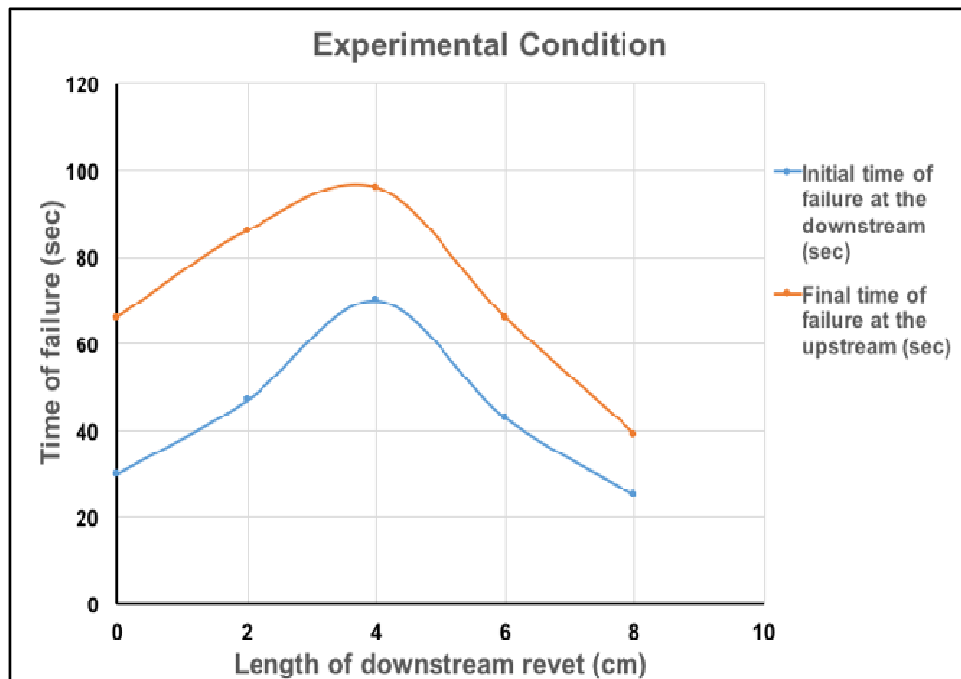
In this embankment model, the maximum shear strength was attained for a 4cm revet length. This illustrates that as water rises up an embankment, water percolates into soil pores and the cohesion forces holding soil particles weakens and becomes loose, matric suction dissipates gradually while it gets more saturated. In reference to Table 3, case 2, phreatic surface appears; the point where pore pressure equals zero below which is expected a saturated zone of soil mass and Table 4, next case 3 after 60s of overtopping further highlights the emergence of a small waterfall creating a strong erosion power, thus reducing the ability of the embankment to resist seepage failure thus reducing its time of failure.

Figure 4. The chart showing time of failure of embankment against varying length of downstream revet

II.   Distribution of pore pressure head

For Table 3 illustrating the pore pressure head distribution, case 2 can be seen to have a cluster of weak positive pore pressure head (dissipating matric suction) and transducer 1 marks the phreatic zone after overtopping but case 3 shows no matric suction at the upstream slope of the embankment. So, the embankment with 4cm revet reveals the elastic limit strength for the embankment.

5 CONCLUSION

This embankment model was constructed largely to elucidate the effect of varying revet length on time of embankment failure by conducting flume experiments. First, the rapid erosion observed visibly on the embankment slope in Figure 5, cases 0 and 3 denote that these two zones if protected from overtopped permeability could prolong the lifespan of embankment. Also, we proved that a dry sand in a test has a minimum tensile strength; "when overtopping begins, the tensile strength increases to a maximum depending on the particle size and porosity followed to a reduction to zero near full saturation' (Lu et al., 2009). Being like that, our embankment model shows that case 2 (4cm revet) draws out the zone of maximum shear strength before its reduction along the downstream slope and also highlights a zone of phreatic surface (zero pore pressure head) while at the same time points out the peak matric suction before it starts to dissipate. Perhaps it is advisable to keep the whole embankment slope plastered (more research is needed). Meanwhile, the experimental results are influenced by the degree of compaction of the embankment, type of construction materials, experimental procedures and uniformity in water rise across all cases.

REFERENCES

Bhattarai, P.K., Nakagawa, H., Kawaike, K. & Zhang, H. (2014). Experimental Study on River Dyke Breach Characteristics Due to Overtopping Flow. *Journal of Japanese Society of Natural Disaster Science*, 33, 65-74.

Fredlund, D.G. & H. Rahardjo, T. Ng. (1993), Effect of Pore-Air and Negative Pore-Water Pressures on Stability at The End of Construction.

Fujita, Y. & Tamura, T. (1987). Enlargement of Breaches in Flood Levee on Alluvial plain. *Journal of Natural Disaster Science,* 9(1), 37-60.

Hilf, J. (1948). Estimating Construction Pore Pressures in Rolled Earth Dams. *Proceedings, 2nd International Conference on soil mechanics and Foundation Engineering, Rotterdam, The Netherlands,* 3, 234-240.

Islam, M.Z., Okubo, K., Muramoto, Y. & Morikawa, H. (1994). Experimental Study on Sedimentation over the Flood Plain Due To River Embankment Failure. *Annual of Disaster Prevention Research Institute, Kyoto University,* 44(2), 69-92.

Lu, Y., Chiew, Y.M. & Cheng, N.S. (2008). Review of Seepage Effects on Turbulent Open-Channel Flow and Sediment Entrainment. *Journal of Hydraulic Research,* 46(4), 476-488.

Morris, M.W., Hassan, M., Kortenhaus, A. & Visser, P.J. (2009). *"Breaching processes, a state of the art review".* FLOODSITE Report T06-06-03.

Nakagawa, H., Mizutani, H., Kawaike, K., Zhang, H., Yoden, Y. & Shrestha B. (2013). *"Numerical Modelling of Erosion of Unsaturated River Embankment due to overtopping Flow"*. Advances in River Sediment Research, Taylor and Francis Group, London.

Nakagawa, H., Utsumi, T., Kawaike, K., Baba, Y. & Yhang, H. (2012). "Erosion of unsaturated embankment due to overtopping water". *Japan Society of Civil Engineers Series B1. Hydraulic Engineering*, 67(4), 1-4.

Pickert, G., Weitbrecht, V. & Bieberstein, A. (2011). Breaching of Overtopped River Embankments Controlled By Apparent Cohesion. *Journal of Hydraulic Research,* 49(2), 143-156.

Powledge, G.R., Ralston, D.C., Miller, P., Chen, Y.H., Cloppner, P.E. & Temple, D.M. (1989). Mechanics of Overflow Erosion on Embankments I: Research activities. *Journal of Hydraulic Engineering,* 115(8), 1040-1055.

Robert, B. (2010). 'Comment on Embankment Breach Due To Overtopping and Seepage Along Jones Tract in California'. *Retrieved from http://berkeley.edu/news/media/release.*

Schmocker, L. (2011). "Hydraulics of Dyke Breaching", *PhD Dissertation.* VAW-Mitteilung 218, R.M. Boes, ed, ETH Zurich, Zurich.

Skempton, A.W. (1956). The Pore Pressure Coefficients A and B. *Geotechnique*, 4, 143-147.

Tingsanchali, T. & Chinnarasri, C. (2001). "Numerical Model of Dam Failure Due to Overtopping". *Hydrological Science Journal,* 46(I), 113-130.

Xie, L., Duan, X. & Yang, C. (2012). Study on Physical Model Experiment of Dam's Seepage Stability Base on Coastal Sand. *Procedia Engineering,* 28, 534-541.

Luo, Y., Zhang, C., Nie, M., Zhan, M. & Sheng, J. (2014*).* An Experimental study on embankment failure induced by prolonged immersion in flood water. *Water science and Engineering*, 9(1), 81-86.

SUBWAY INUNDATION BY FLUVIAL FLOODING AND EVACUATION FROM SUBWAY STATIONS

MITSUHIRO TERADA[1], TAISUKE ISHIGAKI[2], TAIRA OZAKI[3], YASUYUKI BABA[4] & KEIICHI TODA[5]

[1] Section Head of Engineering, Original Engineering Consultants,
2-2-7, Kawaramachi, Chuo-ku Osaka-shi, Osaka, 541-0048, Japan
terada-a1314@oecsolution.co.jp
[2, 3] Faculty of Environmental and Urban Engineering, Kansai University,
3-3-35 Yamate-cho, Suita-shi,Osaka, 564-8680, Japan
ishigaki@kansai-u.ac.jp; ozaki_t@kansai-u.ac.jp
[4] Disaster Prevention Research Institute, Kyoto University,
2500-106 Katata, Shirahama, Nishimuro, Wakayama, 649-2201, Japan
baba.yasuyuki.7z@kyoto-u.ac.jp
[5] Graduate School of Engineering, Kyoto University,
Kyoto-Daigaku-Katsura, Nishikyo-ku, Kyoto 615-8540, Japan
toda.keiichi.4z@kyoto-u.ac.jp

ABSTRACT

Mega cities in Japan, for instance Tokyo, Nagoya or Osaka, are susceptible to floods, because they are located in lowlands which are below flood water level of rivers. These areas are prone to floods caused by rainwater, river-water and sea-water. More than 640 subway stations and 78 underground malls are located in Japan. And so many underground parking, underpasses and basements are also in these cities. Underground inundation has been investigated in the case of pluvial, fluvial, tsunami and storm surge flooding in Osaka, Japan by authors. In a fluvial flooding case, the flood water covers almost all area and 42 percent of total amount of overtopping flood water intrudes into underground spaces such as underground shopping mall, subway stations and underground parking areas. This intruded flood water flows through subway tunnels, however, spreading process has been investigated only in the pluvial flooding case before by authors. In this paper, subway inundation in this study area is investigated by using a numerical model including underground mall, subway stations and ten subway lines. From calculation results of inundation by fluvial flooding, it is found that subway inundation quickly spreads through subway tunnels. Subway inundation spreads through subway lines and stations located in the area, where ground level inundation has not occurred, are also inundated or filled up. At some stations, the flood water spills out to the ground. In this case, people on platform should evacuate until flood water recedes. The critical condition of safe evacuation from inundated underground spaces has been investigated by the authors and the criteria of safe evacuation has been pointed out by authors. By using the criteria and calculation results, the lead time for safe evacuation is also investigated here and the result shows that people on the platform should evacuate as soon as possible.

Keywords: Urban flood; subway inundation; fluvial flood; numerical model; evacuation.

1 INTRODUCTION

In Japan, torrential rainfalls over 50 mm/hr are observed frequently in recent years. These heavy rainfalls induced subway inundations in 1993, 1999, 2000, 2003, 2012 and 2013. These events happened in Tokyo, Fukuoka, Nagoya, Fukuoka, Osaka and Kyoto, respectively. Pluvial and fluvial floods induced the disasters and these cities are vulnerable to another kind of floods by storm surge or tsunami, because Japanese cities have low-lying areas where the ground level is lower than sea level. As many cities have underground spaces such as subways, underground shopping malls, underpasses and basements, they have been additionally threatened by such underground inundations. It is needed to study underground inundation to prevent or reduce these flood disasters.

To reduce such flood damage, water-related disasters of pluvial, fluvial, storm surge and tsunami flooding have been investigated in recent years. Studies on underground inundation have been started by Takahashi et al. (1990). They made a 2D shallow flow model for simulating underground inundation and verified the model by using experimental data of hydraulic model tests. After then, underground inundation were investigated by experimental and numerical methods (Toda et al., 2004, 2006, 2009; Sekine et al., 2009; Ishigaki et al. 2009, 2010, 2011, 2013, 2016). In addition, subway inundations have also investigated by Okabe et al. (2016), Takeda et al. (2016) and Murase et al. (2016). Takeda et al. investigated the inundation by fluvial flooding in Nagoya and Okabe et al. dealt it by pluvial flooding in Osaka. In this paper, subway inundation by fluvial flooding and evacuation from subway stations are discussed by using the results of calculation in the fully urbanized area, Osaka, Japan.

2   STUDY AREA AND NUMERICAL METHOD

2.1   Study area

Figure 1 shows the study area of 12.15km^2 in Osaka. The west and central parts are under the sea level or less than 1 m. As this study area is surrounded by two rivers on the north, east, and south sides, this area is vulnerable to fluvial floods. However, flooded water is drained only by the drainage system of which design rainfall intensity is 60 mm/hr. Drainage water is pumped up to the surrounding rivers by four pumps. Therefore, this area is vulnerable to pluvial and fluvial floods. As this area is near the bay, tsunami or storm surge also cause floods. Subway network connected to the outside of the study area and the assumed overtopping point are also shown in Figure 1. As this area is surrounded by rivers, the assumed overtopping water covers the area and some part of flooded water intrudes into subway stations and inundates subway tunnels. This means that fluvial flooding in the area makes an impact outside of the area and subway users are exposed to unexpected flood disaster.

Figure 1. Study area and subway network.

2.2   Numerical method

Ground level inundation and subway inundation are calculated by using 1D-2D urban drainage model (InfoWroks CS). Figure 2 is the model including drainage pipes, four pumping stations, underground shopping mall and subway network in this study. Ground level inundation and inflow discharge into the underground spaces were calculated. Flow in drainage pipes was calculated by 1D model of Preissman Slot model considering pipes of larger than 0.2 m diameter, and flow on roads was treated by using 2D shallow flow model with unstructured mesh. Inundation into houses was not considered. The entrances to underground space were treated as rectangular weirs and inflow discharge was calculated with discharge formula. The width and step-up height of 191 entrances were getting from field survey. Three railway tunnel mouths are also considered in the calculations. Overtopping point of fluvial flooding is shown in Figure 2. The width of overflow section is set at 145 m. Figure 2 shows also subway lines. In this model, inundation water runs through subway station and tunnels. We have set the subway tunnels as pipes and stations are treated as manholes. We were surveying the elevation of the subway station. In order to find the elevation of the platform, the number of steps from ground level to platforms and step height were counted. Ten railway lines are considered in this study. There are eight lines of Osaka Municipal Subway, Japan Railway line (J line), Hanshin Railway line (H line) passing through the study area and Osaka Municipal Subway Chuo line (C line) that is not passing through the subject area. Chuo line is possible transfer to 5 lines of Osaka Municipal Subway. In this model, underground mall and subway are connected each other. Height of the underground shopping mall's ceiling is set at the measuring results of field survey.

Extreme flood conditions in pluvial and fluvial cases used here area listed on Table 1. In fluvial flooding case, an overtopping flow from Yodo River, of which return period of design rainfall is 200 years, is treated here. The listed condition is two times of the design rainfall that is equivalent to the rainfall of Tokai flood disaster in 2000, Nagoya. Predicted data have been disclosed in the cases of fluvial flooding by Japanese governments. As buildings and houses were treated as roughness elements in the calculations, the same condition was used in the model verifications here. Inflow conditions on the table are determined to get same results as the disclosed data by the government. The inundation on the ground level and the intruding discharge into underground spaces were calculated here. Total volume of water is different in the two cases as listed on the Table 1. This comes from the difference of duration time. Pluvial condition is also listed for comparing with fluvial case.
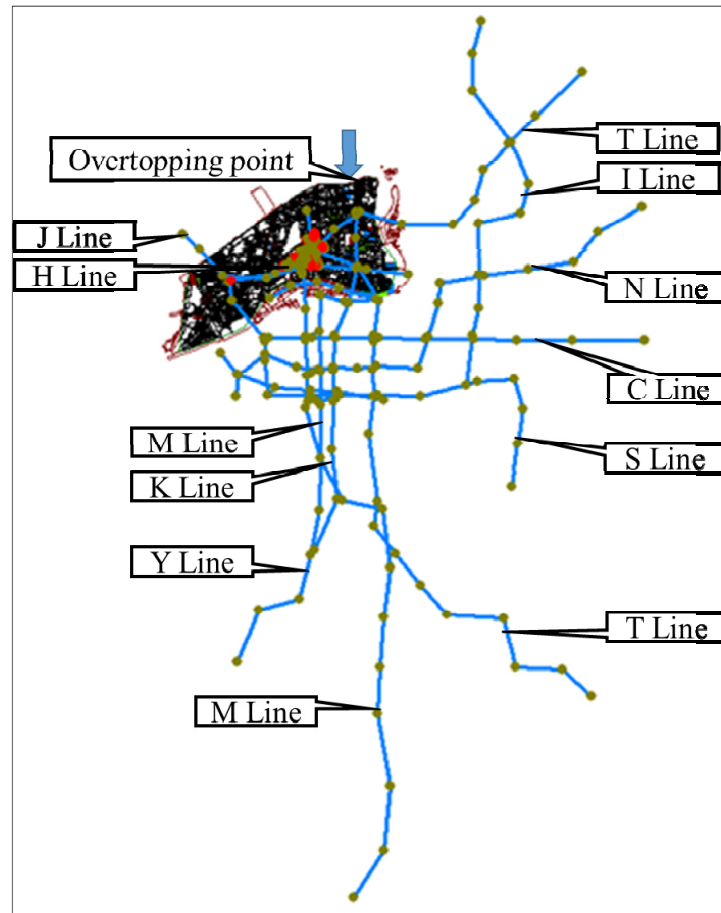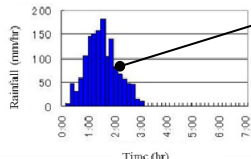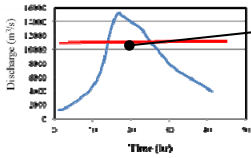
Figure 2. Subway model for Info Works CS.

Table 1. Extreme flood conditions used in this study.

Flooding	Extreme flood condition	Inflow condition of calculation	
Pluvial	Rainfall in Okazaki, Japan Date: 29.8.2008 Total: 242mm/3hr Max. per 1hr : 146.5 mm (2.5 times of design rainfall, 60mm)		
Fluvial	Discharge with two times of the design rainfall Date: 25.9.1953 (design rainfall) Total: 500mm/2days(=2 times data) (released by Japanese government)		

3 SUBWAY INUNDATION

3.1 Ground level inundation

Spreading pattern of inundation is different from each other in the fluvial and pluvial cases. Inundation starts near the overtopping point in fluvial case, however, this in pluvial case is all over the area. Figure 3 is the distribution of maximum depth in the case of fluvial flooding comparing with the result of pluvial flooding case. In the pluvial flooding, the Inundation area covers almost the whole area and the maximum depth is less than 2 m. Meanwhile, the depth in the fluvial case is over 5 m in the northeast part of this area near the overtopping point. Total amount of water and inflow rate in fluvial case is extremely large compared to pluvial case. Total inflow rate to underground spaces including subway stations, underground parking and mega mall is 13 % in pluvial flooding case and 42 % in fluvial flooding case.
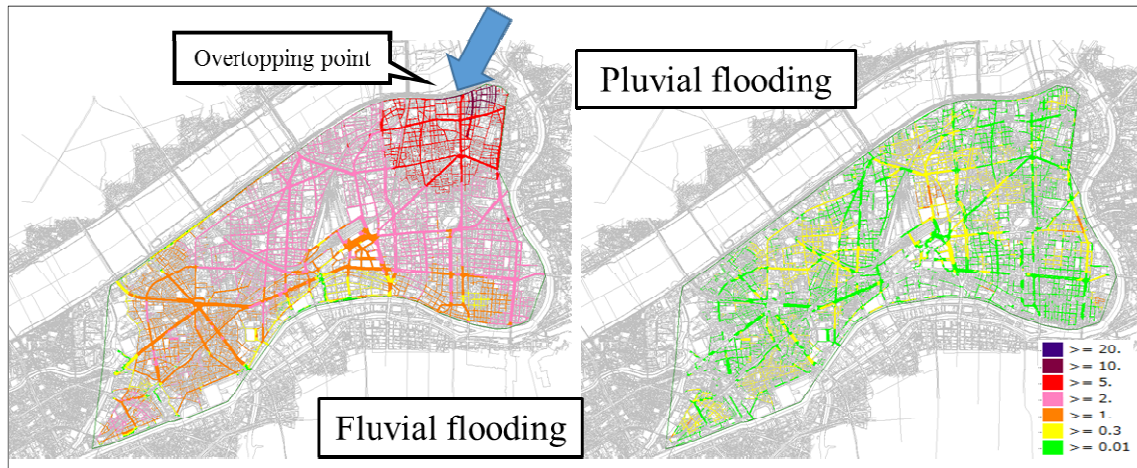
Figure 3. Maximum depth distributions of ground level inundation.

3.2 Subway tunnel inundation

Figure 4 shows spreading process of inundation through subway lines. Three threshold depth are used in this figure. 0.2 m is the depth covered a rail, in which depth people on a platform can recognize the state of subway inundation. 1.4 m is equivalent depth to platform height, before which depth people have to evacuate as soon as possible. Full depth means that subway tunnel is filled with flooded water. Flooded water on the ground intrudes into subway network through a tunnel mouth after only 15 minutes from the beginning of overtopping, and inundates subway tunnels and stations. Inundation water spreads to outside of study area through tunnels after 1 hour and the spreading of inundation peaks at 12 hours from the beginning. At the stations with red circle, total head of inundation flow reaches the ground level and spills out to the ground. This means that fluvial flooding could affect to another area where no inundation was observed.
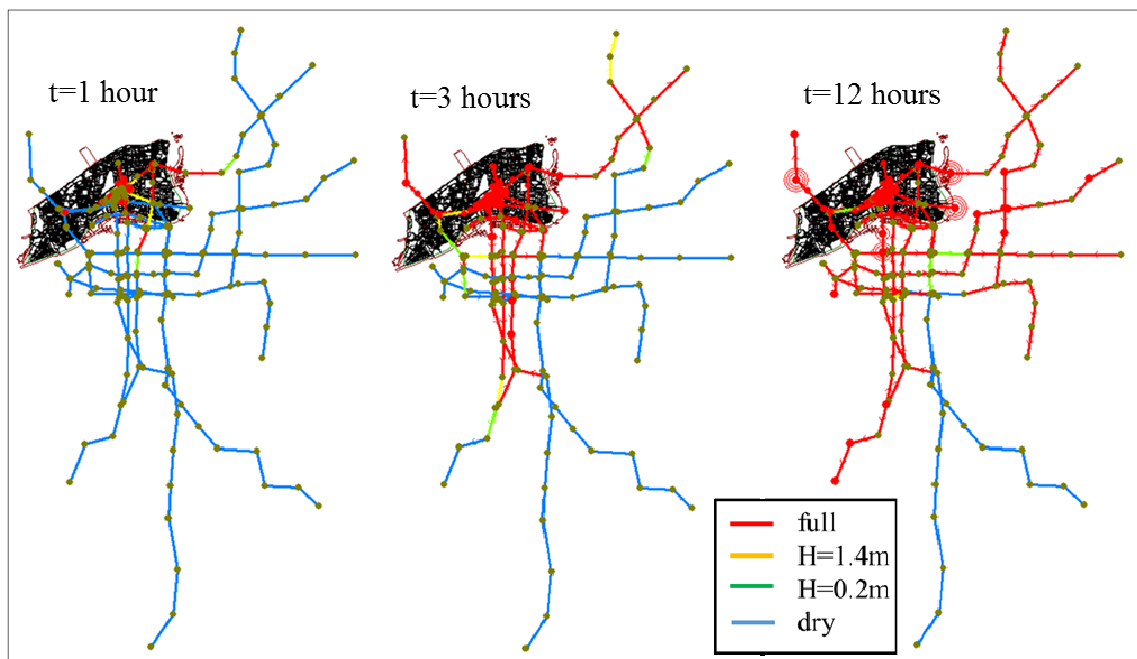
Figure 4. Spreading process of subway inundation in fluvial case.

4   EVACUATION FROM SUBWAY STATIONS

Figure 5 shows the direction of spreading the inundation through subway lines. The inundation starts from subway stations in the study area and it goes to western and southern stations. Stations outside of the study area are also inundated for the last time, because each subway lines are connected each other. Figure 6 shows the maximum inundation depth of Midousuji line (M Line). It is found that the tunnel and stations outside of the study area are submerged completely. Tunnel bottom level is not same and depends on the ground level. As this M line runs through Uemachi terrace of which height is from 15 to 30 m, the tunnel inundation stops at the highest station as shown in Figure 6. If there was not such a high level station in a subway line, inundation would go to the terminal station.
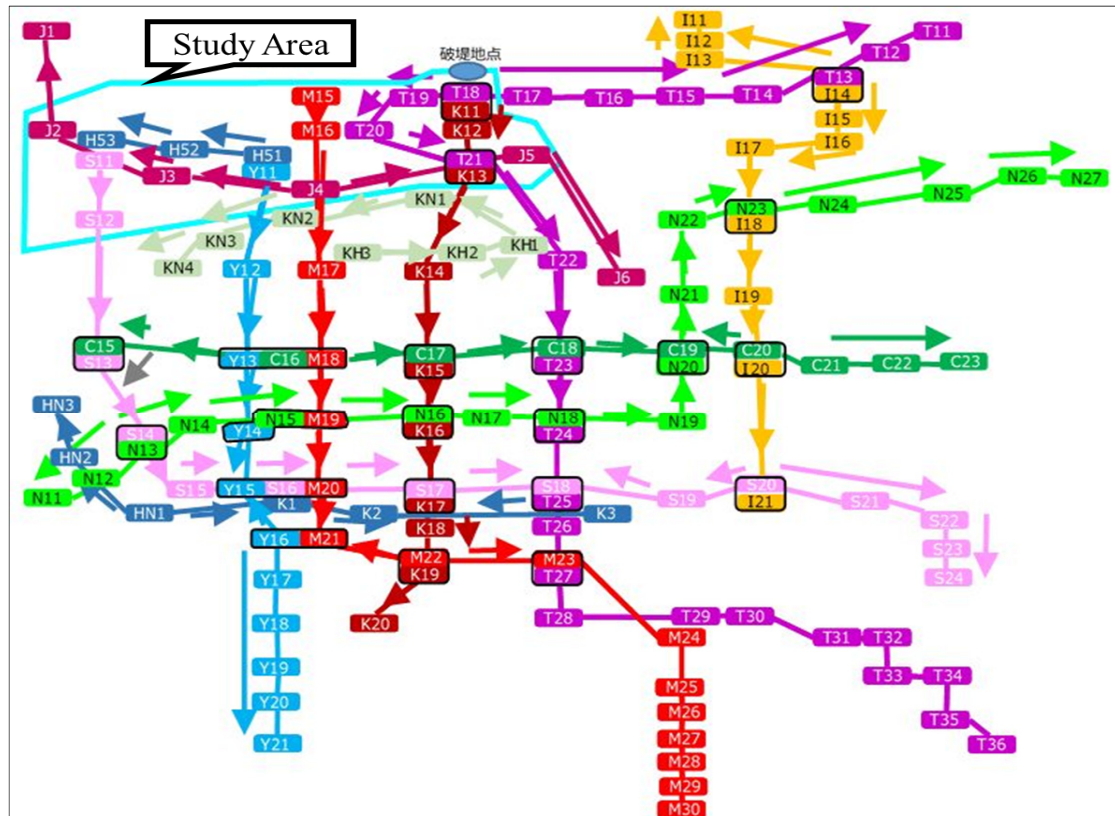
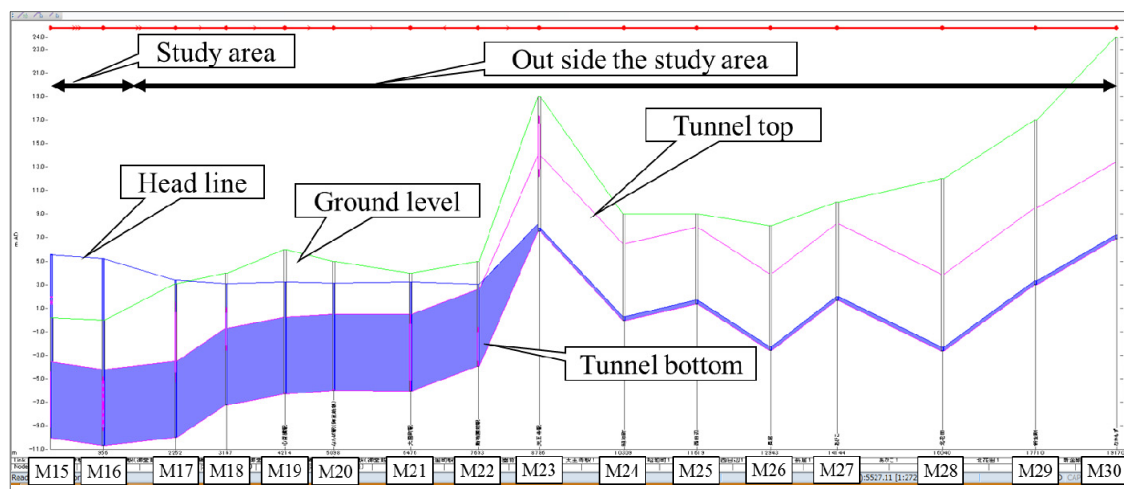**Figure 5.** Direction of inundation spreading through subway lines.

Figure 6. Maximum inundation depth of M Line.

Time-series of inundation depth at each station can be obtained from the results of calculation of subway inundation. These data indicates time of appearance of the threshold depth mentioned before. Difference in the time of depth reaching to 0.2 m and 1.4 m can be calculated as a lead time of evacuation from subway station. Table 2 shows the lead time of evacuation from outside stations of the study area along M Line. The lead time in the fluvial case is shorter than those in the pluvial case. Lead time is less than 15 minutes in the case of Q=4000 m3/s, and flood board is not effective. At the transfer station flood water comes from another line, and lead time becomes shorter. If platform would cover with flooded water, people could not walk safely because flow conditions would be over the criteria of safe evacuation (Ishigaki et al., 2010).

Table 2. Lead time for evacuation in M Line.

| Line | Station | Fluvial flooding | | | | Pluvial flooding | |
| | | $1000m^3$/s | $2000m^3$/s | $4000m^3$/s | | without flood board | with flood board |
				without flood board	with flood board		
M Line	M17	0h 15m	0h 10m	0h 05m	0h 05m	0h 50m	1h 00m
	M18	0h 10m	0h 10m	0h 05m	0h 10m	1h 55m	-
	M19	0h 10m	0h 15m	0h 05m	0h 10m	-	-
	M20	0h 20m	0h 15m	0h 05m	0h 15m	-	-
	M21	0h 20m	0h 20m	0h 15m	0h 10m	-	-
	M22	0h 35m	0h 20m	0h 00m	0h 10m	-	-
	M23	-	-	-	-	-	-

5   CONCLUSIONS

Subway inundation by fluvial flooding and evacuation from inundated stations are discussed here. Numerical model was made with subway and underground mall on the basis of field survey results. The results shows that 42% of flooded water intrudes into underground space and subway, and intruding water spreads subway network through tunnels and transfer stations. The lead time for evacuation until flooded water depth reaches to the height of platform is very short, and flood board is not effective. This results means that stakeholders of subway should announce the waring of evacuation to users of subway stations and trains as soon as possible. And they should consider another kinds of inundation in tsunami and storm surge cases.

ACKNOWLEDGMENTS

REFERENCES

Ishigaki, T., Onishi, Y., Asai, Y., Toda, K. & Shimada, H. (2009). Evacuation Criteria during Urban Flooding in Underground Space. *Proceedings of 11th ICUD,* Scotland UK. (On CD-ROM)

Ishigaki, T., Asai, Y., Nakahata, Y., Shimada, H., Baba, Y. & Toda, K. (2010). *Evacuation of Aged Persons from Inundated Underground Space.* Water Science and Technology, IWA Publishing, 62(8), 1807-1812.

Ishigaki, T., Ozaki, T., Inoue, T., Shimada, H. & Toda, K. (2011). Drainage System, Rainwater Flooding and Underground Inundation in Urban Area. *Proceeding of 12th International Conference on Urban Drainage, Porto Alegre/Brazil.* (On CD-ROM)

Ishigaki, T., Asano, N., Morikane, M., Ozaki, T. &Toda, K. (2013). Extreme Hazard of Pluvial and Tsunami Floods in a Densely Urbanized Area. *International Conference on Flood Resilience Experiences, in Asia And Europe.* (On CD-ROM)

Ishigaki, T., Kawanaka, R., Ozaki, T. & Toda, T. (2016). Vulnerability to Underground Inundation and Evacuation in Densely Urbanized Area. *Journal of Disaster Research,* 11(2), 298-305.

Murase, M., Takeda, M., Nishida, K., Nakajima, Y., Kawaike, K. & Matsuo, N. (2016). An Inundation Analysis Considering Water Behaviors of Subway in Urban Area. *20th Congress of APD IAHR*, *Colombo, Sri Lanka,* 2A028.

Okabe, R., Terada, M., Ishigaki, T., Ozaki, T. & Toda, T. (2016). Subway Inundation by Pluvial Flooding in Urban Area. *20th Congress of APD IAHR, Colombo, Sri Lanka,* 2A007.

Sekine, M. & Nakayama, J. (2009). Numerical Simulation of Inundation in Underground Space in Highly Urbanized Area in Tokyo. *Proceeding of 8th International Conference on Urban Drainage Modelling, Tokyo,* 2-C1. (On CD-ROM)

Takahashi, T., Nakagawa, H. & Nomura, I. (1990). Simulation Method on Inundation in an Underground Space Due to Intrusion of Overland Flood Flows, *Disaster Prevention Research Institute Annual,* Kyoto University, 33(B-2), 427- 442.

Takeda, M., Shimada, Y., Kawaike, K. & Matsuo, N. (2016). The Examination on Flood Damage of the Shonai River Considering an Underground Space in Urban Area. *20th Congress of APD IAHR, Colombo, Sri Lanka,* 2A027.Pdf.

Toda, K., Inoue, K., Nakai, T. & Oyagi, R. (2004). Hydraulic Model Test of Inundation Water Intrusion in Underground Space. *Proceeding of 14th IAHR-APD Congress*, 1403-1409.

Toda, K., Inoue, K. & Aihata, S. (2006). Urban Flood Analysis with Underground Space, Advances in Geoscience, Hydrological Science. *World Scientific,* 4, 47-56.

Toda, K., Yamamoto, D., Yoneyama, N. & Kuwano, Y. (2009). Risk Analysis of Underground Inundation Considering Evacuation Difficulty. *Proceeding of 8th International Conference on Urban Drainage Modelling, Tokyo,* 2(C3). (On CD-ROM)

A MODEL OF SELECTING OPTIMAL WALKING ROUTES FOR EVACUATION IN FLOOD-PRONE AREAS BASED ON MECHANICAL PROCESS

PENG GUO[(1)], JUNQIANG XIA[(1)*], ROGER A. FALCONER[(2)], QIAN CHEN[(1),]

[(1)] State Key Laboratory of Water Resources and Hydropower Engineering Science, Wuhan University, Wuhan 430072, China,
pengguo@whu.edu.cn
[(2)] Hydro-environmental Research Centre, School of Engineering, Cardiff University, Cardiff CF243AA, UK

ABSTRACT

In the current study, a model of selecting optimal escape routes in flood-prone areas is proposed based on the two-dimensional hydrodynamic module capable of simulating flood inundation processes over real terrains, including: evaluation of hazard risk to evacuees, calculation of evacuation time and selection of optimal escape routes. In the proposed model, a formula for the mechanics-based incipient velocity of a human body for toppling instability has been adopted to assess the hazard degrees of evacuees in floodwaters. Empirical curves relating the water depth and corresponding escape speed for adults presented by previous researchers have been used to calculate the cumulative time for escaping. The selection method of optimal escape routes is presented, comprising the schemes A and B for the scenarios with and without the established road networks being considered. Extreme floods have occurred in the Lower Yellow River in July 1958 and August 1982. Thus, the proposed model has been applied to selected optimal escape routes during these two overbank flood events in the Lankao-Dongming floodplain. According to the calculations, the following conclusions have been obtained: (i) the variation in hazard degrees for evacuees at different times for overbank flood event in July 1958 have been presented, which would be useful to flood risk management in this floodplain area; (ii) optimal escape routes and corresponding final escape moments have been determined for three starting locations using the schemes A and B for overbank flood event in July 1958, which would provide about 3 h and 5 h more for issuing warnings and evacuation operation; (iii) positions of optimal escape routes for overbank flood events in August 1982 and July 1958 have been almost the same for three starting locations, but the final escape moment for overbank flood event in July 1958 would be earlier because of the larger amount of water volume and higher peak discharge.

Keywords: Hydrodynamic module; flood-prone areas; human stability; escape speed; escape routes.

1 INTRODUCTION

Due to climate change and intensive human activity in recent decades, the discharges of many rivers over the world is changing with a consequent increase in occurrence possibility of extreme flood (Wang et al., 2016; Milly et al., 2002). However, there are also amounts of population living in some flood-prone areas and suffering from potential high flood risk because of increasing inhabitant density, especially for China with the world's most populous country (Piao et al., 2010). According to incomplete statistics, more than 30 overbank floods occurred in the Lower Yellow River (LYR) in China after 1949 (Liang et al., 2002), resulting in 13 thousand affected villages and 9 million victims. Once a dike fails and is breached, rapid occurrence of floods often results in very limited opportunity for issuing warnings (Collier, 2007). Thus, overbank flooding is regarded as one of the main sources of casualties, because people are difficult to take effective measures of self-preservation and rescue in floods. It is therefore desirable to present optimal escape routes for victims to save themselves and manage the potential flood risk.

With progress of computer-based simulation, many studies about flood inundation processes have been conducted (Liang et al., 2007; Neal et al., 2009; Xia et al., 2010; Liu et al., 2015). Based on 2D hydrodynamic models that would provide temporal and spatial distributions of flood factors accurately for a specific flood event, evacuation models for flooded people also have been developed. A Life Safety Model (LSM) developed by BC Hydro in Canada, offers a scientifically robust method of generating and assessing outcomes and risk because of regulators and operators of dams or other flood control structures (Johnstone et al., 2005). Zhang et al. (2016) analysed the distribution of water depth in flood inundation processes in MIKE and proposed a method for extraction of impassable flooded roads in ArcGIS. Also, Timeline modelling of flood evacuation operations is effective as a response planning tool and an effective means of communicating the complexity of the problem on evacuation, including: flood prediction, warning delivery, and evacuation operation (Stephen et al., 2010). These models are could couple flood simulation and evacuation planning to solve problems of specific flood events. And the distance of routes and water depth are regarded as two key factors for selecting optimal escape routes.

However, previous studies indicate that the stability and escape speed of people in floodwaters influence the safety of evacuees and time expenditure for evacuation (Xia et al., 2014; Abt et al., 1989; Karvonen et al., 2000; Ishigaki et al., 2008). Abt et al. (1989) reported laboratory experiments of 20 healthy adults toppling instability conducted in a 61m long flume with different ground surfaces. An equation defining the instability threshold of a flooded person was found by linear regression of the experimental data. Karvonen et al. (2000) undertook stability tests using seven human bodies on a steel grating platform towed in a model ship basin. And the product of flow and velocity describing the loss of stability of a person was proposed based on their experimental data. Xia et al. (2014) derived the formulae for the incipient velocity of a human body for toppling instability, and more than 50 tests were conducted for a model flooded human body. And also, the experimental data of model human body and real human body mentioned above were used to calibrate the formulae, respectively. It is therefore that a flooded human stability is closely related to the water depth and corresponding velocity and empirical water depth cannot estimate people safety or not. Furthermore, Ishigaki et al. (2005) conducted laboratory experiments on the evacuation criterion for people from underground spaces in urban floods, and the experimental results indicated that a water depth of 0.3 m was shown to be a critical value for the evacuation from underground spaces through staircases. Obviously, evacuation models for flooded people would be increase its utility and reliability if the stability and escape speed of people in floodwaters were taken into account.

In the current study, a model of selecting optimal escape routes in flood-prone areas is proposed based on the two-dimensional hydrodynamic module (Xia et al., 2010a; 2010b). Evaluation of hazard risk to evacuees, calculation of evacuation time and selection of optimal escape routes are three main components. Further, the selection method of optimal escape routes was presented, comprising the schemes A and B for the scenarios with and without the established road networks being considered. Two extreme floods occurred in the Lower Yellow River in July 1958 ("58.7") and August 1982 ("82.8"), with the corresponding peak discharge of 20500 and 14500 m³/s at the Jiahetan hydrometric station. The proposed model was applied to selected optimal escape routes during these two overbank flood events occurring in the Lankao-Dongming floodplain (LDF), and finally, the optimal escape routes and corresponding final escape were presented for three starting locations.

2 Description of an integrated model

This section introduces an existing 2D hydrodynamic module, evaluation of hazard risk to evacuees, calculation of evacuation time and selection of optimal escape routes. They comprise an integrated model of selecting optimal routes in flood prone areas based on hydrodynamics.

2.1 2D hydrodynamic module

For flood inundation processes simulation, a set of shallow water equations for two-dimensional flows over a horizontal plane have been deduced (Tan, 1992). The depth-averaged 2D shallow water equations are often used for describing flows in natural rivers, flood diversion areas and some other flood prone areas, which can be written in a general conservative form as below:

$$\frac{\partial U}{\partial t} + \frac{\partial E}{\partial x} + \frac{\partial G}{\partial y} = \frac{\partial \tilde{E}}{\partial x} + \frac{\partial \tilde{G}}{\partial y} + S \qquad [1]$$

where U = vector of conserved variables; E and G = convective flux vectors of flow in the x and y directions, respectively; $\tilde{E}$ and $\tilde{G}$ = diffusive vectors related to the turbulent stresses in the x and y directions, respectively; and S = source term including: bed friction, bed slope and the Coriolis force. The above terms can be expressed in detail as:

$$\mathbf{U} = \begin{bmatrix} h \\ hu \\ hv \end{bmatrix}, \; \mathbf{E} = \begin{bmatrix} hu \\ hu^2 + \frac{1}{2}gh^2 \\ huv \end{bmatrix}, \; \mathbf{G} = \begin{bmatrix} hv \\ huv \\ hv^2 + \frac{1}{2}gh^2 \end{bmatrix}, \; \tilde{\mathbf{E}} = \begin{bmatrix} 0 \\ \tau_{xx} \\ \tau_{yx} \end{bmatrix}, \; \tilde{\mathbf{G}} = \begin{bmatrix} 0 \\ \tau_{xy} \\ \tau_{yy} \end{bmatrix} \text{ and } \mathbf{S} = \begin{bmatrix} q_s \\ gh(S_{bx} - S_{fx}) \\ gh(S_{by} - S_{fy}) \end{bmatrix} \qquad [2]$$

where u and v = depth-averaged velocities in the x and y directions, respectively; h = water depth; q_s = source (or sink) discharge per unite area; g = gravitational acceleration; S_{bx} and S_{by} = bed slopes in the x and y directions, respectively; S_{fx} and S_{fy} = friction slopes in the x = and y directions, respectively; and τ_{xx} τ_{xy}, τ_{yx} and τ_{yy} = components of the turbulent shear stress over the plane.

A cell-centered finite volume method (FVM) is adopted to solve the governing equations based on an unstructured triangular mesh. At an interface between two neighboring cells, the calculation of flow fluxes can be treated as a locally one-dimensional problem, thus it can be obtained by an approximate Riemann solver. A Roe's approximate Riemann solver with the scheme of monotone upstream scheme for conservation laws

(MUSCL) is employed for evaluating the normal fluxes across the cell interface, and a procedure of predictor-corrector time stepping is used, to provide second-order accuracy in both time and space (Tan, 1992). Furthermore, a refined procedure for treating wetting and drying fronts is used. This model is validated by experimental data of Toce River physical model.

2.2 Assessment method for evacuees' safety

The flood risk to people at different locations varies with flood inundation processes. Understanding the human body stability criteria that was proposed based on laboratory experiments and theoretical analysis is important in flood risk management. A formula proposed by Xia et al. (2014) for the mechanics-based incipient velocity of a human body for toppling instability, that accounts for the effect of body buoyancy and the influence of a non-uniform upstream velocity profile acting on the flooded human body, was used in this model to assess the hazard degrees of evacuees in floodwaters, and given by:

$$U_c = \alpha (\frac{h}{h_p})^\beta \sqrt{\frac{m_p}{\rho_f h^2} - (\frac{a_1}{h_p^2} + \frac{b_1}{h h_p})(a_2 m_p + b_2)}$$

[3]

where ρ_f is the density of water; h_p and m_p are the height and mass of a human body; a_1 and b_1 are non-dimensional coefficients related to the buoyancy force of human body, with $a_1 = 0.633$ and $b_1 = 0.367$ for a typical human body of a Chinese person; a_2 and b_2 are coefficients determined from the average attributes of a human body, with $a_2 = 1.015 \times 10^{-3}$ m^3/kg and $b_2 = -4.927 \times 10^{-3}$ m^3.

Xia et al. (2014) conducted tests in a flume to obtain the water depth and velocity at the condition of toppling instability for a model human body, after flume tests conducted by Abt et al. (1989) and Karvonen et al. (2000) for a real human body. These two kinds of experimental data are used to calibrate two parameters α and β in Eq. (3), respectively. The computational curve of calibrated the Eq. (3) in Fig. 1 shows the relationship between the water depth and the incipient velocity for Chinese adults with an average height of 1.71 m and an average mass of 68.7 kg. As shown in Fig. 1, computational curve calibrated by experimental data of model human body is more secure for flooded people than that of the real body. For example, the incipient velocities of an adult under the incoming depth of 0.5 m are 1.3 m/s (model human body) and 1.8 m/s (real human body) for these two-calibrated formula.
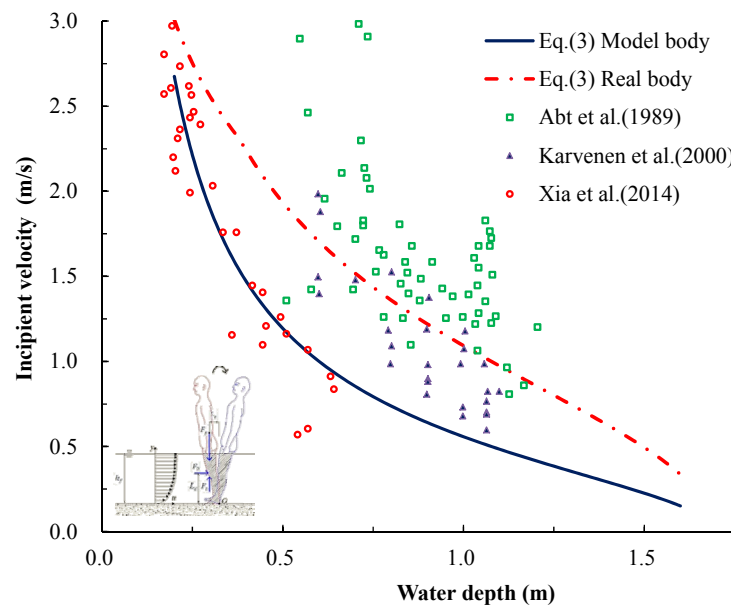

Figure 1. Instability curves for model and real body in floodwaters

The water depth calculated by 2D hydrodynamic module is used to calculated the corresponding incipient velocity for a specific adult using Eq. (3) calibrated by Xia et al. (2014). Thus, the following expression is used to quantify the hazard degree, and given by:

$$HD = Min \left(1.0 , U / U_c \right)$$

[4]

where HD = hazard degree for flooded people. There are three levels of hazard degree for flooded people divided by the value of HD, including: (i) safety ($0 \leqslant HD < 0.6$), (ii) danger ($0.6 \leqslant HD < 0.9$) and (iii) extreme danger ($0.9 \leqslant HD \leqslant 1.0$). This mechanics-based assessment methods in the model account for the water depth and velocity, which is superior to the empirical water depth danger to people in floodwaters.

2.3 Calculation of evacuation time

There is a time competition between people evacuation and flood inundation because these two processes occur concurrently. Therefore, time, is recognized as the most important factor in emergency situations during a disaster (Pel et al., 2012). The evacuation expenditure is determined by escape speed of evacuees, which is related to the flow condition. Ishigaki et al. (2008) conducted evacuation tests in a water tank, under the water depth varied from 0.0 m to 0.5 m with and without flow of 0.5 m/s. Measured escape speed on foot is shown in Fig. 2. The normal walking speed of people for male and female adults are 1.35 and 1.27 m/s, and they would reduce by half the value of normal walking speed under water depths of the experiment. The flow conditions of actual floods are approximate to experiments. However, the long-distance walking and road capacity of people flow would influence the escape speed. Thus, Empirical relationship between the water depth and corresponding escape speed is given by:

$$v_E = \begin{cases} \eta \cdot (1.31 - 3.1h) & (\quad h \leq 0.2\,\text{m} \quad) \\ \eta \cdot 0.5 v_0 & (0.2 \leq h \leq 0.8\,\text{m}) \end{cases} \qquad [5]$$

where v_0 = normal walking speed of adults; v_E = escape speed for people in floodwater; η = reduction coefficient. People will be difficult to escape on foot if $h > 0.8$ m.
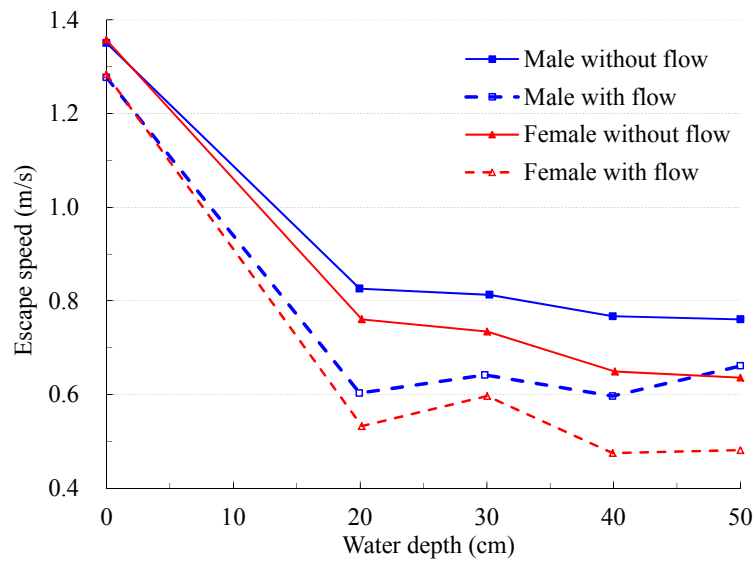
Figure 2. Empirical curves related to the water depths and corresponding escape speeds for adults in floodwaters. (Refer to Ishigaki et al. (2008) for more details.)

Processes of evacuation and flood inundation occur concurrently, and interact with each other. For an escape route, the flow condition of each location on the route is changing. Thus, the escape routes are divided to several short segments. For a segment from locations A_i to A_{i+1} at T moment, time competition between people and flood inundation is shown in Figs. 3-4. The flow condition of locations A_i at T moment would be presented based on 2D hydrodynamic module, which would be used for calculating U_c and HD by Eq. (3) and Eq. (4). If HD approaches 1.0, namely $U > U_c$, people in floodwater would be dangerous; and otherwise, the escape speed on foot of the evacuee can be calculated by Eq. (5) so as to calculate the time expenditure of the segment. If A_{i+1} is in the target safe haven, the evacuee would be survived successfully; and otherwise, the same approach would be used for next segment. Thus, the evacuation expenditure from A_1 to A_N is given by:

$$T_N = T_0 + \sum_{i=2}^{N} \left[\text{V} L_{i-1} / (v_{E,\ i-1}) \right] \qquad [6]$$

where T_N = escape time expenditure of segments from A_1 to A_N; T_0 = moment when they receive warning; $\triangle L_{i-1}$ = segment (i-1) distance from locations A_{i-1} to A_i, and $v_{E,i-1}$ = corresponding escape speed of evacuee on segment (i-1).
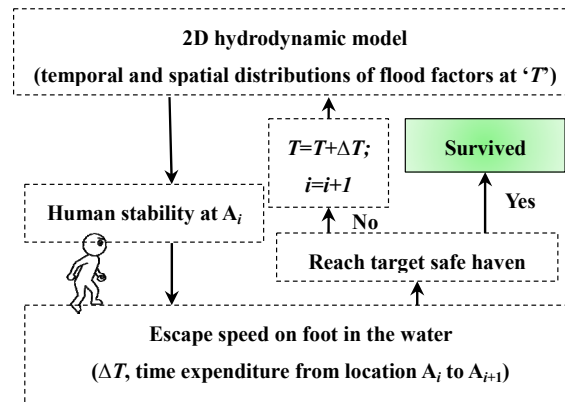

Figure 3. Time competition between people evacuation and flood inundation
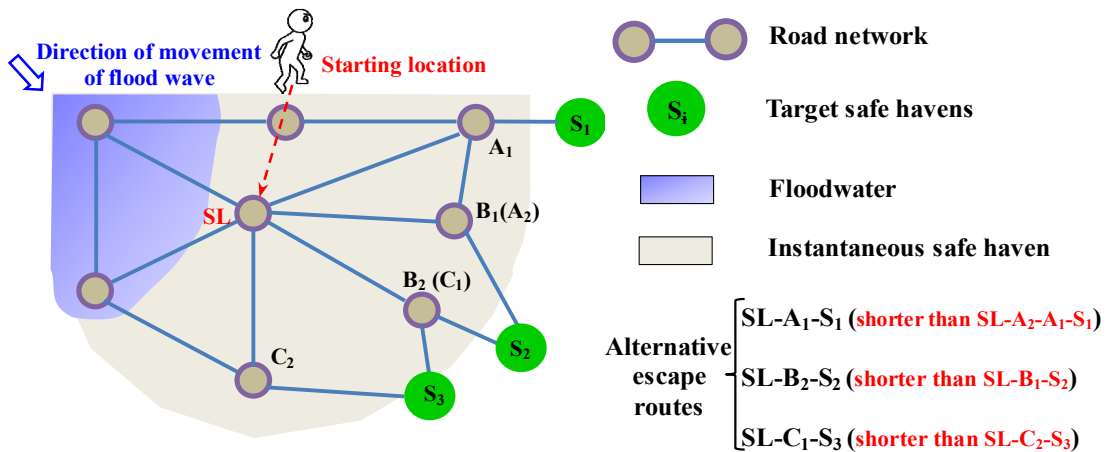

Figure 4. Sketch diagram for a person escaping in a flood event

2.4   Selection of optimal escape routes

In the proposed model, the selection method of optimal escape routes is presented, comprising the schemes A and B for the scenarios with and without the established road networks being considered (Fig. 4).

1)   The Dijkstra algorithm was adopted to derive the shortest routes which are taken to be alternative escape routes for the scheme A, when they received warnings and moved to the target safe havens using the existing road networks. The hazard degree of evacuee and the corresponding escape speed for each alternative route are then evaluated to determine the final escape moment under a specified flood event.

2)   For a flood-prone area with uncompleted road networks, instantaneous safe havens are zoned by the temporal and spatial distributions of hydrodynamic factors under different recurrence frequencies of floods. The shortest routes in the areas are then selected to be optimal escape routes for the scheme B. These routes would provide a reference for locations of new roads construction which would be useful for both transportation and evacuation.

In these two schemes, optimal escape routes and corresponding final escape moment would be presented. They would provide scientific basis for directing evacuation and managing flood risk. However, these methods in the model focus on the mechanism of human stability and escape time expenditure, cannot account for age, gender, educational attainment of evacuees.

3   Model applications

3.1   Study area

In the Lower Yellow River, there are a total number of about 120 nature floodplain areas, which are used for providing living space for 1.9 million residents. However, according to the incomplete statistics, there are serious overbank events in LDF. For example, the consequence due to dike breach in LDF in 2003 is severity, including 114 submerged villages, 12000 hm^2 submerged farmlands, and 160000 affected population. In addition, two extreme floods occurred in LDF in July 1958 ("58.7") and August 1982 ("82.8"), with the corresponding peak discharge of 20500 and 14500 m^3/s at the Jiahetan hydrometric station. The proposed

model was applied to selected optimal escape routes during these two overbank flood events occurring in LDF, and assumed that the discharge hydrograph entering the floodplain zone was equivalent to the hydrograph at Jiahetan subtracting the current bankfull discharge (7000 m^3/s) in this reach. Three Starting Locations (SL$_{1-3}$), two observation points (P1 and P2) and target safety areas were shown in Fig. 5.

The processes of "82.8" flood inundation in LDF were presented in detail. And then, the comparison of locations and final escape moments for optimal escape routes in "58.7" and "82.8" floods were also shown.
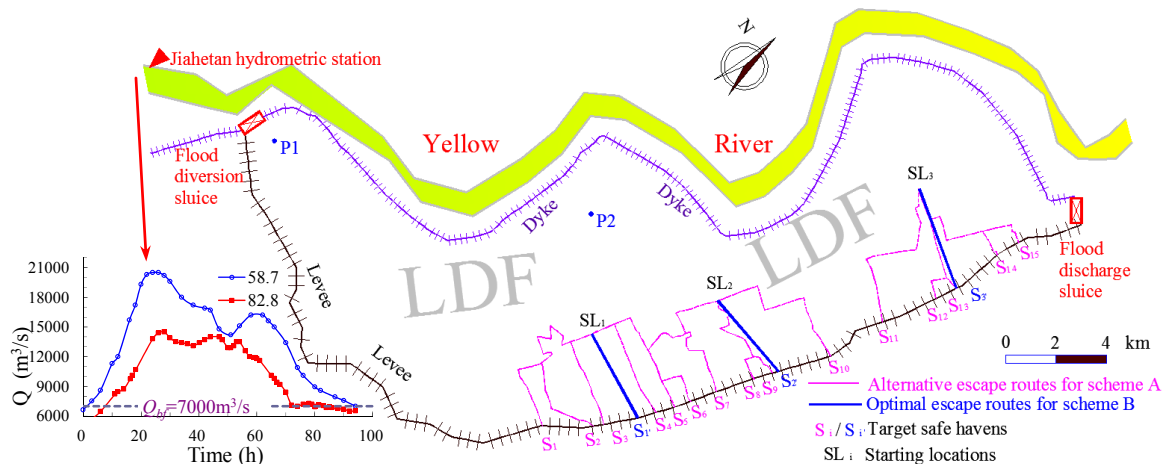
Figure 5. Alternative escape routes for the scheme A and optimal escape routes for the scheme B in LDF

3.2 "82.8"overbank flood simulation

The study area is about 250 km^2 and it was divided into 16064 equilateral triangular cells. The initial topography of LDF is obtained by the algorithm of surface interpolation based on known elevation splashes (Fig. 6). A constant time step of 0.2 s and a constant roughness of 0.06 m$^{-1/3}$s were used in the simulation.

As shown in Fig. 7, the variations of the water depth and hazards degree for people at the observed points (P1 and P2) are similar. However, when hazards degree for people at P1 gets to 1.0 at 10.9 h, corresponding water depth is 1.2 m. Analogously, when hazards degree for people at P2 gets to 1.0 at 35.6 h, corresponding water depth is 1.4 m. P1 is near flood diversion sluice and its velocity is higher than that of P2. Thus, it is more reliability to evaluate human stability using the mechanics-based Eq. (3) and Eq. (4) than empirical water depth, because people also would die at the flow condition of shallow water but high velocity.

In addition, hazards degree distributions for people at t=9, 13 and 33 h are shown in Fig. 8. It is seen that the dangerous zone would expand along the Yellow River levee because of large transverse gradient in LDF. The whole inhabitants would be in danger in 49 h and therefore they must escape on the optimal routes.
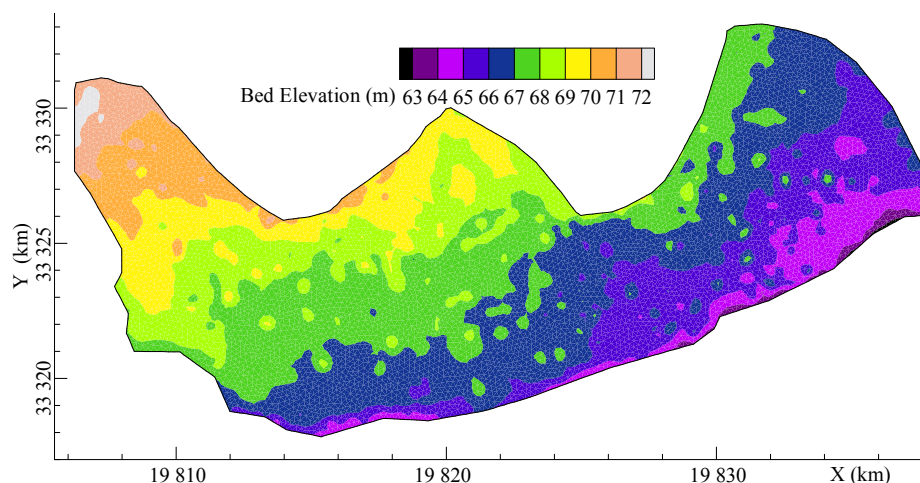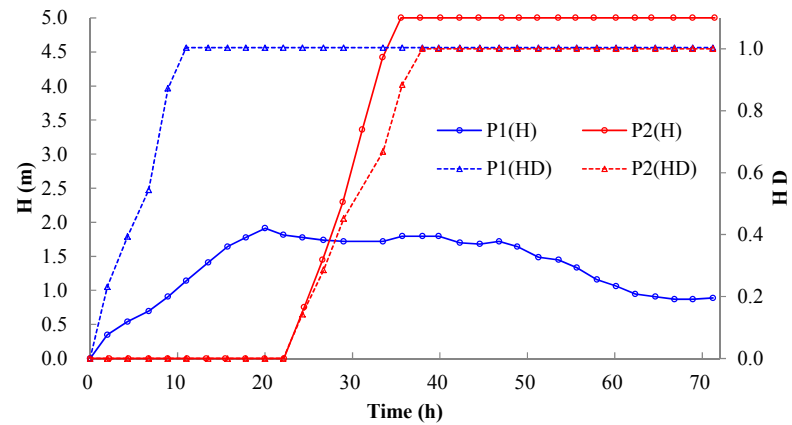

Figure 6. Topographical mapof the study domain

Figure 7. Temporal variations of water depth and hazard degree for people at different points
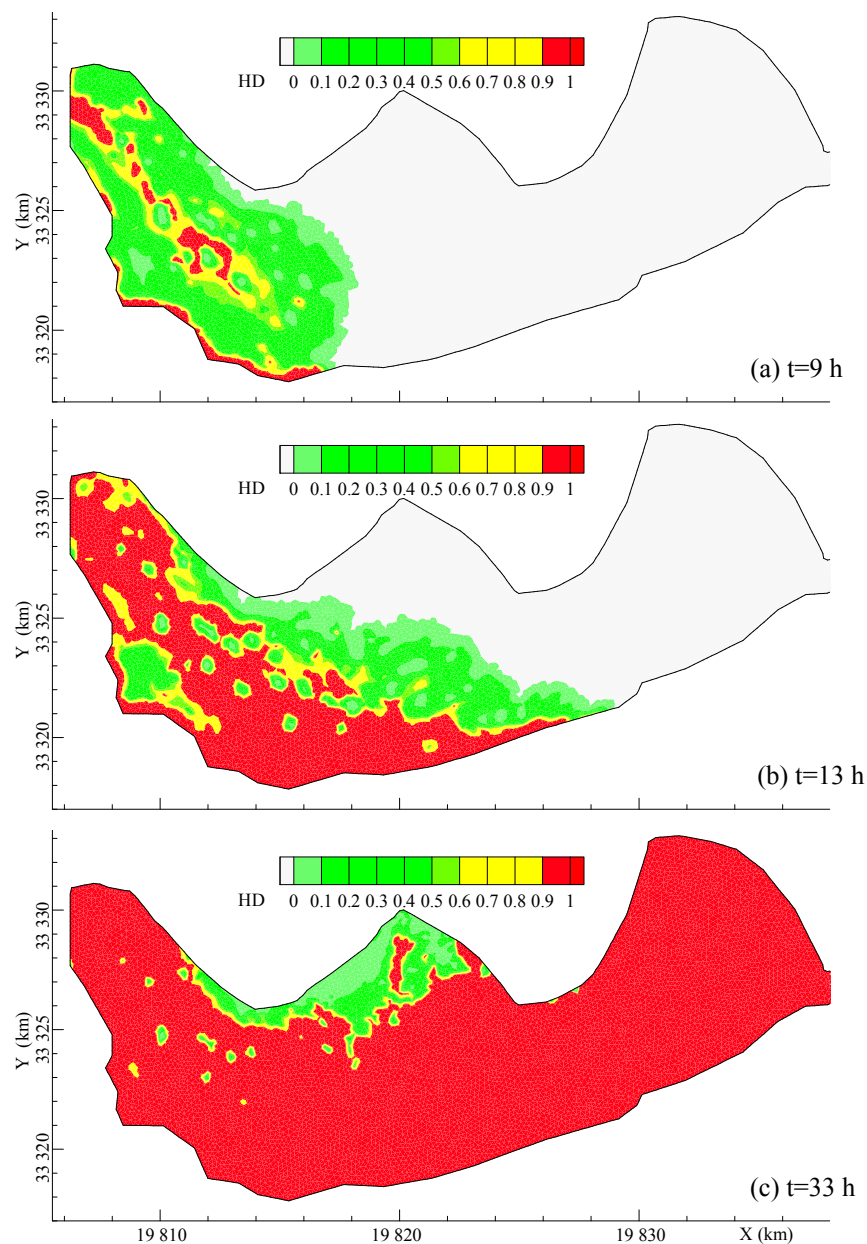

Figure 8. Distribution of hazard degree for people at different time. There are three levels of hazard degree for flooded people divided by the value of HD, including: (i) safety ($0 \leqslant$ HD < 0.6), (ii) danger ($0.6 \leqslant$ HD < 0.9) and (iii) extreme danger ($0.9 \leqslant$ HD $\leqslant 1.0$)

3.3   Optimal escape routes in "82.8"overbank flood events
   (a) Scheme A
   The optimal escape routes are presented, comprising the schemes A and B for three starting locations. As shown in Fig. 9, five alternative routes for each starting location are presented using the Dijkstra algorithm, respectively. The Optimal escape routes for scheme A are selected based on flood inundation processes, assessment on human stability and escape speed in floodwater. The variations of hazard degree for evacuees on optimal and worst routes for three starting locations are shown in Fig. 9. There was only about 1.5 h for *HD* of evacuees on each route changing from 0.0 to 1.0, namely from moment they would escape to would not. However, the evacuees in SL_1 would escape if they selected worst route S_1 to escape and were aware of danger before 6.2 h when *HD* is equal to 0.9, and analogously they would be eventually rescued if they are aware of danger and select optimal route S_5 to escape before 10.7 h. Therefor route S_5 is selected as the optimal route for SL_1 and the corresponding final escape moment is 10.7 h. In a similar way, route S_9 is selected as the optimal route for SL_2 and the corresponding final escape moment is 11.7 h, and route S_{13} is selected as the optimal route for SL_3 and the corresponding final escape moment is 14.7 h.
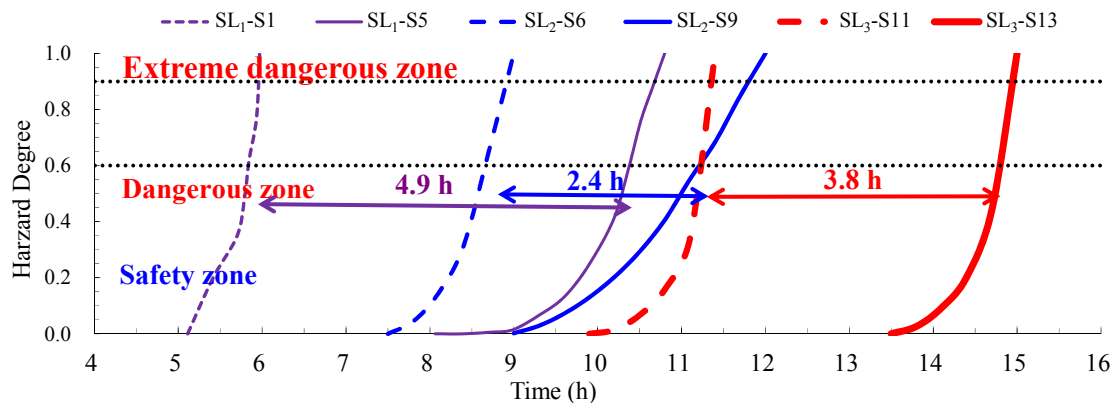
Figure 9. Temporal variation of hazard degree for people at different alternative routes

   (b) Scheme B
   People must escape at SL_1, SL_2 and SL_3, because they would be dangerous if they don't aware of warnings before 19.9, 20.7 and 22.2 h. The locations of optimal escape routes for scheme B are presented in Fig. 5 and corresponding final escape moment are shown in Table. 1. For example, the period form19.9 h to time when people start to escape is increased gradually, and the instantaneous safe havens would contact target safe havens at $S_{1'}$ for the first time when the period is equal to 6.7 h. Thus, 13.2 h is the final escape moment if they chose the route SL_1-$S_{1'}$. In a similar way, final escape moments are 16.6 and 17.5h if they chose the routes SL_2-$S_{2'}$ and SL_3-$S_{3'}$.
   The comparison of final escape moment between scheme A and B is seen in Table. 1. There are 2.5, 4.9 and 2.8 h more than scheme A for evacuees if they select optimal escape routes of scheme B. The locations of optimal routes SL_1-S_2 and SL_1-$S_{1'}$ are close to each other, and there are also the same situations for the locations of optimal routes SL_3-S_{13} and SL_3-$S_{3'}$. This can provide evidence for adjusting existing routes slightly. However, the locations of optimal routes SL_2-S_9 and SL_2-$S_{2'}$ are far from each other. So, for places with incomplete road network, the construction of new routes which are used for escaping and transportation should take the results into consideration.

Table 1 Optimal escape routes and corresponding final escape moments for the "58.7" and "82.8"flood events

Floods		Scheme A			Scheme B		
"82.8"	Optimal escape routes	SL_1~S_5	SL_2~S_9	SL_3~S_{13}	SL_1~$S_{1'}$	SL_2~$S_{2'}$	SL_3~$S_{3'}$
	Final escape moments (h)	10.7	11.7	14.7	13.2	16.6	17.5
"58.7"	Optimal escape routes	SL_1~S_5	SL_2~S_9	SL_3~S_{13}	SL_1~$S_{1'}$	SL_2~$S_{2'}$	SL_3~$S_{3'}$
	Final escape moments (h)	8.4	10.2	13.2	10.5	13.4	14.9

3.4   Optimal escape routes for "58.7"overbank flood events
   The optimal escape routes and corresponding final escape moment for "58.7" overbank flood events were accessible, and the results for schemes A and B could be seen in Table. 1. Locations of optimal escape events two schemes for these two floods were the same, but the final escape moments of scheme A for "58.7" floods were 1-3 h earlier than those for "82.8" floods, and final escape moments of scheme B for "58.7" floods were about 3h earlier than those for "82.8" floods. The main conclusions were available by comparing the results: the submerged order for locations in LDF with special terrain would be almost the same, which results in the locations of optimal escape routes are the same. However, the peak discharge and water volume in

"58.7" floods are greater than those of "82.8" floods, which leads to the final escape moments in "58.7" earlier. Thus, the deduction could be available: for different frequencies of flood recurrence, the locations of escape routes maybe the same, but the final escape moments should be calculated based on simulating two-dimensional hydrodynamic flood inundation processes.

4 CONCLUSIONS

In the current study, an integrated numerical model of selecting optimal escape routes in flood-prone area is developed, including: evaluation of hazard risk to evacuees, calculation of evacuation time and selection of optimal escape routes. In the proposed model, a two-dimensional hydrodynamic module is used to simulating flood inundation processes over flood-prone areas. The formula for the mechanics-based incipient velocity of a human body for toppling instability was adopted to assess the hazard degrees of evacuees in floodwaters. Empirical curves relating the water depth and corresponding escape speed for flooded adults presented by previous researchers were used to calculate the cumulative time for escaping on the road. The selection method of optimal escape routes is presented, comprising the schemes A and B for the scenarios with and without the established road networks being considered.

Numerical model results in LDF for three starting locations shows that: optimal escape routes and corresponding final escape moments are determined for three starting locations using the schemes A and B for the "58.7" overbank flood event, which would provide about 3 h and 5 h more for issuing warnings and evacuation operation. Positions of optimal escape routes for the "82.8" and "58.7" overbank flood events are almost the same for three starting locations, because the submerged order for locations in LDF with large transverse gradient would be almost the same. However, the final escape moment in the "58.7" overbank flood event would be earlier because of the larger amount of water volume and higher peak discharge.

REFERENCES

Abt, S.R., Wittler, R.J., Taylor, A. & Love, D.J. (1989). Human Stability in a High Flood Hazard. *Water Resources Bulletin*, 25(4), 881-890.

Cheng, C., Qian, X., Zhang, Y., Wang, Q. & Sheng, J. (2011). Estimation of the Evacuation Clearance Time Based on Dam-Break Simulation of the Huaxi Dam in Southwestern China. *Natural Hazards*, 57, 227-243.

Collier, C.G. (2007). Flash Flood Forecasting: What Are the Limits of Predictability? *Quarterly Journal of The Royal Meteorological Society*, 133, 3-23.

He, X.Y., Wang, Z.Y. & Huang, J.C. (2008). Temporal and Spatial Distribution of Dam-Failure Events in China. *International Journal of Sediment Research*, 23, 398-405.

Huang, X. (2017). The Decision Method of Emergency Supplies Collection. *Natural Hazards*, 85, 869-886.

Ishigaki, T., Kawanaka, R., Onishi, Y., Shimada, H., Toda, K. & Baba, Y. (2008). Assessment of Safety on Evacuating Route During Underground Flooding. *Proceedings of 16TH IAHR-APD Congress and 3RD Symposium of IAHR-ISHS Najing, China*, 141-146.

Johnstone, W.M., Sakamoto, D., Assaf, H. & Bourban, S. (2005). Architecture, Modelling Framework and Validation of Bc Hydro's Virtual Reality Life Safety Model. *International Symposium on Stochastic Hydraulics, Nijmegen, The Netherlands*, 23-24.

Karvonen, R.A., Hepojoki, H.K., Huhta, H.K. & Louhio, A. (2000). *The Use of Physical Models in Dam-Break Analysis*. Rescdam Final Report. Helsinki University of Technology, Helsinki, Finland, 57.

Liang, D.F., Lin, B.L. & Falconer, R.A. (2007). A Boundary-Fitted Numerical Model for Flood Routing with Shock-Capturing Capability. *Journal of Hydrology*, 332, 477-486.

Liang, L., Ni, J., Borthwick, A. & Rogers, B. (2002). Simulation of Dike-Break Processes in the Yellow River. *Science in China (Series E)*, 45, 606-619.

Liu, Q., Qin, Y., Zhang, Y. & Li, Z.W. (2015). A Coupled 1d-2d Hydrodynamic Model for Flood Simulation in Flood Detention Basin. *Natural Hazards*, 75, 1303-1325.

Milly, P.C.D., Wetherald, R.T., Dunne, K.A. & Delworth, T.L. (2002). Increasing Risk of Great Foods in a Changing Climate. *Nature*, 415, 514-517

Mozumder, P. & Va´Squez, W.F. (2015). An Empirical Analysis of Hurricane Evacuation Expenditures. *Natural Hazards*, 79, 81–92

Neal, J., Fewtrell, T., & Trigg, M. (2009). Parallelisation of Storage Cell Flood Models Using Openmp, *Environmental Modelling & Software*, 24(7), 872-877.

Piao, S.L., Ciais, P., Huang, Y., Shen, Z.H., Peng, S.S., Li, J.S., Zhou, L.P., Liu, H.Y., Ma, Y.C., Ding, Y.H., Friedlingstein, P., Liu, C.Z., Tan, K., Yu, Y.Q., Zhang, T.Y. & Fang, J.Y. (2010). The Impacts of Climate Change on Water Resources and Agriculture in China. *Nature*, 467, 43-51.

Pel, A.J., Bliemer, M.C. & Hoogendoorn, S.P. (2012). A Review on Travel Behavior Modelling in Dynamic Traffic Simulation Models for Evacuations. *Transportation*, 39, 97–123.

Tan, W.Y. (1992). Shallow Water Hydrodynamics: Mathematical Theory and Numerical Solution for a Two-Dimensional System of Shallow Water Equations. Elsevier, New York.

Van. Leer, B. (1979). Towards the Ultimate Conservative Difference Scheme. V. A. Second Order Sequel to Godunov's Method. *Journal of Computational Physics*, 32, 101-136.

Wang, G.Q., Xia, J.Q. & Wu, B.S. (2008). Numerical Simulation of Longitudinal and Lateral Channel Deformations in the Braided Reach of the Lower Yellow River. *Journal of Hydraulic Engineering*, 134(8), 1064-1078.

Wang, K., Wang, L., Wei, Y.M. & Ye, M.S. (2013). Beijing Storm of July 21, 2012: Observations And Reflections. *Natural Hazards*, 67(2), 969-974.

Xia, J.Q., Falconer, R.A., Wang, Y.J. & Xiao, X.W. (2014). New Criterion for the Stability of a Human Body in Floodwater. *Journal of Hydraulic Research*, 53(4), 93-104.

Xia, J.Q., Falconer, R.A., Lin, B.L. & Tan, G.M. (2010A). Modelling Dam-Break Flows Over Mobile Beds Using A 2d Coupled Approach. *Advances in Water Resources*, 33, 171–183

Xia, J.Q., Falconer, R.A., Lin, B.L. & Tan, G.M. (2010B). Modelling Floods Routing on Initially Dry Beds with the Refined Treatment of Wetting and Drying. *International Journal of River Basin Management*, 8(3-4): 225-243.

Zhang, W. (2016). Emergency Evacuation Planning Against Dike-Break Flood a Gis-Based Dss for Flood Detention Basin of Jingjiang In Central China. *Natural Hazards*, 81, 1283–1301.

NUMERICAL PREDICTION OF LOCALIZED HEAVY RAIN BY WRF-ARW MODEL WITH X-BAND RADAR DATA ASSIMILATION

MASATO KITA [(1)], YOSHIHISA KAWAHARA[(2)] & CHO THANDA NYUNT[(3)]

[(1)]Graduate School of Engineering, Hiroshima University, Higashi-Hiroshima, Japan,
d144209@hiroshima-u.ac.jp
[(2,3)] Department of Civil and Environmental Engineering, Hiroshima University, Higashi-Hiroshima, Japan,
kawahr@hiroshima-u.ac.jp; nyunt11@ hiroshima-u.ac.jp

ABSTRACT

Ministry of Land, Infrastructure, Transport and Tourism (MLIT) of Japan has operated X-band dual polarimetric radar network system having high spatio-temporal resolution to monitor heavy rains over big cities in Japan. The radar system has been contributing to the advancement in now casting while its application to short-range weather forecasting has been limited. This study aims to quantify the effects of the data assimilation interval using WRF (Weather and Research Forecasting) model coupled with a 3-D variational method for the torrential rainfall in Hiroshima City in August 2014. It is shown that band-shaped precipitation system at 1:00 is predicted with X-band MP radar data assimilation and that data assimilation at 10-minute interval reproduces the area of heavy rainfall best. Comparison between the case with data assimilation at 10-minute interval and that without data assimilation explains that X-band MP radar data assimilation induces the favorable environment for convective rainfall to develop through modifying wind vectors and vapor fields.

Keywords: Weather Research Forecasting model (WRF); 3-D variational method X-band radar; torrential rainfall.

1 INTRODUCTION

Recently, frequent localized heavy rains in Japan have caused flash floods, slope failures and debris flows. Ministry of Land, Infrastructure, Transport and Tourism (MLIT) of Japan has operated X-band dual polarimetric (Multi-Parameter) radar network to monitor heavy rains over megalopolises in parallel with the existing C-band radar network. The X-band MP radar has provided us with high temporal-spatial resolution data which have contributed to the advancement in now casting and short-time forecasting.

Japan Meteorological Agency (JMA) developed a high-resolution now casting system using X-band MP radar system (2014), which keeps high accuracy within about 30 minutes. The system gradually switches from tracking the movement of rainfall distribution to numerically predicting the convection based on vertical profiles of temperature and humidity. Picciotti et al. (2013) validated the performance of X-band radar now casting using Spectral Pyramidal Advection Radar Estimation (SPARE), which estimates a displacement vector by calculating spatial correlation in filtered radar images. It is recognized that now casting works well only for an hour or so and that weather forecasting using numerical models can offer better results for very short-range (2 to 12 hours) and short-range (12 to 72 hours) forecasting. It is also known that numerical weather predictions are very sensitive to initial conditions whose perfectly accurate data cannot be input (Rabier et al., 1996). To cope with the problem, data assimilation methods have been developed. While the assimilation using radar data (radial velocity and reflectivity) is found to be effective for predicting heavy rains (Xiao et al., 2005), the impact assessment of X-band MP radar data assimilation on numerical weather prediction of convective rains is limited.

This study aims to quantify the effects of the X-band MP radar data assimilation with WRF (Weather and Research Forecasting) model coupled with a 3-D variational method for the torrential rainfall in Hiroshima City in August 2014.

2 TARGET AREA AND RAINFALL

We are going to discuss a multi-cell storm that brought huge amount of rain over a localized area in Hiroshima in August 2014, resulting in a disaster where 74 persons were killed by the attacks of debris flow.

2.1 Target area

Figure 1 depicts the location of Hiroshima city and the contour lines. Hiroshima city stretches at the foot of mountains and is on the coast of the Seto Inland Sea on the south. Moist air can penetrate over the downtown area of Hiroshima city into the northern valleys from the south.

2.2 Target rainfall

The radar-AMeDAS data are the C-band radar data corrected by the rain gauge data of AMeDAS (Automated Meteorological Data Acquisition System by Japan Meteorological Agency). Figure 2 shows the total rainfall distribution observed by radar-AMeDAS from 21:00 August 19 to 5:00 August 20 (JST). The target rainfall hit Hiroshima city with the total precipitation exceeding 250 mm.

2.3 Rain gauge observation

Figure 3 shows hourly rainfall (bar chart) and the total rainfall (line graph) observed from 21:00 August 19 to 5:00 August 20 (JST) at Miiri station whose location is depicted in Figure 2. Strong hourly rainfall started at 2:00 with the peak value of 100 mm/h at 4:00, then the rainfall rapidly decreased. The value of 100 mm/h broke the record of 62 mm/h observed in 2008. The total rainfall during 2:00 to 4:00 recorded about 220 mm. The peak value of 10-minute rainfall exceeded 20 mm/10min at 3:20.
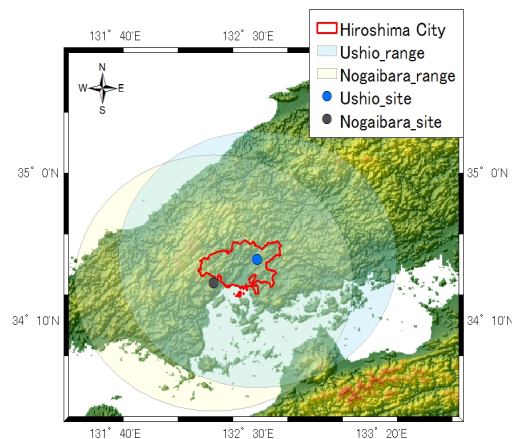
Figure 1. Location of Hiroshima city and X-band MP radar sites.
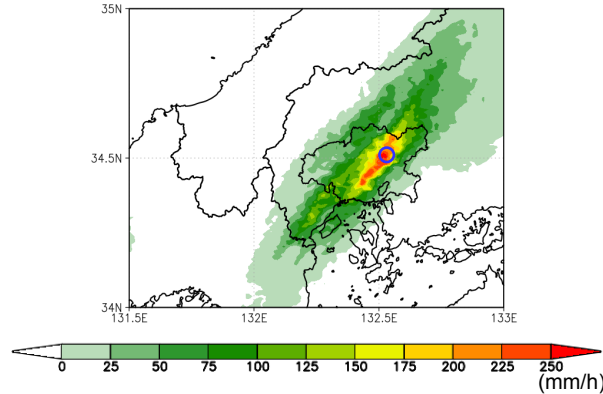
Figure 2. Total rainfall distribution observed by radar-AMeDAS from 21:00 August 19 to 5:00 August 20 (JST). Miiri station is located at a blue open circle.
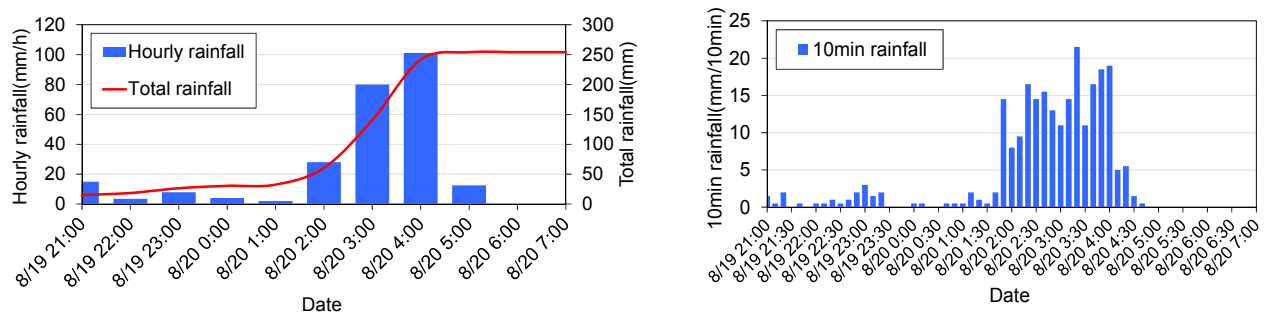
Figure 3. Time series of rainfall observed by rain gauge at Miiri station from 21:00 August 19 to 7:00 August 20 (JST) (left: total and hourly rainfall, right: 10-minute rainfall).

3   OUTLINE OF NUMERICAL PREDICTION

3.1 WRF-ARW

We used WRF-ARW model, a regional weather model developed by NCAR (National Center for Atmospheric Research), USA. It has several advantages. It is free from the assumption of hydrostatic pressure distribution, which enables the model to capture the phenomena ranging from mesoscale to 1 km scale.

3.2 3-D variational method

We chose a 3-D variational method for data assimilation because the computational load is lower than the other methods such as ensemble Kalman filter and 4-D variational method. Variational methods introduce the maximum likelihood estimation. The likelihood distribution of analysis value is expressed in the following equation.

$$L(\mathbf{x}|\mathbf{x}^b,\mathbf{y})=\frac{1}{(2\pi)^{nm}|\mathbf{B}|^{1/2}|\mathbf{R}|^{1/2}}\exp(J) \qquad [1]$$

where,

$$J=\left[-\frac{1}{2}(\mathbf{x}\text{-}\mathbf{x}^b)\mathbf{B}^{-1}(\mathbf{x}\text{-}\mathbf{x}^b)-\frac{1}{2}(H(\mathbf{x})\text{-}\mathbf{xy})\mathbf{R}^{-1}(H(\mathbf{x})\text{-}\mathbf{y})\right] \qquad [2]$$

where $\mathbf{x}$ is the analysis value, $\mathbf{x}^b$ is the background (forecast) value, $\mathbf{y}$ is the observation value, $\mathbf{B}$ is the background error covariance matrix, $\mathbf{R}$ is the observation error covariance matrix, n is the model grid number, m is the observation number, J is the cost function, and H is observation operator which converts forecast variable to observation variable. To obtain the optimal analysis value, the method needs iterations until the cost function reaches the minimum.

3.2.1   Observation operator

The observation data for assimilation in this study are reflectivity and radial velocity, for which observation operators are expressed as follows. The operator for radial velocity is,

$$V_r=\frac{1}{R}\left(u(x\text{-}x_r)+v(y\text{-}y_r)+(w\text{-}v_t)(z\text{-}z_r)\right) \qquad [3]$$

where R is the distance between observation point and radar site, (u,v,w) is the velocity field in the model, (x,y,z) is the location of observation point, (x_r,y_r,z_r) is the location of radar site, and v_t is the fall velocity of rain particle. The operator for reflectivity follows the one developed by Crook et al. (1997).

$$Z=43.1+17.15\log_{10}\left(\rho q_r\right) \qquad [4]$$

where ρ is the air mass density and q_r is rain mixing ratio.

3.3 Calculation conditions

3.3.1   Configuration of WRF-ARW

Figure 4 shows the computational domains. This study employs dynamic downscaling with two-way nesting for high spatial resolution simulation with less computational burden. Table 1 summarizes the calculation condition. The grid size at the inner domain is set to be 1 km to capture detailed atmospheric phenomena. Initial and lateral boundary conditions of the outermost domain are given from the MSM (MesoScale Model) developed by JMA. From the aspect of 'prediction', we used MSM forecast data for boundary conditions. Concerning the topography data, 50 m mesh DEM of Japan, GSI50, prepared by Geospatial Information Authority of Japan was used.

3.3.2   Configuration of 3DVAR

In data assimilations, observation data are combined with forecast data to provide the best estimate called analysis data, which in turn are used as the initial values in the numerical prediction at the next analysis cycle. In this study, we setup 3 types of assimilation intervals (1 hour, 30 minutes and 10 minutes). We statistically estimate the background error $\mathbf{B}$ in Eq. [1] using NMC (National Meteorological Center) method (Parrish et al., 1992). With respect to control variables, we chose five variables, velocity (u,v), temperature (T), surface pressure (Ps), and pseudo relative humidity. These variables are suitable for assimilation against convective scale event (Xie et al., 2002).
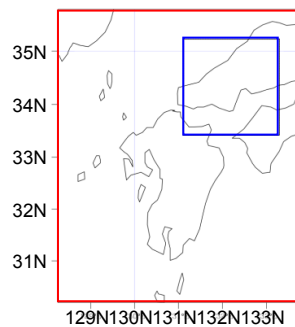
Figure 4. Computational domain (red box: d01, blue box: d02).

(a)

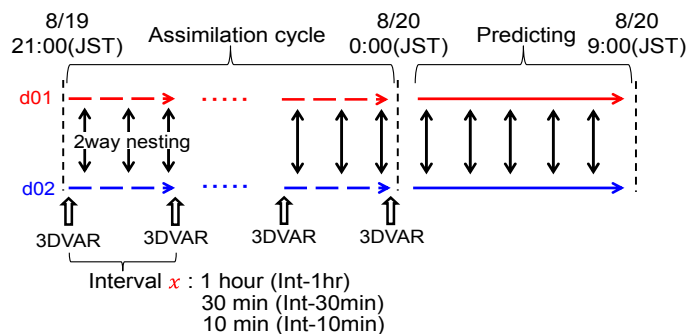|	d01	d02
Grid number	100×120×60	196×196×60
Grid resolution(kn)	5	1
Time step(sec)	25	5
Integration time	2014/8/20 0:00 - 2014/8/20 9:00(JST)	
Surface model	Monin-Obukhov scheme	
Planetary boudary scheme	YSU scheme	
Microphysics	WSM6	

Figure 5. (a) Calculation Condition (b) Schematic of assimilation cycle.

3.3.3   Outline of radar site

Figure 1 shows the location of radar sites on both sides of Hiroshima city with the effective range of 80 km. The radars perform 12 angle level observations during 5 minutes. We used the data at all levels to properly utilize 3-dimensional atmospheric field. The observation error $\mathbf{R}$ was estimated as the standard deviation of observation data within the model grid which is 1 km.

4   RESULTS AND DISCUSSION

4.1 Effects of analysis cycle

4.1.1   Comparison of rainfall intensity after final cycle

Figure 6 shows rainfall intensity distribution obtained after the final cycle. This figure compares the plausibility of initial condition for the prediction. X-band MP radar shows that a band-shaped precipitation system expands near the northwestern edge of Hiroshima city. The high intensity zone in case (b) shows a shift in the southeast direction and overestimates the magnitude compared with X-band MP radar. Case (c) also shows a similar tendency. Case (d), however, can reproduce the location of band-shaped clouds fairly well with underestimation of its intensity. These results indicate that the short interval of analysis cycle can enhance the accuracy of initial condition for prediction.

4.1.2   Statistical error

Figure 7 shows a time series of RMSE (Root Mean Squared Error) for radial velocity and rain mixing ratio during analysis cycles. The line graphs have two values at the same time, where the maximum value means RMSE between background and observation (RMSE (B-O)) and the minimum value RMSE between analysis and observation (RMSE (A-O)). The case at 1-hour interval shows the highest RMSE (B-O) while the case at a 10-minute interval gives the lowest RMSE B-O). This indicates that the assimilation of observation data at a

short interval can hold down the error accumulation during time integration, leading to more suitable rain distribution as shown in Figure 6 (d).
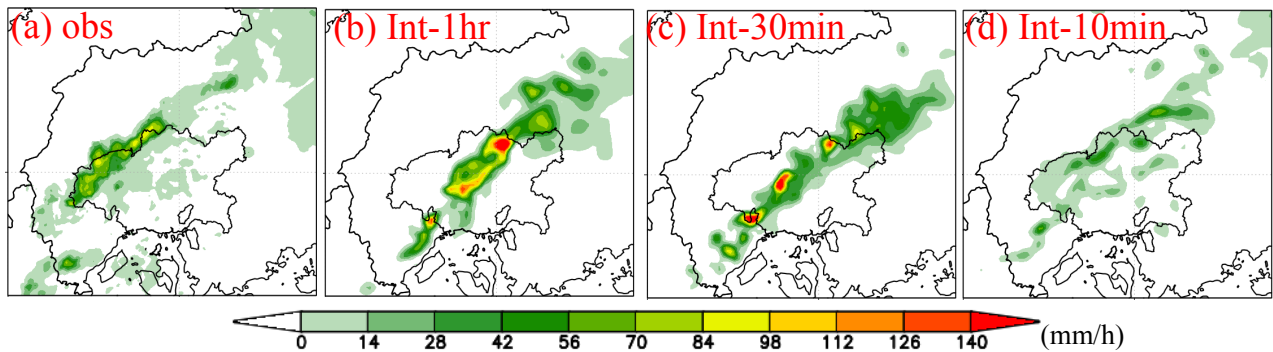

Figure 6. Rainfall intensity distribution at 0:00 August 20. (a) X-band MP radar, (b) Assimilation at 1-hour interval, (c) Assimilation at 30-minute interval, (d) Assimilation at 10-minute interval.
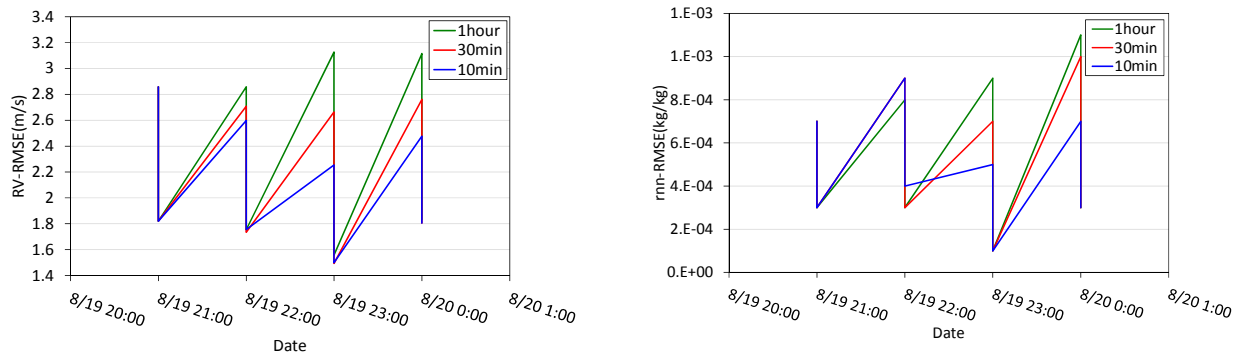

Figure 7. Time series of RMSE (left: radial velocity, right: rain mixing ratio).

4.2 Comparison of hourly rainfall

Figure 8 shows a series of hourly rainfall distributions from 1:00 August 20 to 3:00 August 20. Radar-AMeDAS observed at 1:00 in the western part of Hiroshima city two sets of precipitation cells, which shifted toward the east with merging into a system and increasing its intensity.

At 1:00 WRF-3DVAR predicts only one precipitation system in all cases. The locations of the precipitation system in case (b) at 1-hour interval and case (b) at 30-minute interval are sifted in the northeast direction compared with radar-AMeDAS. WRF-3DVAR in case (d) at 10-minute interval gives slightly better prediction. At 2:00 WRF-3DVAR in all cases fails to predict the heavy rain events in the southwest of Hiroshima city. This comes from the result that the numerical model does not generate the continual development of cumulonimbus in the southwest of Hiroshima city. At 3:00 the results by WRF-3DVAR at 1-hour interval and 30-minute interval show that the precipitation system is going out of Hiroshima city in the northeast direction. The case at 10-minute interval can detain the system in Hiroshima city although the precipitation intensity is significantly underestimated compared with radar-AMeDAS. Figure 8 (e) shows the results with no data assimilation under the same boundary conditions as those in cases (b) to (d) and different initial condition coming from MSM analysis data. The figure 8 (e) clearly claims that the mesoscale convective system that brought heavy rain over Hiroshima city may be overlooked without data assimilation. These results indicate that data assimilation using X-band MP radar data can improve the performances of WRF. Suitable initial condition made by a short interval cycle enhances the accuracy of numerical prediction, resulting in a longer lead time for flood fighting and evacuation.

4.3 Assimilation effects on wind and moisture fields

4.3.1 Comparison of initial fields of wind and vapor mixing ratio

We compare the initial fields of wind and vapor mixing ratio between cases with assimilation and without assimilation to quantify the effect of data assimilation. Figure 9 shows wind vector distribution at 900 hPa. The case without assimilation (left in Figure 9) shows uniform wind direction around Hiroshima city. On the other hand, the results by data assimilation at 10-minute interval (right in Figure 9) demonstrates that the southern wind from Hiroshima bay meets the southwest wind from the neighboring prefecture to convergence, which is indicated by two arrows in Figure 9. The convergence of wind promotes convective motions. Figure 10 shows the difference in vapor mixing ratio between the results with assimilation and without assimilation (assimilation

minus no assimilation) along line A shown in Figure 9. The positive value represents increased mixing ratio induced by assimilation cycle. High mixing ratio area exists on the east side and extends to about 500 hPa. This condition is favorable for convective cells to rapidly evolve.
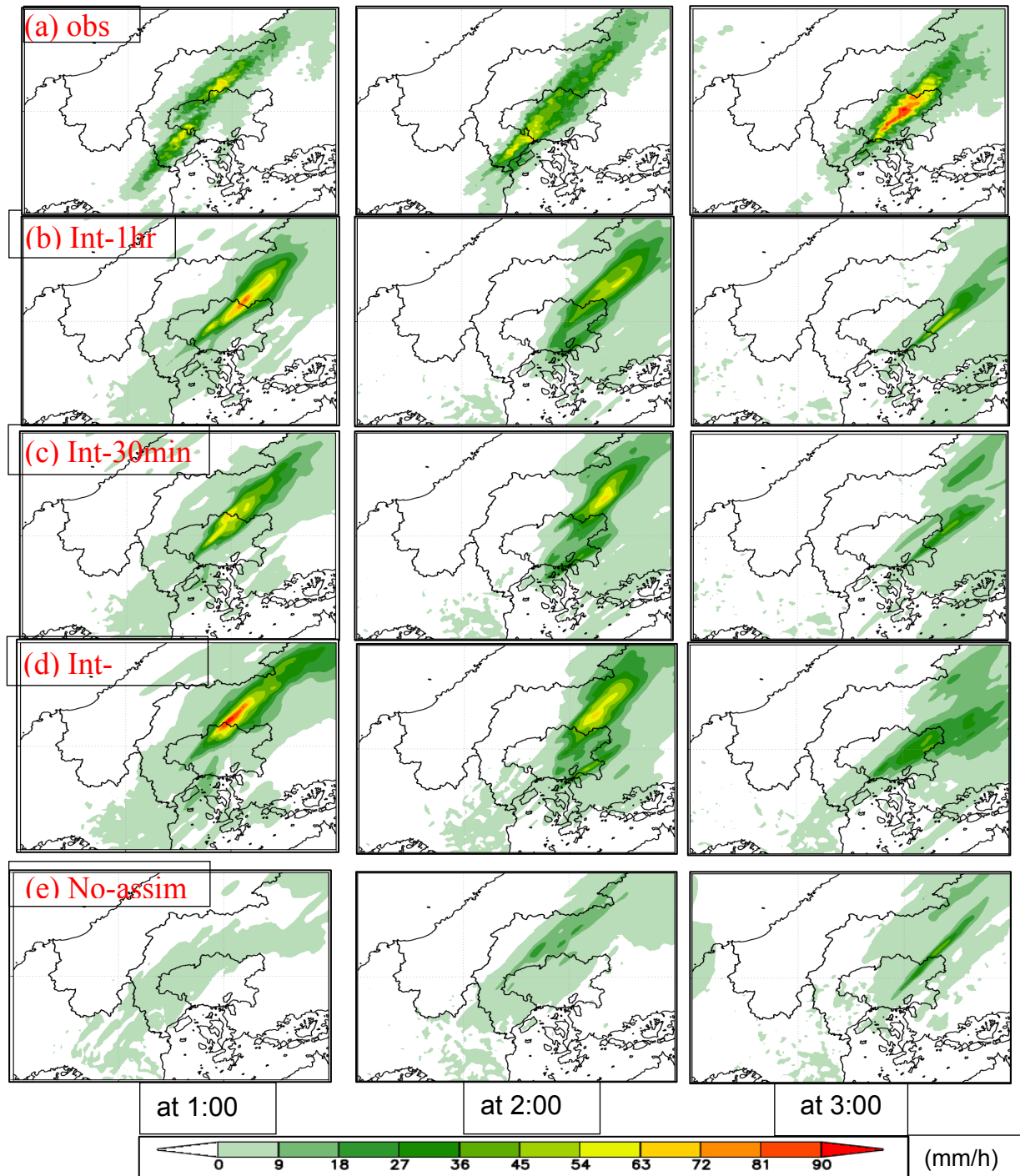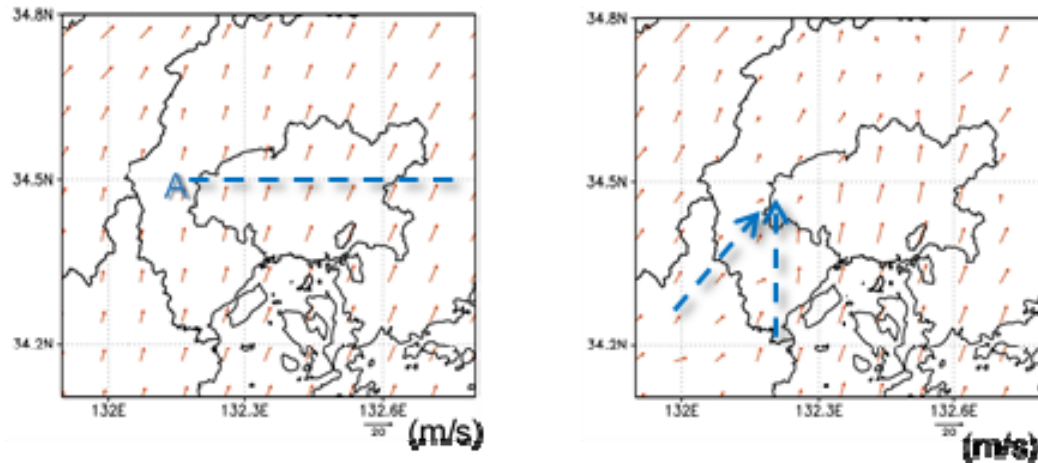

Figure 8. Hourly rainfall distribution from 1:00 August 20 to 3:00 August 2.
(a) radar-AMeDAS, (b) Assimilation at 1-hour interval, (c) Assimilation at 30-minute interval,
(d) Assimilation at 10-minute interval, (e) Non-assimilation.

Figure 9. Initial wind velocity distribution at 900 hPa. Left: non-assimilation, right: assimilation at 10-minute interval.
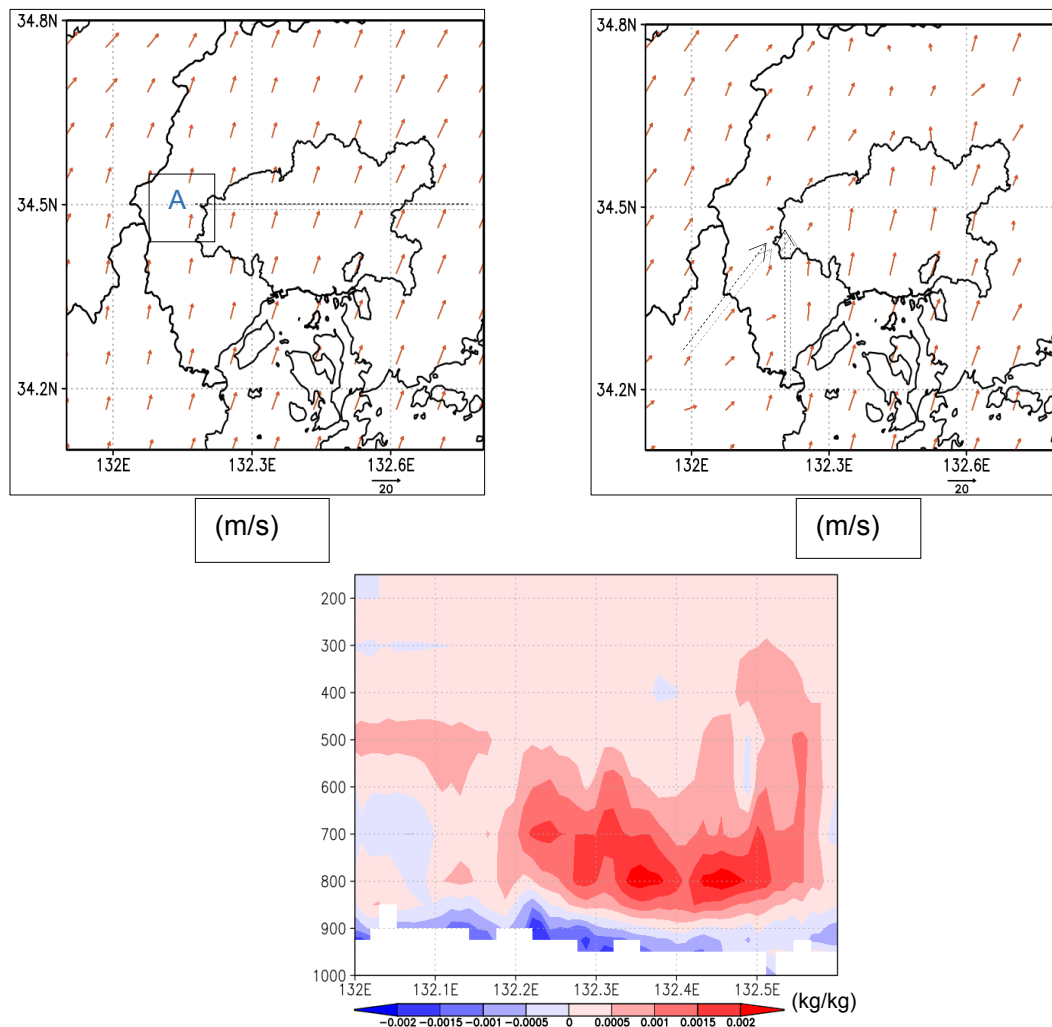
Figure 10. Difference in initial vapor mixing ratio along line A between the cases with and without data assimilation.

4.3.2 Effects of data assimilation interval

We analyze the factors which yield the difference between 10 minute interval cycle and other interval cases at 3:00. Here we discuss how the data assimilation interval changes the vapor supply from the Seto inland Sea into Hiroshima city. Figure 11 shows the magnitude of the vapor flux in the surface layer up to 900 hPa and wind vectors at 900 hPa. The vapor flux is calculated by vertical integration from ground surface to 900 hPa. The figure explains that as the data assimilation interval becomes shorter, the high vapor flux area

over Hiroshima bay approaches to Hiroshima city and winds tend to converge over Hiroshima city as shown in dashed circle. Hence vapor supply to the Hiroshima city is increased at the interval of 10 minutes. The transport of high moisture into Hiroshima city may have played an important role in sustaining precipitation cells.
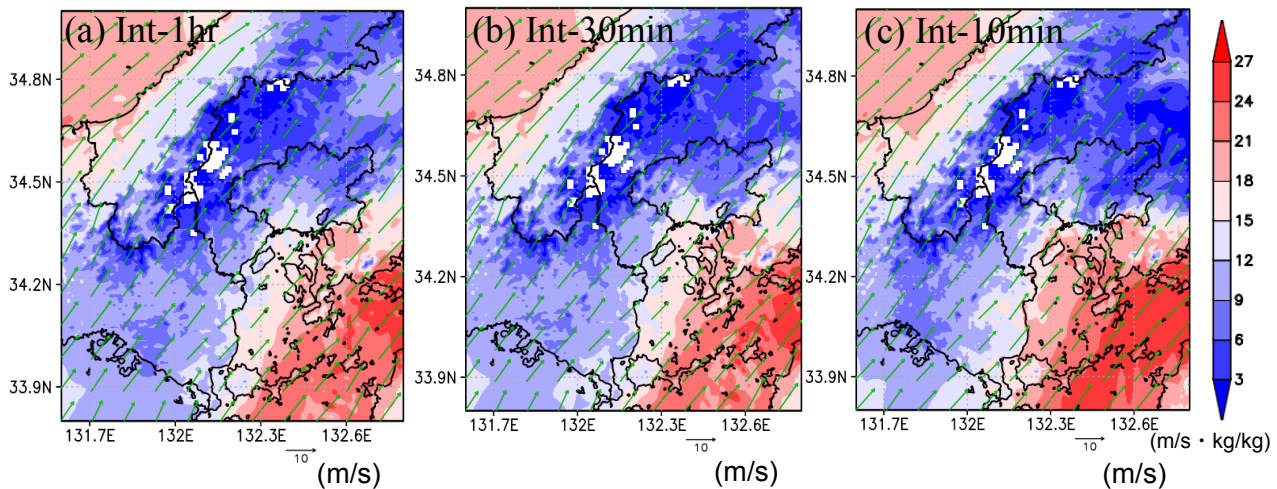
Figure 11. Vapor flux (magnitude) and wind vectors at 900 hPa at 2:00 August 20.Data assimilation interval, (a) 1 hour, (b) 30 minutes, (c) 10 minutes.

5   CONCLUSIONS

We carried out numerical prediction using WRF coupled with a 3-D variational method to quantify the effects of the X-band radar data assimilation. The findings can be summarized as follows:
1. Data assimilation at 10-minute interval produces the most suitable rainfall field probably because the short interval suppresses the error accumulated during time integration.
2. Band-shaped precipitation system at 1:00 is predicted with X-band MP radar data assimilation. In particular data assimilation at 10-minute interval predicts the location of rainfall best.
3. X-band MP radar data assimilation induces the favorable environment for convective rainfall by modifying wind vectors and vapor fields.

REFERENCES

Japan Meteorological Agency, (2014). *Techniques of Precipitation Analysis and Prediction Developed for High Resolution Precipitation Nowcasts.*

Picciotti, E., Marzano, F.S., Anagnostou, E.N., Kalogiros, J., Fessas, Y., Volpi, A., Cazac, V., Pace, R., Cinque, G., Bernardini, L., De Sanctis, K., Di Fabio, S., Montopoli, M., Anagnostou, M.N., Telleschi, A., Dimitriou, E. & Stella, J. (2013). Coupling X-Band Dual-Polarized Mini-Radars and Hydro-Meteorological Forecast Models: The HYDRORAD Project. *Natural Hazards Earth System Science*, 13, 1229-1241.

Rabier, F., Klinker, E., Courtier, P. & Hollingsworth, A. (1996). Sensitivity of Forecast Errors to Initial Conditions. Quarterly *Journal of the Royal Meteorological Society*, 122, 121-150.

Xiao, Q., Kuo, Y.H., Sun, J., Lee, W.C., Lim, E., Guo, Y.G. & Barker, D.M. (2005). Assimilation of Doppler Radar Observations with A Regional 3DVAR System: Impact of Doppler Velocities on Forecasts of A Heavy Rainfall Case. *Journal of Applied Meteorology and Climatology*, 44, 768-788.

Sun, J. & Crook, N.A. (1997). Dynamical and Microphysical Retrieval from Doppler Radar Observations Using A Cloud Model and Its Adjoint, Part 1: Model Development and Simulated Data Experiments. *Journal of Atmosphere Science,* 54, 1642-1661.

Parrish, F. & Derbber, C. (1992). *The National Meteorological Center's Spectral Statistical Interpolation Analysis System.* Monthly Weather Review, 120, 1747-1763.

Xie, Y., Lu, C. & Browning, G.L. (2002). *Impact of Formulation of Cost Function and Constrains on Three-Dimensional Variational Data Assimilation.* Monthly Weather Review*,* 130, 2433-2447.

DESIGNING WITH MULTIFUNCTIONALITY: GREEN INFRASTRUCTURE, FLOOD RESILIENCE AND COMMUNITY WELL-BEING

ZORAN VOJINOVIC[(1)], WEERAYA KEERAKAMOLCHAI[(2)], ALIDA ALVES[(3)], ARLEX SANCHEZ[(4)], SUTAT WEESAKUL[(5)] & MUKAND S. BABEL[(6)]

[(1,2,3,4,)] UNESCO-IHE, Westvest 7, 2611 AX Delft, The Netherlands,
z.vojinovic@unesco-ihe.org
[(2,5,6)] Asian Institute of Technology, P.O. Box 4, Klong Luang, Pathumthani 12120, Thailand

ABSTRACT

The traditional way of approaching flood risk mitigation is heavily based on the so-called grey infrastructure (i.e., hard core engineering measures such as pipes, channels, underground storages, etc.) with the primary aim of conveying flood waters from urban areas as soon as it is possible. The notion of multifunctional design of green infrastructure, which is as a central concept in this paper, is to enforce the framework in which a climate adaptive design of urban drainage infrastructure for flood risk mitigation requires a combination of green, blue and grey measures. The present paper deals with a holistic approach for multifunctional design of green infrastructure. "Multifunctionality" has become a popular term in urban landscape design and planning. It has been particularly influential in Europe, where it resonates strongly with the green infrastructure measures being promoted in the European Water Framework Directive. Multifunctional measures refer to such measures that can provide multiple functions. In this paper, the multifunctionality of green infrastructure is demonstrated through a multipurpose design of a detention facility in Ayutthaya UNESCO heritage site (Thailand) which is also combined with other infrastructure measures. This is done by combining a state-of-the-art landscape and hydraulic engineering practice through 1D-2D hydrodynamic model simulation.

Keywords: Green infrastructure; holistic multifunctional design; climate change adaptation; flood risk mitigation.

1   INTRODUCTION

Floods are typically defined as an overwhelming flow of water onto land that is normally dry and which under certain circumstances can cause unprecedented losses and devastation. It is a well-accepted fact that these losses are often the result of a wide range of interactions between different actors and processes which can be natural, human and technology related. Therefore, solutions to flood-related problems should be sought through a variety of measures. Unfortunately, traditional means for dealing with floods and flood-related disasters have been limited in their reach and effect (Vojinovic and van Teeffelen, 2007; Price and Vojinovic, 2008; Mynett and Vojinovic, 2009). However, with reliable data and models it is possible to explore the generation of floods and to simulate the effects in response to any scenario (Abbott et al., 2006). Therefore, the search for optimal solutions is a great challenge for researchers and practitioners, see for example Vojinovic et al. (2006a; 2006b), Barreto et al. (2006), Barreto et al. (2008; 2010), Vojinovic and Sanchez (2008), Vojinovic and Tutulic (2009), Vojinovic et al. (2011; 2012; 2014), Abdullah et al. (2009; 2011a; 2011b), Seyoum et al. (2012), Kumar et al. (2013), Sanchez et al. (2014), Meesuk et al. (2015), Singh et al. (2016), Alves et al. (2016).

The way to respond to the above mentioned challenges is by developing and implementing multifunctional measures that can provide multiple benefits to urban ecosystem services. Traditional drainage solutions are based on fast conveyance of runoff through pipe systems and disposal to places outside from urban areas. More recently, these traditional solutions are recognized as ineffective to reach long-term sustainable drainage systems. New tendencies are nowadays focused on decentralized alternatives in a long-term planning framework including the use of Green Infrastructure (GI), or sustainable practices (or measures), for stormwater management. These new trends offer sustainable and adaptive strategies in front of an unknown future, exposed to climate variability and urban dynamics.

"Multifunctionality" has become a popular term in urban landscape design and planning. It has been particularly influential in Europe, where it resonates strongly with the green infrastructure measures being promoted in the European Water Framework Directive. Multifunctional measures refer to such measures that can provide multiple functions. If more than one function can be identified for a particular measure then such measure can be referred to as the multifunctional measure. Following Lagendijk and Wisserhof (1999), multifunctional land use is achieved if at least one of the following four conditions is met; (1) increase in the efficiency of land use (intensification of land use); (2) interweaving of land use (which they define as the use of the same area for several functions); (3) use of the third dimension of the land (i.e., vertical space such as the

below and/or above ground level along with the surface area); and (4) use of the fourth dimension of the land (i.e., over a certain time frame). The present paper discusses some of the key aspects concerning design of multifunctional measures for stormwater management and flood mitigation.

2   TOWARDS HOLISTIC WAY OF WORKING

One of the key premises in this paper is that we need to adopt a holistic way of working in our efforts to achieve more sustainable drainage systems. To illustrate the holistic way of thinking and working we can start with analyzing the possibilities for design of urban drainage systems. Currently, we are not sufficiently harvesting rainfall/stormwater runoff as a source of water which can be used to preserve our drinking water reserves. There are many opportunities to utilise rainwater, and amongst others, it can be used for various non-drinking purposes such as the flushing of toilets or irrigation of green spaces. Storing rainwater on sites which have multifunctional purposes can bring greater efficiency in land use. Furthermore, the availability of space in urban areas is scarce, so we can also consider how to utilise the actual water surface in a multifunctional way. A good example of multifunctional use of the water surface is the construction of floating buildings.

Moreover, to deal with the challenge of energy scarcity and to minimise the ecological footprint it is important to develop solutions that can utilise internal sources of water, energy and nutrients first before we go on extracting resources from other areas. Productive landscapes can have multiple functions as they can serve not only for amenity and recreational purposes but also to keep urban areas fresh and mitigate heat stress. To enable such way of working, we need to develop holistic approaches which can help us to identify important interactions and interrelatedness between different process that shape vulnerabilities and risk, Figure 1.
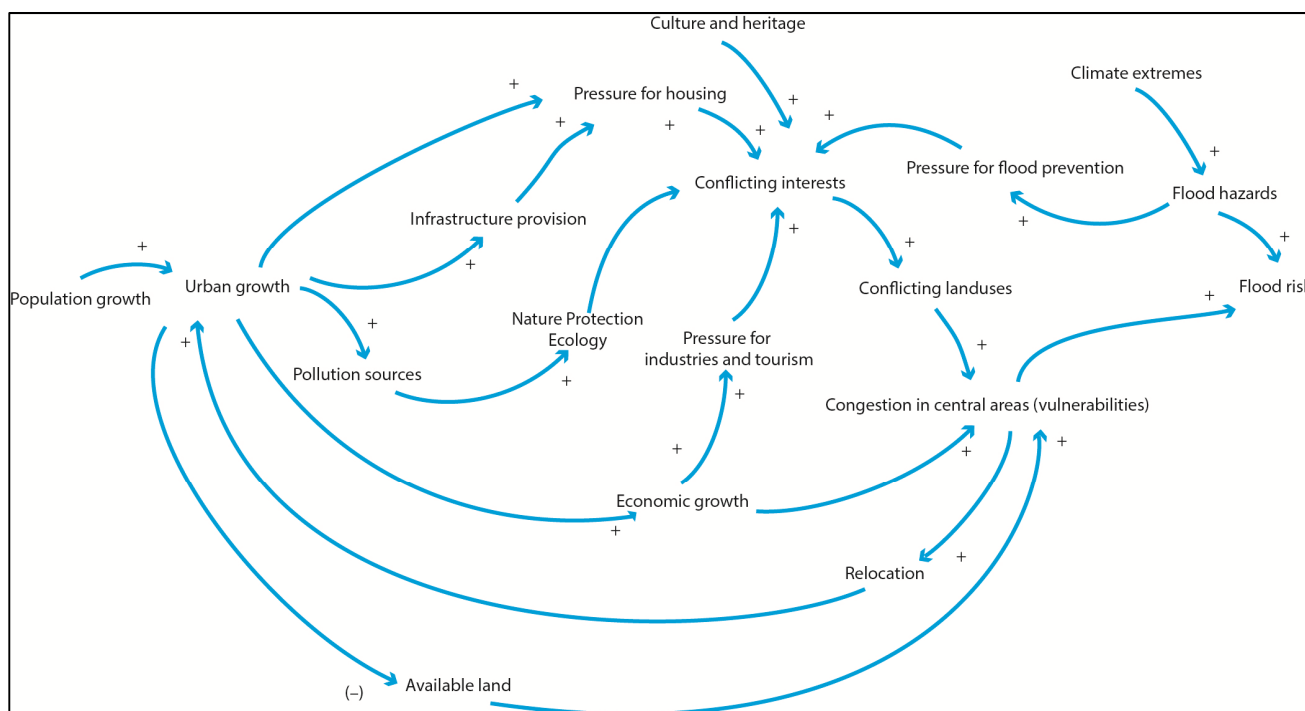

Figure 1. Example of a causal loop representation of urban dynamics – taking the holistic perspective.

Further to the above, holistic planning of drainage systems provides an opportunity for joint efforts by a range of specialists (e.g., water engineers, city planners, micro-climate specialists, building architects, landscape architects and so on) to work together with stakeholders in a continuous pursuit to deliver adaptive and resilient solutions for the positive future.

3   COMBINING DIFFERENT MEASURES FOR FLOOD RESILIENCE

In the holistic planning of urban environments, we will typically look at a variety of measures ranging from green, grey to hybrid. Figure 2 illustrates an example of combining different measures (green, blue and grey) for flood resilience. Starting from the left side, position of a dike/levee aims to mitigate coastal floods at the first place, whereas floating buildings aim at minimizing flood impacts due through its flexible floating structure. If the flood wave would overtop the dike/levee, then the next stage of flood risk mitigation would be to construct amphibious buildings. In case that the flood wave passes further, a set of various green infrastructure measures could be combined. These would be designed to mitigate pluvial floods. The overall idea is that each individual measure is designed in a way so that it works in conjunction with other measures

through an interactive (or interconnected) network (or a set) different means which can enable better adaptive capacity and achieve multiple benefits than any other measure when designed alone.
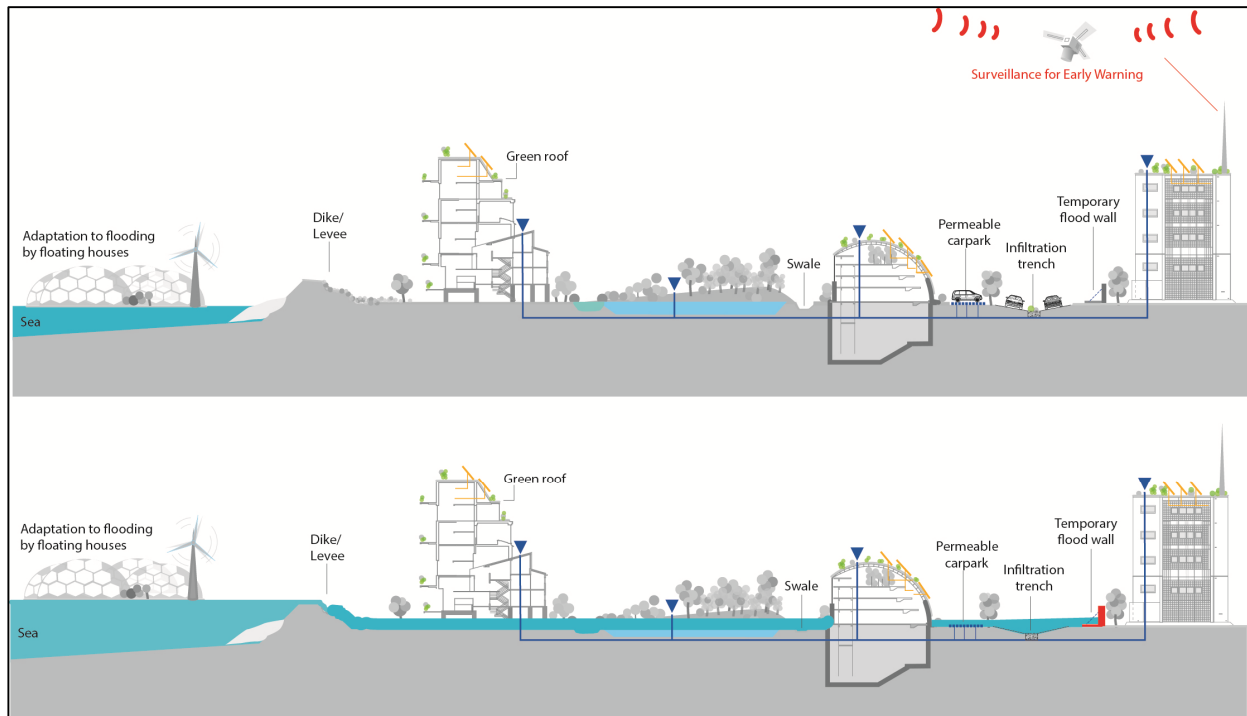

Figure 2. Example of combining different measures (green, blue and grey) for flood resilience (After Vojinovic, 2015).

4   ILLUSTRATION OF THE CONCEPT

4.1   Case study area

The study area is in Ayutthaya province in Thailand which is about 80 km north of Bangkok, the capital city of Thailand, Figure 3. The area is surrounded with three rivers namely Chao Phraya River, Pasak River, and Lop Buri River. The land use is primarily residential with some minor commercial activities. This area is often subject to flooding due to high water levels in these three rivers (and also from local pluvial floods).
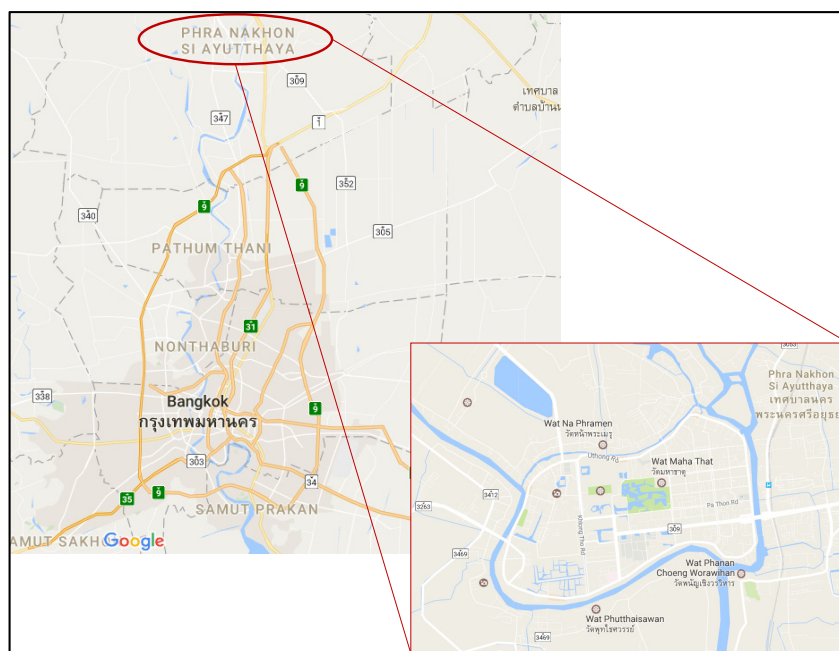
Figure 3. Ayutthaya,Thailand. geographical location is 14°21'08"N latitude and 100°33'38"E longtitude.

4.2 Methodology

For the purposes of the present work, the MIKEFLOOD 1D–2D model of Ayutthaya Island is used to model propagation of excess floodwaters from three main rivers (i.e., Chao Phraya River, Lopburi River, and Pasak Rivers) and canals. 1D MIKE 11 was used for river modelling and 2D MIKE21 model was used for surface flow modelling (Vojinovic et al., 2016a and Vojinovic et al., 2016b). The selection of effective flood mitigation measures was carried out through model simulations of different scenarios. After consultations with key stakeholders the most effective mitigation measures were selected. These measures combined different green and grey measures.

Figure 4 provides an indication of some of the key measures such as construction of a multifunctional detention pond, construction of new canals, strengthening pumping capacity, construction of new openings between different canals, porous pavements, etc. In addition, there is a variety of urban parks and gardens that are proposed around cultural heritage sites which can provide safe routes for walking and cycling for transport purposes as well as sites for physical activity, social interaction and for recreation, Figure 5.

These measures can also enhance environmental benefits through improvements of runoff water quality, infiltration to recharge aquifers, air quality, biodiversity, etc. Furthermore, construction of new canals and fountains would have the ability to moderate temperatures and mitigate heat stress effects.
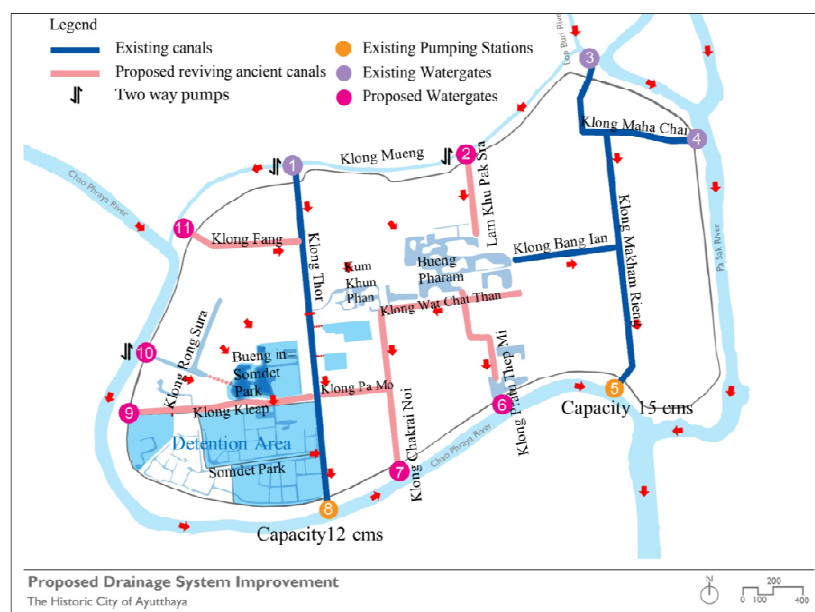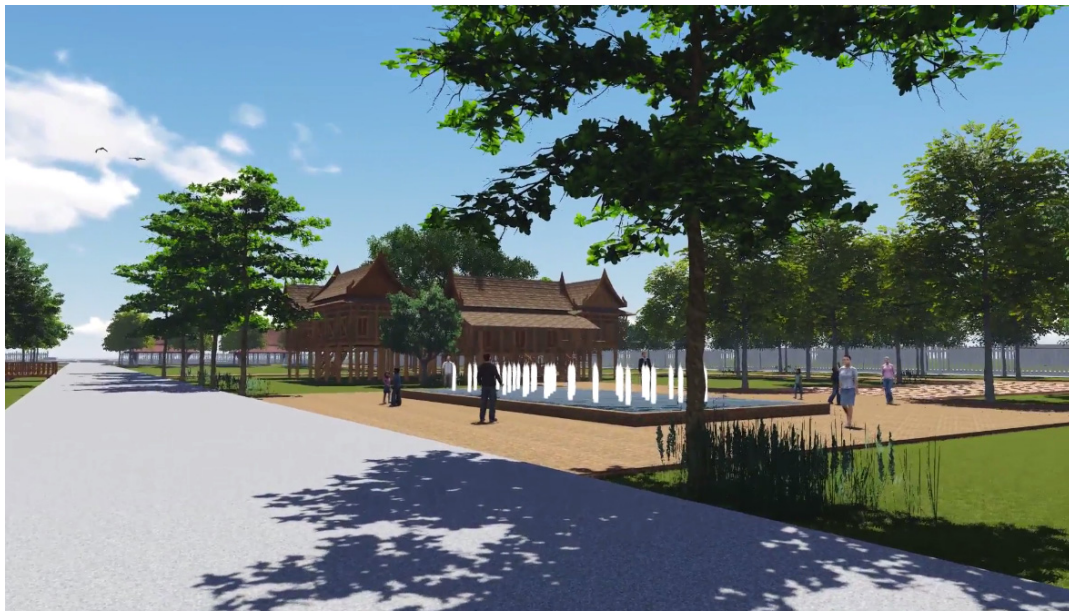

Figure 4. Combination of different infrastructure measures in Ayutthaya, Thailand.

Figure 5. 3D view of the proposed set of measures. The proposed measures can also enhance environmental benefits through improvements of runoff water quality, infiltration to recharge aquifers, air quality, biodiversity, etc.

Figure 6. 3D view of the proposed set of measures. Construction of new canals and fountains would have the ability to moderate temperatures and mitigate heat stress effects.

5   CONCLUSIONS

The present paper describes the efforts to design multifunctional areas in Ayutthaya (Thailand) region that can be used for flood mitigation, recreation and tourism. The same combination of measures also provides a range of social, environmental and cultural benefits by making these areas more vibrant, visually attractive and delivering recreation and cultural/heritage opportunities. The following methodology was applied: stakeholder consultations, data collection and modelling, site selection and evaluation, and development of a conceptual design of multifunctional measures. The work performed demonstrates that the collaboration between different disciplines is a key for successful design of multifunctional flood protection measures.

REFERENCES

Abbott, M.B., Tumwesigye, B.M. & Vojinovic, Z. (2006). The Fifth Generation of Modelling in Hydroinformatics, *7th International Conference on Hydroinformatics*, Acropolis - Nice, France, September, 2091-2098.

Abdullah, A., Rahman, A. & Vojinovic, Z. (2009). LiDAR Filtering Algorithms for Urban Flood Application: Review on Current Algorithms and Filters Test. *Laserscanning*, 38, 30-36.

Abdullah, A.F., Vojinovic, Z. & Price, R.K. (2011a). A Methodology for Processing Raw LIDAR Data to Support 1D/2D Urban Flood Modelling Framework. *Journal of Hydroinformatics*, 14(1), 75-92.

Abdullah, A.F., Vojinovic, Z. & Price, R.K. (2011b). Improved Methodology for Processing Raw LIDAR Data to Support Urban Flood Modelling - Accounting for Elevated Roads and Bridges. *Journal of Hydroinformatics*, 14(2), 253-269.

Alves, A., Sanchez, A., Vojinovic, Z., Seyoum, S., Babel, M. & Brdjanovic, D. (2016). Evolutionary and Holistic Assessment of Green-Grey Infrastructure for CSO Reduction. *Water*, 8(9), 402.

Barreto, W.J., Vojinovic, Z., Price, R. & Solomatine, D. (2006). Approaches to Multi-Objective Multi-Tier Optimisation in Urban Drainage Planning. *7th International Conference on Hydroinformatics*, Acropolis - Nice, France, September.

Barreto, W., Vojinovic, Z., Solomatine, D.P. & Price R.K. (2008). Multi-tier Modelling of Urban Drainage Systems: Muti-objective Optimization and Parallel Computing. *11th International Conference on Urban Drainage*.

Barreto, W., Vojinovic, Z., Price, R.K. & Solomatine, D.P. (2010). A Multiobjective Evolutionary Approach for Rehabilitation of Urban Drainage Systems. *Journal of Water Resources Planning and Management*, 136(5), 547-554.

Kumar, D.S., Arya, D.S. & Vojinovic, Z. (2013). Modelling of Urban Growth Dynamics and its Impact on Surface Runoff Characteristics. *Computers, Environment and Urban Systems*, 41, 124–135.

Lagendijk, A. & Wisserhof, J. (1999). *Meer ruimte voor kennis. Verkenning van de kennisinfrastructuur voor Meervoudig Ruimtegebruik. (Give Knowledge to Space, Give Space to Knowledge, Part 1: Exploration of Knowledge Infrastructure for Multifunctional Land use)* Series, Part 1, RMNO Report 136. Den Haag: NLRO.

Meesuk, V., Vojinovic, Z., Mynett, A. & Abdullah, A.F. (2015). Urban Flood Modelling Combining Top-View Lidar Data with Ground-View Sfm Observations. *Advances in Water Resources*, 75, 105-117.

Mynett, A. & Vojinovic, Z. (2009). Hydroinformatics in Multi-Colours – Part Red: Urban Flood and Disaster Management. *Journal of Hydroinformatics*, 11, 166-180.

Price, R.K. & Vojinovic, Z. (2008). Urban Flood Disaster Management. *Urban Water*, 5(3), 259-276.

Sanchez, A., Medina, N., Vojinovic, Z. & Price, R. (2014). An Integrated Cellular Automata Evolutionary-Based Approach for Evaluating Future Scenarios and the Expansion of Urban Drainage Networks. *Journal of Hydroinformatics*, 16(2), 319–340.

Seyoum, S.D., Vojinovic, Z., Price, R.K. & Weesakul, S. (2012). Coupled 1d and Non-Inertia 2d Flood Inundation Model for Simulation of Urban Pluvial Flooding. *Journal of Hydraulic Engineering*, 138(1), 23-34.

Singh, R., Arya, D.S., Taxak, A. & Vojinovic, Z. (2016). Impact of Climate Change on Rainfall Intensity-Duration-Frequency (IDF) Curves in Roorkee. *Water Resources Management*, 144, 1-14.

Vojinovic, Z., Bonillo, B., Chitranjan, K. & Price, R. (2006a). Modelling Flow Transitions at Street Junctions with 1D and 2D Models. *7th International Conference on Hydroinformatics*, Acropolis - Nice, France, September, 4-8.

Vojinovic, Z., Solomatine, D.P. & Price, R.K. (2006b). Dynamic Least-Cost Optimisation of Wastewater System Remedial Works Requirements. *Water Science and Technology*, 54, 467-475.

Vojinovic, Z. & van Teeffelen, J. (2007). An Integrated Stormwater Management Approach for Small Islands in Tropical Climates. *Urban Water Journal*, 4(3), 211 – 231.

Vojinovic, Z., Sanchez, A. & Barreto, W. (2008). Optimising Sewer System Rehabilitation Strategies between Flooding, Overflow Emissions and Investment Costs. *11th International Conference on Urban Drainage*, Edinburgh, Scotland, 31st August – 5th September, 31.

Vojinovic, Z. & Tutulic, D. (2009). On the use of 1D and coupled 1D-2D Approaches for Assessment of Flood Damages in Urban Areas. *Urban Water Journal*, 6(3), 183–199.

Vojinovic, Z., Seyoum, S.D., Mwalwaka, J.M. & Price, R.K. (2011). Effects of Model Schematization, Geometry and Parameter Values on Urban Flood Modelling. *Water Science and Technology*, 63(3), 462-467.

Vojinovic, Z., Seyoum, S., Salum, M.H., Price, R.K., Fikri, A.F. & Abebe, Y. (2012). Modelling Floods in Urban Areas and Representation of Buildings with a Method based on Adjusted Conveyance and Storage Characteristics. *Journal of Hydroinformatics*, 5, 1150–1168.

Vojinovic, Z., Sahlu, S., Seyoum, S., Sanchez, A., Matungulu, H., Kapelan, Z. & Savic, D. (2014), Multi-Objective Rehabilitation of Urban Drainage Systems under Uncertainties. *Journal of Hydroinformatics*, 16(5), 1044-106.

Vojinovic, Z. (2015). *Flood Risk: The Holistic Perspective, From Integrated to Interactive Planning for Flood Resilience*, IWA Publishing, London.

Vojinovic, Z., Hammond, M., Golub, D., Hirunsalee, S., Weesakul, S., Meesuk, V., Medina, N., Sanchez, A., Kumara, S. & Abbott, M. (2016a). Holistic Approach to Flood Risk Assessment in Areas with Cultural Heritage: A Practical Application in Ayutthaya, Thailand. *Natural Hazards* 2016, 81, 589–616.

Vojinovic, Z., Keerakamolchai, W., Weesakul, S., Pudar, R.S., Medina, N.P. & Alves, A. (2016b). Combining Ecosystem Services with Cost-Benefit Analysis for Selection of Green and Grey Infrastructure for Flood Protection in a Cultural Setting. *Environments*, 4(1), 3.

FLOOD PROCESS IN OTOMO DISTRICT, IWAIZUMI CITY, IWATE PREFECTURE DUE TO TYPHOON NO.10, 2016

HIROTAKA MORIYA[1], YASUO NIHEI[2], RIKITO MIZUNO[3] & TOMOYA KATAOKA[4]

[1,2,3,4]Department of Civil Engineering, Tokyo University of Science, Chiba, Japan
7616630@ed.tus.ac.jp; nihei@rs.noda.tus.ac.jp; 7615618@ed.tus.ac.jp; tkata@rs.tus.ac.jp

ABSTRACT

Typhoon No.10 has brought heavy rain to Northern Japan especially to the Tohoku and Hokkaido regions, and caused heavy flooding. The rain recorded is 66mm per hour in Iwaizumi city, Iwate prefecture. Due to the heavy rain, 21 people are dead or missing in Iwaizumi city. Nine of the dead are in a nursing home located in the Otomo district, Iwaizumi city, and near the Omoto River. In this study, field survey and numerical analysis are conducted to understand the flood inundation mechanism in the Otomo district, Iwate prefecture. The numerical simulation is done with runoff analysis and 2D horizontal flood simulation. From this data, we aim to investigate the inundation process in the initial flooding, which is important for early evacuation. The results show there are two stages of flooding that are mainly caused by mountainous area and the upstream of the Omoto River. The initial flow velocity is about 1.0m/s. Therefore, it is difficult for the elderly to evacuate in this situation. From the above results, it is confirmed that early evacuation is necessary in this kind of situation.

Keywords: Flood disaster; Omoto River; flood simulation; field survey; heavy rain.

1   INTRODUCTION

The occurrence of Typhoon No. 1 was very late in July 2016. Since July 2016, typhoons had been frequent, and in August, Typhoons no. 7, 9, 10 and 11 landed in Japan and moved to the northern part of Japan along the Pacific Coast. Typhoon No. 10 landed on the Pacific side of the Tohoku region for the first time on August 30, 2016. It brought heavy rain mainly to the Tohoku and Hokkaido regions. In the Iwate prefecture, hourly rainfall of 80 mm was observed in Miyako city and Kuji city, and in Iwaizumi city, an hourly rainfall amount of 70.5 mm and 24-hour rainfall of 203.5 mm were recorded (Japan Meteorological Agency, 2016; Michiya et al., 2017).

Due to such heavy rain, Iwate prefecture had major damage in Japan. As shown in Figure 1(a), the number of dead and missing persons was 27 people in Japan and 23 people in Iwate prefecture, of which 21 people were in Iwaizumi city, Iwate prefecture. In a nursing home in Otomo district of the same town, nine elderly people were dead. In order to clarify the above flooding situation, we have conduct a field survey in the Otomo district, Iwaizumi city, on September 9, 2016, and then conducted a numerical analysis to grasp the progress of the flood. In this study, we have first conducted the flood mark survey in the Omoto River that flows through the Iwaizumi city, Otomo district, and investigated flooding conditions and the flow pattern around it. Next, we have carried out a numerical analysis that combines runoff analysis and 2D horizontal flow calculations, and examined the temporal variations of the flood conditions in the Otomo district, Iwaizumi city.

2   STUDY SITE AND FLOOD SITUATION

2.1 Study site

The study site selected was the Omoto River and its surrounding area flowing through the Otomo area of Iwaizumi city, Iwate prefecture. Shown in Figure 1 is the nursing home where the most serious damage occurred as mentioned above and it is located in the Otomo district. The Omoto River flows from Kunizakai Pass located in the Kitakami Mountains with an altitude of approximately 1,300 m. On the way, it merges with Okawa River and Shimizu River and flows into the Pacific Ocean. The Omoto River is a class B river with a length of 65 kilometers in the main stream and 731 km^2 in the river basin. Most of the river basin is in mountainous areas. Designated rainfall is 246 mm per 2 days, which has a return period of 1/50. Designated high water discharge is set at 3000 m^3/s. As a hydrological observation, there is an Akashika water level observatory station at 8.7 km from the estuary and Iwaizumi AMeDAS observatory station 29.9 km away as shown in Figure 1. The Otomo district is located 19.4 km from the estuary of the Omoto River. It is located along National Route 455 and the Omoto River. There is no river dike near this district around the Omoto River. The difference between the low-flow water level of the river and the ground level near the nursing home was about 2.5-3.5 m.

(a)

	Human damage [people]			House damage [case]				
	Dead	Missing	Injured	Entire collapse	Half collapse	Paritial damage	Above the floor level inundation	Under the floor level inundation
Hokkaido	2	2	2	30	91	913	135	302
Iwate prefecture	20	3	4	472	2281	78	104	1362
(Iwaizumi city)	(19)	(2)	(0)	(356)	(367)			
Others	0	0	9	0	0	152	2	30
Total	22	5	15	502	2372	1143	241	1894
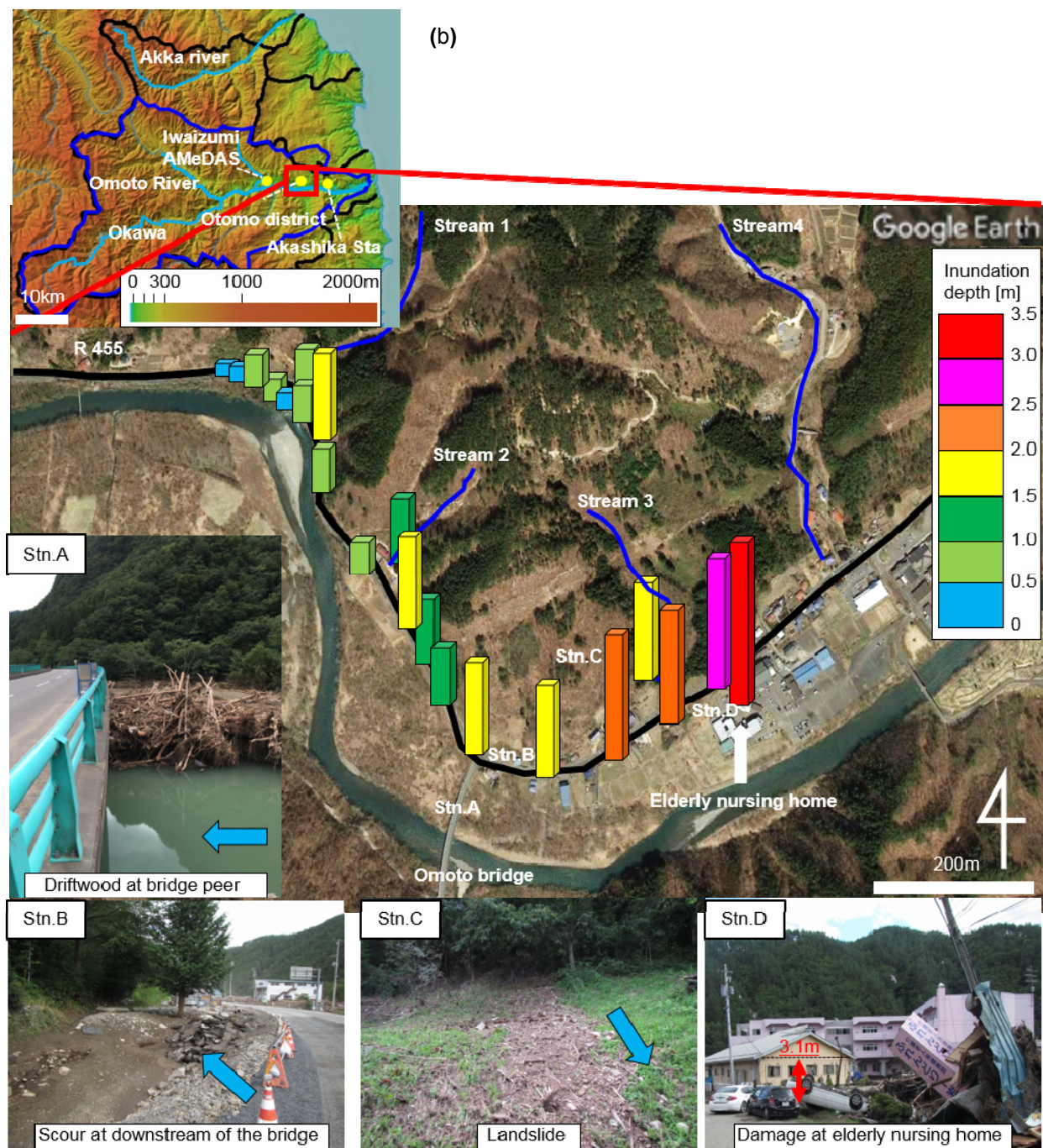
Figure 1. (a) Damage due to Typhoon No. 10 in 2016 (b) Maps for the inundation depth and damages in the study site.

2.2   Summary of rainfall and flood

Typhoon No. 10 occurred near Hachijojima on August 19, 2016, moved southwest and then changed course to the northeast on August 26. It strengthened as it went north, landed near Ofunato city, Iwate prefecture, at 6 pm on the 30th, and passed through the Tohoku region to the Sea of Japan. Figure 2 shows the timeline of the hourly rainfall, accumulative rainfall at the Iwaizumi AMeDAS, and water level at Akashika Station on August 30, 2016. The accumulated rainfall is calculated from 12 am, August 29, 2016. The results indicated that the rainfall rapidly increased at 3 pm on August 30. The hourly rainfall measurements were 33.5, 29, 62.5, and 35 mm at 4 pm, 5 pm, 6 pm and 7 pm, respectively. The daily and 2-day rainfall was 195 mm and 248 mm, respectively. The first and third hours recorded the highest values of rainfall ever. The river water level rose moderately until 3 pm on August 30. Thereafter, the water level increased rapidly and the peak of the water level appeared at 8 pm. Thus, it can be seen that the water level quickly increased in relation to the rapid increase of rainfall.

Figure 2(b) shows the return period of rainfall at Iwaizumi AMeDAS during the flood. Previous data from 1976 to 2016 was used to calculate 1, 3, 24, and 48 hour's rainfall using five different software from the Hydrological Statistics Utility (Japan Institute of Country-ology and Engineering, 2016). The average values are shown in the Figure 2(b). As a result, the average values of the return period of 1, 3, 24, and 48 hour's rainfall amounted to 76, 67, 24 and 30 years, respectively. It was found that the return period for 1 and 3 hours' rainfall was large. Although the 48-hour rainfall (=248 mm) exceeded the designated rainfall (=246 mm), the return period was 30 years.

Figure 2. (a) Time series of hourly and accumulative rainfall at Iwaizumi AMeDAS and water level at Akashika observatory (Accumulative rainfall is calculated from 12 am August 29, 2016.) (b) Return period of 1, 3, 24, 48 hours' rainfall (values in the parentheses shows minimum and maximum values of return periods).

	1hour	3hours	24hours	48hours
Rainfall [mm]	70.5	126.5	195	248
Return period [year]	76 (25~149)	67 (50~91)	24 (20~27)	30 (20~42)
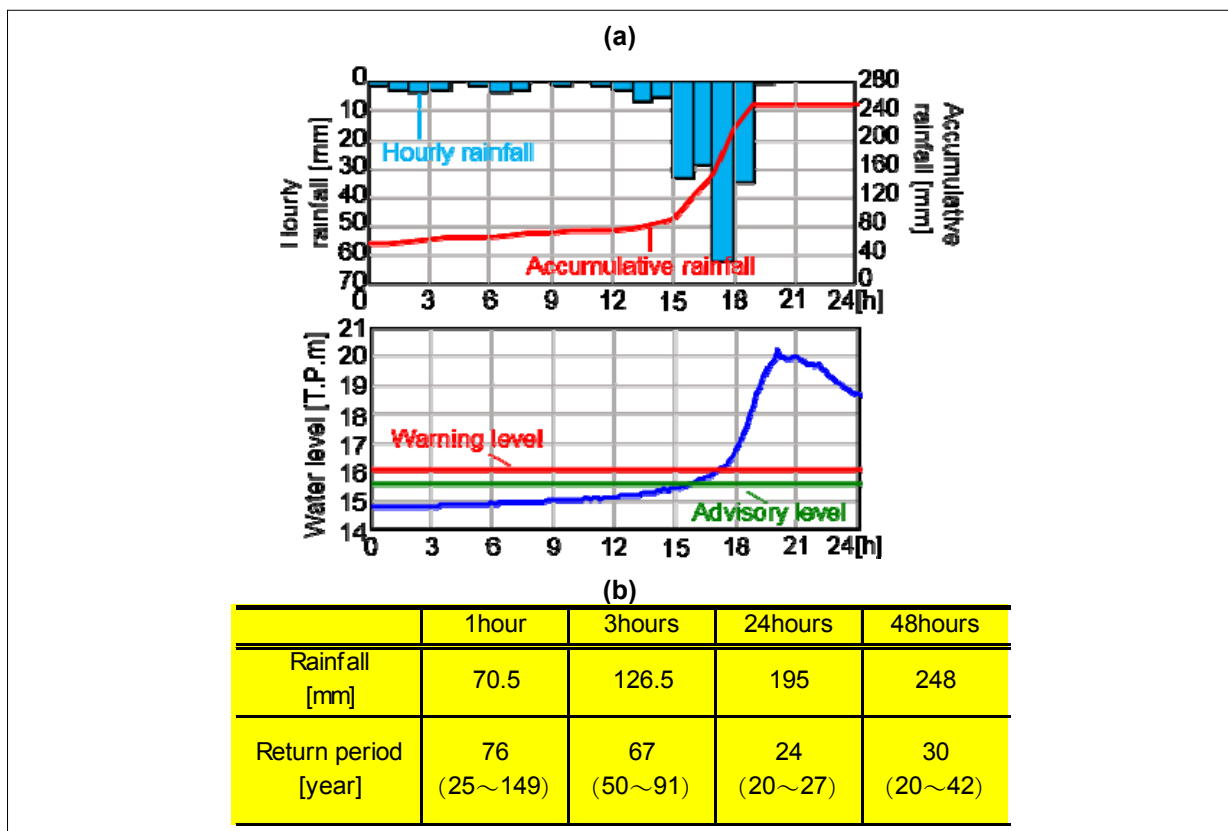
2.3   Flood process based on resident testimony

The testimonies by the residents for the flood process in the Otomo districts were summarized in this section. The mayor of Iwaizumi city confirmed that the water level of the Omoto River around the elderly nursing home was not high at 3:30 pm (Yomiuri Shimbun on Sep. 2). Around 5:30 pm, a person in the nursing home saw that the parking behind the nursing home was flooded (Yomiuri Shimbun on Sep. 1). It was also found that at 5:00 pm, the flooded water from streams flowing into the nearby mountain area reached to Route 455 (Yomiuri Shimbun on Sep. 1). At 6:10 pm, residents of the nursing home unexpectedly noticed that water was coming to the entrance of the nursing home and then the water level increased rapidly (Yomiuri Shimbun on Sep. 1). The water level started to decrease at around 11 pm. It was clear that the water level increased rapidly at 6 pm and flooding started at 5 pm.

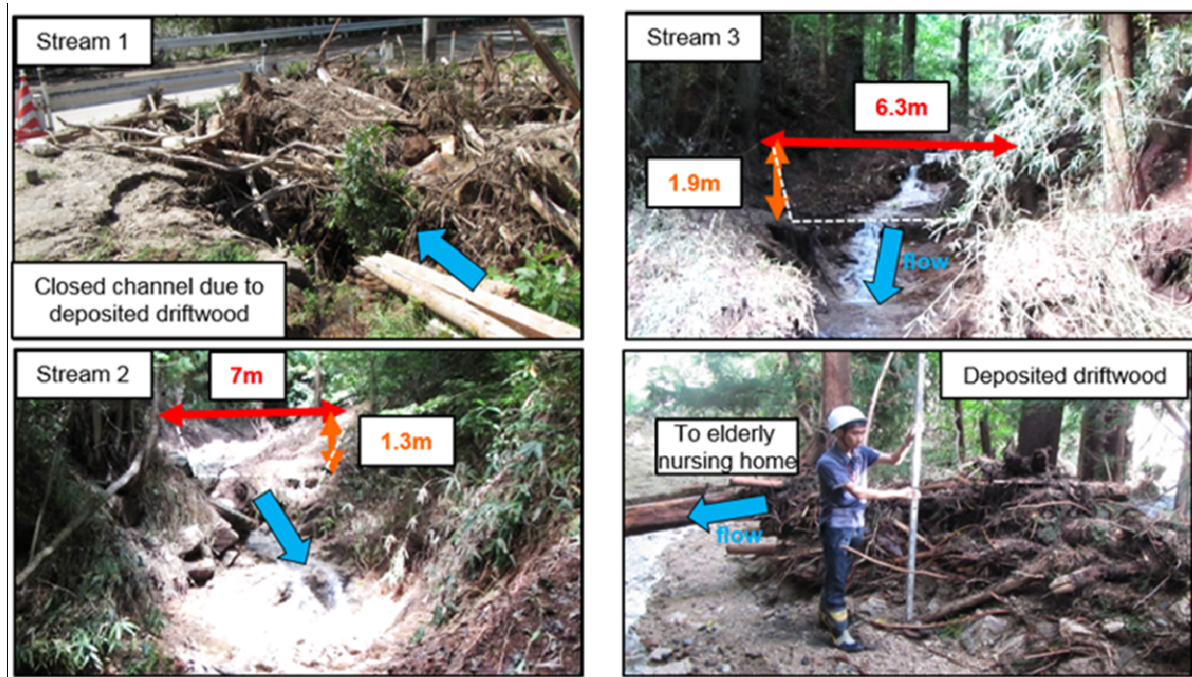## 3 UNDERSTANDING OF INUNDATION SITUATION BASED ON FIELD SURVEY

Figure 3. Water marks in three streams.

3.1 Survey method

To understand the flood process in this disaster, field surveys were conducted on September 9 and October 18, 19, 2016. In this study, we found water marks along the river channel and surrounding roads and then measured the inundation height and depth. We also investigated the water marks and channel width in the surrounding streams. The study area was about 1200 m upstream from the nursing home in the Iwaizumi city, Otomo district, where the remarkable damage occurred as mentioned above. The severely damaged building of the nursing home was a single story, although a three-story building was nearby.

In the measurements, we selected reliable water marks on the side wall of the building and guard rails to measure the inundation depth from the ground using a staff. At the same time, the ground elevation was measured with RTK-GNSS (Trimble R4 and R6). The sum of inundation depth and ground level was taken as the inundation height. Number of measurement points for inundation depth and height were 21; the point before the home was included. Also, we conducted a field survey at three streams near the nursing home as shown in Figure 1.

3.2 Longitudinal distribution of inundation depth and height

Figure 1 shows the longitudinal distribution of measured inundation depth on Google Earth. Photos for representative disaster are shown in the figure. The results indicated that the inundation depth increased from upstream to downstream in the study site. The inundation depth was 0.2 to 1.7 m on the upstream area, 1.0 to 1.8 m near the Otomo Bridge and 1.8 to 2.5 m on the downstream area. In addition, the inundation depth was 3.1 m around the nursing home.

Water marks in the three streams are shown in Figure 3. A lot of driftwood was trapped in Stream 1, which has the largest basin area among three streams. This means that the channel clogging occurred due to driftwood and then water from Stream 1 flooded Route 455 and then inflowed into the Omoto River. The inundation depth was 0.9 m at the Stream 1. At the exits of Streams 2 and 3, the driftwood and a large amount of sediments were deposited and clogging did not appear. The inundation depths were 1.3 m and 1.9 m at Streams 2 and 3, respectively. This fact suggests that a large amount of flood water flowed into all three streams. Also, at Stream 3, which is close to the nursing home, the exit was partially blocked by driftwood and the flow direction was changed to the downstream side corresponding to the nursing home.
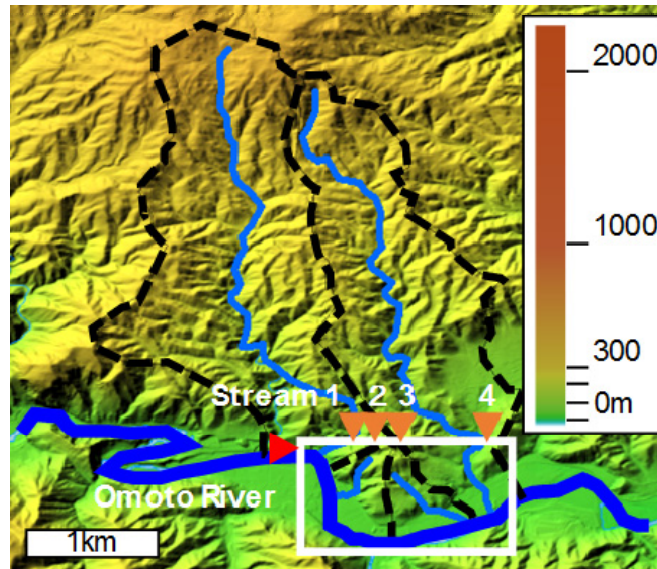
Figure 4. 2D computational domain drawn by a white line and the catchment area of the streams depicted by a black dashed line. The inflow points at upstream of the Omoto.

4 INVESTIGATION OF FLOODING CHARACTERISTICS BY NUMERICAL ANALYSIS

4.1 Computational model and conditions

Flood flooding simulation has been carried out by various researchers (Batesa et al., 2000; Patro et al., 2009; Vozinaki et al., 2012). To investigate the detailed temporal variations of the flood process in the Otomo district, Iwaizumi city, we performed runoff analysis and 2D horizontal flood simulation. The runoff analysis was conducted to evaluate the inflow discharge from the upstream area of the Omoto River and the surrounding streams. We examined the horizontal flow pattern and inundation process from the 2D flood simulation. MIKE 11 RR (Urban model) and iRIC Nays 2D Flood (Wongsa, 2014; Shokory et al., 2016; Jamrussri et al., 2017) were used for the runoff analysis and 2D flow simulation, respectively. The computational area of the 2D horizontal flood simulation is the range of the white frame shown in Figure 4. The computational area included the Otomo district and nursing home and was 1595 m * 755 m. The target area in the runoff analysis used for the inflow conditions was the upper stream from the 2D calculation area of the Omoto River with the basin area of 547 km^2 and the four streams shown in Figure 4. The basin areas of the Streams 1, 2, 3 and 4 were 2.8, 0.2, 0.2, 2.1 km^2, respectively. In the runoff analysis, the rainfall data at 10 min intervals at the Iwaizumi AMeDAS was given as the average rainfall over whole basin of the Omoto River. In the 2D horizontal flood simulation, the inflow discharge obtained from the runoff analysis of the Otomo River was given at the upstream boundary condition. In addition, the lateral inflow from four streams into the computational domain was set using the runoff analysis at each stream. The water level at the downstream boundary was given in line with the measured water level at the Akashika water level observatory. A numerical elevation model with 5 m mesh was applied for the bathymetry data. The computational grid size was set to 5 m. The coefficient of roughness was set at uniform value of 0.025 m$^{-1/3}$ s.

The computational period was from 3 pm to 10 pm on August 30, 2016. During the computational time, the first one-hour was used for spin-up in which a constant discharge was given at the upstream boundary. The temporal variations of the inflow discharge from the upstream area and the four streams was given from 4pm on the same day.

4.2 Computational results

Figure 5 shows the spatial contour map of water depth to grasp the flooding process in the Otomo district. Here, we showed the computational results at 5:00, 6:20 and 8:00 pm at which the peak of the water level appeared. In addition, although the water depth reached up to 10 m, the upper limit of the water depth was set to 4 m to clarify the initial flood condition. The results showed that although at 5:00 pm flooding from the Omoto River was not found, flooding from the four streams appeared and began to inundate in the lowland area around the Omoto River, including the nursing home. Next, at 6:20 pm, the water level of the Omoto River increased rapidly. Flooding from the upstream of the Otomo district was found, and the area around the nursing home was flooded with water from the river. At 8:00 pm, the water depth exceeded 4.0 m in the whole area. From these, inundation patterns were roughly in agreement with the above-mentioned resident testimonies.
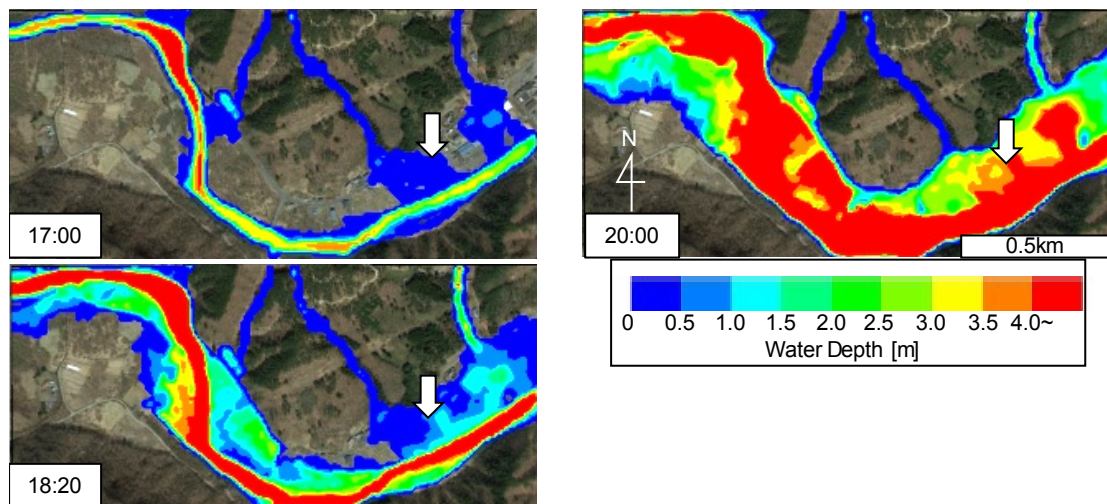
Figure 5. Computational results for spatial patterns of the water depth. The arrow in the figure indicates the location of the nursing home.
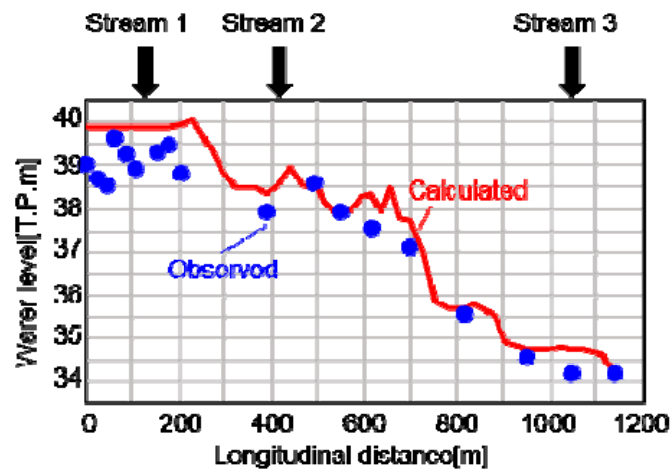

Figure 6. Comparison of longitudinal distribution of observed and calculated inundation height.
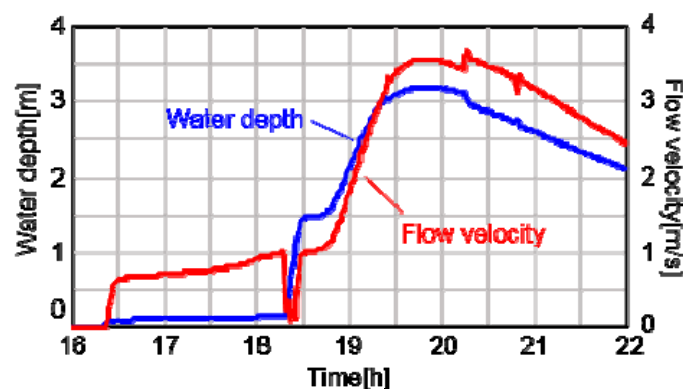

Figure 7. Time series of calculated water depth and flow velocity around the nursing home.

To check the validity of the present calculation, Figure 6 shows the comparison of the longitudinal distribution of observed and calculated inundation height. It was found from this figure that the calculated inundation height gave acceptable congress with the measured values, showing the fundamental validity of the present computation.

Finally, in order to grasp the flooding situation around the nursing home as depicted by the white arrow in Figure 5, the time series of water depth and flow velocity around there is shown in Figure 7. The results revealed that flooding began at 4:30 pm and the same water depth and flow velocity continued until around 6:00 pm. This is due to flowing water from the streams. At this time, the water depth was about 0.2 m, but the

flow velocity was 0.5 to 1.0 m/s. Conditions like these are not ideal for evacuation. After that, the water depth and the flow velocity increased rapidly due to the arrival of the flooding from the upstream region of the Omoto River. The maximum water depth and the flow velocity were 3.4 m and 3.7 m/s, respectively. In this situation, it can be seen that evacuation would have been difficult in these conditions. Therefore, it was once again confirmed that it is more important to carry out evacuations as early as possible before flooding.

5   CONCLUSIONS

The conclusions obtained in this study are as follow: Typhoon No. 10 has brought heavy rain to Northern Japan, especially to the Tohoku and Hokkaido regions, and caused heavy flood disasters. The heavy rain recorded is 66mm per hour in Iwaizumi city, Iwate prefecture. Due to the heavy rain, 21 people are dead or missing in Iwaizumi city. Nine of the dead are concentrated in the nursing home located in the Otomo district, Iwaizumi city, and near the Omoto River. In this study, we have conducted a field survey and a numerical analysis to understand the flood inundation mechanism in the Otomo district, Iwate prefecture. Numerical simulations are done with runoff analysis and 2D horizontal flood simulation. From these data, we are able to investigate the inundation process in the initial flood, which is important for evacuation procedures.

The results show that there are two stages of flooding in the city: flooding from streams and flooding from the Omoto River. The initial flow velocity is 0.5 - 1.0m/s. Therefore, evacuation is difficult. From the above results, it is confirmed that early evacuation is necessary in this kind of situation.

ACKNOWLEDGEMENTS

REFERENCES

Batesa, P.D. & Roo, A.P J. De. (2000). A Simple Raster-based Model for Flood Inundation Simulation. *Journal of Hydrology,* 236, 54-77.

Jamrussri, S. & Toda Y. (2017). Simulating Past Severe Flood Events to evaluate the Effectiveness of Nonstructural Flood Counter Measures in the Upper Chao Phraya River Basin, Thailand. *Journal of Hydrology: Regional Studies*, 10, 82-94.

Japan Meteorological Agency. (2016). RSMC Best Track Data (Graphics) in 2016. Retrieved from http://www.jma.go.jp/jma/jma-eng/jma-center/rsmc-hp-pub-eg/bstve_2016_m.html.

Michiya, I., Higaki, D., Koiwa, N., Takahashi, M., Okamoto, T., Yasuno, M., Tada, N., Nakajima, T., Arai, M., Ochiai, T., Kasahara, R., Saito, A., Sato, S., Hirose, S., Koubu, M., Sato, T., Ootsubo, S. & Makabe S. (2017). Sediment Disasters caused by Typhoon No. 10 on August 30, 2016 in Iwaizumi town and Miyako city, Iwate. J*ournal of the Japan Society of Erosion Control Engineering,* 69(6) 71-79.

Patro, S., Chatterjee, C., Mohanty, S., Singh, R. & Raghuwanshi, N.S. (2009). Flood Inundation Modeling using MIKE FLOOD and Remote Sensing Data. *Journal of the Indian Society of Remote Sensing*, 37, 107-118.

Shokory, J.A.N., Tsutsumi, J.G. & Sakai, K. (2016) Flood Modeling and Simulation using iRIC: A Case Study of Kabul City. *3rd European Conference on Flood Risk Management,* 7.

Vozinaki, A.E.K., Kourgialas, N.N. & Karatzas, G.P. (2012). Estimation of Agricultural Flood Loss in the Koiliaris River Basin in Crete, Greece. *European Water*, 39, 53-63.

Wongsa, S. (2014) Simulation of Thailand Flood 2011. *International Journal of Engineering and Technology*, 6(6), 452-458.

FIELD SURVEY ON THE COMPOUND DISASTER DUE TO
THE KUMAMOTO EARTHQUAKE AND THE FLOOD OF JUNE 2016

TAKUYA SAKURABA[1], YASUO NIHEI[2] & YUKI KURAKAMI[3]

[1,2,3] Department of Civil Engineering, Faculty of Science and Technology, Tokyo University of Science,
7616609@ed.tus.ac.jp;nihei@rs.tus.ac.jp;7615701@ed.tus.ac.jp

ABSTRACT

This study aims to understand the compound disaster at the Kiyamagawa River during the 2016 Kumamoto earthquake and the subsequent flooding in June 2016. Two field surveys had been carried out: one, to study the levee damage during the earthquake, and another, to understand the extent of flood inundation and levee damage at the Kiyamagawa River. The Kumamoto earthquake has caused extensive longitudinal and transverse cracks and crest subsidence of the levee in the water system of the Midorigawa River as well as the Akitsugawa and Kiyamagawa Rivers. The compound disaster around the Kiyamagawa River has occurred as a result of the heavy rain; the rain has caused the levee to collapse, and, in turn, the levee breach has led to flood inundation. In addition to the failure of the sandbags, which have been placed as a countermeasure to crest subsidence, the surveys have revealed the possibility of the sandbags collapsing owing to the piping directly below them.

Keywords: 2016 Kumamoto earthquake; flood disaster; dike; compound disaster; sandbag.

1   INTRODUCTION

In 2016, the Kumamoto earthquake caused a foreshock of magnitude 6.5 on April 14 and a mainshock of magnitude 7.3 on April 16 in the Kumamoto region of Kyushu Island, Japan. The depth of the epicenter was ~10 km in both shocks. A maximum seismic intensity of 7 was observed in these two earthquakes (JMA, 2016). The maximum seismic acceleration values recorded were 1580 and 1791 Gal in the foreshock and mainshock, respectively. The peak period of the earthquake ranged from 0.1 to 1.0 s. This large earthquake caused significant damage to various infrastructure, such as levees and roads. As shown in **Table 1**, severe damage of levees was observed in the Midorigawa and Shirakawa Rivers, which are located near the epicenter of the earthquake. The damage to the levees included longitudinal and transverse cracks and crest subsidence. Emergency restoration work was carried out soon after the earthquake. Small cracks were repaired using cement milk, and the crest subsidence of the levees was restored by setting sandbags on the crest.

Table 1. Damage to levees due to the 2016 Kumamoto earthquake (as of May 2, 2016).

	River system	Number of rivers	Number of damaged areas
Country management river	Midorikawa	4	127
	Shirakawa	1	44
	Kikuchigawa	1	1
Prefecture and city management river	Kumamoto Prefecture	44	318
	Kumamoto City	3	3
	Ooita Prefecture	1	1
	Summation		494

Two months after the earthquake, heavy rains hit the entire region of Kyushu, including Kumamoto Prefecture, over June 20 and 21, 2016. An hourly rainfall of more than 100 mm was recorded in Kumamoto Prefecture. Owing to the heavy short-term rainfall, a levee breach occurred in the Kiyamagawa River, a branch of the Midorigawa River. After the earthquake, several sandbags had been placed on the levee crest as an emergency measure upon observing crest subsidence. As a result of the heavy rains, the water level rose high enough to cause a levee breach and overflowed over the top of the sandbags. The earthquake and flood resulted in a compound disaster at the Kiyamagawa River. Previous examples of compound disasters include the 1948 Fukui earthquake and the heavy rain that followed immediately after. Such compound disasters around large rivers flowing near metropolitan areas may cause catastrophic damage. To mitigate

compound disasters in the future, it is important to investigate the compound disaster caused by the earthquake and flood in the Kiyamagawa River as a case study.

This study aims to understand the compound disaster at the Kiyamagawa River caused by the 2016 Kumamoto earthquake and the subsequent flooding in June 2016. We carried out two kinds of field surveys: one was to study the levee damage during the earthquake, and the other was to understand the extent of flood inundation and levee damage at the Kiyamagawa River.

2   FIELD SURVEY OF LEVEE DAMAGE DUE TO THE 2016 KUMAMOTO EARTHQUAKE

2.1   The 2016 Kumamoto earthquake

As shown in Figure 1, the epicenters of the foreshock and mainshock of the 2016 Kumamoto earthquake were located near the Hinagu and Futagawa faults, respectively. The surface ruptures appeared at 6 km at the Hinagu fault and 28 km at the Futagawa fault (JMA, 2016). A 2.2 m long lateral displacement was observed in Mashiki town, where the seismic intensity was 7. The rivers of the Midorigawa water system are located along the faults, resulting in damage to the river levee as described below.

2.2   Field surveys of the levee damage

2.2.1   Outline of the survey method

We conducted the field surveys on April 27 and over May 18 and 19, about ten days and one month from the occurrence of the earthquake, respectively. It is difficult to comprehensively measure all the damaged levees over such a wide area; therefore, we surveyed only specific damage that we had previously received information about. The target rivers belonged to the Midorikawa water system, as shown in Figure 1. In the field survey, we mainly examined the levee deformation, vertical and transverse cracks, steps, subsidence and slope failure of the levees. In addition, a cross-sectional shape of the levees that suffered destructive damage was surveyed using RTK-GNSS (Trimble R4 and R6).
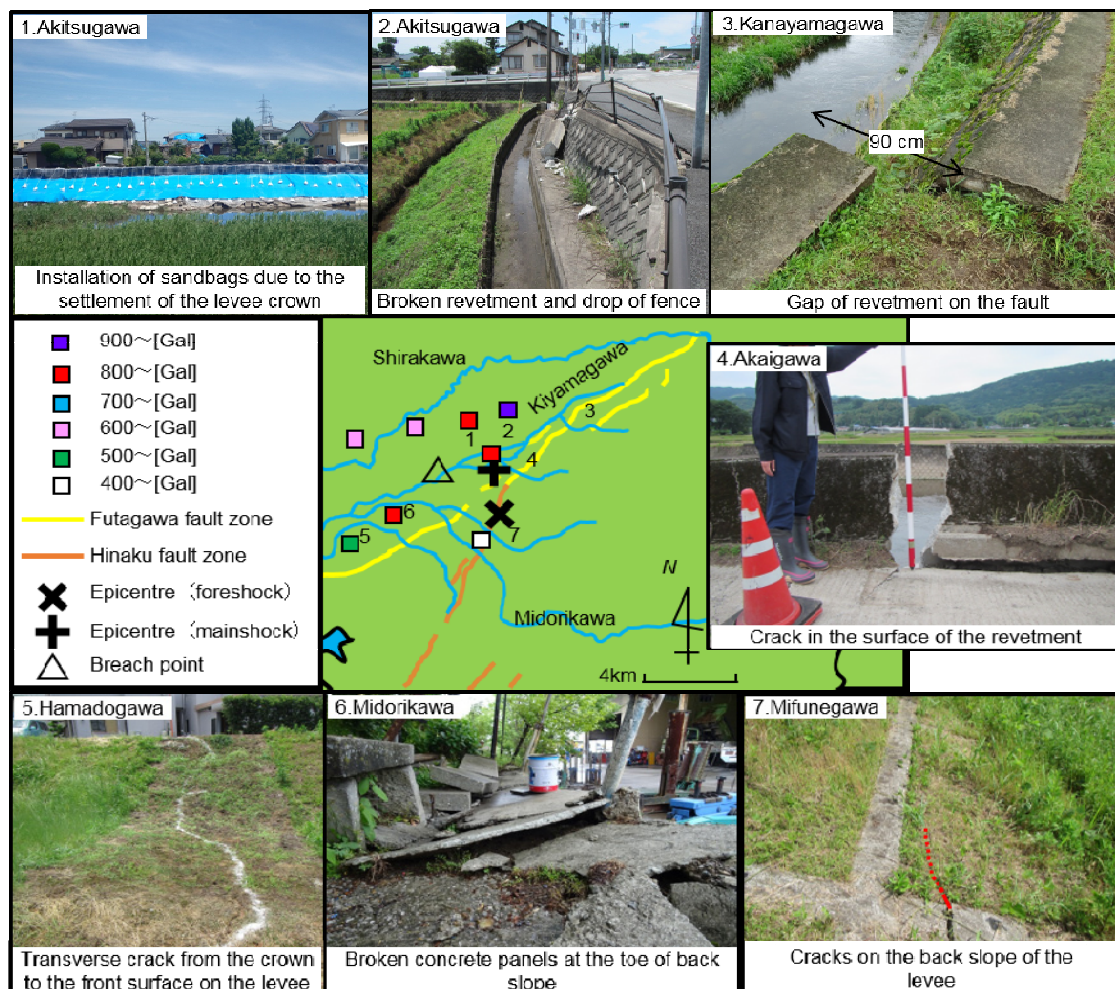

Figure 1. Maps of the epicenters, maximum acceleration levels of the 2016 Kumamoto Earthquake, and photos of damage to levees.

2.2.2 Results and discussion

Figure 1 shows photographs of the typical damage to the levees, and Table 2 summarizes the details of the levee damage and the cross-sectional shapes at each point. The Kanayamagawa and Akaigawa Rivers were located along the faults, and they showed cracks of 0.9 m length at the revetment. Longitudinal and transverse cracks were confirmed not only at the crest of the levee but also on the surface slopes in the Hamadogawa and Mifune Rivers adjacent to the fault. The concrete panels located along the back slope were damaged in the Midorikawa River.

In the Akitsugawa River, which flows near the point where there was significant earthquake acceleration (904 Gal), the front and back slopes were damaged. Sandbags at a height of 1 m and blue sheets were placed at the levee crown and the front slope of the Akitsugawa River. The river seems to have been affected by crest subsidence and sliding on the surface. To analyze the extent of crest subsidence in the Akitsugawa River, Figure 2 illustrates the crest height at the right bank of the Akitsukawa River before and after the earthquake. In the figure, the horizontal axis indicates the longitudinal distance from the Souryou bridge (N 32.7794°, E 130.8022°). The crest height after the earthquake was measured using RTK-GNSS on May 18, 2016. The height before the earthquake was evaluated using a DEM (digital elevation model) released by the GSI (Geographical Survey Institute) in Japan. The crest subsidence was found to range from 0.5 to 1 m over the longitudinal section of 200 m. In addition, some liquefaction was observed at the left bank of Akitsugawa River. Ground subsidence in a wide region affected by the 2016 Kumamoto earthquake was found to be 20 cm (GSI, 2016). This indicates that the subsidence of the levee crest in the Akitsugawa River was greater than that of the ground in the vicinity.

Table 2. Survey results on damage to levees

| Rivre	Photo number	Damage situation	Levee shape		
			Height[m]	Crown width[m]	Slope
Akitsugawa R.	1	Right bank：Levee settlement and installation of sandbag with 1 m height			
		Left bank：Sliding of front slope	2.75	9.41	23%(front)
	2	Left bank：A lot of damages of concrete panels on front and back slopes	1.97	11.34	9%(back)
Kanayamagawa R.	3	Both banks：Steps in the revetment and damage on the levee crown	3.11	0.94	8%(back)
Akaigawa R.	4	Both banks：Steps in the revetment and longitudainal crack on the levee crown	2.6		4%(front)
Hamadogawa R.	5	Left bank：Longitudinal and transverse cracks in levee crown and front slope	3.14	4.6	23%(front)
Midorigawa R.	6	Left bank at 10.8k：Broken concrete panels at toe of back slope			
Mifunegawa R.	7	Right bank at 3.8k：Longitudinal and transverse cracks in levee crown and front slope and sliding at back slope	3.81	20.53	50%(front)
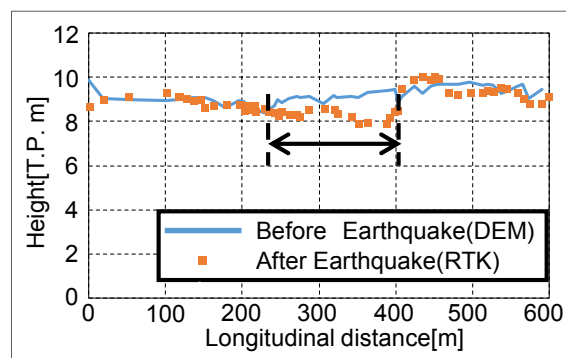
Figure 2. Comparison of longitudinal distribution of crown height before and after earthquake

3 FIELD SURVEY OF THE COMPOUND DISASTER IN KIYAMAGAWA RIVER AFTER HEAVY RAIN ON JUNE 20, 2016

3.1 Outline of heavy rain on June 20, 2016

To understand the rainfall and flood situation during the heavy rains on June 20, 2016, the hourly rainfall, as measured by Mashiki AMeDAS observatory, and the water mark in the Kiyamagawa River, as measured by the Akai water-level observatory, are shown in Figure 3. The data illustrates that hourly rainfall over 50 mm continued for 2 h, and 6-hours rainfall reached to 177 mm. Owing to the short-term heavy rain, the water level of the Kiyamagawa River rose rapidly after 11 pm on June 20, reaching 10.5 [T.P.m] and exceeding the emergency water level at midnight on June 21. At 1 am, although the hourly rainfall was 31 mm, the water level remained at 10.5 [T.P.m].
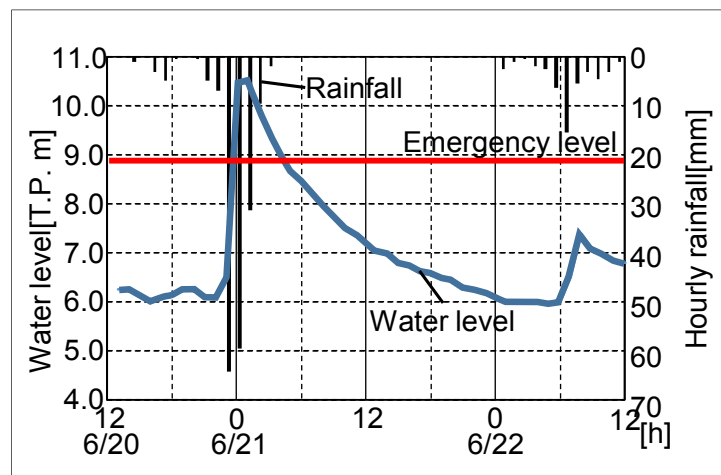

Figure 3. Time series of hourly rainfall (Mashiki AMEDAS) and water level (Akai water-level observatory) on June 20 and 21, 2016.

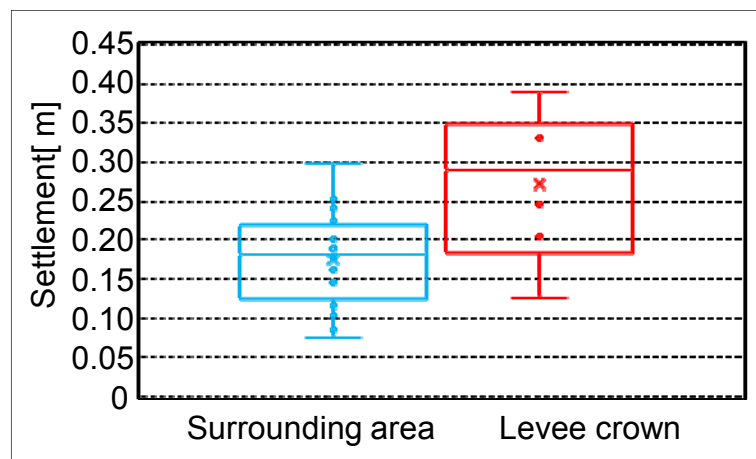**Figure 4.** The damage around the Kiyamagawa breakwater point

Figure 5. A comparison of crest subsidence and landsides in the areas around the Kiyamagawa River. The steps of the sluice pipes (n = 6) in the levee are regarded as evidence of crest subsidence. The uplift of manholes (n = 18) in the area affected by landsides near the river showed signs of subsidence.
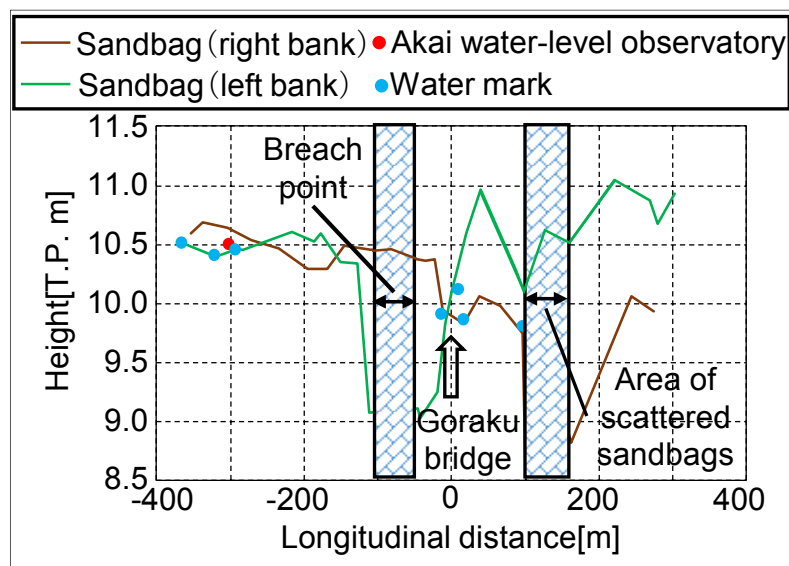

Figure 6. Vertical distribution of trace levels in Kiyamagawa and the sandbag height on the levee crown.

The crest subsidence at the Kiyamagawa River was caused by the earthquake, as was the case with other rivers in the Midorigawa water system. After the 2016 Kumamoto earthquake, many sandbags were set on the levee crown at a height of 1 m as a countermeasure. However, the heavy rain on June 20 resulted in a massive flood, and a levee breach occurred on the left bank at the 5.4 km point in the Kiyamagawa River. The levee breach was located 200 m downstream from the confluence of the Akaigawa River and 60 m upstream from the Goraku bridge, as shown in Figure 4. The breach width extended to ~50 m.

3.2   Field survey

3.2.1   *Outline of the survey method*
To understand the outcome of the compound disaster caused by the earthquake and the flood in the Kiyamagawa River, we conducted a second field survey on June 23 and July 21, 2016, where we examined the levee damage and measured the water marks due to the heavy rain and the earthquake near the breach point. In addition, by using RTK-GNSS, we measured the subsidence on the levee crest and the landside area in the vicinity.

3.2.2   *Results and discussion*
Figure 4 shows photographs of the levee damage caused by the compound disaster near the breach point of the Kiyamagawa River. Several sandbags with vinyl sheeting were placed at a height of 1 m along the river side. We confirmed that there were no visible gaps or holes in the sandbags and vinyl sheets. However, the crest sediment near the boundaries between the sandbags was locally scoured, as shown in Stn. K1, a

little upstream of the breach point. This is because of a kind of piping on the sandbags. The depth and length of the local scouring were 0.13–0.20 m and 1–2 m, respectively. Some of the scoured gaps extended to the back slope of the levee crest. Such local scouring around the sandbags was found in a wide area of the levee crest without an asphalt pavement. Further, at Stn. K3, the sandbags placed at the levee crown were scattered. At this point, the overflow of water was confirmed, but no erosion on the crest and the back slope of the levee was observed. At Stn. K4, a step with a height of 34 cm was formed between the Goraku bridge and the levee crown owing to crest subsidence.

To quantitatively examine the crest subsidence in the Kiyamagawa River, Figure 5 shows the steps of the sluice pipes (n = 6) in the levee and the uplifts of the manholes (n = 18) in the landside area near the river, where subsidence was found in the crest and ground surrounding the levee. The figure shows the average, maximum, and minimum values of each data point. The results indicate that the average values of the steps of the sluice pipes and the manhole uplifts were 0.18 m and 0.27 m, respectively. This means that the subsidence of the levee crest was 0.1 m larger than that of the nearby landside area. The longitudinal distribution of the water marks along the levee is shown in Figure 6. The figure also shows the height of the sandbags and the highest water level measured by the Akai water-level observatory. The results show that the water mark reached at least the top of the sandbags, and overflow occurred around the sandbags that were placed at a relatively lower height. The height of the levee crest at the breach point was 9.0 [T.P.m], which was lower than the nearby levee crest, indicating the possibility that overflow was the main reason for the levee breach. Furthermore, local scouring around the sandbag caused the inclination and movement of the sandbags, as shown in Figure 4. It seems that the local scouring of the sandbags promoted the levee breach. We conducted laboratory experiments for steady infiltration under sandbags, and the results showed local scouring around the sandbags (the results are omitted in this paper).

4   CONCLUSIONS

The main conclusions of this study are as follows:

1) As a result of the 2016 Kumamoto earthquake, many longitudinal and transverse cracks on the front slope and crest are found near the faults in the Midorigawa water system. The subsidence of the levee crest is larger than that in the nearby area affected by the landside, at least around the Akitsugawa and Kiyamagawa Rivers.

2) The Kiyamagawa River is affected by a compound disaster caused by the earthquake of April 2016 and the flood on June 20, 2016. The earthquake caused a crest subsidence of ~10 cm and a levee breach. The height of the levee crest at the breach point is 9.0 [T.P.m], which is lower than the nearby levee crest, indicating the possibility that overflow is the main reason for the levee breach. Furthermore, local scouring around the sandbag caused the inclination and movement of the sandbags, which promoted the levee breach.

REFERENCES

Japan Meteorological Agency Earthquake Research (2016): *Evaluation of the Kumamoto earthquake*, Promoti on Headquarters Earthquake Investigation Committee.

Ministry of Land, Infrastructure, Transport and Tourism (2016). *The Kumamoto earthquake in 2016 (28th repor t),* Ministry of Land, Infrastructure, Transport and Tourism.

Cabinet Office (2016). *Damage due to heavy rain in the western Japan from June 20 in 2016*, Japan Cabinet Office Report.

Cabinet Office (2016). *1948 Fukui Earthquake,* Japan Cabinet Office Report.

Geographical Survey Inst (2016). http://www.gsi.go.jp/kiban/faq.html#3-3（Browsing date: November 17, 201)

Geographical Survey Inst (2016). http://www.gsi.go.jp/common/000142434.pdf (Browsing date: September 28, 2016)

PLANNING STRATEGIES FOR FLOOD DISASTER RISK PREVENTION WITH HUMAN BEHAVIOR MODELS

NEILER MEDINA[1], ARLEX SANCHEZ[1] & ZORAN VOJINOVIC[1]

[1] Environmental Engineering & Water Technology department (EEWT),
UNESCO-IHE, Westvest 7, Delft, Zuid Holland 2611AX, The Netherlands,
n.medina@unesco-ihe.org; a.sanchez@unesco-ihe.org; z.vojinovic@unesco-ihe.org

ABSTRACT

This paper describes the use of an Agent Based Model (ABM) to implement a human behavioral model in order to explore different planning strategies for city evacuation under threat of a flood disaster as a measure to deal with urban flood management. The model mimics the daily behavior of individuals and the interactions between them on a city scale and how this behavior will evolve once a flood disaster is forecasted or is actually unfolding. The aim of this approach is to gain understanding on which are some of the key elements that affect and must be improved to have less or zero casualities due to failure in the evacuation process. For this purpose, different scenarios of flooding have been tested, in particular a combination of different communication strategies and communication means. As a result, the overall performance of the evacuation has been measured as the number of people that reached safe the shelter and the number of people in contact with the hazard for each scenario. Additionally, some physical infrastructure measurements have been discovered as needed for the case study city, such as road widening and shelter improvements (as location and resources).

Keywords: Flood risk; Agent Based Models (ABM); human behavior; natural disasters; planning strategies.

1 INTRODUCTION

Taking into account the latest reports of the Intergovernmental Panel on Climate Change it is clear that extreme weather events are notoriously in an increase trend on the amount of events as well as the associated disasters in terms economical and human life losses (IPCC, 2014). The causes of this can be somehow explained as a combination of most severe weather events associated with uncontrolled urban growth, climate change and the lack of planning for the expansion of most of the coastal cities around the globe (Jha et al., 2011). The previous trend is also expected to continue growing in the coming years (Vojinovic & Van Teeffelen, 2007; Price & Vojinovic, 2008; Mynett & Vojinovic, 2009; Vojinovic 2015; Sanchez et al., 2014; Kumar et al., 2013).

The use of physically-based modelling techniques is invaluable for modelling floods and assessing flood risk (e.g., Vojinovic et al., 2014a; 2014b; 2013; 2016). However, for the reasons expressed above, preparedness and planning strategies for flood disaster risk prevention and mitigation at individual, organizational and city level is a must and there is a need for continued upgrade and revision from the academia, policy makers and more active participation of communities to be able to cope and to have a more effective management of existing and future flood risks, and due to the increase on complexity of the challenge of dealing with urban floods there are demands innovative solutions to an always evolving problem such as floods (Vojinović, 2015a). It is therefore advisable to explore the use of new concepts, frameworks, theories and tools such as human behavior models and its implementation through the use of different modelling techniques i.e. Agent Based Models (ABM) to expand the knowledge of some of the main factors that are contributing to the formation of risk to floods and therefore understand what needs to be done in order to reduce risk and tackle the problem from a holistic point of view (Vojinović, 2015; Vojinovic et al., 2014).

2 CONCEPTUAL FRAMEWORK

This section provides the conceptual framework used to implement the ABM used in this research to test the different evacuation scenarios and communication warnings strategies. It is divided in the software and hardware requirements and flowed up by the human behavioral model implemented.

2.1 Hardware and software

All the simulations are run in a personal laptop running under Windows 7 Professional, 64-bit operating System with an Intel Core i7 processor and CPU @ 2.4GHz with 16 GB of RAM memory. The software chosen to implement the ABM is Repast Symphony version 2.4.0 (latest version at the moment of writing this conference paper). Repast Symphony is software that runs under Java as a programming language, it is a

free and open source modelling system for creating, running, displaying and collecting data from Agent Based Simulations. This software is currently considered for many ABM modelers as the most powerful and popular free and open source environment to implement ABMs due to its robustness and the huge support from the online community and repast forums, another big advantage is that its implementation is fully object oriented that allows the construction of any ABM model to be much easier and allows to implement any ABM in blocks and make a modular, adaptable and reusable model.

2.2 Human behavioral model

Two general concepts are used during the implementation of the AMB model: 1. The ABM is built in such manner that it has the ability to represent the daily behavioral pattern of a complex environment such as it is an urban city: interactions between agents (humans) and agents with the environment (the city). 2. The ABM includes a module where human cognition is represented in order to be able represent the complex decision-making process of humans during evacuation of cities during flood events. The process of implementing the ABM cab be summarized as a 5-step process as shown in the text below and in Figure 1 and Table 1:

- Agent's Description: Type of agents to be used in the model. Individuals and organizations for this ABM
- Agent's Classification: Sub classification of different type of agents based on own characteristics
- Environment Characterization: Physical representation of the space where agents interact, i.e Buildings, roads, water, etc. As well a list of the possible agents' interactions are defined at this level.
- Model Parametrization: Consist a set rules known as WWW, WHO (each agent) does WHAT (specific action) and WHEN (time)
- Cognitive Module: Using this module of the ABM is possible to give the agents the like behavior when the flood is perceived or acknowledge.
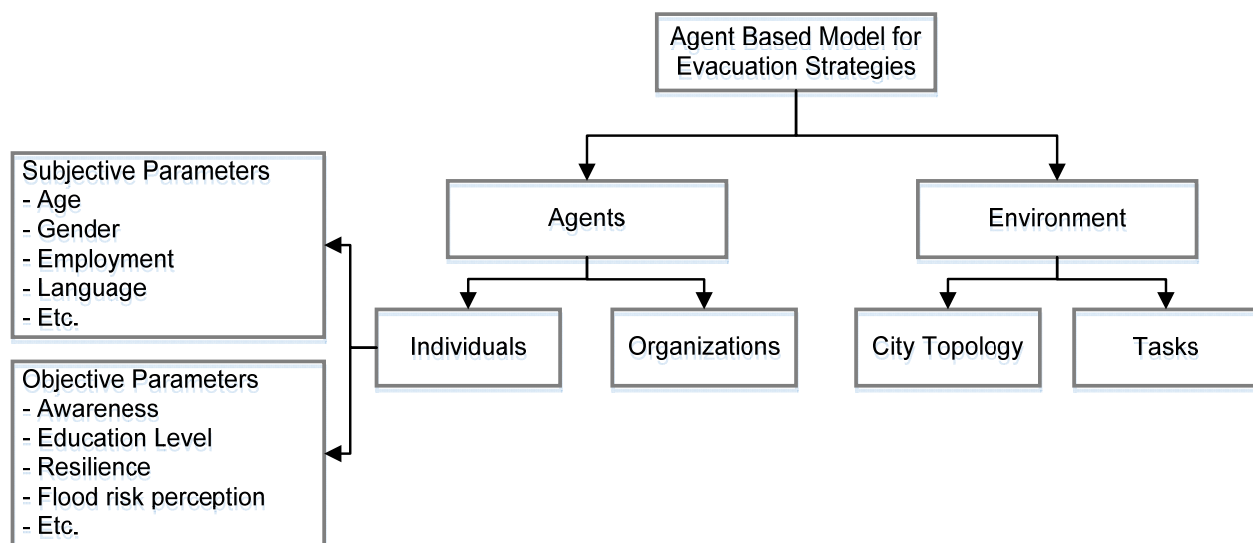

Figure 1. Agents and Environment Description and Characterization.

Table 1. Individual Agents Classification Actions.

Action	Observation
Evacuation	Planned and Organized, Follow instructions.
Fight	Prepare in situ
Flight	Random Evacuation (not follow orders)
Sideration[1]	Inability to respond
Search Relatives	Wife, children, parents, etc.
Return home or work place	Feel safe in these places and stay there.
Assist Others	The agent becomes an organization actor.
Antisocial Behaviour	Panic, looting, etc.

---

[1] The sideration term within this research is defined as the inability to respond from the psychological perspective

3 MODEL SET UP AND RESULTS

As a case study city to implement the agent based model for evacuation strategies, the Dutch side of Sint Maarten in the Caribbean was selected. A total of 6046 agents were used to represent the population of the island. The model was set up to run for an entire week from Monday to Monday and as a start of the simulation it was selected 04:00 hours considering that rush hour is estimated to be around 9 am. At the beginning of the simulation, every agent selects a destination and start its movement towards it, which is chosen based on the individual's classification (Figure 1) and according to the day and the time of the day for each agent, going from home to work, leisure, school and so on (see Figure 2). For the flood hazard representation, a hurricane was introduced in the ABM to test the evacuation capabilities of the agents This flood model came from a 2D MIKE by DHI hydrodynamic simulation.
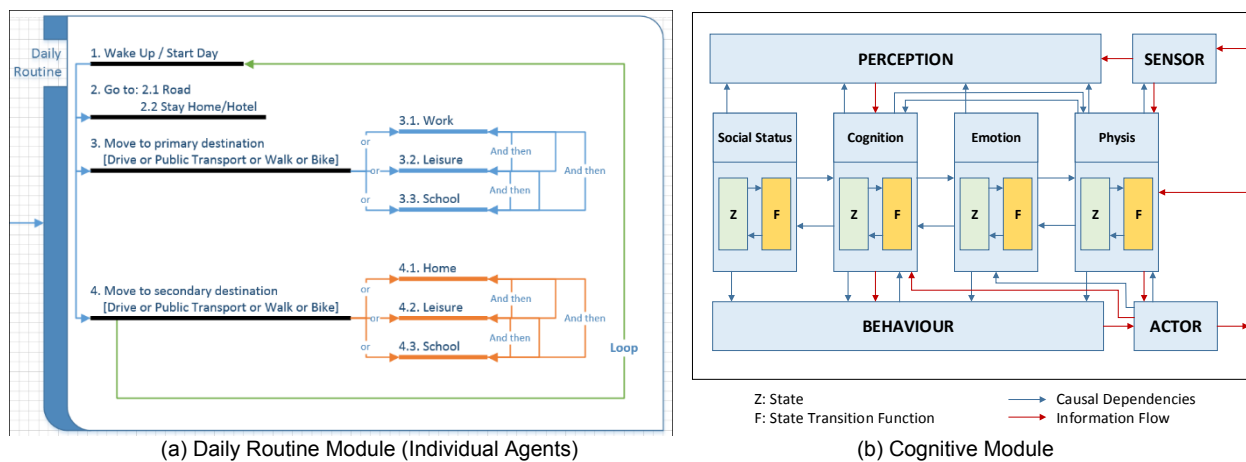

(a) Daily Routine Module (Individual Agents)   (b) Cognitive Module

Figure 2. Behavioral Modules.

Furthermore, to explore and evaluate the effects of the warning information in terms of content and dissemination strategies, 4 different scenarios were set up in the ABM: 1. A baseline scenario, were agents evacuate randomly based on previous knowledge (or non) of where to evacuate. 2. A clear message to where to evacuate is sent to the whole population on the island (scenario 1). 3. A stage evacuation message, this is the evacuation message is sent gradually according with the expected arrival time of the hazard (scenario 2) and finally a targeted message to only those that are within the area expected to be hit by the hazard (Scenario 3). Figure 3 shows the model running and preliminary results from this model.
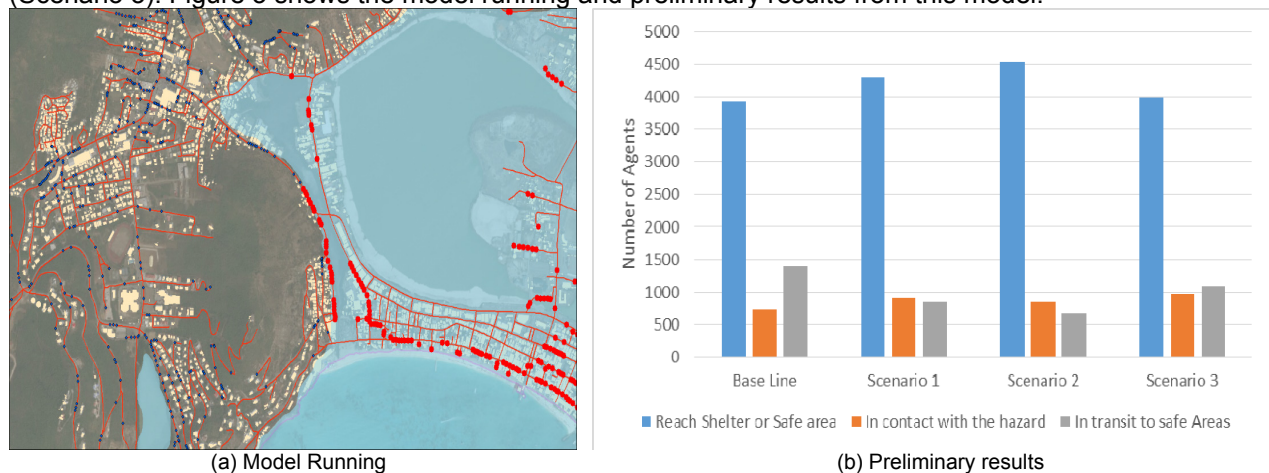

(a) Model Running   (b) Preliminary results

Figure 3. Agent based model for evacuation strategies in the island of Sint Maarten.

As can be seen in Figure 3 (b) for all three scenarios that were tested in this research, an increase in the number of inhabitants that manage to reach a shelter or safe area in comparison with the base line scenario, with values of 9.2%, 15.4% and 1.5% for scenario 1,2 and 3 respectively. The results for people in contact with the hazard (orange bars in the graph) for all three scenarios show an increase in the number of exposed if compared with the base line in relative values as low as 16.5 % for scenario # 2 up to 33.2% or 241 more people exposed in Scenario # 3.

Finally, after the 4 scenarios were run, two other improvements to Sint Maarten Evacuation plan can be inferred in terms of infrastructure. Two major roads were identified to be the preferred (or only) routes to get

into safety to the major Shelters in the island for this hurricane that was used during a flood hazard and also two major shelters were also occupied at first. (Figure 4).
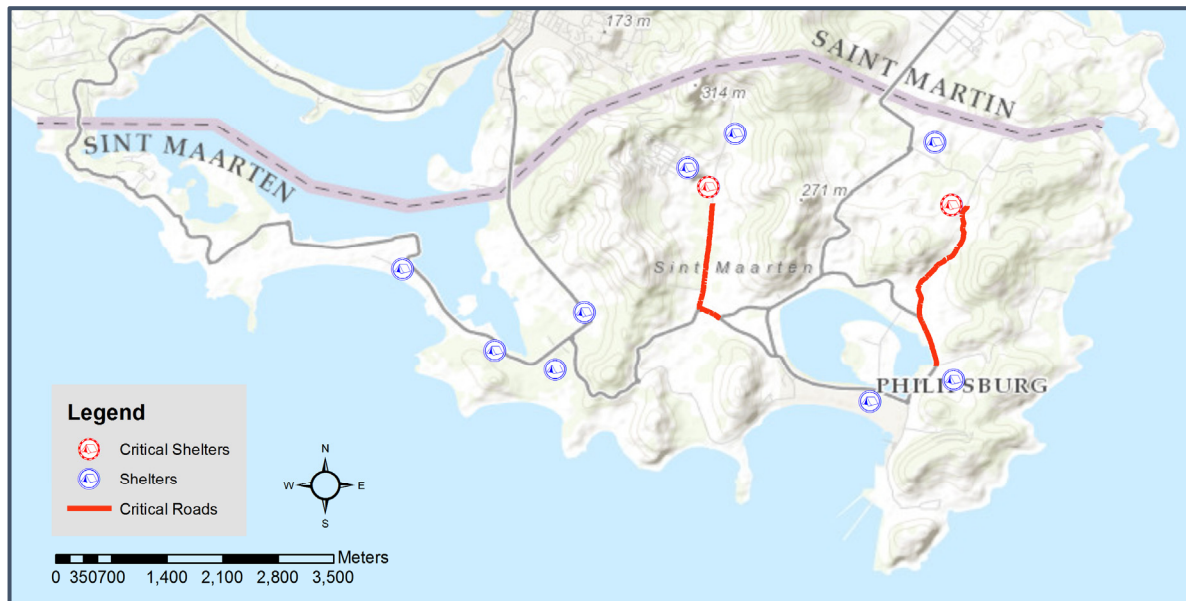

Figure 4. Critical Roads and Shelters in Sint Maarten for this research.

4   CONCLUSIONS

The ABM used in the research can be seen as an integrative tool between a social or human behavioral model, a hydrodynamic model (hazard) and a communication module. The novel implementation of this research allows to conclude that ABM can be used to gain a deeper understanding on some of the main elements for a more successful evacuation. And is probe of the feasibility of ABM to test large scale city evacuations.

The main conclusions that can be drawn until this part of the development are: 1. During large city evacuation, not only the message content matters but the way the message is deliver, accepted and understood by individuals and the community plays a major role in the effectiveness of the evacuation itself, 2. It can also be concluded that in the era of social media there is a clear need to better understand the effects that social networks have on evacuation processes and how them can be used to achieve better evacuations results instead of creating new problems to an already complex problem and 3. ABM has the potential of becoming a powerful tool for operational risk management purposes such as: Determination of evacuation patterns, identification of critical infrastructure, can be used to identify the need to improve existing emergency locations (i.e. number of beds, food storage, etc).

Based on the results of number of inhabitants that reach shelter or safe area in each one of the simulation scenarios tested in this research, it is not surprising that having a more informed community on how to react to a certain flood threat will lead to a major number of people reaching safe area. However, it is revealing that, for this particular case study, having a stage evacuation (scenario #2) outperform almost as much as double scenario # 1 where all the community is informed at the same time, which can be explained on having major roads congestion for scenario number 1 due to the fact that more people try to evacuate at the same time. A comparison between scenario 2 and 3 gives also an expected outcome, having as much as 10 times the number of people reaching safe area for scenario #2 since scenario # 3 is about informing only the people expected to be within the hit area.

One of the most interesting findings at this stage of the research, is that for all the three simulated scenarios of warning dissemination, it was observed an increase on the number of people being exposed to the hazard, in one hand this can be explained as more people is aware of the threat and looking to reach shelter, but in the other hand it is also a clear indication that the lead time for the flow of information in this particular case study should increase to prevent this unwanted situation. Future work, will explore the effects of different lead times in the overall performance of the evacuation for this case study. In addition, it is necessary to remark that at this stage of the research the module of loos of life has not been fully implemented and the model only accounts for people in contact with the water not if they is an actual loss of life, the so called loss of life module is under current development and it includes both: characteristics of the hazard (water depth and velocity) and characteristic of the human (age, genre, etc), it is believe that this module will help to understand if by adding more information on evacuation into the system (city) lead to a better or worse overall performance on the evacuation.

ACKNOWLEDGEMENTS

REFERENCES

IPCC, 2014. *Contribution of Working Group Ii to the Fifth Assessment Report of the Intergovernmental Panel on Climate Change. Asia*, Intergovernmental Panel on Climate Change.

Jha, A., Lamond, J., Bloch, R., Bhattacharya, N., Lopez, A., Papachristodoulou, N., Bird, A., Proverbs, D., Davies, J. & Barker, R. (2011). Five Feet High and Rising: Cities and Flooding in the 21st Century. *World Bank Policy Research Work*, WPS5648.

Mynett, A.E. & Vojinović, Z. (2009). Hydroinformatics in Multi-Colours-Part Red: Urban Flood and Disaster Management. *Journal of Hydroinformatics*, 11, 166. Doi:10.2166/Hydro.2009.027

Price, R.K. & Vojinović, Z., (2008). Urban Flood Disaster Management. *Urban Water Journal*, 5, 259–276. Doi:10.1080/15730620802099721

Sanchez, A., Medina, N., Vojinović, Z. & Price, R. (2014). An Integrated Cellular Automata Evolutionary-Based Approach for Evaluating Future Scenarios and the Expansion of Urban Drainage Networks. *Journal of Hydroinformatics*, 16, 319. Doi:10.2166/Hydro.2013.302

Sathish Kumar, D., Arya, D.S. & Vojinović, Z. (2013). Modeling of Urban Growth Dynamics and its Impact on Surface Runoff Characteristics. *Computers, Environment, and Urban Systems*, 41, 124–135. Doi:10.1016/J.Compenvurbsys.2013.05.004

Vojinović, Z. (2015*). Flood Risk: The Holistic Perspective From Integrated to Interactive Planning for Flood Resilience*. IWA Publishing, London, Uk.

Vojinović, Z. & Abbott, M.B. (2012*). Flood Risk and Social Justice: From Quantitative to Qualitative Flood Risk Assessment and Mitigation*. IWA Publishing, London.

Vojinović, Z., Abebe, Y., Sanchez-Torres, A., Medina, N., Nikolic, I., Manojlovic, N., Makropoulos, C. & Pelling, M. (2014). Holistic Flood Risk Assessment in Coastal Areas-The Pearl Approach. *11th International Conference on Hydroinformatics*, New York City, Usa.

Vojinović, Z., Hammond, M., Golub, D., Hirunsalee, S., Weesakul, S., Meesuk, V., Medina, N., Sanchez, A., Kumura, S. & Abbott, M.B. (2016). Holistic Approach to Flood Risk Assessment in Areas with Cultural Heritage: A Practical Application in Ayutthaya, Thailand. *Natural Hazards*, 18(1), 589-616

Vojinović, Z., Sahlu, S., Torres, A.S., Seyoum, S.D., Anvarifar, F., Matungulu, H., Barreto, W., Savic, D. & Kapelan, Z. (2014). Multi-Objective Rehabilitation of Urban Drainage Systems Under Uncertainties. *Journal of Hydroinformatics*, 16, 1044–1061.

Vojinović, Z., Seyoum, S., Salum, M.H., Price, R.K., Fikri, A.K. & Abebe, Y. (2013). Modelling Floods in Urban Areas and Representation of Buildings with a Method Based on Adjusted Conveyance and Storage Characteristics. *Journal of Hydroinformatics*, 15, 1150–1168. Doi:10.2166/Hydro.2012.181

Vojinović, Z. & Van Teeffelen, J. (2007). An Integrated Stormwater Management Approach for Small Islands in Tropical Climates. *Urban Water Journal*, 4, 211–231. Doi:10.1080/15730620701464190

VARIATIONS IN MAGNITUDE AND FREQUENCY OF EXTREME FLOODS AND MAXIMUM PRECIPITATION EVENTS IN 24 HOURS IN THE OCCIDENTAL EDGE OF THE ANDES BETWEEN PARALLELS 30° 50´ AND 39° 40´ OF SOUTH LATITUDE

JOSE VARGAS BAECHELER[1] & FELIPE VÁSQUEZ CORDERO[2]

[1,2] Department of Civil Engineering, University of Concepción, Concepción, Chile,
jvargas@udec.cl; fvasquezc@udec.cl

ABSTRACT

This study aims to analyse the distribution of daily maximum precipitation with T=10 years and the variability both in magnitude and in frequency of the maximum floods that took place between parallels 34-39° of South latitude in the occidental edge of the Andes within the last 30 years, to find spatial trends in them, and also to establish links between these two variables. In order to develop a correct analysis, the decision of which stations should be used follows a minimum set of criteria, including the duration and quality of the data, the correct register of the most important floods within the last years, among others. For the precipitation study, 72 weather stations are used, which have complete daily rainfall information of the period from 1985 to 2015. In the case of extreme floods events, there is a total of 26 stream gauging stations that present information on the most important floods in that period. Daily maximum precipitation isohyets are made through different interpolation methods and are compared to previous studies. Furthermore, in the case of streams, annual maximum series, annual excess series and partial duration series with up to 4 times the amount of data per registered year are developed. In extreme flood events, it could be noticed that in stations of lower latitude in the area of study, the magnitude and frequency of flood tends to increase, while in places further south of the area, the behaviour is the complete opposite. In intermediate latitudes of the area of study significant trends are not seen, therefore presenting a more random behaviour. In the case of daily maximum precipitations, the behaviour is the opposite. In higher latitudes, an increase in this variable is seen. However, in lower latitudes the values decrease.

Keywords: Maximum precipitation events; extreme floods; variability.

1   INTRODUCTION

The interaction of varied climatic subsystems such as atmosphere, hydrosphere, lithosphere and biosphere affect, in different scales, the precipitations registered by different territories around the world. These effects are explained in part by climatic factors of a geographic type (latitude, altitude, distance from the sea, etc.) and also by thermodynamic factors (atmospheric circulation, winds, etc.), where depending on the studied area some have more importance than others. The main quality of this interaction between subsystems is their continuous variability, which in the last centuries, especially during the 20th century, increased due to human influence; playing a big role in climatic trends, even more so than natural variability.

In this respect, the climatic conditions, in which high intensity precipitations in short periods of time and extreme rainwater floods have occurred, was altered these past years by no following the historic data, which could lead to an alteration of the necessary parameters for the design of civil works such as excess works in small dams, sewers that go through road works, drainage system in urban areas, bridges, among others. This translates into a sub-dimensioning of the entire infrastructure which creates a potential risk for society.

Currently, hydrological models are estimated with historic data obtained through measuring stations. There should be no problem with this traditional proceeding if the basins were to have a seasonal hydrological behaviour, but if a trend appears and each time the extreme events are more intense, then our traditional models would underestimate the calculation of future events.

In basins of the central-southern zone of Chile, a change in the behavioural pattern of extreme floods is seen. In the Mataquito River basin (34° 50'-35° 30´ S), it was determined that an average of 6-7 out of the 10 largest floods generated between 1976 and 2008 occurred between 2000 and 2008 (Vicuña, 2013). Furthermore, in the Ñuble River a similar behaviour has been seen (Figure 1), (Carrasco, 2011), suggesting that indeed the seasonal behaviour of these kind of hydro-meteorological events has been lost.
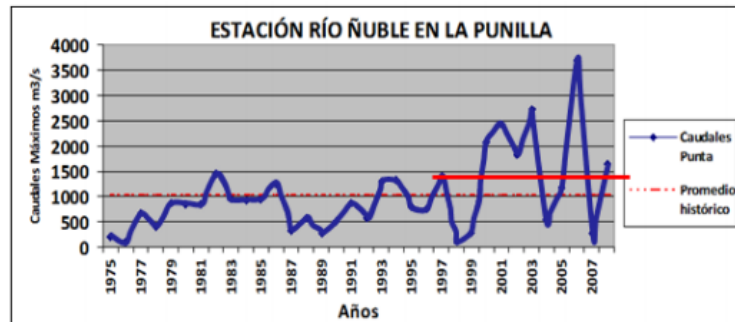
Figure 1. Increase of peak flows. Río Ñuble en la Punilla.

One of the last IPCC reports (2013) considers that global warming is a reality and points out that the last three decades are the hottest ones since 1850, with a probable increase in temperature of 0.85 degrees between 1880 and 2012. In addition, Chile's continental weather towards the end of the 19th century obtained through the regional PRECIS model presents significant changes in temperature and precipitation, mostly under the most severe scenario (Fuenzalida, 2006; Garreaud, 2011).

2   OBJECTIVE

This study aims to examine the variability both in magnitude and in frequency of the maximum floods that took place between parallels 34-39° of South latitude (S) in the occidental edge of the Andes within the last 30 years and to analyse the distribution of daily maximum precipitations with T=10 years, to find spatial trends in them and also to establish links between these two variables.

3   AREA OF STUDY

This study focused in the area between parallels 34°50'S and 39°40'S. This is one of the main basins of the central-southern zone of Chile (Figure 2).
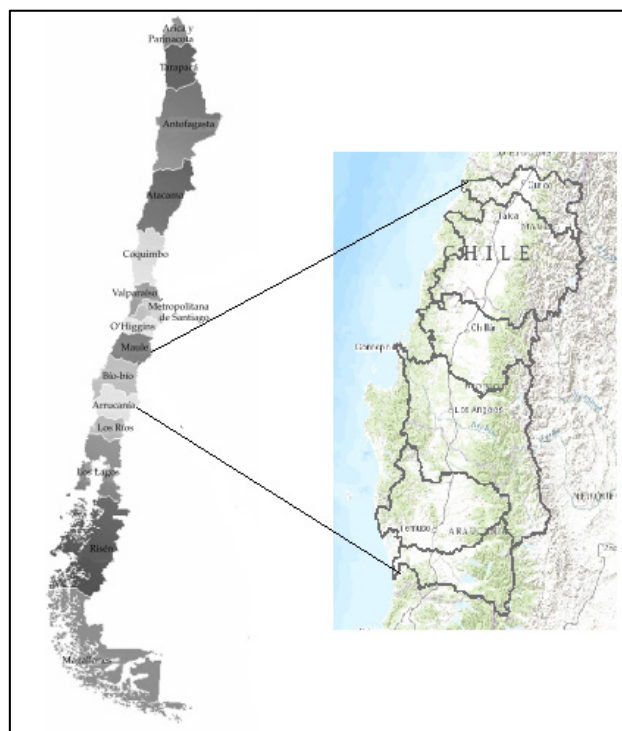

Figure 2. Area of study.

3.1 Mataquito River Basin

Mataquito River basin (Figure 3), extends from latitude 34°50'S by the North to 35°30' by the South, creating part of the VII Maule Region and covering an area of 6,190 km^2 (MOP, 2004).

3.2 Maule River Basin

Maule River basin (Figure 4), extends from 35°05'S by the North to 36°30'S by the South, covering an area of 20,295 km^2, being the fourth largest one of the country. It is part of the VII Maule Region (MOP, 2004).

3.3 Itata River Basin

Itata River basin (Figure 5) is located between 36°00' and 37°20' of South latitude. Is part of the VIII Biobío Region, and covers an area of 11,294 km^2 (MOP, 2004).

3.4 Biobío River Basin

Biobío River basin (Figure 6) is located between parallels 36°42'S and 38°49'S. It is one of the largest basins, covering a total of 24,264 km^2. It is mainly in the VIII Biobío Region, but it also occupies part of the Malleco province and Cautín province, which belong to the IX Region (MOP, 2004).

3.5 Imperial River Basin

Imperial River basin (Figure 7) extends from 37°40'S to 38°50'S. It is part of the IX Araucanía Region and it has an extension of 12,763 km^2. It takes place mainly west of the Biobío River high basin (MOP, 2004).

3.6 Toltén River Basin

Toltén River basin (Figure 8) extends from 38º40' by the North to the latitude 39º40' by the South. It is part of the IX Araucanía Region and it has an extension of 8,398 km^2, being relatively small (MOP, 2004).
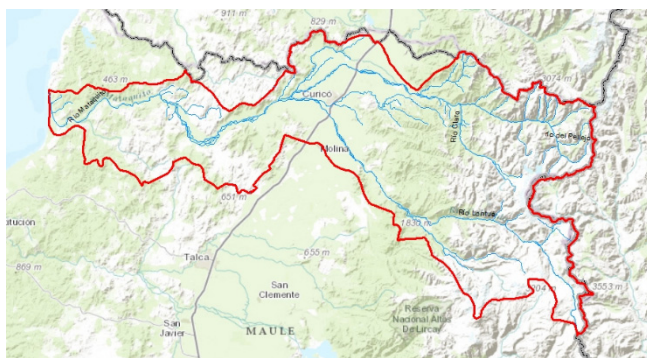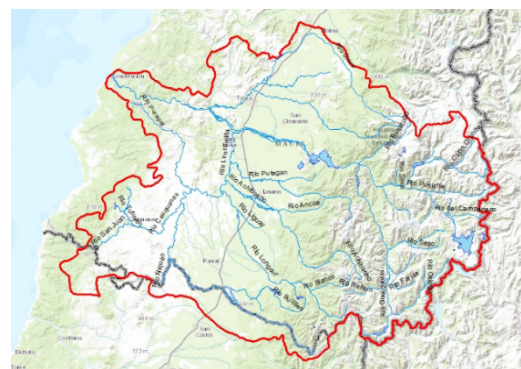

Figure 3. Mataquito River basin.
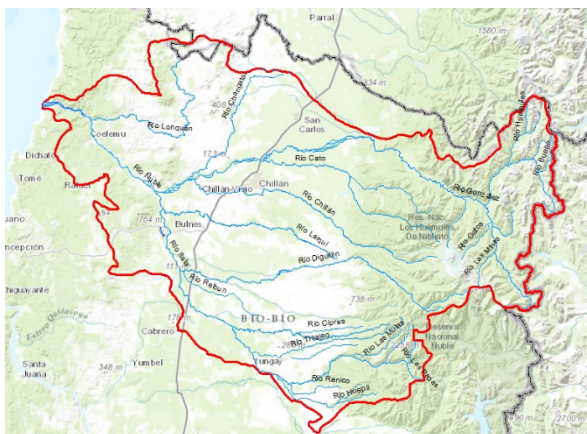

Figure 4. Maule River basin.

Figure 5. Itata River basin.
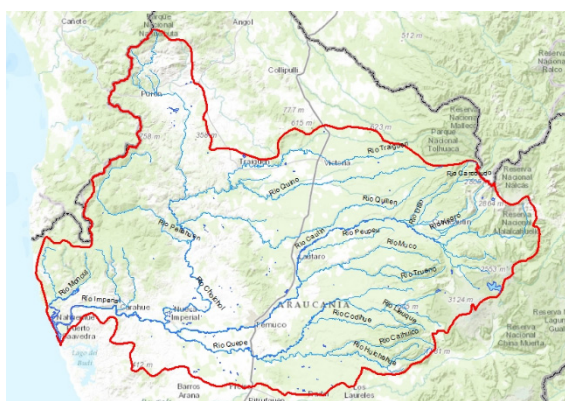

Figure 6. Biobío River basin.

Figure 7. Imperial River basin.

Figure 8. Toltén River basin.

4   METHODOLOGY

Firstly, once the area of study was determined, the existent information was reviewed. In the case of floods, data respecting height and instant flow was used and in the case of maximum precipitations, the data was formed by a series of rain gauge stations that had daily registers of the last 30 years.

After that, the stations used in this study were selected. In order to do that, a series of criteria that had to be met were defined. In the case of floods there was:

a)   Stream gauging stations with limnological data.
b)   Data of 30 years.
c)   The most important floods was to be correctly registered, especially the flood of July 2006.
d)   They must belong to rain gauge basins from the same hydro-meteorological event.
e)   The maximum flood events should not be controlled by lakes, dams, etc.

Once the stations were chosen, the annual maximum series, the annual excess series and the partial duration series with up to 4 times the amount of data per year registered were created.

Firstly, with the series of annual maximum, a graphical analysis was carried out. The behaviour of moving averages with a window of 15 years was studied and a trend line was added to observe the gradient.

Then, in order to make a statistic analysis, the non-parametric Mann-Kendall test was run to the annual maximum series. The null hypothesis is that there is no trend in the series, and the alternative hypothesis is that there is, this for a trusted interval of 95%.

Finally, three-dimensional graphics were created, where the stations were arranged by latitude and 95% of maximum floods were represented using the partial duration series. The magnitude of each flood is shown in the diameter of the point in the graphic. In order to make a better analysis, the flow values were normalized by the maximum value of each station. These graphics were developed for station with 30 years' worth of data, and for stations with 40 years.

In the case of stations with precipitation measurements, the following criteria was to be followed: (a) have 30 years of daily continuous register of data, (b) each station has to have the most amount of data per year, a minimum of 11 registered months.

After choosing the stations, a consistency analysis was made through double mass curve analysis with the purpose of detecting possible mistakes in the translation of data collected in site, situation that affects the representation of the register; this with the aim of correcting the statistic if necessary.

Afterwards, a statistic gap filling was made on the days that didn't present precipitation measurement through rain gauge modules in order to have data 365 days of the year.

Once the register was completed, to find the daily maximum precipitation with T=10 days the following steps were applied to each rain gauge station: The 365 days of each year of the 30 years of data were observed and their daily precipitation value was examined, registering only the highest. This way for each year of the 30 years of data a daily maximum precipitation value (DMP) was obtained, therefore, for each station there are 30 different DMP values. Then, the 30 values were entered into the software "Easyfit", which adjusted different "probability functions" (Gamma, Lognormal 3p, Pearson, Gumbel max, etc.) to the 30 values of each station.

Later on, the Kolmogorov-Smirnov goodness-of-fit test was run to each probability function and based on the test results the probability function that best adjusted the data was selected. That way, using said function, the precipitation value that exceeds only 10% of the time was found, that means the value associated to a return period of 10 years.

With these precipitation values a map of isohyets was made throughout the area of study with the SIG Arcgis.

Finally, these daily maximum precipitation values associated to T=10 years were compared with the daily maximum precipitation values of an official study carried out by the Dirección General de Aguas (DGA) in 1991 called *Precipitaciones máximas en 1,2 y 3 días* with the aim of knowing the variations in the last years of this variable.

5   RESULTS

In relation to the basins, regarding the aforementioned criteria, a total of 26 stations were selected, which are detailed in Table 1. In each basin, a number of stations was used: 3 in Mataquito Basin (34°50´-35°30´S), 7 in Maule Basin (35°05´-36°30´S), 4 in Itata Basin (36°00´-37°20´S), 7 in Biobío Basin (36°42´-38°49´S), 4 in Imperial Basin (37°40´-38°50´S) and 2 in Toltén Basin (38°40´-39°40´).

Table 1. Selected Station for the study. (*) Year in which limnological data starts.

| Basin | Station | Rain gauge station number | | | | |
		Latitude (S)	Longitude (W)	Height (m a.s.l.)	Starting year (*)	Duration (years)
Mataquito	Teno después de junta con Claro	34°59′46′′	70°49′14′′	647	1961	53
Mataquito	Palos en Junta con Colorado	35°16′28′′	71°00′56′′	600	1967	47
Mataquito	Colorado en junta con Palos	35°16′42′′	71°00′10′′	600	1967	47
Maule	Claro en Camarico	35°10′42′′	71°23′05′′	220	1969	45
Maule	Lircay en Puente Las Rastras	35°29′08′′	71°17′36′′	240	1977	37
Maule	Loncomilla en Las Brisas	35°37′01′′	71°46′04′′	68	1984	30
Maule	Ancoa en el Morro	35°54′31′′	71°17′53′′	402	1960	54
Maule	Longavi en la Quiriquina	36°13′49′′	71°27′25′′	449	1952	62
Maule	Perquilauquen en San Manuel	36°22′33′′	71°37′24′′	266	1953	61
Itata	Ñuble en La Punilla	36°39′30′′	71°19′15′′	635	1965	49
Itata	Diguillin en Longitudinal	36°52′00′′	72°20′00′′	80	1981	33
Itata	Diguillin San Lorenzo	36°55′28′′	71°04′32′′	727	1959	55
Itata	Itata en Cholguan	37°09′00′′	72°04′00′′	220	1962	52
Biobío	Biobio en Desembocadura	36°50′19′′	73°03′43′′	16	1963	51
Biobío	Duqueco en Villucura	37°33′00′′	72°02′00′′	228	1963	51
Biobío	Biobio en Rucalhue	37°42′38′′	71°54′06′′	261	1971	43
Biobío	Lirquen en Cerro el Padre	37°46′32′′	71°51′46′′	340	1963	51
Biobío	Mininco en Longitudinal	37°51′49′′	72°23′39′′	125	1963	51
Biobío	Malleco en Collipulli	37°57′53′′	72°26′10′′	153	1977	37
Biobío	Lonquimay antes de junta con Biobio	38°26′00′′	71°14′00′′	901	1985	29
Imperial	Lumaco en Lumaco	38°09′00′′	72°54′00′′	70	1975	39
Imperial	Cautin en Rari Ruca	38°25′49′′	72°00′38′′	425	1979	35
Imperial	Cholchol en Cholchoñ	38°26′29′′	72°50′52′′	20	1964	50
Imperial	Quepe en Quepe	38°51′00′′	72°37′00′′	80	1975	39
Tolten	Liucura en Liucura	39°15′22′′	71°49′28′′	402	1977	37
Tolten	Trancura antes de río Llafenco	39°20′00′′	70°46′00′′	386	1987	27

When the annual maximum series (Fig. 9, 10, 11, 12), their moving averages with a window of 15 years and trend lines were analysed, the result was that of the 26 stations, 13 present a positive trend (Fig. 9, 10), 5 don't present a noticeable trend (Fig. 11), and 8 have a negative trend (Fig. 12). For each basin, the results are detailed in Table 2.
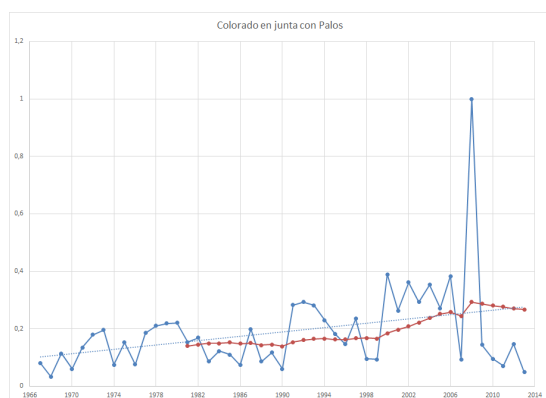

Figure 9. Annual Maximum Graph, with their moving averages (15) and trend line for the Colorado en junta con Palos station. Positive trend.
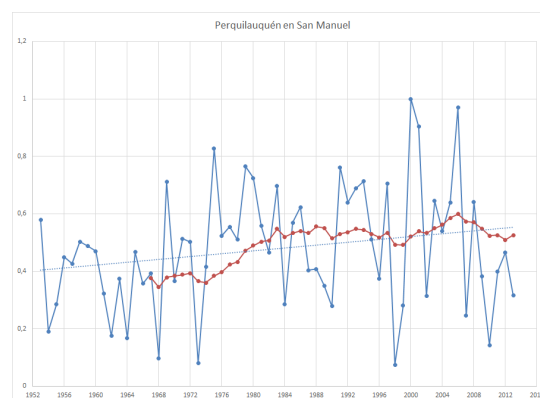

Figure 10. Annual Maximum Graph, with their moving averages (15) and trend line for Perquilauquén en San Manuel station. Positive trend.
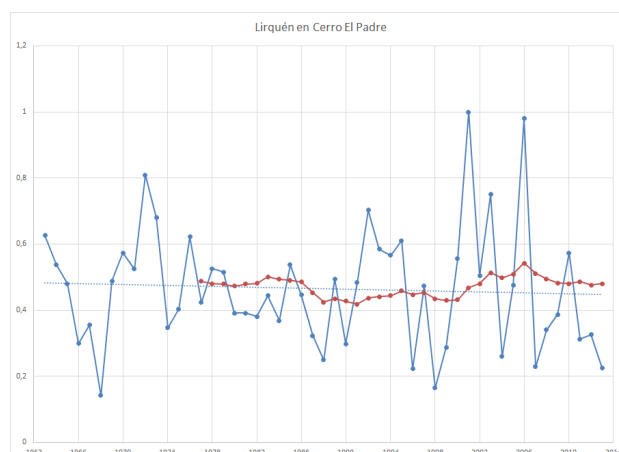
Figure 11. Annual Maximum Graph, with their moving average (15) and trend line for Lirquén en Cerro El Padre station. A significant trend is not seen.
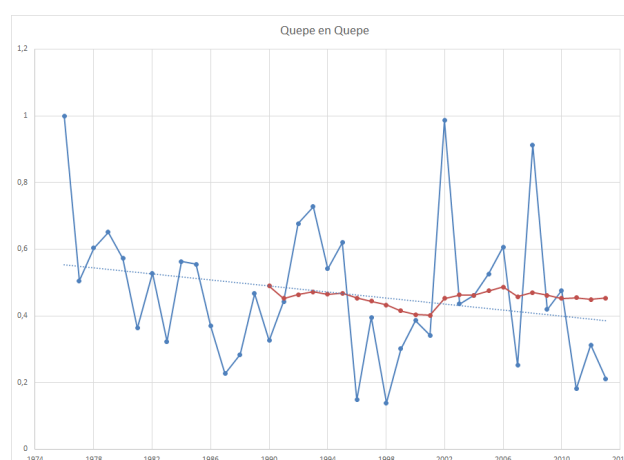

Figure 12. Annual Maximum Graph, with their moving averages (15) and trend line for Quepe en Quepe station. A negative trend is seen.

The graphic results of trends are summarised in Table 2.

Table 2. Graphic analysis of trends by basins.

Basin	Positive Trend	No Trend	Negative Trend
Mataquito	3	0	0
Maule	3	2	1
Itata	4	0	0
Biobío	1	3	3
Imperial	0	0	4
Toltén	2	0	0
Total	13	5	8

In the case of maximum precipitations, a total of 72 stations were selected following the criteria previously defined. The geographic distribution of the stations can be seen in Figure 13.

The daily maximum precipitation of the area is represented in Figure 14, where the isohlines in red represent the isohlines calculated with data of the last 30 years, and the isohyets in green correspond to the study carried out by the DGA in 1991.
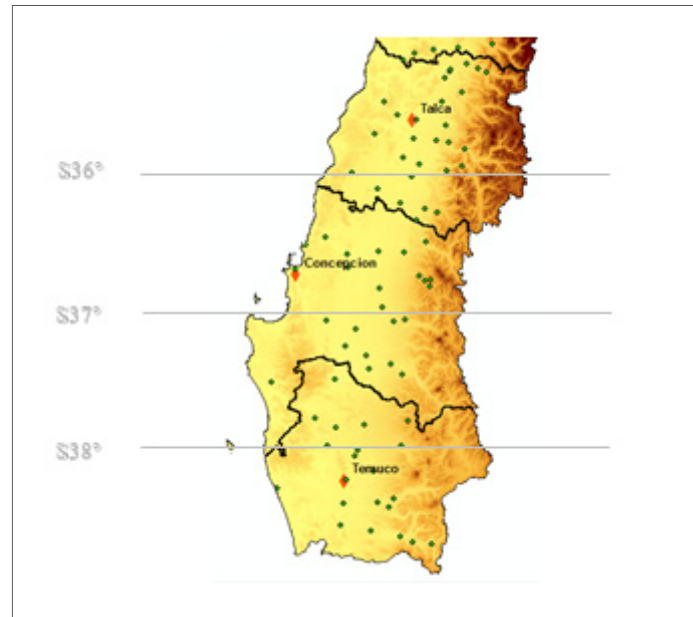
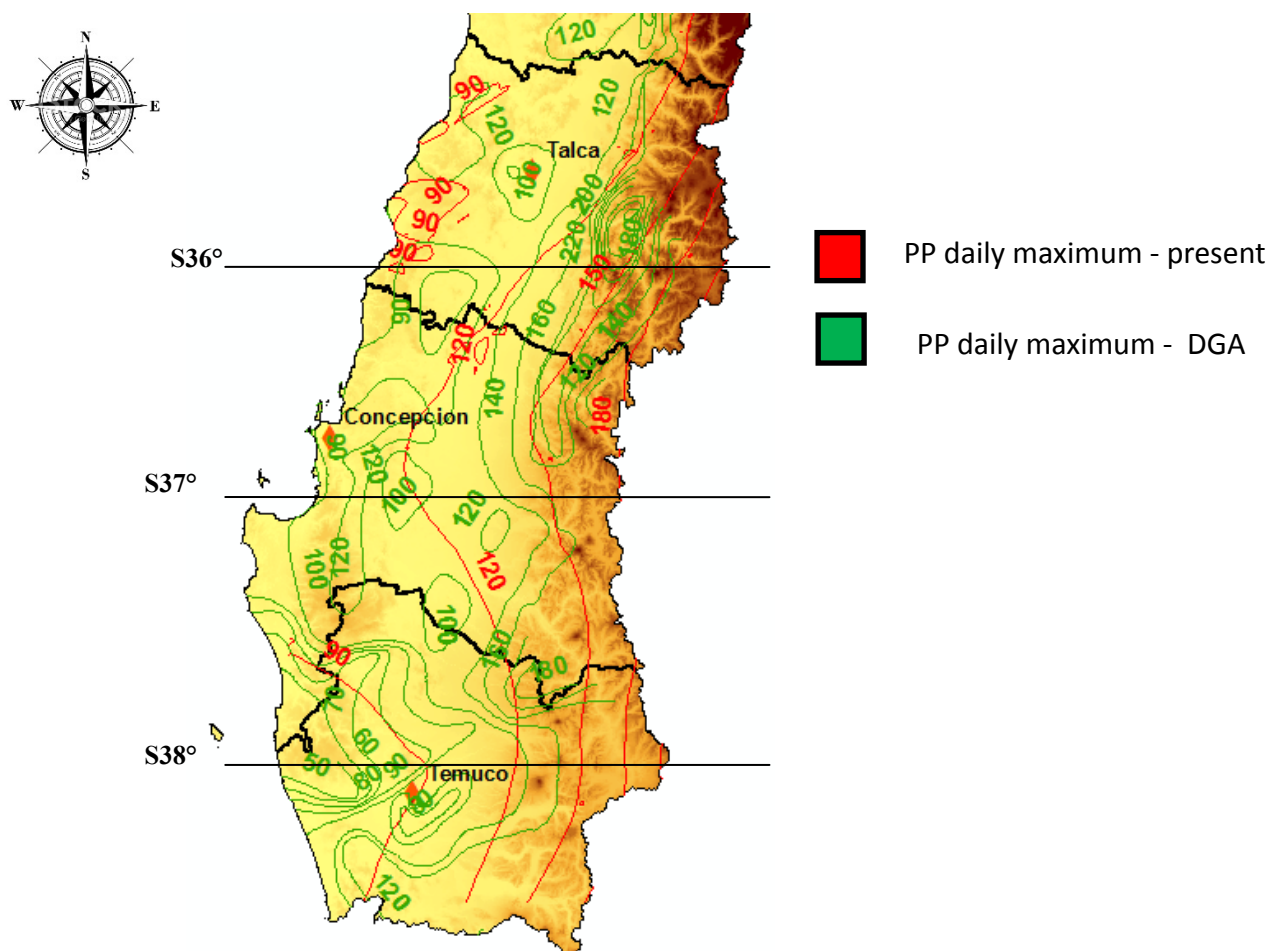**Figure 13.** Geographic distribution of rain gauge stations.

Figure 14. Isohyets of daily maximum precipitation.

When analysing the changes in maximum precipitations, all localities that have a rain gauge station were taken into account. It is important to point out that many of the main localities of the area didn't have a precipitation measuring station; therefore, it was impossible to use them in the analysis. That way, the number of examined stations decreased significantly and comparatively it was much lower than the total of stations that were used in the study.

After the localities were defined, the values measured in 1991 were compared with the ones obtained in the last 30 years, finding increases and decreases within the different regions. This exercise was carried out in the most important cities and localities of the studied territory. It was found that 60% of them reduced its daily precipitation value, while the remaining 40% presented a precipitation increase comparing with the study from 1991. The interesting aspect of this result is that the majority of stations that presented an increase in the daily maximum values are located in high latitudes.

6   COMMENTS AND CONCLUSIONS

Regarding the floods, it can be pointed that out of the 26 stations, 13 have an increasing trend, 5 present no trend and 8 stations have a decreasing trend. Although this result does not indicate a clear trend in the area of study, by analysing the basins some conclusions can be drawn.

In the basins of Mataquito (34°50´- 35°30´S), Maule (35°05´- 36°30´S) and Itata (36°00´-37°20´S), the majority of the analysed stations have an increasing trend. In the Biobío Basin (36°42´- 38°49´S), dominates the stations with no trend, or a small decreasing trend, and in the Imperial Basin (37°40´-38°50´S) all decreasing trends are found.

From this reasoning, it can be concluded that the area with latitude 36°46'S is a turning point, by not showing any trend and by dominating positive trends North of this latitude, and negatives to the South.

When analysing by latitude the magnitude and frequency of the maximum floods using series of partial duration, it can be determined that from 37°15'S, meaning from the Biobío basin to the North of the area of study the maximum flood has concentrated since 2000 and on. And further North, from latitude 35°30'S to the North, 6 out of 10 of the biggest floods in the last 40 years occurred during the last 15 years.

The increase in the annual maximum flows in the Mataquito basin (34°50´- 35°30´S) and Maule basin (35°05´- 36°30´S) might confirm, from a hydrologic point of view, processes of climatic change, which has generated a bigger flow input, due to the fact that no other phenomenon that affects greatly the flows are seen (Pizarro et al., 2013). The same could be concluded for the decrease in the maximum flows of the Imperial Basin (37°40´-38°50´S).

In regard to precipitations, the most relevant results indicated that the spatial distribution of rainfalls has not significantly changed during the last decades.

In the case of intense rainfalls in short periods, it is determined that in 40% of the analysed localities the precipitation value increased compared to the study of 1991, mainly in areas of high latitude.

The magnitudes of the daily maximum precipitation have an opposite behaviour to the one of the floods, that is, they have been increasing in high latitudes and decreasing in lower latitudes of the area of study during this period. From this, it can be concluded that there is no direct relation between this two variables. Therefore, the floods are not completely explained by high intensity precipitations, but there are other factors that affect the creation of maximum flows.

REFERENCES

Carrasco, J., Casassa, G., Pizarro, R. & Saravia, M. (2011). *Impactos del Cambio Climático, Adaptación y Desarrollo en las Regiones Montañosas de América Latina*. Santiago. Chile

Fuenzalida, H., Aceituno, P., Garreaud, R., Rojas, M. & Falvey, M. (2006). *Estudio de la Variabilidad Climática en Chile para el siglo XXI*. Informe. Realizado por el Departamento de Geofísica de la Universidad de Chile para CONAMA. Santiago.Chile

Garreaud, R. (2011). Cambio Climático: Bases físicas e impactos en Chile. *Revista Tierra Adentro (INIA-Chile)*, 93, 13-19

Ortiz, F. (2015) *"Evolución de la frecuencia y magnitud de las crecidas en cuencas de la VII, VIII y IX regiones"*. Memoria para optar al título de Ingeniero Civil. Universidad de Concepción.Chile.

MOP – DGA (1991) *Precipitaciones Máximas en 1, 2 y 3 Días.* Dirección General de Aguas. Chile.

Quintana, J. M. (2012) *Changes in the rainfall regime along the extratropical west coast of South America* (Chile):30-43° S Atmósfera vol.25 no.1 México

Pizarro, R., Balocchi, F., Vera, M., Aguilera, A., Morales, C., Valdés, R., Sangüesa, C., Vallejos, C., Fuentes, R., Abarza, A. & Olivares, C. (2013) Influencia del cambio climático en el comportamiento de los caudales máximos en la zona Mediterránea de Chile. *Tecnología y Ciencias del Agua*, 4(1), 5-19.

Vicuña, S., Gironás, J., Meza, F.J., Cruzat, M.L., Jelinek, M., Bustos, E., Poblete, D., & Bambach, N., (2013). Exploring possible connections between hydrological extreme events and climate change in central south Chile. *Hydrological Sciences Journal*, 58(8), 1598–1619.

ANALYSIS OF RAINFALL IN AN ARID ZONE OF SOUTH AMERICA

JOSE VARGAS BAECHELER[1] & PABLO VIDAL SALAZAR[2]

[1]Department of Civil Engineering, University of Concepción, Concepción, Chile
jvargas@udec.cl; pvidals@udec.cl

ABSTRACT

The aim of this paper is to study the rainfall patterns of an arid zone of South America located in the Norte Grande of Chile. In addition, the current temporal and spatial distribution of rainfall is analyzed and possible rainfall patterns reevaluated during these last years. For this evaluation, several annual and daily rainfall isohyet maps have been made. For this, working with data of current rain gauge stations, quantifying and selecting the most suitable data for the period of time to study. Finally, the required rainfall values are generated where the values are interpolated to create isohyet maps. The most relevant results indicate that the spatial distribution of rainfall has not significantly changed during the last decades. However, the average annual rainfall values have gradually decreased throughout this period. Based on this, it is presumed that they will continue with this decreasing trend.

Keywords: arid zones, rainfall, *Wadis*, ENSO, PDO.

1   INTRODUCTION

Precipitation is a phenomenon that by nature is not easy to predict. In the arid zones of the world, this phenomenon is scarce, erratic and highly variable both in time and space (Salas, J. D., 2000).

Although it seems illogical, in arid zones the bare soil is exposed to diverse physical and chemical processes which form a "crust" on the surface, which considerably reduces the infiltration capacity in these zones (Assouline, S., et al., 1997; Mualem, Y., 1997), the "crust" is shown in Figure 1.

Figure 1. Superficial crust (Sabkha), UAE (Sen, Z., 2008).

These zones are characterized by scarce and highly infrequent rainfall events. However, when these events occur, these are presented as convective storms which results in intense rainfall in a reduced time and space.

These characteristics and others make us think that arid zones are atypical places and are prone to generate extraordinary phenomena and so far these are rarely known, as is the case of *Wadis* or commonly called Floods.

Wadis are an ephemeral stream where torrents sporadically flow, these occur in arid or semi-arid zones and are generally caused by convective storms (Salas, J. D., 2000). They have lots of energy, which results in a high erosive capacity and sediment transport, therefore they can be highly destructive and risky for mining sites and/or residential areas located in arid zones (Sen, Z., 2008), as is the case in the Norte Grande of Chile (17º-27ºS, 68º-71ºW). Particularly, in the arid zone of South America, *Wadis* or Floods have become more frequent and intense in recent years, possibly due to the effects of El Niño-Southern Oscillation (ENSO), Pacific Decadal Oscillation (PDO) and others, causing significant economic losses and jeopardizing human lives.

It should be noted that in South America there are no official studies that propose concrete solutions to the phenomenon of *Wadis* in arid zones, despite the fact that these continually threaten the population and mining sites of northern Chile and most of desert zones of the world.

Therefore, this work is part of a macro study that seeks to understand the main characteristics of *Wadis*. The long-term purpose of this work is to identify the most flood-prone zones and ideally to predict when they might occur, thus to protect both inhabitants and different engineering works of the zone, or to somehow make the most of the immense energy they possess and to store the enormous water volume they carry. In order to achieve the main objective of this macro study, it was decided to study the weather that the arid zone of the Norte Grande of Chile possesses and then to study in detail the rainfall patterns of this zone.

2   FIELD OF STUDY

According to definitions, about 47% of the land surface can be classified as arid zone (Kassas, 1995). Although there are no clear territorial boundaries, arid zones are considered as the areas where average rainfall is less than the potential humidity losses through evaporation and transpiration. According to the World Atlas of Desertification (Kassas, 1995), arid zones have an average annual rainfall (AAR) vs. a potential evapotranspiration (PET) ratio lower than 0.65 (AAR / PET <0.65).

A great part of the world's arid zones are found near the tropics of Cancer and Capricorn, specifically between 20º and 35º latitude. Between these latitudes the most arid deserts in the world can be found such as the Sahara, the Gobi, and the Atacama, among others. The Atacama Desert is precisely located within the study area, the Norte Grande of Chile, located in South America between 17º - 27º South latitude and between 68º - 71º West longitude. See Figure 2.

Figure 2. The red area represent the Norte Grande of Chile, South America.

This arid zone borders to the north with Peru, to the east with Bolivia, to the south with the Copiapó River (27º25' S) and to the west with the Pacific Ocean. It extends throughout 4 regions of Chile: Arica and Parinacota, Tarapacá, Antofagasta and the northern half of the Atacama Region (See Figure 3).
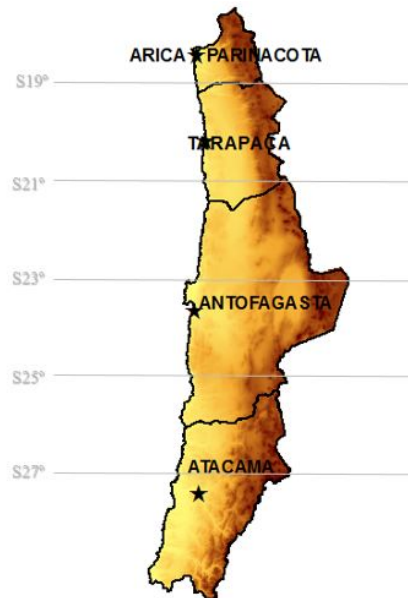
Figure 3. Map of the Norte Grande of Chile, South America.

The weather of this continental zone is influenced by the proximity of the Pacific Ocean and the South Pole, the orographic effect of the Andean Mountains, the Chilean Coastal Range and other mountain ranges, as well as the general atmospheric circulation, with the great influence of the South Pacific High and its position. The permanent warm anticyclonic influences eliminate almost all the possibilities of receiving effects of polar fronts. In the coastal and central zones, there is practically no precipitation and humidity is very low. Occasionally, bad weather fronts enter into the coastal and central zones which can generate severe rainfall events, causing significant damage due to their unexpected nature. However, in the eastern zone, formed by a high plateau, it receives summer rains similar to the ones on the Amazon and also snow accumulation in high peaks. This particular characteristic of the zone allows that the average of annual rainfall gets to 200 mm on high Andean plateau zones.

In relation to the hydrological factors of the zone, rainfall is scarce and variable both in time and space. Convective rainfall, typical in this zone, tend to be highly intense, of short duration and they affect reduced surfaces. These usually occur after noon or even more often in the afternoon and evening. This makes that rainfall have a daily periodicity at smaller time scales, e.g. hourly (Obeysekera et al., 1987).

In relation to the geomorphological factors, these are the result of several geophysical (tectonic, volcanic, and climatic), geochemical, biological events and processes; and anthropogenic factors which contribute, in different ways, to the relief and shapes of the world's diverse landscapes. In the case of desert arid zones, such as Chile, there are extensive plains covered with sand and with scarce or almost no vegetation. In addition, there are more rugged reliefs and even rocky mountains. The soil is usually dry, sandy, and rocky, with a lot of roughness and with cliffs, which are formed by the erosion of wind, temperature and intense rainfall.

Furthermore, in relation to the flora and fauna of the zone, although the conditions are not suitable for the growth and development of life, there is a variety of species that have adapted to these conditions. The flora tends to be prickly to allow the efficient heat loss, have less wind-exposed surfaces and grow with enough space between them to use the available water the best possible way. The fauna of these desert areas are mainly spiders, locusts, scorpions, snakes and others for a domestic use such as goats, camels, donkeys, cattle and others. (Heathcote, 1983).

3   METHODOLOGY

The most relevant procedures used to obtain the several rainfall isohyet maps, on which the final analysis of the investigation was based are presented below.

3.1   Geographical distribution

A registry of all the current rain gauge stations located in the study area, which contained daily, monthly and annual rainfall data was first carried out. There were a total of 55 research stations. Then, it was necessary to determine how these stations were distributed in the zone, and thus to see if they actually covered the territory under study, or if they just were located in a particular place.

The software ArcGIS was used to elaborate a map of the Norte of Chile, which contained its characteristic relief, its respective regional boundaries, and the spatial location of each of the 55 rain gauge stations. Figure 4 shows the geographical distribution of the stations considered in the analysis.
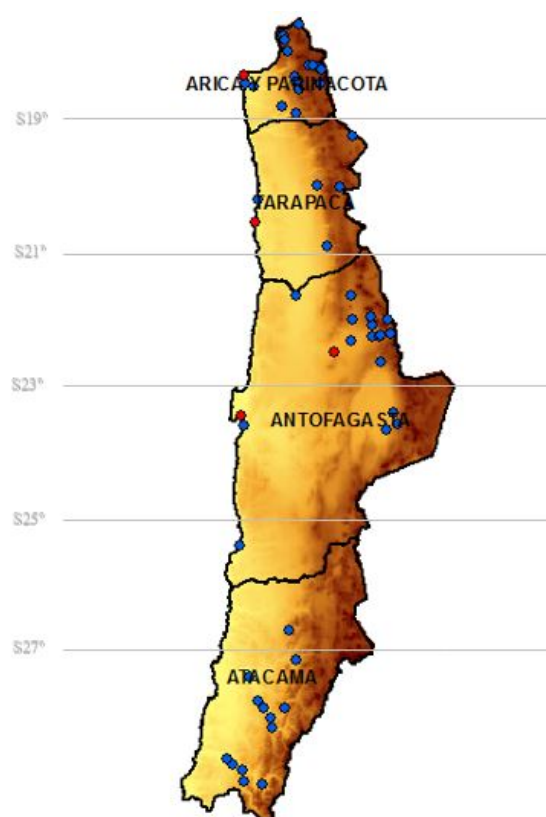
Figure 4. Geographical distribution of the evaluated stations.

3.2   Period of analysis

After having the exact number of stations for the analysis with their respective coordinates, it was necessary to choose the time period on which the study was going to be based. For this, three possible periods of analysis were proposed and for each the number of stations that they contained and the extension of the period were calculated. Subsequently, the periods were compared to each other, the advantages and disadvantages of each were examined, and finally the optimal period was chosen. Table 1 summarizes the three different periods of analysis and their respective characteristics.

Table 1. Possible periods for the study.

Period of analysis	Nº of Years	Number of rain gauge stations				
		Arica and Parinacota	Tarapacá	Antofagasta	Atacama	TOTAL
I (1975 – 2015)	40	11	0	10	11	32
II (1985 – 2015)	30	17	6	19	13	55
III (1995 – 2015)	20	19	6	21	15	61

In order to choose the optimal period of analysis, it was necessary to maximize the registry of continuous years and the number of rain gauge stations, since both provide more accurate results. However, these variables were inversely proportional to each other, since as the registry of continuous years increased the number of stations decreased. That is, the longest period (period I) is the one that contains the least number of available stations, and the least extensive period (period III) has the highest number of available stations, see Table 3.2.

Finally, after examining the characteristics of each of them, period II was chosen for the development of this work. For the election, both the length of the period and the current number of stations were maximized. Although the longest period was period I with 40 years of measurements, this did not contain enough stations in relation to the other 2 periods. On the other hand, period III had 6 more stations than period II, but the II had 10 more years. That was the main reason to choose period II, composed of 30 years of data, to carry out the analysis of the present work.

3.3 Average Annual Rainfall

The first analysis carried out with these data was to determine the Average Annual Rainfall (AAR), during the selected time period (1985 – 2015), and for each of the 55 stations. That is, 55 AAR values were obtained, one for each rain gauge station.

3.4 Maximum Daily Rainfall

Similar to the AAR analysis, a Maximum Daily Rainfall (MDR) analysis associated to a return period of 10 years was performed. For this, the next steps were followed to each of the rain gauge stations:
(i) The 365 days of the year for each of the 30 years of the study period were observed and for each of them the daily rainfall value was examined, and only the highest value was registered. (ii) For each of the 30 years of study the MDR was obtained, i.e. 30 MDR values for each station. (iii) Then, based on these 30 values, it was necessary to find the MDR with a return period of 10 years, therefore, the 30 values were inputted in the software "Easyfit", which adjusted diverse "probability functions" (Gamma, Lognormal, Pearson, etc.) to the 30 data of each station. (iv) Subsequently, a "goodness of fit" test (Kolmogorov-Smirnov) was done to each probability function, and based on the evaluation of the test, the function that best fit the data was selected. (v) Afterwards, using this software function, the rainfall value which exceeded 10% of the time was found, i.e. the value associated with a return period of 10 years. (vi) Finally, this value represents the maximum rainfall in 1 day associated with a return period of 10 years, for that particular station. That way 55 values were obtained, one for each rain gauge station.

It should be noted that the maximum rainfall in 2 days was determined with the same procedure, for each station, also associated with a return period of 10 years.

3.5 Spatial Interpolation

Once the AAR and MDR values were obtained for each station, spatial interpolation was required. This technique, in general, is the process of manipulating spatial information to extract new and meaningful information from the original data. Usually the spatial interpolation is run with a Geographic Information System (GIS). A GIS provides spatial analysis tools to calculate statistics and to perform geoprocessing activities such as data interpolation. In simple terms, spatial interpolation estimates the value of a variable at an unknown point from other nearby points, in which the value of that variable is known. Currently, geostatistical techniques are a useful tool in the spatial prediction of variables such as rainfall, temperature and others.

The main technique of interpolation, used in this work, for the development of rainfall isohyets is briefly described below.

3.5.1 Cokriging

This technique provides a kind of value interpolation for non-sampled points in situ, using the knowledge about the underlying spatial relationships by making it into a set of data. Cokriging is superior to other interpolation techniques, since it has the advantage of better estimating the value of a variable of interest using values of other correlated variables that are better sampled. If measuring the primary variable is difficult or has a high monetary value, then this tool can greatly improve the interpolation calculations without having to exhaustively test that variable. The variables correlated to the study are incorporated by the elaboration of a cross variogram that considers the spatial correlation of the variables (ESRI, 2010; Childs, 2004).

4 RESULTS

The purpose of this section is first to visualize the results of the interpolations, and then to perform an analysis of them and the phenomena that are observed, to finally raise certain questions and formulate conclusions.

The performed interpolation made it possible to elaborate two types of rainfall isohyets, those of Average Annual Rainfall and those of Maximum Daily Rainfall.

4.1 Average Annual Rainfall Isohyets

As was previously mentioned, the isohyets were made with the Cokriging interpolation technique using the 55 rain gauge stations in the 30 year period between 1985 and 2015. The result of these isohyets are shown in Figure 5a.
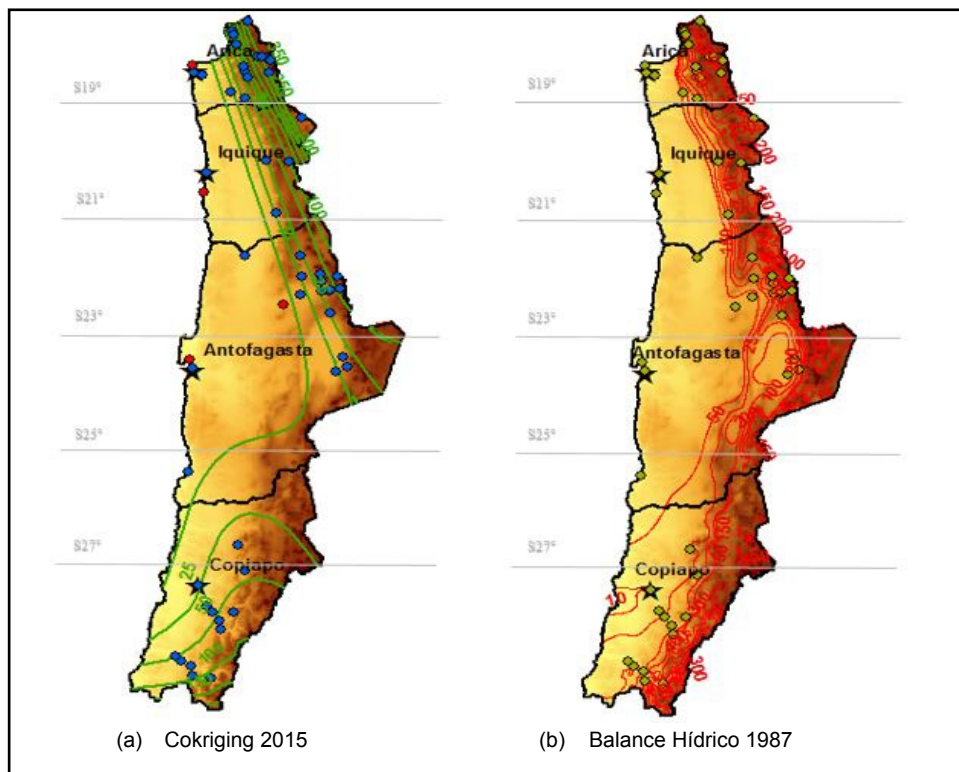
(a) Cokriging 2015   (b) Balance Hídrico 1987

Figure 5. Average Annual Rainfall Isohyets.

The first analysis performed was a visual comparison between the isohyet maps, made with Cokriging, and an equivalent previous study, in the same zone, published in 1987. This study was titled "Balance Hídrico de Chile" (B.H. 1987). See Figure 5b.

Comparing both figures, a high degree of similarity can be seen in the shape of the isohyets and the position they occupy within the study area. It was observed that in both cases rainfall intensifies as we move towards the Andean zone, indicating a clear increasing trend in the East direction.

On the coastal zone, a large fraction of it remains free of rainfall; from Copiapó to the South zone low rainfall values are visualized, phenomenon that can be seen in both figures. On this basis, it can be affirmed that the spatial distribution of rainfall has mainly remained during these last years. Nevertheless, that does not mean that the magnitudes of rain events have also remained, they could have increased or decreased.

In order to determine whether rainfall values during the last 30 years (1985 – 2015) have increased or decreased compared to the 30 previous years (1955 – 1985), on which the 1987 study was based, AAR values from the common rain gauge stations in both studies were examined (B.H. 1987 and the present study), thus a consistent results were obtained.

Of the 55 rain gauge stations used in the present study, 49 were also used in the 1987 study. The AAR values of these 49 stations were compared in both studies. Some of these results are shown in Table 2.

Table 2. AAR values of the Balance Hídrico 1987 vs Cokriging 2015.

Nº	Name of the station	Latitude S	Longitude W	Altitude (m.a.s.l.)	AAR - B.H. 1987 (mm)	AAR - Cokriging (mm)	VARIATION
1	V. INDUSTRIAL	17 46 00	69 43 00	4080	337,10	271,73	Decreased
2	ALCERRECA	17 59 00	69 39 00	3990	193,60	204,36	Increased
3	GUALLATIRE	18 29 00	69 09 00	20	344,80	230,14	Decreased
4	AZAPA	18 30 00	70 10 00	365	2,30	0,80	Decreased
5	CHIU-CHIU	22 20 00	68 38 00	3240	3,50	5,10	Increased
6	C. CHAPIQUIÑA	18 22 00	69 32 00	3350	195,50	149,05	Decreased
7	CHUC. RETEN	18 12 00	69 17 00	4400	338,20	328,38	Decreased
8	HUMAPALCA	17 50 00	69 42 00	4585	306,00	258,93	Decreased
9	CHUN. RETEN	18 16 00	69 08 00	4570	331,00	270,93	Decreased
10	CODPA	18 49 00	69 44 00	1870	13,40	17,75	Increased

This table represents an extract from the original table, which contains the 49 common stations compared in both studies. The summary analysis of the original table is shown in Table 3.

Table 3. Proportion of stations in which their AAR value varied.

VARIATION	Number of stations	Percentage (%)
Increased	18	36,7
Decreased	31	63,3
TOTAL	49	100

Based on Table 3, it is concluded that the AAR value of the common stations mainly decreased compared to the equivalent previous study (B.H. 1987). This current deficit in the annual rainfall coincides with what Schulz et al. (2012) and Boisier et al. (2016) affirm.Finally, to complement Tables 2 and 3, a map was elaborated to show the location of the stations where AAR increased/decreased. The circles in red represent the 31 stations in which rainfall decreased, while the green circles represent the 18 stations in which that variable increased. Now, the stations in which the rainfall variation was significant, these were represented with larger circles, maintaining the same colors. A significant variation was considered when the variable increased or decreased around 40% or more. See Figure 6.
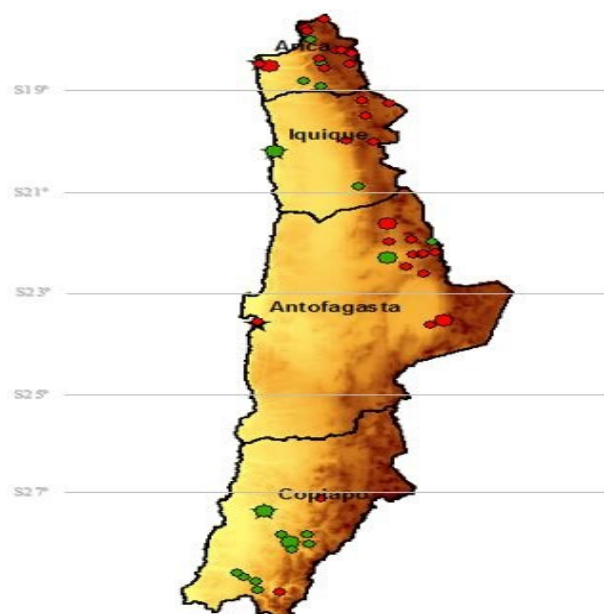

Figure 6. Stations in which AAR increased/decreased.

4.2 Maximum Daily Rainfall Isohyets

Similar to the AAR isohyets, these were made with the Cokriging technique and the same 55 rain gauge stations were used, in the same period of 30 years. These correspond to maximum rainfall isohyets in 1 and 2 days associated to a return period of 10 years. The result of each of these two cases is shown in Figure 7a and Figure 7b, respectively.

Simultaneously observing the results of both maps, there are no significant differences between them. Both of them have a clear increasing trend towards the Andean zone and a certain increase of rainfall as we move towards the South, that phenomenon is clearer observed from Copiapó to the south.

When representing the values of maximum rainfall in 1 and 2 days, which are known to be highly influenced by the orography of the zone (Sen, Z., 2008), the isohyets show a close correlation with the local relief, which supports the erratic and variable nature of convective storms that occur there.

Subsequently, a comparison between the isohyets of maximum rainfall in 1 day, Figure 7a, and equivalent isohyets was carried out, these last were obtained in an earlier study in 1991. This study was titled "Precipitaciones máximas en 1, 2 y 3 días".

Specifically, a contrast between the maximum daily values of rainfall of that time, and the values obtained in the present study was completed in the main localities of the zone.
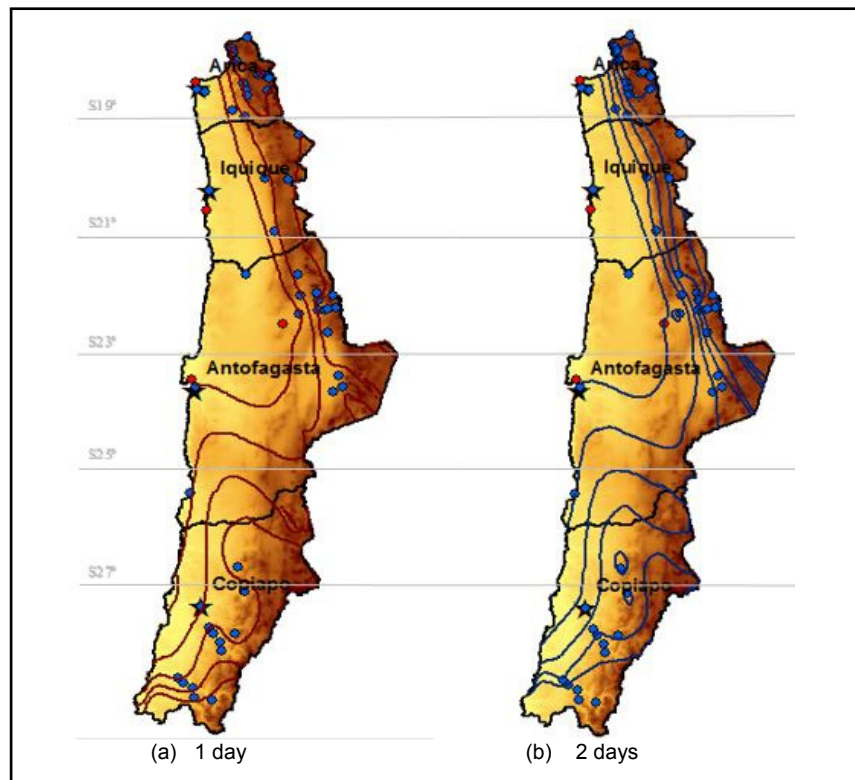
Figure 7. Maximum Daily Rainfall Isohyets.

In the same way of the AAR comparison, it was necessary to examine the values of the common rain gauge stations in both studies, in order to determine whether the MDR values had recently increased or decreased. However, the previous study (1991) did not show these values, therefore it was not possible to examine the rainfall values of each station. In fact, the main locations of the zone and the rainfall values of these were examined, guided by the isohyet maps of both studies. See Figure 8.
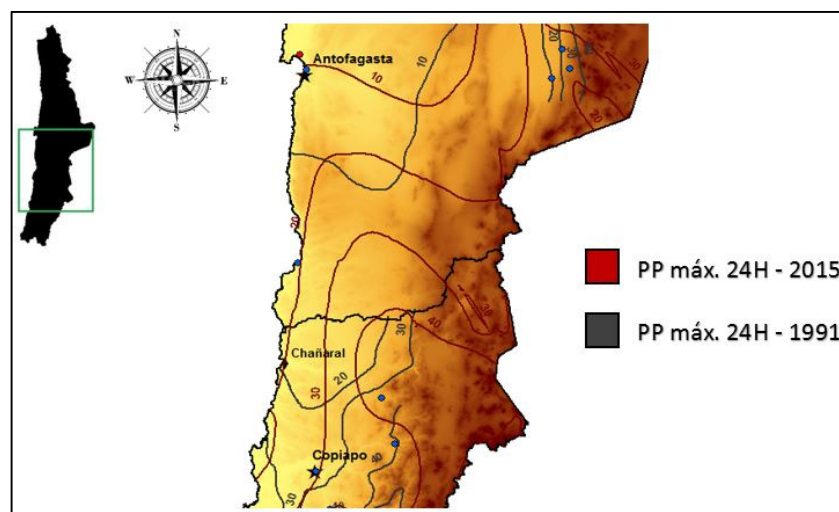

Figure 8. Maximum Daily Rainfall Isohyets; 1991 vs 2015.

Figure 8 illustrates a close-up view of a particular fraction of the studied area (23º - 28º S), which includes a section of the II Region of Antofagasta and other section of the III Region of Atacama. The dark red lines represent the maximum rainfall isohyets in 1 day elaborated in this work and the dark gray lines symbolize the equivalent isohyets made in the 1991 study.

The analysis performed of this figure was:

(i) Select a location on the map to evaluate it, for example Copiapó. (ii) Observe the old isohyets (gray) and define between which isohyets Copiapó is located. (iii) In this case, it is located between the 20 and 30 mm. (iv) An approximate value of the MDR (between 20 and 30 mm) is visually estimated for Copiapó, in this case approximately 27 mm. (v) The same procedure is performed for the red isohyets (new ones). (vi) In this case,

it is exactly 30 mm. (vii) Finally, the two values were compared, and it was concluded that if in the past it rained 27 mm a day and at this time 30 mm, then that variable has recently increased, at least in that particular location. (viii) Repeat the same procedure for the different locations or important cities.

After executing the same procedure for the most important cities and locations in the Norte Grande of Chile, it is evident that about 50% of them did not show a variation of the MDR, while 40% of the locations showed an increase of rainfall compared to the previous study. It is important to mention that most of the locations in which MDR increased are located near Copiapó and Antofagasta. In fact, these two cities have been repeatedly damaged in the last decades by powerful floods produced by intense rains. (Vargas et al., 2000; Garreaud and Rutllant, 1996; Maldonado Solís et al., 2016).

5   CONCLUSIONS

The analysis of the results of the AAR indicated that the spatial distribution of rainfall has mainly remained in the Norte Grande of Chile during these last decades. The increasing trend of rainfall has remained towards high Andean plateau zones, while the coastal zone is still characterized by a dry and rain-free weather. However, this does not imply that the magnitude of rainfall events has remained. In fact, it was found that rainfall has been gradually decreasing in recent years (Boisier et al., 2016) and based on the trend, it is presumed that this situation will continue the same way (Schulz et al., 2012). This condition could only be modified by possible effects of inter-annual and/or inter-decadal variation (Montecinos, 2015; Mantua 1997).

In relation to the results obtained from the maximum precipitation in 1 day with a return period of 10 years, it was determined that around 40% of the locations and cities of the zone registered a rainfall increase compared to the equivalent study carried out in 1991.

In general, it seems that the rainfall pattern in the area is changing, since rainfall events in the north area are becoming increasingly scarce, decreasing the number of rainy days, which could also imply the reduction of the total annual rainfall. Moreover, intense rainfall events, such as convective storms, are apparently becoming more usual, which would possibly increase the probability of generating floods and *Wadis* in the arid zone of the north of Chile.

Finally, due to the climatic characteristics of the studied arid zone, such as the temporal and spatial variability of rainfall and its erratic nature (Salas, JD., 2000), there could be some uncertainty linked to the results of this kind of studies (Schulz et al., 2012).

REFERENCES

Assouline, S. & Mualem, Y. (1997). Modeling the Dynamics of Seal Formation and Its Effect on Infiltration as Related to Soil and Rainfall Characteristics. *Water Resources Research*. 33(7), 1-10.

Boisier, J. P., Rondanelli, R., Garreaud, R. D. & Y Muñoz, F. (2016). Anthropogenic and Natural Contributions to the Southeast Pacific Precipitation Decline and Recent Megadrought in Central Chile. *Geophysical Research Letters*. 43(1), 413-421.

Childs, C. (2004). *Interpolating Surfaces in Arcgis Spatial Analyst*. Arcuser. July-September, 32-35.

ESRI (2010) *Arcgis. Version 10.1.* Environment System Research Institute.

Garreaud, R. & Y Rutllant, J. (1996). Análisis Meteorológico De Los Aluviones De Antofagasta Y Santiago De Chile En El Período 1991-1993. *Atmósfera*, 9(4), 251-271.

Heathcote, R.L. (1983). *The Arid Lands: Their Use And Abuse*. Longman. London. England.

Kassas, M. (1995). Desertification: A General Review. *Journal of Arid Environments*, 30(2), 115-128.

Maldonado Solís, S., Durán, M., Trujillo, R., Sáez, H., Fernández, A. & Y Vojkovic Acevedo, E. (2016). *Evaluación De Predios Agrícolas Afectados Por Aluviones En La Región De Atacama: Comunas De Copiapó Y Tierra Amarilla*, Centro De Información De Recursos Naturales. Chile.

Mantua, N. J., Hare, S. R., Zhang, Y., Wallace, J. M., & Francis, R. C. (1997). A Pacific Interdecadal Climate Oscillation With Impacts On Salmon Production. *Bulletin of the American Meteorological Society*. 78(6), 1-11.

Montecinos, A. (2015*) Generación De Modelos Climáticos Para El Pronóstico De La Ocurrencia Del Fenómeno El Niño. Boletín Técnico*, Instituto Geofísico Del Perú (IGP). 2(1).

Obeysekera, J. T. B., Tabios, G. Q. & Y Salas, J. D. (1987). On Parameter Estimation Of Temporal Rainfall Models. *Water Resources Research*. 23(10), 1837-1850.

Salas, J. D. (2000). Hidrología De Zonas Áridas Y Semiáridas. *Ingeniería Del Agua*. 7(4), 409-429.

Schulz, N., Boisier, J. P. & Y Aceituno, P. (2012). Climate Change along the Arid Coast Of Northern Chile. *International Journal of Climatology*, 32(12). 1803-1814.

Sen, Z. (2008). *Wadi Hydrology*. CRC Press. New York.

Vargas, G., Ortlieb, L. & Y Rutllant, J. (2000). Aluviones Históricos En Antofagasta Y Su Relación Con Eventos El Niño/Oscilación Del Sur. *Revista Geológica De Chile*, 27(2), 157-176.